Supported Nanoparticles: From Electrochemical Deposition to Electrocatalytic Properties

Wenbo Ju

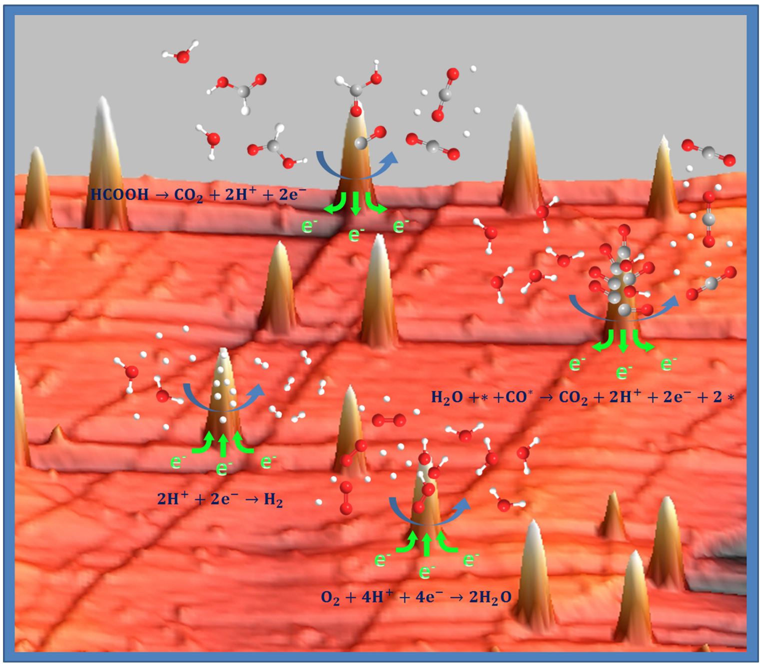

München 2016

TECHNISCHE UNIVERSITÄT MÜNCHEN

Fakultät für Physik

Technische Physik

Supported Nanoparticles: From Electrochemical Deposition to Electrocatalytic Properties

Wenbo Ju

Vollständiger Abdruck der von der Fakultät für Physik der Technischen Universität München zur Erlangung des akademischen Grades eines

Doktors der Naturwissenschaften (Dr. rer. nat.)

genehmigten Dissertation.

Vorsitzende(r): Univ.-Prof. Dr. M. Knap
Prüfer der Dissertation: 1. Univ.-Prof. Dr. U. Stimming
(schriftliche Beurteilung)
2. Priv.-Doz. Dr. O. Schneider
(mündliche Prüfung)
3. Univ.-Prof. Dr. A. S. Bandarenka

Die Dissertation wurde am 22.03.2016 bei der Technishcen Universität München eingereicht und durch die Fakultät für Physik am 03.05.2016 angenommen.

Acknowledgments

I would like to give the deepest appreciation to PD. Dr. Oliver Schneider, who is a respected scientist dedicating immeasurable time and energy to research, scholarship and teaching. His suggestions help me solve many theoretical and practical problems. The discussions with him are always interesting and fruitful. Without his guidance and persistent help this dissertation would not have been possible.

My sincere acknowledgment is given to Prof. Dr. Ulrich Stimming for offering me the position in his group in Munich and supervising me the doctoral research. His profound knowledge and innovative ideals are always encouraging me to learn from former colleagues and to explore unknown fields.

I would like to express the appreciation to Prof. Dr. Aliaksandr Bandarenka for kind help in research and administration. He has revised this dissertation and given many constructive comments.

My acknowledgment is given to all the colleagues in the former E19 and in the ECRG. The experience of working with them in four years is an invaluable treasure in my life. Here I would like to specially thank Dr. Tine Brülle, who helped me with great patience at the beginning of the topic. Thanks are given to Prof. Dr. Gaetano Granozzi and his group at the University of Padova for the fruitful collaboration, especially, to Dr. Marco Favaro who collaborated with me in many experiments and in the preparation of articles and a project report. I would like to thank the technicians who maintained the equipment in the lab, manufactured mechanic and electronic parts in the workshop. The acknowledgment is given to all the people who helped me during the preparation of this dissertation.

The research leading to this dissertation has received funding from the European Union's Seventh Framework Programme (FP/2007-2013) for the Fuel Cells and Hydrogen Joint Technology Initiative under grant agreement n°[303492], from Deutscher Akademischer Austauschdienst (DAAD) within the Vigoni bilateral program and from the Carl von Linder foundation at Technische Universität München, which is gratefully acknowledged. I would like to thank the China Scholarship Council for financial support. I thank the American Chemical Society and the Beilstein-Institut for permissions to include copyrighted figures as part of my dissertation.

At last, I would like to thank my wife, Yue Yuan, and my parents. Without their persistent support and meticulous care this work would not have been completed.

Abstract

Electrochemical devices, such as fuel cells and batteries, are critical enabling technologies for energy conversion and storage. Proton exchange membrane fuel cells (PEMFCs) are a competitive technology to power electric vehicles for long-range driving. However, the world-wide commercialization and sustainable operation of PEMFCs still require lower cost, a high durability and better efficiency. Efforts are thus needed to enhance the activity and stability of catalysts for the electrode reactions, especially for the oxygen reduction reaction (ORR). This thesis discusses fundamental studies on the electrocatalytic behavior of Palladium (Pd) nanoparticles (NPs) supported on different substrates. In addition, the preparatory research for electrodeposition of highly active catalyst materials from ionic liquids is discussed.

Pd has a potential to substitute platinum (Pt) as electrocatalysts in PEMFCs. In this work, Pd NPs were deposited electrochemically on highly oriented pyrolytic graphite (HOPG) by applying a potentiostatic double-pulse technique. The particle densities for all samples were controlled in the order of 10^9 per cm^2. Particles grew in a constant-current mode with a narrow size distribution. The average particle size was adjusted by the growth pulse duration in a range of 1 to 50 nm. A size-dependent hydrogen absorption behavior was observed at Pd NPs when smaller than 8 nm. Smaller Pd NPs tend to have a lower hydrogen content due to the change of lattice structure. In the hydrogen evolution reaction (HER), Pd NPs showed an increased specific current density at selected potentials with decreasing particle size. The activity for HER is primarily affected by the hydrogen content in the Pd lattice. The binding energies of Pd NPs with oxygen atoms and carbon monoxide (CO) molecules increased with the decrease of particle sizes so that a higher overpotential for ORR and a higher oxidation potential for CO stripping were required at smaller Pd NPs. For formic acid oxidation, small Pd NPs showed relatively low activity and poor poisoning tolerance. If structural factors are considered with the change of particle size, small Pd NPs tend to possess more well-ordered (111) facets and a high ratio of edge and corner atoms.

Nitrogen-doped HOPG (N-HOPG) was used as substrate to investigate the influence of nitrogen functional groups to the activity and stability of supported Pd NPs. Increased oxidation states of Pd at the interface between Pd NPs and the substrates were detected by X-ray photoelectron spectroscopy (XPS) due to the strong electron withdrawing force of doped nitrogen. The oxidized Pd was vulnerable at moderate oxidation potentials so that the stability of the Pd NPs became lower. A support effect on the activity of Pd NPs for ORR was not observed in this work.

Some Pt-based rare earth metal alloys are known to be highly active for ORR, but a viable process for nanoparticle mass-manufacturing is still missing. In this early-stage investigation, ionic liquids were used as solvent for electrochemical studies on Pt-,

yttrium (Y)- and $\mathrm{Pt}_x\mathrm{Y}$ alloy deposition. Pt has been successfully deposited through a two-step process. However, no solid evidence can confirm the formation of metallic Y.

Contents

Chapter 1

Introduction

The continuous prosperity and economic growth in the present age require an affordable, reliable and sustainable energy supply. However, the conventional energy supply relies deeply on fossil fuels, and is therefore not sustainable. The worldwide energy consumption has soared unprecedented by more than 47 % in the past quarter century [1, 2]. If most of the nations keep current energy policies, it is predicted to increase by another 45 % in the next 20 years [1]. Global carbon dioxide (CO_2) emission, which is mainly from the combustion of fossil fuels, increased in 2013 to the new record of 35.3 gigatons [3]. Current road transportation, which is primarily powered by internal combustion engines by consuming liquid fuels (e.g. gasoline and diesel), contributes nearly one-fifth of the world's CO_2 emission and volume of pollutants [4, 5]. The rapid increase of CO_2 content in the atmosphere is expected to significantly impact the environmental system and human beings, such as the global warming, the acidification of oceans and the loss of human habitats in consequence of the sea-level rising. The harmful pollutants cause series of health issues, especially in urban areas. The world needs an energy revolution that the fossil fuels should be replaced by some new energy sources, which should be renewable, low or even none in CO_2 emission and pollution-free. A good sign has emerged in the past two decades that the market share of renewable energy has increased more than 8 times all over the world. Until 2014, renewable energy has produced nearly 6% of global electricity [2]. The international community is collaborating to upgrade the energy infrastructure and restrict the CO_2 emission. Extensive efforts have been made to develop the energy conversion and storage techniques. A systematic innovation is happening in industry, transportation, household and every aspect of our society.

Electrochemical devices, e.g., fuel cells and batteries, are able to convert chemical energy directly to electricity and vice versa through electrochemical processes. They are being extensively researched because of many advantages such as the partially high efficiency in energy conversion, simple mechanical structure and high flexibility for centralization and decentralization. Some electrochemical devices have been successfully marketed, e.g., batteries, especially lithium-ion batteries, are widely applied in portable electronic devices. The next opportunity will be in road transportation that electrochemical devices provide power instead of internal combustion engines.

Proton exchange membrane fuel cells (PEMFCs) are very competitive: the hydrogen-oxygen (H_2-O_2) reaction under standard conditions at 25 °C has a thermodynamic efficiency of 83 % by producing liquid water, and 94 % with gaseous water as product [6]; even under load their efficiency in the medium- or low-temperature running conditions can reach 50 % [7], which is still higher than that of heat engines of which the theoretical efficiency is limited by the Carnot cycle. Besides PEMFCs, some other devices, such as direct alcohol fuel cells (DAFCs) and direct formic acid fuel cells (DFAFCs), have good prospects to be applied in transportation, distributed power plants and portable electronics.

The overall performance of PEMFCs depends essentially on the activity of used catalysts at both electrodes. Platinum (Pt) is commonly used due to its excellent performance in activity and durability, while, as a precious metal, it contributes significantly to the cost. Although the improvement of the catalyst layer at both electrodes has been obtained in the past half century, which led a significant decrease of Pt loading from 35 mg cm^{-2} in the Gemini fuel cell system in 1960s down to 0.25 mg cm^{-2} in the state-of-the-art system in 2011 [8–10], the world-wide commercialization of PEMFCs has not yet achieved because of their weakness in durability and cost as compared with internal combustion engines and turbine engines. The targets of the US department of energy (DOE) are by 2020 to reach a cost of 40 $\$\,kW^{-1}$ and a lifetime of 5000 h for mobile H_2-O_2 fuel cells, and a cost of around 1000 $\$\,kW^{-1}$ and a lifetime of 60000 h for stationary fuel cells [9]. Many efforts are still needed to reduce the amount of precious metals in the membrane electrode assembly (MEA) without the decrease of activity and durability.

Catalysts at both PEMFC electrodes are commonly prepared in the form of nano-sized particles for the purpose of sustaining a high surface-to-volume ratio. As compared with bulk materials, the properties of the corresponding nanoparticles (NPs) show significant differences. Some physical or chemical properties are unable to be predicted with those of bulk materials, but show strong dependence on particle sizes. A single supported NP in contact with an electrolyte forms a complex system where several interfaces should be considered. Its electrochemical properties are influenced by many factors: low- / high-index facets, low-coordinated atoms (steps, defects, edge and corner atoms), particle size, support material, electrolyte and so on. If the NP consists of more than one element, the factor of the composition at surface or subsurface should be accounted for [11–13]. All aforementioned factors operate through two intrinsic effects: (1) a structural effect, by which some structure-sensitive reactions can be influenced through the ratio of active sites in all existing surface structures; and (2) an electronic effect, which identifies all the changes of electronic state at the active sites caused by the composition of NP, the support material and the solid-liquid interface. The knowledge of structural and electronic effects are obtained from both experimental and theoretical investigations. Some reactions are studied on single-crystal electrodes, of which the surface parameters such as facet, terrace width, step density and step structure are carefully adjusted, in order to recognize the structure-dependence of certain reactions, or to identify the active sites for a specified reaction. The understanding of structure effects guides the design of catalysts with the maximum ratio of desired surface structure, e.g., the development of shape- and structure-controlled nanocrystals in recent years [14–16]. Specific activities are mainly considered in these works, although stability issues should be solved as well. Theoretical simulations were addressed the adsorption energies of reaction intermediates on different surface structures in order to hunt for the most active structure, on which the key intermediate has a moderate adsorption strength [17–20]. The catalytic activity of a specified structure can be optimized through electronic effects. For example, the change of compositions at surface or subsurface of a catalyst can modify the electronic state of surface atoms, further, to influence their binding strength with reaction intermediates and thus the reaction rate. Some model structures of bimetallic, trimetallic catalysts as well as nanoclusters on specific substrates are intensively investigated [21–28]. The achievements are impressive, e.g., the discovery of Pt-based rare earth metal (REM) alloys as catalysts for oxygen reduction reaction (ORR) using density functional theory (DFT) computations [21, 27–29]. Until now, the knowledge obtained from the experiments on model structures and the theoretical simulations is widely used to describe and predict the properties of particulate and extended catalysts. However, the approaches still have limitations due to the high complexity of catalysts in practice and too many atoms for theoretical description. Two other descriptors, particle size and support material, are frequently used and, from the aspect of engineering, easy to control. At PEMFC electrodes, a strategy to keep a high performance at a low catalyst loading is to optimize the size of the catalyst and the support material [30]. Therefore, size effects and support effects are two significant topics in discussion of supported mono-metallic NPs.

Pt and Pt alloys are commonly used as state-of-the-art PEMFC catalysts in the form of highly dispersed NPs supported on high-surface-area carbon due to their high activity, especially for ORR, and stability in acidic media [31]. However, the widespread application of Pt is always limited by its high price (ca. 33 $\$\,\mathrm{g}^{-1}$ in Feb. 2016) and scarcity. As a member of platinum-group metals (PGMs), palladium (Pd) has a lower price than Pt (ca. 18 $\$\,\mathrm{g}^{-1}$ in Feb. 2016). Although the electrocatalytic activities of pure Pd for the hydrogen oxidation/evolution reaction (HOR/HER) and ORR are at least five times lower than those of pure Pt [32], the advantage of Pd in price is continuously driving the research efforts aiming to improve the Pd activity by surface modification and alloying. Previous investigations indicate that the catalytic properties of monometallic Pd NPs for ORR and formic acid oxidation (FAO) are size-dependent [33–39]. However, the optimal particle sizes for ORR and for FAO are still in debate. Some authors suggested that the Pd NPs did not have an optimal size for ORR [33–35], whereas others insisted that Pd NPs in the range of 5.0 to 6.0 nm had the best performance for ORR [36]. For FAO, the debate on “which particle size shows the highest activity” is still in presence [37–39]. The electrocatalytic activity of supported Pd NPs depends on many factors as discussed above. Any small difference in measurements leads to a divergence in the observed results. If the intrinsic properties of supported NPs, e.g., the surface composition and structure details, are supposed to be the same, some other factors such as the particle size distribution, the dispersion of particles on the substrate and the composition of the support material should be considered additionally in comparisons. In order to obtain a further understanding of the size-related effects, the particle size distribution should be restricted to a small range. The influence of support material and particle dispersion should be minimized as much as possible.

In this thesis, highly oriented pyrolytic graphite (HOPG), of which the carbon atoms are sp^2 hybridized to form a two-dimensional (2D) graphene layer, was used as substrate, when the size effect was investigated. Due to its chemical inertia and weak binding to noble metal particles, the support effect can be minimized, or even eliminated [40–42]. The HOPG surface exhibits a long-range atomic-level smoothness with few steps and defects. During an electrochemical deposition, metal particles nucleate predominantly at the steps and defects, which leads to an inhomogeneous dispersion of particles on the substrate [43]. Therefore, additional defects on the HOPG surface were created purposefully by electrochemical oxidation such that the homogeneously distributed defects provided locations for nucleation and growth of NPs. The potentiostatic double-pulse deposition method, in which one short-time high-overpotential nucleation pulse is followed by a long-time low-overpotential growth pulse, was used to prepare Pd NPs with a narrow size distribution [44–46]. The growth of metal particles on HOPG follows the Volmer-Weber mode so that three-dimensional (3D) metal particles grow uniformly in all directions [43]. The particle size was evaluated by the height obtained from taping-mode atomic force microscopy (TM-AFM) images. It is confirmed that the particle size can be effectively controlled by the duration of the growth pulse. From the TM-AFM images, the particle densities were observed to be of the same order of magnitude, when the nucleation parameters were kept the same, no matter of the duration of the growth pulse. The electrocatalytic activities of Pd NPs with different sizes were investigated for ORR and FAO. Additionally, the electro-oxidation of monolayer carbon monoxide (CO) was studied, in which a size-dependent CO oxidation peak was observed. The study of the HER on a Pd surface is obstructed in acidic media by the hydrogen absorption behavior of Pd. When the potential is in the range for HER, three hydrogen-related reactions,-adsorption, absorption and evolution-, take place at the same time [47]. According to the relation between the atomic ratio of hydrogen to Pd (H / Pd) and the open circuit potential (OCP) of Pd in a hydrogen saturated acidic solution, a size-dependent hydrogen absorption behavior of Pd NPs has been observed. The activity of Pd NPs for HER is considered to be strongly dependent on the hydrogen content in the Pd lattice.

The influence of a substrate on the catalytic activity of supported metal NPs is still in open debate [48]. Significant progress was made in the last decade when many authors discussed the support effect based on the intrinsic factors, namely, the structural and electronic effects [49–53]. Lattice strain, ligand effect, charge transfer between support and catalyst are all possible effects which can be introduced by a substrate. Pristine HOPG is an ideal substrate to minimize the support effect. Once some functional groups are introduced onto the HOPG surface, the support effect caused by these functional groups onto the supported metal NPs can be detected by some methods in surface science and electrochemistry. Several authors [54–56] have reported a beneficial effect of nitrogen doped HOPG (N-HOPG) on the electrocatalytic activity of supported Pt NPs for ORR. The nitrogen functional groups interact with supported Pt nanoclusters leading to a downshift of the Pt d-band center. The Pt nanoclusters with a lower d-band center bind the atomic oxygen a bit weaker so that the oxygen adsorption energy approaches the optimum. Hence, a higher reaction rate for ORR can be observed. Similar to Pt, pure Pd binds the atomic oxygen slightly stronger than the optimum [57]. A downshift of the Pd d-band center is desirable to weaken the oxygen adsorption energy, and to achieve a higher activity for ORR. N-HOPG was prepared by ion implantation in an ultrahigh vacuum (UHV) system. Pd NPs were electrochemically deposited with the potentiostatic double-pulse method. The Pd NPs on N-HOPG (Pd / N-HOPG) samples were thoroughly characterized with surface science methods (TM-AFM and X-ray photoemission spectroscopy (XPS)) and electrochemistry (potential sweeps and impedance spectroscopy). The support effects on the activity and stability of Pd NPs were investigated.

The binding energy of an oxygen atom on a catalyst surface is commonly used to predict the activity of the catalyst for ORR. According to this descriptor, a surface which binds the atomic oxygen up to 0.4 eV more weakly than Pt(111) exhibits a higher activity for ORR than Pt. The optimum is at a binding energy of approximately 0.2 eV weaker than that of Pt. Both the experimental activity data and the theoretically predicted activity based on Greeley's DFT model indicate that the activities of Pt-based transition metal alloys for ORR form a Sabatier-type volcano plot with the oxygen adsorption energy as x-axis [21]. Some Pt-based REM alloys, such as Pt alloying with lanthanum (La), cerium (Ce), gadolinium (Gd) and yttrium (Y), have outstanding performance for ORR in all investigated Pt-based alloys. Their activities are confirmed by experiments with extended surfaces to be enhanced relative to pure Pt by a factor of 3 to 6 at 0.9 V [21, 27, 29]. Besides the polycrystalline bulk Pt-based REM alloys, the mass-selected $\mathrm{Pt}_x\mathrm{Y}$ and $\mathrm{Pt}_x\mathrm{Gd}$ NPs have been reported to be successfully synthesized using the gas aggregation technique under UHV conditions. These NPs have a core-shell structure that a Pt skin envelops an alloying core. Due to the surface compressive strain caused by the alloyed REMs in the core, they behave much more active than pure Pt NPs where the specific and mass activities have been enhanced more than 6 and 3 times, respectively, in comparison with pure Pt NPs [58, 59]. The nanoparticulate Pt-based REM alloys represent promising cathode catalysts for PEMFCs. However, their synthesis has proved challenging. The synthesis of Pt-based REM alloys in nanoparticulate form with chemical or electrochemical methods, which are much cheaper and more feasible for industry, has not been reported hitherto. The most interesting REM elements (La, Y, Gd) have very negative standard electrode potentials: La^{3+} / La $\sim$ -2.379 V,

Y^{3+} / Y ~ -2.372 V and Gd^{3+} / Gd ~ -2.279 V vs. standard hydrogen electrode (SHE) [60]. Hence, their metal phase deposition should avoid water and strong oxidants, e.g., oxygen. Ionic liquids (ILs), which are molten salts with melting points lower than 100 °C, have wide potential windows and high conductivities which are comparable with aqueous solutions [61–64]. If a suitable IL, of which the lower potential window is more negative than the reduction potential of the studied REMs, and the ionic species are inactive to the metallic REMs, can be identified, the electrochemical deposition of REMs will be possible in a large scale. Additionally, ILs have the specialty that the electrodeposition potentials of the metal ions are much closer together than in aqueous solutions, enabling the preparation of Pt-based REM alloys in one solvent, although the standard potential of Pt^{2+} / Pt (~ 1.188 V vs. SHE) is nearly 3.5 V more positive than those of REMs in aqueous solution. In this work, the electrochemical deposition of pure Pt and Y in two ILs, 1-octyl-1-methyl-pyrrolidinium bis(trifluoromethylsulfonyl)imide ([OcMePy][TFSI]) and N,N-diethyl-N-methyl-N-(2-methoxyethl)ammonium tetrafluoroborate ($[N_{122,2O1}][BF_4]$), were initially investigated. Pt metal was successfully deposited in both ILs following a multi-step reduction process from Pt^{4+} via Pt^{2+} to Pt^0. Yttrium fluoride (YF_x) and yttrium oxide (YO_x) were detected by ex-situ energy-dispersive X-ray spectroscopy (EDS) at the deposits from $Y(NO_3)_3$ + $[N_{122,2O1}][BF_4]$ precursor. The Y deposition was observed to be hampered by passivation in [OcMePy][TFSI] solution. Further electrochemical processes on HOPG and gold (Au) electrodes in ILs were investigated. After this introduction, some fundamentals from physics, chemistry and electrochemistry are introduced in the second chapter. Some investigated electrochemical reactions are reviewed according to literature results. The electrochemical behavior of supported NPs and some key effects to the activity and stability are summarized. The used materials, techniques and instrumentation are described in chapter 3. The experimental results are reported from chapter 4 to chapter 6. Chapter 4 focuses on the electrochemical deposition and characterizations of supported Pd NPs. The stability and degradation process of supported Pd NPs in potential cycles are reported and discussed as well. Chapter 5 reports the electrocatalytic properties of supported Pd NPs for some investigated reactions, such as HER, ORR, CO stripping and FAO, including size and support effects. Chapter 6 presents some initial results of the electrodeposition of Pt, Y and Pt-Y alloys in IL solutions. As the early-stage investigation of the synthesis of Pt-based REM alloys with electrochemical methods, this work summarizes the experimental details, interesting phenomena and some results with preliminary conclusions. In chapter 7, all the investigated topics are summarized leading to the finial conclusions.

Chapter 2

Fundamentals

This chapter introduces the general concepts and theoretical foundations of this work. Some fundamental concepts in electrochemistry, such as the electrode-electrolyte interface, thermodynamics and kinetics of an electrochemical process and mass transport, are discussed in section 2.1. The mainly investigated reactions, e.g. HER, ORR, CO oxidation and FAO, are introduced in section 2.2 where the general reaction mechanisms and the reaction processes at specific electrodes are focused. In section 2.3, the electrocatalytic properties of supported NPs are discussed with different descriptors consisting of two intrinsic effects (structural and electronic effects) and some parameters (size and support effects) widely used in engineering.

2.1 Electrochemical interface and reactions

Electrochemistry, as a branch of chemistry, studies electric and chemical processes taking place at an interface between an electronic conductor (electrode) and an ionic conductor (electrolyte). An electrochemical process involves the charge or mass transfer at the electrode-electrolyte interface as well as in the electrolyte. In this section, the electrode-electrolyte interface is described at first. Then, the equilibrium state of an electrochemical system is discussed based on the theory of thermodynamics. The 3^{rd} and 4^{th} parts focus on the kinetics and mass transport, respectively.

2.1.1 Electrode-electrolyte interface

The physical and chemical properties of an electrode-electrolyte interface and events occurring there when applying an electric potential are interested in the investigation of an electrochemical process. The charge carriers at both sides of the interface are different: charge is transported in an electrode by the movement of electrons or holes (in semiconductors), while charge transfer in an electrolyte is carried out by the movement of ions (cations and anions). In a non-faradaic process, charge does not pass through the interface, but a current may exist in the external circuit, when some changes, e.g., the applied potential at the electrode, the interface area or the concentration of the electrolyte, happen at the electrode-electrolyte interface. When an electrode, which is held at an external potential in the non-faradaic potential range, is brought in contact with an electrolyte, an electrified interface, consisting of electronic charges at the electrode side and counter ions in the near electrolyte, forms a double layer structure in which two layers are in opposite polarity. The Helmholtz model [65] gives the simplest description of the interfacial structure, in which a compact charge-free solvent layer separates two charged planes containing extra electronic charges and the counter ions. This system is analogous to a molecular-level capacitance. The Gouy-Chapman model [66, 67] improves the Helmholtz model by introducing the distribution of point charges as a function of distance from the electrode surface into the bulk electrolyte following the Maxwell-Boltzmann statistics. Hence, the electric potential in this model decreases exponentially away from the surface of the bulk electrolyte. O. Stern [68] suggested combining the Helmholtz model with the Gouy-Chapman model. In his model, some ions, which adsorb to the electrode surface as Helmholtz suggested, form an internal Stern layer; and some ions form a diffuse layer as described in Gouy-Chapman model. D.C. Grahame [69] modified the Stern model by introducing the concept of specifically adsorbed ions. These ions, which are initially ionic or uncharged species, can penetrate the Stern layer to contact with the electrode directly. The Grahame model, shown in Figure 2.1, suggests the existence of three regions in the interface: the inner Helmholtz plane (IHP) within a distance between the electrode surface and the centers of specifically adsorbed ions, the outer Helmholtz plane (OHP) passing through the centers of closest-approached solvable ions, and the diffuse layer beyond the OHP. The potential drop across the interface is the sum of contributions from the compact (IHP and OHP) and diffuse layers, which can be expressed as

$$\Delta\varphi^{m/s} \equiv E + \Delta\varphi^{ref} = \varphi_H(\sigma) + \varphi_{GC}(\sigma, c) \tag{2.1}$$

where both terms depend on the electrode charge density σ, while the second term depends additionally on the concentration of counter ions c. E and φ^{ref} are the potential difference measured at external circuit and the interfacial potential drop at the reference electrode, respectively.

In a faradaic process of O + ze $\rightleftharpoons$ R, charge transfers across the electrode-electrolyte interface involving electrochemical reactions, e.g., the forming or breaking of chemical bonds, or the change of oxidation states. An electrochemical reaction is considered as a heterogeneous process which occurs only at the interface. The amount of product in an electrochemical reaction can be estimated by the charge passing through the external circuit according to the Faraday's electrochemical law:

$$Q = zFN \tag{2.2}$$

where Q is the total charge passing through the interface, z is the number of electrons transferred per reactive species, N is the number of reactive species in mole unit, and F is the Faraday constant which equals to 96485.3 C mol^{-1}. The interface structure during a faradaic process becomes more complex: besides the species, e.g., electrons, solvent molecules, specifically adsorbed ions and dissolved ions, existing in

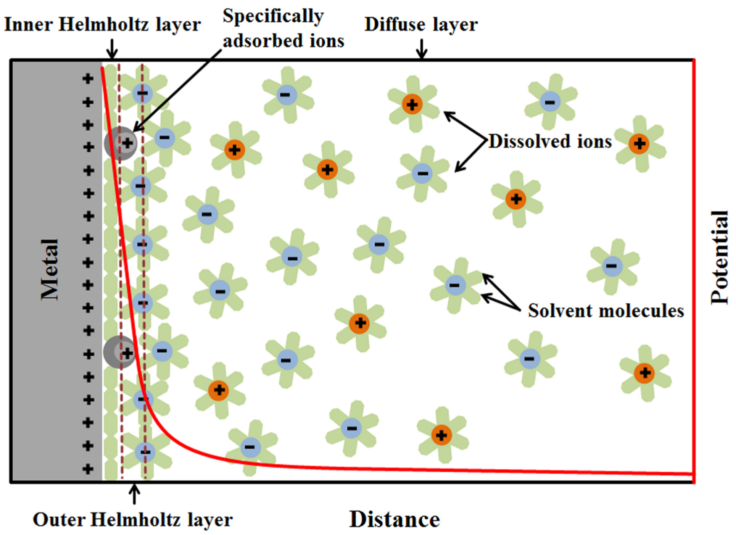

Figure 2.1: Schematic description of the double-layer structure based on the Grahame model. The metal electrode is positively charged along with the specifically adsorbed cations. The red solid line indicates the potential drop in the double-layer region.

the non-faradaic process, some other substances, such as adsorbed reactants, reaction intermediates or products, are present in the interfacial region as well. The interface structure in a faradaic process depends strongly on the reactants and the reaction process.

2.1.2 Thermodynamics and electrode potential

Electrochemical thermodynamics and Nernst equation [70]

In thermodynamics, the Gibbs free energy defines the energy associated with a chemical reaction that can be used to do non-expansion work. For an electrochemical process, the infinitesimal reversible change of the Gibbs free energy at an equilibrium state can be written as:

$$d\bar{G} = -SdT + Vdp + \sum_i \mu_i dN_i + F\sum_i z_i\varphi_i dN_i \tag{2.3}$$

where S is the entropy, T, V and p are the temperature, volume and pressure of the system, respectively. μ_i, N_i and z_i are the chemical potential of species i, number of species i in mole unit and the charge of species i, respectively. φ_i is the electric potential at the location point of species i, which is also called the internal potential of the corresponding species. The electrochemical potential of species i in any phase α is expressed as:

$$\bar{\mu}_i^\alpha = (\frac{\partial\bar{G}}{\partial N_i})_{p,T,N_{j\neq i}} = \mu_i^\alpha + z_iF\varphi_i^\alpha \tag{2.4}$$

For an uncharged species, the electrochemical potential $\bar{\mu}_i^\alpha$ is equal to the chemical potential μ_i^α. The chemical potential of species i in the phase α at temperature T can be written as:

$$\mu_i^\alpha = \mu_{i,0}^\alpha + RT\,ln a_i^\alpha \tag{2.5}$$

where $\mu_{i,0}^{\alpha}$ is the standard chemical potential, and a_i^{α} is the activity of species i in phase α. The difference between electrochemical potentials referred to phase α and β is

$$\bar{\mu}_i^{\beta} - \bar{\mu}_i^{\alpha} = (\mu_i^{\beta} - \mu_i^{\alpha}) + z_i F(\varphi_i^{\beta} - \varphi_i^{\alpha}) \tag{2.6}$$

The electric potential drop can be measured only between the points where the phase and chemical compositions are the same. In this case, $\mu_i^{\beta} = \mu_i^{\alpha}$, and the electrical potential drop $\varphi_i^{\beta} - \varphi_i^{\alpha}$ is linearly related to the difference of electrochemical potentials. When two systems in contact are at electrochemical equilibrium, the electrochemical potentials of both are equal, i.e. $\bar{\mu}_i^{\beta} = \bar{\mu}_i^{\alpha}$. The internal potential (φ^{α}) is the sum of the external potential (ψ^{α}) and the surface potential (χ^{α}). For simplification, the surface potentials (χ_i^{α} and χ_i^{β}) are neglected in the analysis that the external potential drop ($E = \psi_i^{\beta} - \psi_i^{\alpha}$), which is induced by the difference of the free electrostatic charges of the two phases, is given to the value of the internal potential drop, then

$$E \approx \Delta\varphi_{\alpha}^{\beta} = \varphi_i^{\beta} - \varphi_i^{\alpha} = -\frac{1}{z_i F}(\mu_i^{\beta} - \mu_i^{\alpha}) = E_{00} - \frac{RT}{z_i F} ln \frac{a_i^{\beta}}{a_i^{\alpha}} \tag{2.7}$$

where E_{00} is the standard potential, which can be expressed by the standard Gibbs free energy ΔG_{00} as

$$E_{00} = -\frac{\Delta G_{00}}{zF} \tag{2.8}$$

As discussed above, ΔG_{00} is the difference between the standard chemical potentials in phase β and α, i.e. $\Delta G_{00} = \mu_{i,0}^{\beta} - \mu_{i,0}^{\alpha}$. For a cell reaction with z electrons transfer per reactive species, the Nernst equation can be expressed generally as

$$E = E_{00} - \frac{RT}{zF} \sum_{i=1}^{N} \nu_i \, ln a_i \tag{2.9}$$

where ν_i is the stoichiometric number, $\nu_i < 0$ for the reactants and $\nu_i > 0$ for the products. Through the Nernst equation, the external potential drop, or the electromotive force (emf), of an electrochemical cell at any temperature, activity and stoichiometric number can be derived from the standard potential.

Reference electrodes

The internal potential drop $\Delta\varphi$ of two phases in contact is one of the most important parameters in an electrochemical process. However, a measured potential drop, in practice, is a sum of several interfacial potential differences, and, unfortunately, $\Delta\varphi$ cannot be measured for a single interface. In order to study the potential change at one concerned electrode (working electrode), this electrode should be connected to another electrode with a fixed potential, which is named reference electrode. A reference electrode has a stable interface and a well-known electrode potential. It consists of a redox system with constant concentrations of each participants of the redox reaction [60]. The passage of current within a limit does not influence the potential of the reference electrode, which means the reference electrode approaches to ideal non-polarizability. Table 2.1 shows some conventional reference electrodes frequently used in electrochemical measurements.

Table 2.1: Some conventional reference electrodes.

Reference electrode	**Potential vs. NHE (aqueous systems at 25 °C) / V [60, 71]**	**Electrode material**	**Media**
Saturated calomel electrode (SCE)	0.241	Hg / Hg_2Cl_2	Saturated KCl
Silver / silver chloride electrode	0.197	Ag / AgCl	Saturated KCl
Mercury / mercurous sulfate electrode	0.682	Hg / Hg_2SO_4	0.5 M H_2SO_4
Silver / silver sulfate electrode	0.72	Ag / Ag_2SO_4	0.5 M H_2SO_4
Copper / copper sulfate electrode	0.316	Cu / $CuSO_4$	Saturated $CuSO_4$

All potentials of these conventional reference electrodes are taken versus the normal hydrogen electrode (NHE), which is determined by the redox reaction of hydrogen at a platinized platinum electrode. The experimental conditions are restricted to 1 bar hydrogen gas pressure and 1 M proton concentration in a solution. The thermodynamic reference point of 0.0 V is standard hydrogen electrode (SHE). Its definition is similar to NHE, but the 1 M proton concentration is replaced by the unity of the proton activity in a solution. SHE is more of a theoretic ideal electrode. In practice, a reversible hydrogen electrode (RHE) is favored. It may or may not be operating under standard conditions. The measured potentials referring to a RHE are able to be converted to referring a SHE through the Nernst equation. At 25 °C and 1 atm, the electrode potential of a RHE follows a conversion equation of $E_{RHE} = 0.000 + 0.059 \times pH$ V versus SHE.

For a nonaqueous solvent, a quasi-reference electrode (QRE), such as a metal wire (Ag, Pt), is often used. The QRE is expected to have an invariable electrode potential during measurements. The actual potential of a QRE is always unknown, so it is necessary to calibrate it with a real reference electrode. Usually it can be calibrated by a reference redox system by adding the internal reference into the electrolyte during the experiments or measuring its potential after the experiments by using a reference redox system or a conventional reference electrode. The redox couple of ferrocene / ferrocenium (Fc / Fc^+) is commonly used for the calibration of a QRE. Both Fc and Fc^+ are soluble and stable in many nonaqueous solvents. Their redox has an intrinsic process and highly reversible [72]. The QREs are immersed directly into the electrolyte such that the ohmic resistance is small, no liquid junction potential appears, and normally there is no contamination which can be introduced by the solvent molecules or ions in a conventional reference electrode. However, the QREs are lack of the thermodynamic equilibrium. Because they are not ideally non-polarizable, their potentials during the measurements can shift which depends on the current density applied. Their working conditions, such as pH or temperature, are limited in a range. When the conditions are out of the range, the electrode potentials become unpredictable [73].

2.1.3 Kinetics and electrode reactions

In an electrochemical process, electric potentials and chemical potentials are closely related and convertible under some conditions. Chemical energy converts to electric energy in a galvanic cell, conversely in an electrolytic cell. The net reaction rate can be quantitatively evaluated by the current passing through the external circuit. A distinctive feature of electrochemical reactions is that the direction of charge transfer and the reaction rate are highly dependent on the potential applied at the electrode. According to the current-potential relation, the trend of a reaction and the reaction rate are predictable at any a given potential.

Arrhenius equation [60, 74]

According to experimental results, the rate coefficient k of a reaction in solution phase is temperature-dependent that lnk is linearly related to $\frac{1}{T}$. Arrhenius proposed an empirical relation

$$k = Ae^{\frac{-E_A}{RT}} \tag{2.10}$$

where A is the frequency factor, E_A is the activation energy, R is the universal gas constant, and T is the absolute temperature. The exponential factor can be considered as the probability of any attempt driven by the thermal energy at temperature T to surmount the energy barrier E_A. The frequency factor A is the frequency of attempts. In the picture of a 2-dimensional (2D) potential energy surface (PES) shown in Figure 2.2 a, the PES in a reaction is separated to two regions, a reactant region (R) and a product region (P), which can be found before and after the reaction, respectively. Reactants and products, which are considered to be naturally in stable states, have relatively lower potential energy as compared to other unstable states. The reaction happens along the most favorite path (red-dotted line), in which the lowest activation energy is needed. The potential energy is plotted along a reaction coordinate shown in Figure 2.2 b. The process from reactants to products goes through the transition state (T), which is at the maximum of the potential energy. The energy difference between the reactants and the transition state is the activation energy, which is the minimum energy required for the reaction to proceed. If the activation energy is designated as the standard internal energy of activation $\Delta E^{\ddagger}$, the standard enthalpy of activation $\Delta H^{\ddagger}$ can be defined as $\Delta H^{\ddagger} = \Delta E^{\ddagger} + \Delta(pV)^{\ddagger}$. $\Delta(pV)$ is negligible in a condensed-phase reaction, then $\Delta H^{\ddagger} \approx \Delta E^{\ddagger}$. The standard free energy of activation $\Delta G^{\ddagger}$ is defined as $\Delta G^{\ddagger} = \Delta H^{\ddagger}$ - $T\Delta S^{\ddagger}$, where $\Delta S^{\ddagger}$ is the standard entropy of activation. The Arrhenius equation can be written in terms of $\Delta G^{\ddagger}$

$$k = A' e^{\frac{-\Delta G^{\ddagger}}{RT}} \tag{2.11}$$

where the new factor A' is the product of the initial frequency factor A with an exponential part containing $\Delta S^{\ddagger}$

$$A' = A e^{\frac{-\Delta S^{\ddagger}}{R}} \tag{2.12}$$

The factor A' is a dimensionless constant. It can be predicted using statistical mechanics, and its quantity depends on the shape of the energy surface at the transition state. Eyring [75] firstly gave the expression of A' for some simple cases that

$$A' = \kappa \frac{k_B T}{h} \tag{2.13}$$

where k_B and h are the Boltzmann and Planck constants, κ is the transmission coefficient, which takes a value from zero to unity.

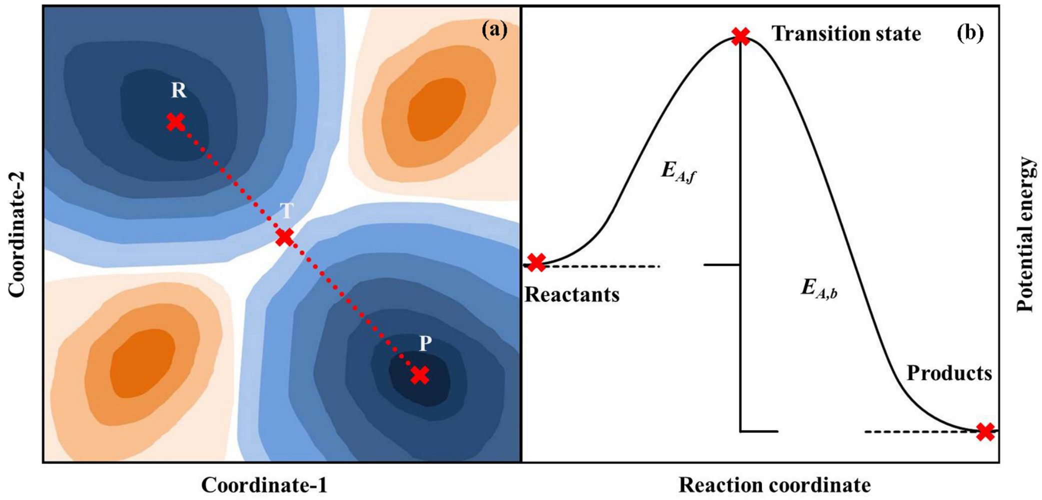

Figure 2.2: Schematic description of a 2-dimensional potential energy surface (a) and the potential energy along the marked reaction path (b). Blue regions represent energy wells, and red regions indicate energy barriers. The color depth represents the energy difference from the zero point.

Butler-Volmer equation [60]

An electrochemical process involves oxidants, reductants and transferred electrons. A multi-electron-transfer reaction at an electrode is likely to be a series of one-electron, one-step processes. Therefore, the discussion starts from the simplest model of the one-electron, one-step process $\mathrm{O} + \mathrm{e} \rightleftharpoons \mathrm{R}$, where O, R and e are the oxidant, reductant and transferred electron, respectively. The forward reaction is a reduction reaction (cathodic process). In contrary, the backward reaction is an oxidation reaction (anodic process). The rate coefficients of the cathodic and anodic reactions are denoted as k_c and k_a, respectively. According to the Arrhenius equation, the two rate coefficients can be written as

$$k_c = A' e^{\frac{-\Delta G_c^\ddagger}{RT}} \tag{2.14}$$

and

$$k_a = A' e^{\frac{-\Delta G_a^\ddagger}{RT}} \tag{2.15}$$

with the free activation energy for the forward reaction $\Delta G_c^\ddagger$ and for the backward reaction $\Delta G_a^\ddagger$, which are both potential-dependent. The free activation energy can be expressed by a Taylor expansion around the standard equilibrium potential E_{00}. For the cathodic reaction, it can be written as

$$\Delta G_c^\ddagger(E) = \Delta G_c^\ddagger(E_{00}) + \beta_c F(E - E_{00}) \tag{2.16}$$

with the cathodic transfer coefficient

$$\beta_c = \frac{1}{F} \frac{\partial \Delta G_c^\ddagger}{\partial E} |_{E_{00}} \tag{2.17}$$

which takes values in the range from zero to unity. For the anodic process, the equation is similar,

$$\Delta G_a^\ddagger(E) = \Delta G_a^\ddagger(E_{00}) - \beta_a F(E - E_{00}) \tag{2.18}$$

with the anodic transfer coefficient

$$\beta_a = -\frac{1}{F} \frac{\partial \Delta G_a^\ddagger}{\partial E} |_{E_{00}} \tag{2.19}$$

The free activation energy in an electrochemical process contains two major components: the chemical free energy (1^{st} term), which is potential-independent, and the electric free energy (2^{nd} term) showing a linearly relation with the external potential. The transfer coefficient describes the change of the free activation energy corresponding to an applied potential. Figure 2.3 shows the change of a potential energy with an applied positive potential. In an one-electron, one-step process, only the electron is charged, thus it can be influenced by the electric field. A positive potential with a difference of ΔE to the equilibrium potential reduces the free energy of the oxidant side by $-F\Delta E$. However, it does not influence the free energy of the reductant side because of no charged species here. The free activation energies for the forward ($\Delta G_c^\ddagger$) and backward ($\Delta G_a^\ddagger$) reactions have been changed as equation 2.16 and 2.18, so that the cathodic reaction needs a higher free activation energy, while the activation energy for the anodic direction becomes lower. The sum of the two transfer coefficients is unity, i.e. $\beta_a + \beta c = 1$. The influence of a negative potential to the free activation energies for both directions can be analyzed with the same method.

At the standard equilibrium potential E_{00}, the free activation energies for the forward

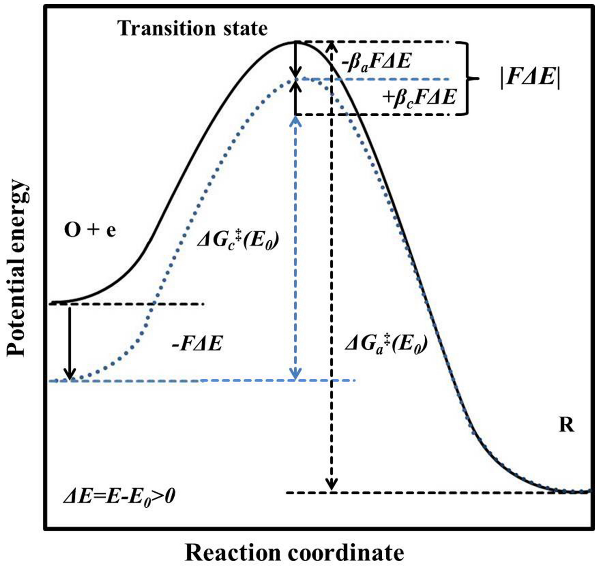

Figure 2.3: Scheme of the potential energy change caused by an applied positive potential ΔE. The variation of the free activation energy for the forward and backward reactions depends on the corresponding transfer coefficients.

and backward reactions are identical,

$$\Delta G_c^{\ddagger}(E_{00}) = \Delta G_a^{\ddagger}(E_{00}) = \Delta G_{00}^{\ddagger} \tag{2.20}$$

where $\Delta G_{00}^{\ddagger}$ is the standard free energy of activation. In the discussion of a potential-dependent reaction rate, an equilibrium potential E_0 is conventionally used instead of the standard equilibrium potential E_{00}. Their relation can be expressed by Nernst equation

$$E_0 = E_{00} + \frac{RT}{F} ln \frac{a_{ox}}{a_{red}} = E_{00} + \frac{RT}{F} ln \frac{\gamma_{ox} C_{ox}}{\gamma_{red} C_{red}} \tag{2.21}$$

in which C_{ox} and C_{red} representing the bulk concentrations of oxidant and reductant are used in the equation based on the assumption of no concentration difference between electrode surface and the bulk solution. The activity coefficients for the oxidant and the reductant are γ_{ox} and γ_{red}, respectively. In a dilute solution, the ionic strength can be neglected so that the activity coefficients approach unity, i.e. $\gamma_{ox} \approx \gamma_{red} \approx 1$. An overpotential can be defined as $\eta = E - E_0$, then the rate coefficients for the cathodic and anodic reactions can be expressed with overpotential η,

$$k_c = A_c e^{-\frac{\beta_c F \eta}{RT}} \tag{2.22}$$

$$k_a = A_a e^{\frac{\beta_a F \eta}{RT}} = A_a e^{\frac{(1-\beta_c) F \eta}{RT}} \tag{2.23}$$

where the factors A_c and A_a represent the constant parts before exponential terms. They can be written as

$$A_c = A'(\frac{C_{ox}}{C_{red}})^{-\beta_c} e^{\frac{-\Delta G_{00}^{\ddagger}}{RT}} \tag{2.24}$$

$$A_a = A'(\frac{C_{ox}}{C_{red}})^{\beta_a} e^{\frac{-\Delta G_{00}^{\ddagger}}{RT}} \tag{2.25}$$

The reaction rate is the product of the reactant concentration with its corresponding rate coefficient. For the aforementioned process, the reaction rate for the reduction reaction can be expressed as

$$\upsilon_c = k_c C_{ox} \tag{2.26}$$

and the reaction rate of the oxidation is

$$\upsilon_a = k_a C_{red} \tag{2.27}$$

The net reaction rate υ_{net} is defined as

$$\upsilon_{net} = \upsilon_c - \upsilon_a = k_c C_{ox} - k_a C_{red} \tag{2.28}$$

If the direction of current is defined as the same direction of a flow of positive charges, the current density of the net reaction can be expressed as

$$j = -F\upsilon_{net} = -F(k_c C_{ox} - k_a C_{red}) \tag{2.29}$$

From equations 2.22-2.25, the current density can be written as

$$j = Fk_0[(C_{ox})^{\beta_a}(C_{red})^{1-\beta_a}e^{\frac{\beta_a F\eta}{RT}} - (C_{ox})^{1-\beta_c}(C_{red})^{\beta_c}e^{-\frac{\beta_c F\eta}{RT}}] \tag{2.30}$$

where k_0 is the standard rate coefficient expressed as

$$k_0 = A'e^{-\frac{\Delta G^{\ddagger}_{00}}{RT}} \tag{2.31}$$

According to the relation of transfer coefficients $\beta_a + \beta_c = 1$, equation 2.30 can be simply expressed in the form

$$j = j_0(e^{\frac{(1-\beta_c)F\eta}{RT}} - e^{-\frac{\beta_c F\eta}{RT}}) \tag{2.32}$$

where j_0 is the exchange current density defined as

$$j_0 = Fk_0(C_{ox})^{1-\beta_c}(C_{red})^{\beta_c} \tag{2.33}$$

Equation 2.32 is the well-known Butler-Volmer equation, which describes the potential-dependent current density in an electrochemical process. The dependence of the electrode reaction to the overpotential is described by two kinetic parameters: the exchange current density j_0 and the transfer coefficient β_c. The former measures the standard activation energy of both reactions at the equilibrium; and the latter measures the symmetry of the change of the energy barrier by the overpotential.

Tafel equation [60]

At a high overpotential either negative or positive, i.e. $|\eta| \gg \frac{RT}{F}$, the small current contributed by the inverse reaction can be neglected. The Butler-Volmer equation at a high cathodic overpotential can be expressed in the form

$$j = -j_0 e^{-\frac{\beta_c F \eta}{RT}} \tag{2.34}$$

The expression of the overpotential with the base 10 logarithm is

$$\eta = a + b\, log_{10}|j| \tag{2.35}$$

which is so called the Tafel equation with

$$a = \frac{2.3RT}{\beta_c F} log_{10} j_0 \tag{2.36}$$

and

$$b = -\frac{2.3RT}{\beta_c F} \tag{2.37}$$

where the number of 2.3 is from $ln 10 \approx 2.3$, and b is the Tafel slope. The Tafel equation holds when the inverse reaction contributes less than 1 % of the current density. When the cathodic current dominates the reaction, the condition can be expressed as

$$\frac{e^{\frac{(1-\beta_c)F\eta}{RF}}}{e^{\frac{-\beta_c F\eta}{RF}}} \leqslant 0.01 \tag{2.38}$$

In a system at 25 °C with a transfer coefficient of 0.5, the Tafel equation holds when the overpotential is larger than 118 mV. A plot of $log_{10}|j|$ against overpotential η, which is known as the Tafel plot, is often used to evaluate the kinetic parameters of an electrochemical process, such as the transfer coefficients (β_c and β_a) and the exchange current density j_0. The overpotential range, which is valid for a Tafel plot evaluation, is constrained by the equation-holding condition 2.38 and the mass transport limitation.

Multi-step reactions

The aforementioned one-electron, one-step process ($O + e \rightleftharpoons R$) is the simplest model. Most reactions investigated in practice are complex such that more than one steps are involved accompanied by several electron transfers. For instance, the reduction of oxygen from molecular phase (O_2) to water (H_2O) involves three intermediates (*OOH, *O and *OH) with four electron transfers [76]. A multi-step reaction can be divided into several elementary reactions. The kinetic parameters of the entire reaction can be evaluated through analyzing each elementary reaction. Therefore, additional parameters corresponding to the intermediate states, such as the transfer coefficients and the exchange current densities of all elementary reactions as well as the surface concentrations or coverages of all possible intermediates, should be taken into account out of the initial conditions. The reaction rate of a multi-step process depends on that of the slowest elementary step, thus the analysis of a multi-step reaction is always simplified to analyze a single-step reaction, of which the kinetics is the most sluggish. This single step is called the rate-determining step (RDS).

Other elementary steps in analysis are assumed to be at equilibrium. A multi-step electrochemical process can be expressed with an equation O + ne $\rightleftharpoons$ R. By a RDS, the overall process can be separated to three parts:

$O + se \rightleftharpoons O'$ (net process before RDS);
$\nu(O' + re \rightleftharpoons R')$ (RDS);
$R' + ze \rightleftharpoons R$ (net process after RDS).

The overall charge transfer is $s + \nu r + z = n$. The overall reaction is supposed to occur one time requiring ν times of occurred RDS. The stoichiometric number ν is introduced in order to distinguish different possible reaction mechanisms. If the value of r is zero, the RDS is a chemical step without charge transfer. When r is unity, the RDS is a one-electron electrochemical process. Higher values of r is unlikely in the quantum mechanical consideration. As the derivation in [77], the Butler-Volmer equation for the specific multi-step process discussed above can be written as

$$j = j_0(e^{(\frac{z}{\nu}+r\beta_a)\frac{F\eta}{RT}} - e^{-(\frac{s}{\nu}+r\beta_c)\frac{F\eta}{RT}}) \tag{2.39}$$

here, the apparent transfer coefficients in cathodic and anodic reaction can be defined respectively as

$$\alpha_c = \frac{s}{\nu} + r\beta_c \tag{2.40}$$

and

$$\alpha_a = \frac{z}{\nu} + r\beta_a = \frac{n-s}{\nu} - r\beta_c \tag{2.41}$$

Obviously, the sum of the two apparent transfer coefficients is

$$\alpha_c + \alpha_a = \frac{n}{\nu} \tag{2.42}$$

The apparent transfer coefficients can be obtained from experimental data, but they are different to the transfer coefficients discussed in the one-electron, one-step model. The apparent transfer coefficients include parameters relating to all elementary electron-transfer steps, especially, the number of charges transferred before the RDS and the number of times the RDS occurred for one overall reaction. If some suitable assumptions are made, the apparent transfer coefficients can be simply related to the transfer coefficients.

2.1.4 Mass transport

An electrochemical process occurs only at the interface between electrode and electrolyte, where the reactants participate in an oxidation or reduction along with charge transfers. As compared to the fast charge transfer, the movement of reactants in the electrolyte is much slower. Along with the prolonging of reaction time, a concentration gradient of reactants forms at the electrode surface, which drives the movement of reactants toward the interface. In the discussion of kinetics, a significant assumption is that the surface concentration equals to the bulk concentration, i.e., the mass transport is neglected. In this part, the factor of mass transport is considered.

The concentration at an electrode surface is not a constant but depending on the rate of mass flow. Further, the current measured in an electrochemical process is dependent not only on the applied overpotential but also on the mass transport.

General mechanisms of mass transport [60]

The general equation of mass transport in an electrochemical process is the Nernst-Planck equation:

$$\vec{J_i} = -D_i \vec{\nabla} C_i - \frac{z_i F}{RT} D_i C_i \vec{\nabla} \varphi + C_i \vec{v_i} \tag{2.43}$$

which accounts for the flux of species i in the neighboring region of an electrode surface. D_i, C_i and z_i are the diffusion coefficient, concentration and charge number of the species i, respectively. φ is the electrical potential, and $\vec{v_i}$ is the velocity of fluid. From the Nernst-Planck equation, there are three terms representing three different mechanisms of mass transport. The first term is the diffusion flux in a concentration gradient $\vec{\nabla} C_i$. Diffusion is a random thermal motion, such that the species in the electrolyte tends to have a uniform concentration. The second term is the migration flux, which accounts for the flux of charged particles driven by the electric field. When an excess of nonelectroactive ions are added into the electrolyte (a supporting electrolyte), the contribution of migration of the electroactive species can be almost eliminated. The third term represents the contribution of convection under the influence of a flow field with a fluid velocity $\vec{v_i}$.

The aforementioned Nernst-Planck equation describes the flux of species in a mass transport. If the species i is charged with a charge number z_i, the flux of the species is equivalent to a current density, which can be written as

$$\vec{j_i} = -z_i F (D_i \vec{\nabla} C_i - \frac{z_i F}{RT} D_i C_i \vec{\nabla} \varphi + C_i \vec{v_i}) \tag{2.44}$$

The entire current density for all species is in the form

$$\vec{j} = -F \sum_i z_i D_i \vec{\nabla} C_i - \frac{F^2}{RT} \vec{\nabla} \varphi \sum_i z_i^2 D_i C_i + F \vec{v} \sum_i z_i C_i \tag{2.45}$$

Diffusion control [60]

The mass transport of an electroactive species in the neighboring region of an electrode surface can be restricted to the contribution of diffusion only by adding nonelectroactive supporting electrolyte and avoiding any external thermal or mechanical stirring. The flux of species in such a case can be expressed only by the diffusion term as

$$\vec{J_i} = -D_i \vec{\nabla} C_i \tag{2.46}$$

which is known as Fick's first law, i.e. the flux of a species is proportional to its concentration gradient. If the concentration is time-dependent, the change of concentration at a time scale at an observation point is quantitatively equal to the gradient of the flux with an opposite sign, so that the change of concentration with time can be expressed as

$$\frac{\partial C_i}{\partial t} = -\vec{\nabla} J_i = D_i \vec{\nabla}^2 C_i \tag{2.47}$$

which is called the Fick's second law. $\vec{\nabla}^2$ is the Laplacian operator, of which the form depends on the geometry of the electrode. For a planar electrode, $\vec{\nabla}^2$ in the vertical direction (x-axis) can be written as $\frac{\partial^2}{\partial x^2}$. For the spherical and cylindrical electrodes, $\vec{\nabla}^2$ in the radius direction r can be written as $\frac{\partial^2}{\partial r^2} + (\frac{2}{r}\frac{\partial}{\partial r})$ and $\frac{\partial^2}{\partial r^2} + (\frac{1}{r}\frac{\partial}{\partial r})$, respectively. In order to solve the diffusion equation, the initial conditions and appropriate boundary conditions are necessary.

Diffusion at a planar electrode [60]

The diffusion-limited current density and the concentration profile at a planar electrode can be obtained by solving the linear diffusion equations. The Fick's second law in such case can be written as

$$\frac{\partial C_i(x,t)}{\partial t} = D_i \frac{\partial^2 C_i(x,t)}{\partial x^2} \tag{2.48}$$

where x is the distance to the electrode surface. For a reversible electrode process, the initial and boundary conditions of a potential step applied at $t = 0$ are

$$C_i(x,0) = C_{i,0} \tag{2.49}$$

$$\lim_{x \to \infty} C_i(x,t) = C_{i,0} \tag{2.50}$$

$$C_i(0,t) = C_{i,s} \tag{2.51}$$

The initial condition (2.49) supposes that the solution is homogeneous before the potential step. The boundary conditions (2.50) and (2.51) assert that the concentrations at infinity and electrode surface are constant values of $C_{i,0}$ and $C_{i,s}$, respectively, during the experiment ($t > 0$). Solving the second-order partial differential equation with the Laplace transformation, the concentration can be obtained that

$$C_i(x,t) = C_{i,0} - (C_{i,0} - C_{i,s})(1 - erf(\frac{x}{\sqrt{4D_i t}})) \tag{2.52}$$

The error function $erf(\varepsilon)$ is defined as

$$erf(\varepsilon) = \frac{2}{\sqrt{\pi}} \int_0^{\varepsilon} e^{-t^2} dt \tag{2.53}$$

When the function yields for a small ε, it can be simplified to

$$erf(\varepsilon) \approx \frac{2}{\sqrt{\pi}} \varepsilon |_{\varepsilon \to 0} \tag{2.54}$$

The concentration can be written as

$$C_i(x,t) = C_{i,0} - (C_{i,0} - C_{i,s})(1 - \frac{x}{\sqrt{\pi D_i t}})|_{x \to 0} \tag{2.55}$$

According to the Fick's first law, the current density of species i is

$$j_i(0,t) = -z_i F D_i \frac{\partial C_i(x,t)}{\partial x}|_{x=0} = z_i F \sqrt{\frac{D_i}{\pi t}}(C_{i,0} - C_{i,s}) \tag{2.56}$$

If the species i is completely consumed at the electrode surface after the potential transition, the surface concentration $C_{i,s}$ at $t > 0$ is zero. The current-time response is the well-known Cottrell equation:

$$j_i(0,t) = z_i F \sqrt{\frac{D_i}{\pi t}} C_{i,0} \tag{2.57}$$

Diffusion at a spherical electrode [60]

The diffusion-limited current density and the concentration profile at a spherical electrode can be obtained by solving the spherical diffusion equations. The spherical type of Laplacian operator should be used, and Fick's second law is written as

$$\frac{\partial C_i(r,t)}{\partial t} = D_i(\frac{\partial^2 C_i(r,t)}{\partial r^2} + \frac{2}{r}\frac{\partial C_i(r,t)}{\partial r}) \tag{2.58}$$

where r is the radial distance from the electrode center. For a reversible electrode process, the initial and boundary conditions of a potential step applied at $t = 0$ are

$$C_i(r,0) = C_{i,0}|_{r>r_0} \tag{2.59}$$

$$\underset{x\to\infty}{lim} C_i(r,t) = C_{i,0} \tag{2.60}$$

$$C_i(r_0,t) = C_{i,s} \tag{2.61}$$

where r_0 is the radius of the electrode. The solution is homogeneous for the species i before the experiment. Once the reaction starts, the concentration at infinity remains at the same concentration $C_{i,0}$, while the concentration at the electrode surface becomes $C_{i,s}$. The concentration of species i at a position with distance r to the spherical center is obtained as

$$C_i(r,t) = C_{i,0} - (C_{i,0} - C_{i,s})\frac{r_0}{r}(1 - erf(\frac{r - r_0}{\sqrt{4D_i t}})) \tag{2.62}$$

When the radical distance approaches to the radius of the electrode, the concentration can be simplified in the form

$$C_i(r,t) = C_{i,0} - (C_{i,0} - C_{i,s})(1 - \frac{r - r_0}{\sqrt{\pi D_i t}})|_{r\to r_0} \tag{2.63}$$

The current density of species i at the electrode surface is

$$j_i(r_0,t) = -z_i F D_i \frac{\partial C_i(r,t)}{\partial r}|_{r=r_0} = z_i F D_i(\frac{1}{r_0} + \frac{1}{\sqrt{\pi D_i t}})(C_{i,0} - C_{i,s}) \tag{2.64}$$

If the species i is completely consumed at the electrode surface after the potential transition, the surface concentration $C_{i,s}$ is zero. The current-time response can be written as

$$j_i(r_0, t) = z_i F D_i C_{i,0}(\frac{1}{r_0} + \frac{1}{\sqrt{\pi D_i t}}) \tag{2.65}$$

The constant part in the equation is called the steady-state current density $j_i(r_0, \infty)$, which can be expressed as

$$j_i(r_0, \infty) = \frac{z_i F D_i C_{i,0}}{r_0} \tag{2.66}$$

The current density reaches the steady state after a long-time reaction. From the equation 2.66, the steady-state current density at a spherical electrode depends on the radius of the electrode so that a larger radius of electrode corresponds to a smaller steady-state current density.

Diffusion at a particle-modified electrode

A particle-modified electrode is considered for which the faradaic reactions occur only on the supported particles; the substrate surface is electrochemically inert. The electroactive species is consumed at the particle surface leading to the formation of a depletion layer. The depletion layer of an isolated particle is approximate to the shape of the particle at very beginning of the reaction. For example, the depletion layer of a spherical particle is spherical in shape; and a microdisc electrode has a planar depletion layer. At a long time scale, the depletion layer is approximately hemispherical [78]. For a particle-modified electrode, particles are randomly distributed on the substrate. When neighboring depletion layers overlap, a shielding effect will happen. Therefore, the diffusional current becomes lower as compared with that when the depletion layers do not overlap. The diffusional behavior of the electroactive species to the particle surface can be affected.

The diffusional behavior for randomly distributed spherical particles can be described in terms of four categories [79]. For category 1, the particles do not have overlap of diffusion layers, and the diffusion layer thickness of each particle is much smaller than the particle radius. The diffusional behavior at a particle-modified electrode surface under such condition is approximate to that at a planar electrode. For category 2, the particles are diffusionally independent, while the diffusion layer thickness is comparable to the particle radius. The diffusional behavior depends on the shape of the particle. The diffusion to a microscopic spherical particle is similar to that to a macroscopic spherical electrode. As the depletion layers start to overlap, the diffusion is defined to category 3. Neighboring particles experience a shielding effect, so that the electroactive species transferred to each particle becomes less. With the growth of the depletion layers, a limiting situation arises, such that the depletion layers of all particles form a planar profile. The current response is similar to that of a planar electrode, even through the substrate surface is electrochemically inert. This condition is described as category 4.

The coverage of particles on the substrate can strongly affect the diffusional behavior. Streeter et al. [80] investigated the influence of particle coverage on the voltammogram with numerical simulation and experimental works. They reported that, when the coverage of particles is equal or smaller than 0.01 %, there is no significant overlap between neighboring depletion layers. The diffusional behavior can be described as category 2. At a slow scan rate, the profile of the voltammogram is similar to that for steady-state diffusion with a constant maximum current. With the increase of particle density, the magnitude of the specific current density in the voltammogram becomes smaller; and the profile becomes more peak shaped, which can be attributed to the change of the diffusional behavior from category 2 to category 3. The shielding effect reduces the flux of the electroactive species to the particle surface. When the coverage of particles is higher than a limit, the diffusional behavior becomes to category 4. The current response is similar to the planar diffusion model so that, for a reversible process, the peak current is described by the Randles-Sevcik equation [60]

$$i_p = 0.4463nFAC^*(\frac{nFvD}{RT})^{\frac{1}{2}} \tag{2.67}$$

where A is the geometric area of the electrode; C^* and D are the bulk concentration and diffusion coefficient, respectively. The value of the peak current i_p is proportional to the square root of the scan rate $v^{\frac{1}{2}}$.

2.2 Investigated electrochemical reactions

Several electrochemical reactions, e.g. hydrogen ad-/absorption, HER, ORR, CO stripping and FAO, were investigated on extended and nano-sized electrodes. From the Butler-Volmer equation, the reaction rate depends on some parameters, i.e. temperature, overpotential and concentration of electroactive species, which can be adjusted by external conditions. However, the standard rate coefficient and the transfer coefficient are sensitive to the solid surface of the used catalyst. Some fundamental concepts are needed to understand how a solid surface acts as a catalyst, and how reactants interact with the solid surface via some intermediates to the final product. In this section, the reaction mechanisms of the investigated reactions are discussed. The reactions on PGMs are the research interest in this work.

2.2.1 Hydrogen evolution reaction

General description

The stoichiometry of the HER in an acidic solution is

$$2H_3O^+ + 2e^- \rightarrow H_2 + 2H_2O \tag{2.68}$$

The reaction occurs at a cathodic overpotential. The H_3O^+ ion is the proton source. The overall reaction on a metal surface can be generally partitioned to three steps (shown in Figure 2.4) [81]:

(1) Volmer step

$$H_3O^+ + e^- + M \rightarrow MH_{ads} + H_2O \tag{2.69}$$

One proton is discharged at the metal surface forming adsorbed hydrogen intermediate MH_{ads}.

(2) Tafel step

$$2MH_{ads} \rightarrow H_2 + 2M \tag{2.70}$$

Two adsorbed hydrogen atoms form a hydrogen molecule, which is transported away from the electrode surface.

(3) Heyrovsky step

$$MH_{ads} + H_3O^+ + e^- \rightarrow H_2 + M + H_2O \tag{2.71}$$

One adsorbed hydrogen atom combines with a dissolved proton to form a hydrogen molecule accompanied with an electron transfer. Step 2 and step 3 are alternative desorption steps of H_2. Each of them is successive to the step 1. Therefore, the hydrogen evolution occurs by two pathways: the Volmer-Tafel process and the Volmer-Heyrovsky process.

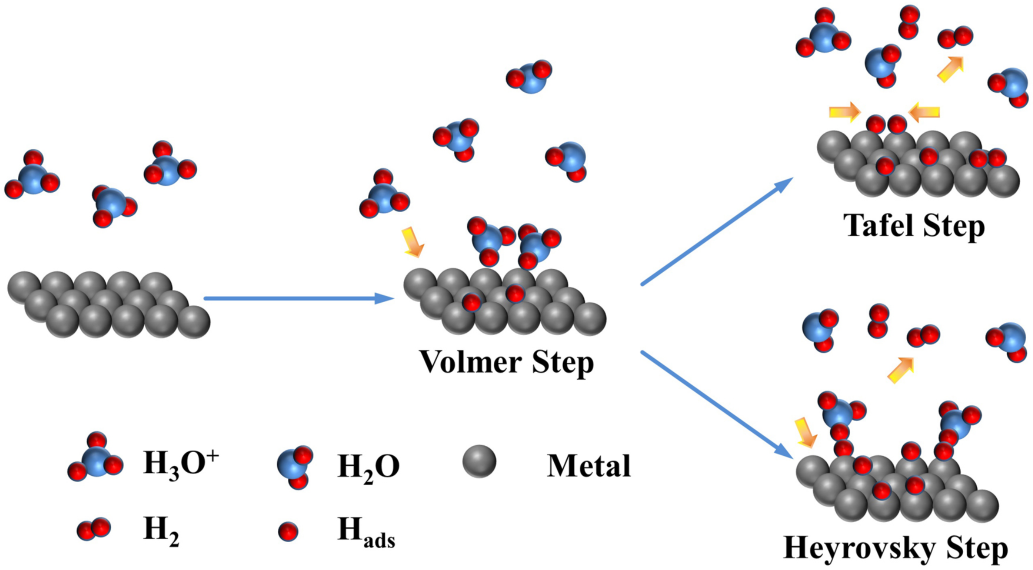

Figure 2.4: Scheme of the three reaction steps of the HER on a metal surface in an acidic solution.

Theoretical description [81]

The Volmer step is an electrochemical process, thus the current density j_V can be expressed by the Butler-Volmer equation:

$$j_V = F(k_{V,a}\theta_H e^{\frac{\beta_{V,a}F\eta}{RT}} - k_{V,c}C_{H^+}(1-\theta_H)e^{-\frac{\beta_{V,c}F\eta}{RT}}) \tag{2.72}$$

where C_{H^+} is the concentration of protons. θ_H is the coverage of adsorbed hydrogen atoms so that the free metal sites have a coverage of 1-θ_H. The transfer coefficients for cathodic and anodic reactions are $\beta_{V,c}$ and $\beta_{V,a}$, respectively. The rate coefficients for the cathodic and anodic reactions in the Volmer step are $k_{V,c}$ and $k_{V,a}$, respectively. When the reaction is at an equilibrium state, the net reaction current density equals to zero. The exchange current density $j_{V,0}$ can be written as

$$j_{V,0} = Fk_{V,c}C_{H^+}(1 - \theta_{H,0}) = Fk_{V,a}\theta_{H,0} \tag{2.73}$$

where $\theta_{H,0}$ is the equilibrium coverage of hydrogen atoms. Equation 2.72 can be rewritten with the exchange current density as

$$j_V = j_{V,0}(\frac{\theta_H}{\theta_{H,0}}e^{\frac{\beta_{V,a}F\eta}{RT}} - \frac{1-\theta_H}{1-\theta_{H,0}}e^{-\frac{\beta_{V,c}F\eta}{RT}}) \tag{2.74}$$

If the Volmer step is the RDS, the hydrogen coverage θ_H tends to be very small due to the sluggish adsorption process or the rapid consumption in the consecutive steps. The Tafel step is a chemical process without electron transfer. The coverage of the adsorbed hydrogen atoms changes due to the hydrogen atoms participating in some electron transfer steps, i.e. the Volmer step and Heyrovsky step. Therefore, the chemical process is associated with the electrochemical processes. The change of the coverage contributes an overpotential. With the Nernst equation, the overpotential can be expressed as

$$\eta = -\frac{\nu RT}{zF}ln(\frac{\theta_H}{\theta_{H,0}}) \tag{2.75}$$

where ν and z are the stoichiometric number and the number of charge transferred in the associated process, respectively. In the case of the cathodic reaction, $\nu = 2$ and $z = 2$, the overpotential can be rewritten as

$$\eta = -\frac{RT}{F}ln(\frac{\theta_H}{\theta_{H,0}}) \tag{2.76}$$

The reaction rate υ_T for the Tafel reaction can be written as

$$\upsilon_T = k_{T,f}{\theta_H}^2 - k_{T,b}(1-\theta_H)^2 C_{H_2} \tag{2.77}$$

where $k_{T,f}$ and $k_{T,b}$ are the rate coefficients of forward and backward reactions, respectively. When the process is at equilibrium, the exchange reaction rate is

$$\upsilon_{T,0} = k_{T,f}{\theta_{H,0}}^2 = k_{T,b}(1-\theta_{H,0})^2 C_{H_2,0} \tag{2.78}$$

The reaction rate can be expressed by the exchange reaction rate as

$$\upsilon_T = \upsilon_{T,0}[(\frac{\theta_H}{\theta_{H,0}})^2 - (\frac{1-\theta_H}{1-\theta_{H,0}})^2\frac{C_{H_2}}{C_{H_2,0}}] \tag{2.79}$$

For a large cathodic overpotential, the coverage of the adsorbed hydrogen atoms approaches 1 ($\theta_H \rightarrow 1$), so that the backward reaction can be neglected. The reaction rate at a large cathodic overpotential can be expressed as

$$\upsilon_{T,c} = \upsilon_{T,0}(\frac{\theta_H}{\theta_{H,0}})^2 \tag{2.80}$$

The overpotential showed in equation 2.76 can be expressed by the exchange and cathodic reaction rates as

$$\eta = -\frac{RT}{2F} ln(\frac{\upsilon_{T,c}}{\upsilon_{T,0}}) \tag{2.81}$$

The reaction rate is proportional to the corresponding current density. Thus, the ratio of the reaction rates $(\frac{\upsilon_{T,c}}{\upsilon_{T,0}})$ is equal to the ratio of the current densities $(\frac{j_{T,c}}{j_{T,0}})$. From equation 2.81, the Tafel slope is $b = -29.6$ mV at 25 °C.

The Heyrovsky step is an electrochemical process that the current density j_H can be expressed by the Butler-Volmer equation as well

$$j_H = F(k_{H,a}(1-\theta_H)e^{\frac{\beta_{H,a}F\eta}{RT}} - k_{H,c}C_{H^+}\theta_H e^{-\frac{\beta_{H,c}F\eta}{RT}}) \tag{2.82}$$

where $\beta_{H,c}$ and $\beta_{H,a}$ are the transfer coefficients for the cathodic and anodic reactions, respectively. The exchange current density $j_{H,0}$ can be obtained at the equilibrium potential that

$$j_{H,0} = Fk_{H,c}C_{H^+}\theta_{H,0} = Fk_{H,a}(1-\theta_{H,0}) \tag{2.83}$$

Equation 2.82 can be rewritten as

$$j_H = j_{H,0}(\frac{1-\theta_H}{1-\theta_{H,0}}e^{\frac{\beta_{H,a}F\eta}{RT}} - \frac{\theta_H}{\theta_{H,0}}e^{-\frac{\beta_{H,c}F\eta}{RT}}) \tag{2.84}$$

Conway et al. [82] summarized the Tafel slopes for the three steps based on an assumed transfer coefficient of $\beta = 0.5$ shown in Table 2.2.

Table 2.2: Tafel slopes for the three steps in hydrogen evolution reaction.

Step	**Tafel slope (low θ_H) / mV**	**Tafel slope (high, η-dependent θ_H) / mV**
Volmer	-118	-b$_{\theta_H \ll 1}$
Tafel	-29	$\rightarrow \infty$ (limiting current)
Heyrovsky	-118	-42

In the case of the Volmer-Tafel pathway, the coverage of adsorbed hydrogen atoms tends to be very low at a large negative potential, the Volmer step is the RDS, thus the Tafel slope is determined by the Volmer step. In the case of the Volmer-Heyrovsky pathway, both steps involve electron transfer so that the apparent Tafel slope depends on which reaction is the RDS, and on how much the surface is covered by the adsorbed hydrogen.

HER on metal surfaces

The catalytic activity of a material for the HER can be plotted as a function of the free energy of hydrogen adsorption ΔG_H, in which a volcano-shaped form can be found [83]. This behavior is related to the Sabatier principle [20] so that the optimal catalytic activity can be achieved on a catalyst with intermediate free energies of adsorption for reactive intermediates. If the intermediates adsorb on the catalyst surface too weakly, the activation energy barrier for the reaction will be too high. But if they adsorb too strongly, the active sites will be occupied and poisoned. The chemical nature of the catalytic material influences the kinetics of the HER. Greeley et al. [25] plotted experimentally measured HER exchange current densities on various pure metals and metal overlayers against ΔG_H values calculated using DFT. According to the plot, the most active metals for the HER are PGMs (Pt, Pd, Rh, Ir). The exchange current densities of other noble metals, such as Au, Ag and Cu, are two orders of magnitude lower than those of PGMs. Pd overlayers on Pt or PtRu show the highest activity for HER.

The electrocatalytic activity of the Pt surface for HER has been extensively studied. The exchange current density in H_2SO_4 is 5×10^{-4} to 10^{-3} A cm^{-2}; the Tafel slope is 30 mV dec^{-1} at low overpotentials and 120 mV dec^{-1} at high overpotentials [84], which indicates the reaction follows the Volmer-Tafel mechanism at low overpotentials and the Volmer-Heyrovsky mechanism at higher overpotentials. The reaction kinetics of the HER depends strongly on the crystal facets. Marković et al. [85] have observed that the activity decreases in the order: Pt(110) $>$ Pt(100) $>$ Pt(111). The most stable facet Pt(111) shows the lowest activity, which is attributed to the blocking effect of the underpotential adsorbed hydrogen atoms (H_{upd}). Only the overpotential adsorbed hydrogen atoms (H_{opd}), which bond weakly with Pt atoms, are involved in the HER.

The free energy of hydrogen adsorption on Pd surfaces is higher than that on Pt surfaces. The strong adsorption should cause a lower reaction rate for the HER due to the blocking effect of the adsorbed hydrogen atoms. However, the measured exchange current density for HER is comparable with that on a Pt surface of 10^{-3} A cm^{-2} in H_2SO_4 solutions [86], which indicates the kinetics for HER on Pd surfaces is similar to that on Pt surfaces. However, the hydrogen absorption at a Pd electrode, which can contribute an additional current, obstructs the understanding. Considerable efforts have been dedicated towards investigating the activity of supported Pd overlayers. Marković et al. [87] demonstrated that the HER kinetics could be enhanced significantly on Pd / Pt(111). Greeley et al. [25] found the Pd / PtRu more closer to the volcano peak than other metals and alloys, the exchange current density is, hence, keeping the record. The supporting materials result in the downshift of the Pd $d-$band center and a weakened hydrogen adsorption.

2.2.2 Oxygen reduction reaction

General description

The ORR is a multi-step reaction with more than one electron transfer. In an aqueous solution, the ORR occurs mainly through two pathways: the “direct” 4-electron reduction pathway from the oxygen molecule (O_2) to water (H_2O), and the indirect 2-electron reduction pathway from O_2 to hydrogen peroxide (H_2O_2). The stoichiometry of the direct ORR pathway in an acidic solution is

$$O_2 + 4H_3O^+ + 4e^- \rightarrow 6H_2O \tag{2.85}$$

and the indirect pathway can be expressed as

$$O_2 + 2H_3O^+ + 2e^- \rightarrow H_2O_2 + 2H_2O \tag{2.86}$$

H_2O_2 is unstable which undergoes chemical or electrochemical decomposition to the final products of H_2O and O_2. Wroblowa et al. [88] introduced a scheme which simplified the complicated reaction pathway at metal electrodes. The scheme is recreated and shown in Figure 2.5. O_2 reacts with 2 H^+ and 2 e^- on a metal surface to form an adsorbed peroxide ($H_2O_{2,ads}$), which can be electrochemically reduced to H_2O, chemically decomposed to O_2, or dissociated into the bulk solution as H_2O_2. Marković et al. [49] suggested that the peroxide species is the key intermediate for the splitting of the O-O bond. The direct reduction of adsorbed O_2 to H_2O, which is marked with a dashed arrow, is kinetically impossible on all Pt and Pt bimetallic catalysts.

Theoretical description

The ORR mechanism on a metal surface was studied theoretically using DFT calculations [21, 28, 76]. Several elementary steps are included in the process involving the key intermediates, such as the adsorbed oxygen atom (O_{ads}), hydroxyl (OH_{ads}) and superhydroxyl (OOH_{ads}) groups. Nørskov et al. [76] suggested two mechanisms: one is dissociative mechanism shown in equation 2.87, in which the splitting of O-O bond occurs during the O_2 adsorption leading to the formation of O_{ads}; the other one is associative mechanism shown in equation 2.88, in which O_2 does not dissociate before it is hydrogenated.

$$\frac{1}{2}O_2 + M \rightarrow MO_{ads} \xrightarrow{H^+ + e^-} \rightarrow MOH_{ads} \xrightarrow{H^+ + e^-} \rightarrow H_2O + M \tag{2.87}$$

$$\begin{split} O_2 + M \rightarrow MO_{2,ads} \xrightarrow{H^+ + e^-} \rightarrow MOOH_{ads} \xrightarrow{H^+ + e^-} \rightarrow H_2O + MO_{ads} \\ \xrightarrow{H^+ + e^-} \rightarrow H_2O + MOH_{ads} \xrightarrow{H^+ + e^-} \rightarrow 2H_2O + M \end{split} \tag{2.88}$$

The free energies of adsorbed intermediates in each electrochemical step were calculated with neglecting the kinetic activation barrier. A free-energy diagram was constructed for the overall reaction. In the dissociative mechanism, the dissociated

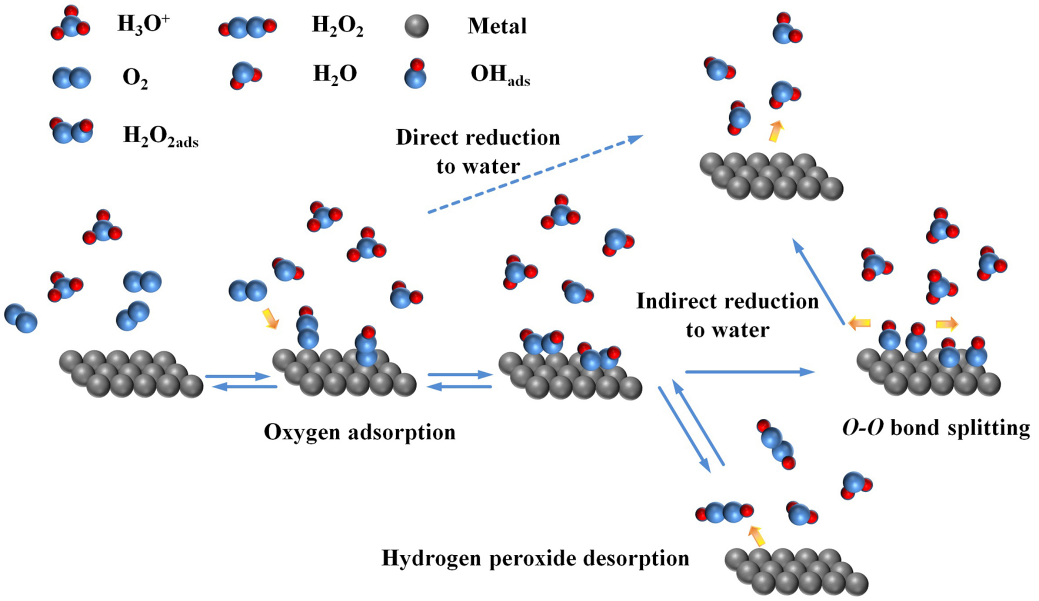

Figure 2.5: Schematic showing of the reaction mechanisms of oxygen reduction on a metal surface in an acidic solution. Both water and hydrogen peroxide are the possible products. The direct reduction of adsorbed oxygen molecules to water is marked with a dashed arrow indicating the kinetic unlikeliness at Pt-based electrodes.

oxygen atom bonds strongly on the Pt surface at the equilibrium potential (1.23 V) so that the first electron- and proton-transfer for the formation of adsorbed hydroxyl requires a certain activation energy to exceed the energy barrier, and the value of the energy barrier is independent of the coverage. In contrary to Pt, the adsorption of an oxygen atom on the Au electrode at 1.23 V requires external energy, which means the Au bonds too weakly to adsorbed oxygen atoms at this potential. The trends of the ORR activity on different metal surfaces were plotted against the binding energy of oxygen atoms as a Sabatier-type volcano plot shown in Figure 2.6. The metals at the left arm (Pt, Pd, Cu, Ni) bond more strongly with oxygen atoms than the optimum state. Thus additional activation energy is necessary to exceed the energy barrier for the hydrogenation process. However, the metals at the right arm (Ag, Au) bond weakly with oxygen atoms so that the energy barrier for the dissociation of an oxygen molecule on such a metal surface is relatively large. In the associative mechanism, the hydrogenation of the adsorbed oxygen molecule occurs before the dissociation of the O-O bond. The hydrogenated oxygen molecules are peroxide intermediates (OOH_{ads}), which may or may not be further reduced to water depending on the kinetics of reactions to two other products (H_2O_2 and O_2). In either case, the RDS is the first electron transfer for forming $O_{2,ads}$. The reaction current density can be expressed as

$$j = k_c F C_{O_2} (1-\theta)^x e^{-\frac{\beta F \eta}{RT}} e^{-\frac{\gamma r \theta}{RT}} \tag{2.89}$$

where k_c is the rate coefficient, C_{O_2} is the concentration of O_2 in the solution, θ is the coverage by all adsorbed species. x is the number of active sites for an oxygen adsorption which can be 1 or 2. β and γ are the transfer coefficients. The second exponential term is the Frumkin correction [89], by which the effect of the adsorption layer to the current density can be corrected. r is a parameter characterizing the rate of the free energy change of the key intermediate adsorption with the surface coverage by adsorbing species [90]. The coverage of adsorbing species have influences on the activity for ORR. When the oxygen coverage on a Pt electrode approaches zero, the O_2 dissociation is not activated, and the dissociative mechanism has the lowest energy barrier. When the Pt is at a high oxygen coverage, the associative mechanism has lower free-energy barriers than the dissociative mechanism. Therefore, the associative mechanism dominates the reaction. Additionally, the reaction mechanism depends strongly on the applied potential. At potentials equal to or lower than 0.8 V, the associative mechanism dominates over the dissociation path on a Pt electrode, which means that both mechanisms are operating in parallel [76].

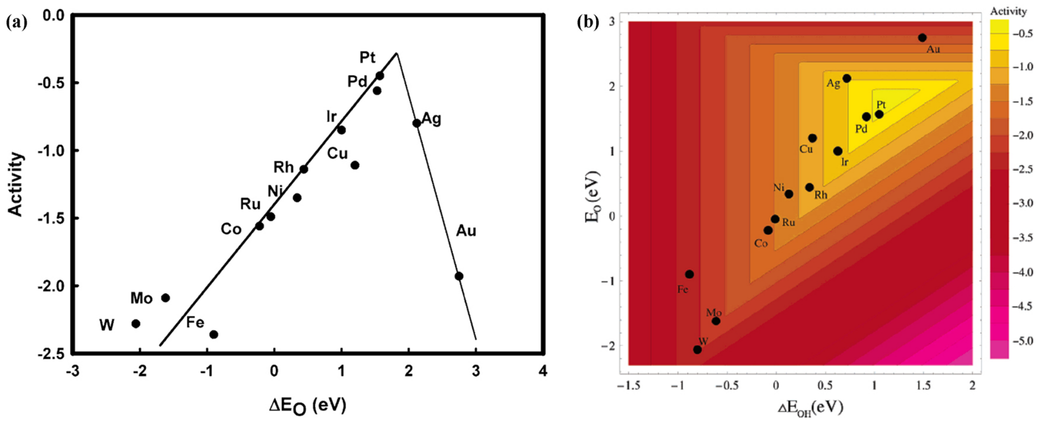

Figure 2.6: Trends in oxygen reduction activity plotted as a function of the oxygen binding energy (a) and as a function of both the O and the OH binding energy (b). [Reprinted from [76], with permission from American Chemical Society.]

ORR on a Pd electrode

The thermodynamic potential of the ORR is 1.23 V, which is so high that no metal electrode can remain pure. The Pd electrode surface, which is similar to the Pt electrode, undergoes oxidation. It is commonly agreed that the onset potential of Pd electro-oxidation is in the range of 0.6 to 0.75 V vs. RHE [91]. Therefore, the Pd surface is expected to be a mixture of Pd metal and PdO at the normal working potential (~ 0.85 V) for ORR. Due to the different surface structures at high potentials (> 0.75 V) and low potentials (< 0.75 V), the kinetics for ORR should be different. For a Pt electrode, the Tafel slope is -60 mV dec^{-1} in the high potential range (with a low current density) and -120 mV dec^{-1} in the low potential range (with a high current density) [92]. On a Pd electrode, the same Tafel slopes were reported [33, 34, 93]. The different Tafel slopes indicate that the ORR at the high and low potentials follows two different reaction mechanisms: the RDS on a Pd /

PdO surface is a pseudo two-electron process relating to the O-O bond dissociation (dissociative mechanism); the RDS on a pure Pd surface is a one-electron process relating to the first electron transfer to an oxygen molecule (associative mechanism). The exchange current density of a Pt electrode for ORR is ca. 2.5 - 5.0 × 10^{-7} A cm^{-2} at a room temperature [94, 95]. The value is about five times of that measured on a polycrystalline Pd electrode [32, 96]. The ORR kinetics is sensitive to the surface structures of Pd. On a Pd single crystal surface, the activity increases following the order of Pd(110) $<$ Pd(111) $\ll$ Pd(100) [97]. The highly active performance of Pd(100) for ORR has been confirmed by experiments with high-index Pd single crystals where the kinetic current densities for ORR positively correlate to the width of the Pd(100) terrace [97, 98]. Therefore, one strategy to enhance the activity of a Pd electrode for ORR is to increase the ratio of the Pd(100) facet in all surface structures.

2.2.3 Carbon monoxide oxidation reaction

The electro-oxidation of CO is a heterogeneous process, in which adsorbed or gas-phase CO reacts with adsorbed oxygen species to form CO_2. The reaction proceeds through two major mechanisms: the Langmuir-Hinshelwood (L-H) mechanism and the Eley-Rideal (E-R) mechanism (shown in Figure 2.7).

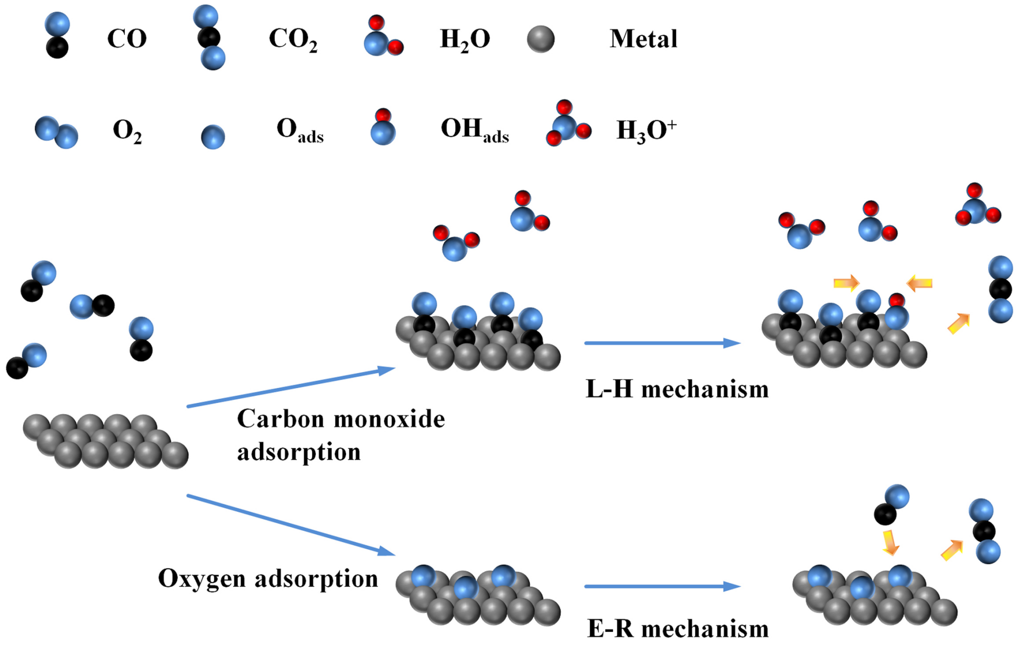

Figure 2.7: Scheme of the mechanisms of CO oxidation. The Langmuir-Hinshelwood mechanism indicates the reaction occurring in an aqueous solution. The Eley-Rideal mechanism represents the reaction occurring in a gaseous atmosphere.

In the L-H mechanism, the oxidation of adsorbed CO molecules requires reaction partners such as adsorbed hydroxyls (OH_{ads}) or oxygen atoms (O_{ads}) to produce CO_2 molecules, which desorb from the metal surface. The reaction mechanism in aqueous solution can be written as follows:

$$CO + M \rightleftharpoons MCO_{ads} \tag{2.90}$$

$$H_2O + M \rightleftharpoons MOH_{ads} + H^+ + e^- \tag{2.91}$$

$$MCO_{ads} + MOH_{ads} \rightarrow CO_2 + H^+ + e^- + 2M \tag{2.92}$$

In this process, the adsorption of reactants initiates the following steps. It is widely accepted that the CO molecule adsorbs on a metal surface by binding through the carbon atom. There are three typical geometric locations, -on-top, bridge and 3-fold hollow site-, available. CO adsorption on Pd single-crystal surfaces exhibits structure sensitivity. On a Pd(111) surface, CO adsorbs at the 3-fold hollow site at a low coverage (< 0.3), at the bridge site at a medium coverage (~ 0.5) and at the on-top site at a high coverage. However, only the CO adsorbed at the bridge and on-top site can be observed on a Pd(100) surface [99]. It has been suggested that, on a Pt electrode, CO is adsorbed in the form of islands, CO oxidation occurs mainly at steps and defect sites, and CO oxidation requires a diffusion of CO molecules to the active sites [81]. On Pd, Rh and other metal surfaces, the density of active sites and the diffusion coefficient of CO molecules on the metal surface should be considered when discussing the reaction kinetics [100]. Here, the steps and defect sites are considered to be active sites for OH_{ads} formation, which initiates a L-H mechanism.

An interesting feature of CO electro-oxidation on a Pt electrode has been observed: a lower potential is required for oxidizing CO when CO molecules are present in the solution, than for stripping a CO adlayer in CO-free electrolyte [81]. This phenomenon can be attributed to the different CO coverages on the metal surface in the two conditions. The coverage of the CO adlayer on a metal surface is considered to be fixed in the absence of CO in the electrolyte. When CO molecules are contained in the bulk solution, the CO coverage on the metal surface depends on the CO concentration in the electrolyte, and, normally, the coverage is higher in such a case than the absence of CO. The repulsion between neighboring CO molecules becomes higher with an increase in CO coverage. The repulsion effect causes the decrease of the CO adsorption energy on the metal surface [101]. As a result, the potential for CO oxidation in CO containing solution is lower than that in CO-free solution. In addition to the repulsion effect, the competition between CO_{ads} and OH_{ads} for the adsorption sites should be considered. When the CO concentration in the electrolyte is lower than a critical value, the increase of CO concentration, which is able to increase the CO coverage on the metal surface, enhances the reaction rate for CO oxidation at a fixed potential due to the repulsion effect. Beyond the critical value, the increase of the CO concentration in the electrolyte causes a decrease of the reaction rate. CO molecules compete with water molecules for adsorption sites. A high CO coverage inhibits the formation of OH_{ads}, further, blocks the reaction through the L-H mechanism.

In the E-R mechanism, the adsorbed oxygen species reacts with the gas-phase CO molecules. The reaction mechanism can be expressed as

$$O_2 + 2M \rightleftharpoons 2MO_{ads} \tag{2.93}$$

$$CO + MO_{ads} \rightarrow CO_2 \tag{2.94}$$

The O$_{ads}$ should have a medium binding strength with the metal surface so that, when the CO molecules collide with the O$_{ads}$, the O$_{ads}$ is active enough to react with the CO without further activation energy. The metal surface influences the reaction rate through the interaction with the O$_{ads}$. Neither a weak nor a strong binding energy to O$_{ads}$ is favorable. The former leads to a low coverage of O$_{ads}$. In contrary, the latter requires more energy to activate the O$_{ads}$ for CO oxidation.

2.2.4 Formic acid oxidation reaction

The study of electrocatalyzed FAO, as an interesting topic in the electro-oxidation of small organic molecules, has attracted much attention during past decades due to the desire for an alternative fuel for low-temperature fuel cells. The FAO occurring on PGMs was intensively investigated as a model reaction to understand the mechanism as well as to develop potential applications, such as DFAFCs [102–104].

It is widely accepted that the FAO proceeds generally via two pathways: the direct pathway in which the adsorbed formic acid molecule (HCOOH) dehydrogenates to CO$_2$, and the indirect pathway in which the HCOOH initially dehydrates to adsorbed CO (CO$_{ads}$), and then is oxidized to CO$_2$ [105–107]. The direct FAO reaction can be expressed as:

$$HCOOH + M \rightarrow M \cdots HCOOH \rightarrow CO_2 + 2H^+ + 2e^- + M \tag{2.95}$$

In the direct pathway, HCOOH adsorbs on the electrode surface forming several weakly adsorbed intermediates. The carboxylic acid species (*COOH) has for a long time been assumed to be a reactive intermediate for FAO. The *COOH, which is adsorbed on a Pt surface via the carbon atom, was considered as the key intermediate to determine the reaction rate of the direct pathway [108, 109]. Osawa's group [110–114] successfully detected adsorbed formate (HCOO*) on both Pt and Pd electrodes, and proposed it to be a reactive intermediate for FAO. The HCOO* adsorbs on the Pt surface through a bridge bond. An adjacent vacancy is necessary for C-H bond scissoring during its oxidation. Cuesta et al. [115, 116] suggested that the HCOO* is the key intermediate for both the dehydrogenation and dehydration processes, and two adjacent adsorbed HCOO* react through a bimolecular decomposition mechanism for dehydrogenation. However, the role of the HCOO* in the direct pathway is still in debate. Behm's group [117–120] suggested that HCOO* is a spectator rather than a reactive intermediate. The coverage of a HCOO* adlayer is dominated by a fast dynamic ad-/desorption equilibrium with the HCOOH in the electrolyte, and the HCOO* desorption is considered much faster than its decomposition [118]. A HCOOH adsorbed on a metal surface via an oxygen atom is suggested to be inactive for FAO due to its high stability [121]. The species adsorbed via a carbon atom is the reactive intermediate. A newly proposed mechanism by Osawa's group suggested that formate ions ($HCOO^-$) rather than HCOOH can be oxidized via a weakly adsorbed formate precursor. This precursor should compete with other adsorbed species for active surface sites [122, 123].

The indirect FAO via a dehydration process involves strongly adsorbed CO_{ads} and OH_{ads}. The entire reaction process can be expressed as follows:

$$HCOOH + M \rightarrow MCO_{ads} + H_2O \tag{2.96}$$

$$H_2O + M \rightarrow MOH_{ads} + H^+ + e^- \tag{2.97}$$

$$MCO_{ads} + MOH_{ads} \rightarrow 2M + CO_2 + H^+ + e^- \tag{2.98}$$

The CO_{ads} is identified as the major poisoning species formed through the dehydration pathway. Therefore, OH_{ads} is necessary for the oxidation of CO_{ads} to the final product of CO_2. However, the formation of OH_{ads} requires a potential much higher than the potential range for DFAFCs operation. The indirect pathway is undesired in applications.

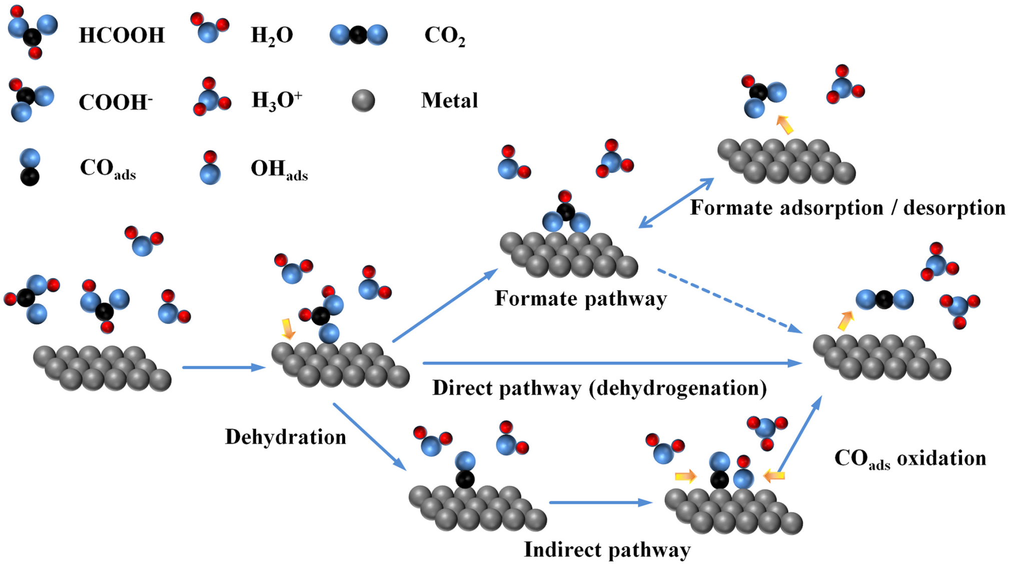

Figure 2.8: Scheme of the mechanism of formic acid oxidation in an acidic solution. Both carbon dioxide and formate ions are the possible products in this reaction.

On Pt-based electrodes, the "ensemble effect" has been introduced to understand the improvement of FAO on some surface-modified electrodes. The ensemble effect refers to the effect that a reaction requiring a large ensemble of active sites can be suppressed by diluting the active sites with a second inert metal [124]. FAO on a cyanide-modified Pt(111) electrode proceeds exclusively through the dehydrogenation pathway without the formation of CO_{ads}, because the hexagonally packed cyanide partially covers the Pt(111) surface, and blocks the three contiguous Pt sites which are necessary for dehydration of HCOOH [125]. The DFT calculations by Neurock et al. [121] also suggested that the indirect pathway requires a larger ensemble size and defect sites (more than two) while the direct pathway just needs one or two Pt atoms. The suppressed CO_{ads} coverage was also observed on Sb- and Bi-modified Pt single crystal electrodes [126, 127].

On the Pd-based electrode, the dehydration pathway of FAO is not favored [106]. This statement has also been confirmed by a DFT calculation in which FAO occurs on a Pd(111) surface through the dehydrogenation pathway with CO_2 as the dominant product [128]. However, the deactivation of Pd catalysts has been observed as well during FAO [102]. The deactivation has been explained as the surface poisoning caused by a strongly adsorbed inactive species. At carbon supported Pd NPs, which were used previously for FAO in concentrated formic acid, anodic stripping measurements were performed in $HClO_4$ solution, and the cyclic voltammogram (CV) revealed a CO_{ads}-like stripping characteristics [129]. The existence of CO_{ads} was confirmed by Wang et al. [130] with in situ attenuated total reflection surface-enhanced infrared adsorption spectroscopy (ATR-SEIRAS). Additionally, the CO_{ads} coverage depends on the surface concentration of CO_2. Therefore, many authors proposed another reaction pathway, i.e., the dehydrogenation product CO_2 is electrochemically reduced to CO_{ads}, in which the Pd plays the role of a catalyst for the electro-reduction [130, 131].

2.3 Nanoparticles in electrocatalysis

Nanostructured and nanoparticulate materials are widely used in practice in order to maximize the surface-to-volume ratio. Based on the established knowledge with bulk materials, some properties of nano-sized materials can be predicted. However, many new properties, which have never been observed on bulk materials, were reported for nano-sized materials, such as the change of color with size, the lower melting point as compared with its bulk, unexpected toxicity and so on [132–134].

Electrocatalysts, especially precious metals, are typically produced as NPs. If the apparent structural sensitivity of different catalytic reactions can be neglected, a high dispersion of the active materials yields a high mass activity. However, the specific activity and the selectivity for certain reactions are strongly dependent on the surface conditions, which can be changed in dispersion. Therefore, an increased dispersion may positively, or negatively, impact on the performance of the catalyst, e.g., the activity on a specific area.

A NP, which is always supported on an inert and conducting material, works as a reaction center for adsorbing reactants, intermediates and products along with the charge transfer. A single NP in an electrochemical process is considered as a complex system that many descriptors are involved, i.e. surface structures (such as facets, edge or corner atoms and defects), surface and bulk compositions (such as bimetallic or trimetallic alloys, core-shell structures), particle size and support materials. Besides aforementioned descriptors revealing the intrinsic properties of the electrode, some other descriptors from the electrolyte (such as the composition of the electrolyte) should be taken into account. In order to improve the electrocatalytic activity, selectivity and stability of supported NPs, the influence of all the descriptors to the electrocatalytic behavior should be understood. In this part some significant descriptors are discussed.

2.3.1 Electronic and structural factors

The parameters originating from the nature of the electrode can be categorized into two intrinsic factors: the electronic factor and the structural one. The electronic factor depends on the electronic status of surface atoms, which describes the binding energies between active sites and reactive species as well as the free energies of activation for completing catalytic reactions. The structural factor is attributed to the fact that different surface structures offer different active sites for electrocatalysis with various performance for certain reactions [74]. The overall performance of a NP in a certain reaction is primarily contributed by one or some specific surface structures, such that the optimization of the surface structures is able to enhance the catalytic activity for an investigated reaction. Both factors make influences simultaneously to the performance of a NP that they should be considered equally in the design of new catalysts.

Electronic effect [74]

Transition metal surfaces are always interesting in electrocatalysis. Their electronic states can be divided into two types: the $sp-$bands, which originate from the metal valence $s-$ and $p-$orbitals, and the $d-$bands, which are from the metal valence $d-$orbitals. The $d-$orbitals interact with the adsorbates weakly to form narrow bands which are close to the Fermi level. The adsorption energy is contributed by the bonding energy of the $sp-$electrons and the $d-$electrons. For example, an adsorbed oxygen atom (O_{ads}), which provides $2p-$orbitals, establishes bonding states with the metal $sp-$electrons, so that the $2p-$orbitals are filled to form the adsorbed O^{2-}. Meanwhile, the narrow $d-$bands couple with the renormalized oxygen $2p-$bands to form the bonding and anti-bonding states. The $d-$bands model assumes that the bonding energy of the $sp-$bands is independent of the metal; the variations of the bond strength for adsorbates on metals depend on the energy of the $d-$bands, which is determined by the distribution of the metal $d-$states relative to the Fermi level. Two descriptors, the $d-$band center and the $d-$band width, are always used in the discussion of the variations of the adsorption energy. The filling of the bonding and anti-bonding states of the adsorbates determines the bond strength with transition metals. Normally, a highly filled anti-bonding state corresponds to a weak bond strength. When the $d-$band of a certain metal is low-lying and fully filled, the bonding energy between the metal and the adsorbate will be the weakest due to the repulsive interaction between the bonding and anti-bonding states.

The $d-$band center of the adsorption site can be locally changed by several methods. One way is the change of the surface structures, such as the variation of the coordination number. The highly-coordinated atoms have broad bands due to the high overlap of electrons among the neighboring atoms. When the coordination number is lowered, the $d-$band width becomes narrower so that the $d-$band center shifts up in order to keep the constant filling of electrons at the Fermi level, which results in a stronger bonding. Strain effect can change the $d-$band width and the $d-$band center as well. The tensile strain, which increases the lattice distance of the surface atoms, causes the decrease of the electronic overlap and the $d-$band width, and leads to the up-shift of the $d-$band center. The compressive strain makes the converse effect. Another way of changing the $d-$band center is the stoichiometrically controlled change of the composition adjacent to the adsorption sites, such as the surface and subsurface alloying. The foreign atoms with different electronic structures induce the change of the host atoms electronically. When the foreign atoms do not exist on the surface but near to the surface atoms, this kind of near-surface alloying caused the change of the $d-$band center can be termed as the ligand effect. When the foreign atoms exist on the surface, the foreign atoms either induce the electronic change of the adsorption sites, or participate in the adsorption process, the ensemble effects should be considered additionally.

For mono-metallic NPs, different surface structures, such as facets, steps, corner and edge atoms, are present together. The electronic states of different surface structures are different, which is mainly attributed to the difference in coordination numbers. This kind of structure-related electronic effects is always combined with the purely geometric effects, and generally difficult to distinguish. The variation of the lattice constant of a NP as compared with its bulk material causes the strain effect. The strain effect is always dependent on the particle size. For nanoparticulate alloys, the foreign atoms on the surface or in the near-surface layer can directly modify the electronic states of the active sites. In some cases, the foreign atoms are not locating at the immediate vicinity of the surface atoms but forming alloys in bulk. The change of the lattice constant in the bulk by alloying can influence the electronic states of the surface atoms through the strain effects.

Structural effect

The structural effects are closely concerned and widely studied in electrocatalysis when complex surface structures are present at the catalysts, and the investigated reactions are sensitive to the surface structural. For a certain reaction, only one structure on the catalyst surface is usually considered to be the most active. However, some reactions, which involve several reaction steps and intermediates, are sensitive not only to one but several structures. Therefore, the understanding of a single structure as well as the synergistic effect of different structures is necessary for the development of new catalysts.

The structural factors impact on the performance of the electrocatalysts through two ways: the structure-related electronic effects, which have been discussed in the electronic effect, and the purely geometric effect. The geometric effect originates from the fact that different surface geometries provide different configurations for the molecular binding. It has been observed that the activation energies for a specific reaction on a series of transition metals with the same structure are roughly linearly correlated to the reaction energies, which is normally plotted as a Brønsted-Evans-Polanyi (BEP) line. The structure-related electronic effect corresponds to the displacement along the BEP line from one metal to the other due to the shift of the $d-$band center. For another surface structure, a new BEP line can be plotted which is normally parallel to the one of the former surface structure. If a value of the reaction energy is selected, the difference of the activation energies between two BEP lines, which are plotted based on two different surface structures, is contributed by the purely geometric effect [74]. The structural sensitivity of reactions can be classified to several types [12]. In some reactions like C-O, N-O and C-C dissociation, the structural sensitivity originates from the geometric effects, in which the change of the surface structure influences the activation energy strongly, and hence the BEP line shifts obviously along the axis of the activation energy. Some reactions, such as C-H and O-H bond breaking, prefer to occur at steps, since the products are more stable at the step sites than at terrace sites. This kind of structural sensitivity is caused by the structure-related electronic effects. Some reactions are weakly sensitive to the structure. Although the reactants prefer to locate at the step sites, the activation energies of the reactions at the steps do not show significant difference to those at the terraces [12]. Apart from all the reactions which are structural sensitive, other reactions do not prefer to specific structures, which are namely structure-insensitive. A truncated octahedron is always used to model the equilibrium shape of a face-center-cubic (fcc) nanocrystal according to the Wulff construction. The surface of a truncated-octahedral particle is covered by the (111) and (100) facets as well as the edge and corner atoms. The change of the ratio of the surface structures, which depends on the diameter of the particle, affects the electrocatalytic activity. Some NPs with a preferentially-orientated surface, such as nanocubes (bounded by (100) facets) or nano-octahedra (bounded by (111) facets), exhibits the similar properties with the extended single-crystal electrode with the same facet. For the FAO and the ORR, the investigations on some extended Pd single-crystal surfaces indicated that the Pd(100) is much more active than the other two Pd low-index facets [97, 135]. In latter works, the same result was observed that the Pd nanocubes show an enhanced activity for both reactions as compared to other nano-structures with a lower Pd(100) ratio [136, 137].

2.3.2 Size and support effects

There is no standard model to generally describe the shape of a NP. Although the truncated-octahedral shape is considered to be thermodynamically most stable for fcc nanocrystals, many NPs, which are synthesized with different methods and in various conditions, show significant difference in shape. Even the surface structures are not always stable in electrochemical processes where they can change from metastable states to the one with the lowest surface energy. The composition of NPs at the surface or near the surface cannot be determined accurately. Therefore, some electronic effects, which have been proved by some standard models or predicted by DFT calculations, are difficult to extend to the nano-structures. In practice, the particle size, which can be easily evaluated by existing microscopic techniques, is a frequently used descriptor. The understanding of size-dependent activity, selectivity and stability helps researchers to optimize the size of NPs, especially, precious metal NPs. Support materials, which contact with the NPs directly, can induce a change of electronic states of atoms at or near the interface. Additionally, some support materials are active to bind reactants or intermediates, which are necessary for the electrocatalytic processes occurring on the NPs, so that the active sites at the boundary show a much higher turnover frequency. In this part, the size and support effects are discussed in general.

Size effect

The size of a NP is a convenient descriptor which is always correlated with the observed properties, although it influences the properties indirectly through two intrinsic effects: the electronic and the structural effects. Generally, reactions occurring on NPs show three kinds of size dependence: The reaction rate increases with the decrease of the particle size (smaller better); the reaction rate decreases sharply when the particle is smaller than a critical size (smaller worse); and the reaction rate is insensitive to size [138]. The observed sensitivity of reactions to the particle size is based on the sensitivity to the geometric and electronic states which are size-dependent. Transition metal nanoclusters with a size smaller than 1 nm perform as molecules so that they can reconstruct when contacting with foreign molecules or atoms. Quantum size effect can be observed in such scale so that the activity of the clusters is significantly influenced by their electronic states, which change strongly with the number of atoms. NPs with sizes from 1 to 3 nm always have a convex-polyhedron shape, which consists of several polygonal facets. The number of interior atoms becomes more than that of exterior ones, thus the structure is more stable. The atoms at facets, edges or corners have different coordination numbers. Therefore, their binding strengths with adsorbing molecules or atoms are different. In the size scale of 3 to 10 nm, the interior atoms of transition metals may form a lattice structure, but the structure can be different to the most stable one of their bulk materials. For example, small cobalt particles have the fcc structure instead of the more stable hexagonal-close-packing (hcp) structure [139]. The activities of different structures at a particle surface can be predicted by that at an extended surface, but additional surface energy should be counted in. When particles are larger than 10 nm, the surface structures of the particle are comparable to the structures of the termination of the bulk material. The overall performance of the particle is more dependent onto the ratio of the different structures.

The truncated-octahedral particles were modeled as a Wulff construction of (100) and (111) facets using a ratio between the respective surface free energies of $\gamma_{100}/\gamma_{111}$ =1.189 [140]. The ratios of different surface structures are highly dependent on the particle size. When the diameter of the particle is larger than 10 nm, the ratio of edge and corner atoms is lower than 20 %; the ratio of (100) facets is higher than that of edge and corner atoms; the ratio of (111) facets is around 60 %. When the particle becomes smaller than 10 nm, the ratio of (100) facets drops down dramatically from around 20 % at 10 nm to less than 5 % at 2 nm. The ratio of (111) facets decreases sharply when the particle is smaller than 5 nm. Meanwhile, the ratio of low-coordinated atoms increases exponentially from around 10 % at 18 nm to more than 75 % at 2 nm. It is a rule that the relative amount of low-coordinated atoms (edge and corner atoms) increases with the decrease of the particle size, whereas the relative amount of atoms at terraces ((100) and (111) facets) becomes fewer. This rule is generally accepted for all polyhedron-shaped NPs. Low-coordinated atoms tend to bond more strongly with adsorbates due to the higher $d-$band center as compared with the highly coordinated atoms. For some reactions, the key intermediate in the RDS bonds to the terrace atoms of the transition metal surfaces stronger than the optimum so that the decrease of the particle size, viz. the increase of the ratio of low-coordinated atoms, leads to an activity decline. In contrary, the decrease of the particle size is able to enhance the activity for some reactions in which the key intermediate bonds to the transition metal surfaces weaker than the optimum.

Support effect

In electrocatalysis, support materials are commonly used on which NPs disperse homogeneously. The atoms at, or near, the interface between NPs and support materials can be influenced geometrically or electronically. Some support induced effects superpose the intrinsic properties of the supported NPs so that the performance of the transition-metal NPs in some reactions can be different. The ligand effect is present at the contiguous atoms between the NPs and the support materials due to the electronic effects caused by the foreign atoms. Charge transfers across the interface to fill the electron orbitals of the elements with higher electron negativity, which leads to the formation of some oxidation states at the interface. The oxidation states modifies the electronic structures of the metal NPs, and influences their adsorption behavior. For instance, the electronic structures of Au NPs are affected by titania by charge donating that the activation barrier for the CO oxidation is lowered at the Au surface. In electrochemical measurements, Au NPs supported on titania, as a result, show a higher activity for the CO oxidation than on carbon support [30].

Besides the electronic effect caused by the direct charge transfer, strain effects are able to change the electronic structures of supported NPs, especially in the bimetallic systems. Epitaxially-grown overlayers normally adapt to the lattice structure of the support materials so that the resultant lattice strains change the position of the $d-$band center; meanwhile, their binding strength to adsorbates varies correlatively. The support-induced lattice strains have been reported by many authors [141–143]. Pd monolayer on Au(111) yields a tensile strain that the $d-$band center is higher than that of Pd(111) surface atoms; while the lattice constant of a Pd monolayer on Pt(111) is compressed such that the $d-$band center shifts down. The binding strength of these three surfaces with hydrogen atoms shows a sequence of Pd/Pt(111) < Pd(111) < Pd/Au(111). The same sequence was observed for the adsorption of oxygen atoms [141]. By increasing the number of overlayers, the strain effects become weaker until to disappearance. Then the lattice constant recovers to the same value as the bulk material.

In some reactions, the substrate surface adsorbs certain reactants or intermediates, which are necessary for the overall reaction. The boundary of the NPs and the support materials behaves as active sites where the reactants from both surfaces have opportunity to meet each other [144]. Additionally, some intermediates adsorbed initially on the NPs can also spill over onto the substrate surface, and react continuously to form the final product [52, 145]. The substrate surface plays the role of intermediate storage and, partially, the reactive site. Therefore, the specific activity of NPs is increased by such synergistic effects.

2.3.3 Stability and poisoning

A stable electrocatalyst should preserve its activity over a long-term operation, and avoid the loss of the electrochemically active surface area (ECSA). However, the gradual loss of the ECSA is inevitable in practice. The ECSA of supported transition-metal NPs can decrease physically or chemically through reforming of surface structure and dispersion, or poisoning by harmful impurities or byproducts. The degradation through reforming of surface structures and dispersion follows several mechanisms [146]. The surface atoms can dissolve into the solution as ions. The dissolution rate strongly depends on the inertness of the material as well as the working conditions, such as temperature, pH value, potential and composition of the electrolyte. If the dissolved atoms keep staying in the solution, or diffuse out of the catalyst layer, the dissolution causes the loss of the catalyst loading. If the dissolved atoms redeposit on a larger particle, the growth of this particle occurs which leads to an increase of the average particle size and a loss of the ECSA. This kind of degradation is called Ostwald ripening. The driving force for the Ostwald ripening is the minimization of the surface energy by reducing the exposed surface atoms, which works against a high dispersion of NPs. Particles always migrate on the substrate surface, especially, when they are weakly bound to the substrate. A particle moving on the substrate is possible to collide with another particle to form a bigger one. After successive collisions, some large particles, of which the surface-to-volume ratio is much lower, appear among smaller ones, and the dispersion of particles becomes lower, which is known as particle agglomeration. Besides the 2D migration, particles are able to detach from the support, and diffuse into the solution. When the degradation of particles follows the detachment mechanism, the average particle size changes only slightly, but the number of particles decreases in the testing period. Additionally, the corrosion of support materials is an important issue in the degradation of supported NPs. The corrosion may weaken the interactions between NPs and substrate, or break the surface structures for holding particle dispersion, which leads to more serious degradation of the ECSA of supported NPs.

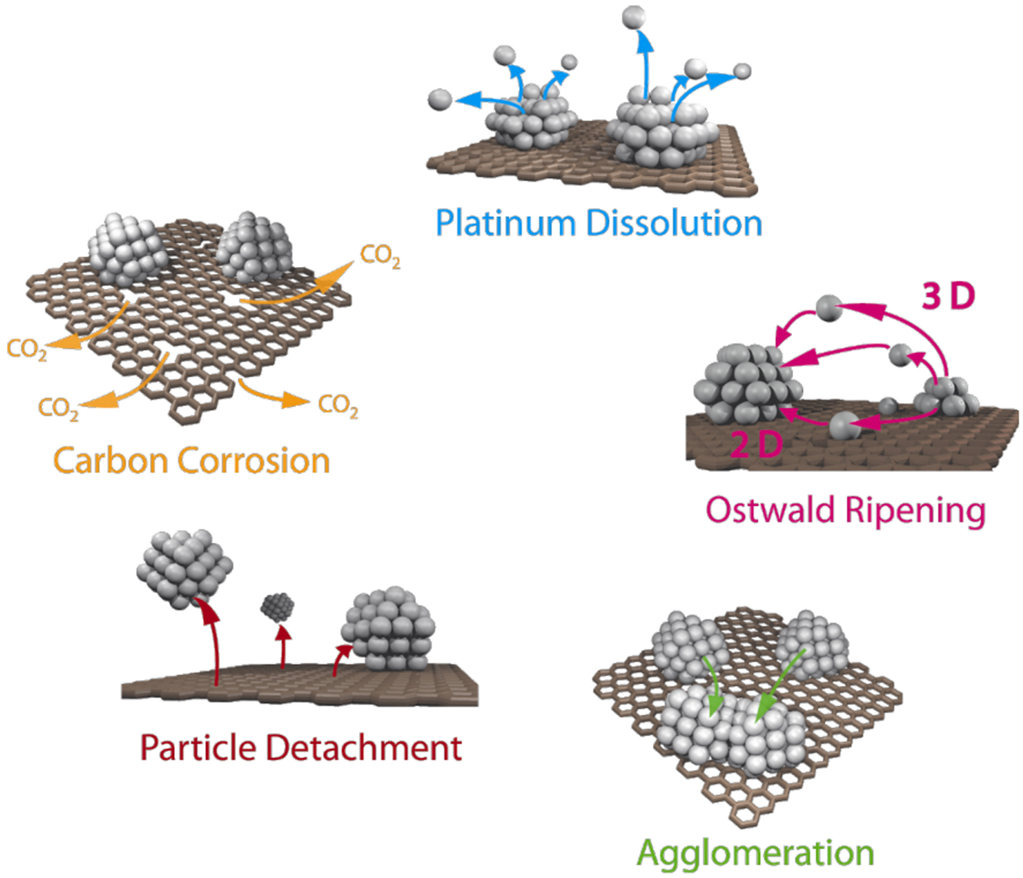

Figure 2.9: Simplified representation of degradation mechanisms for Pt NPs on a carbon support in fuel cells. [Reprinted from [146], with permission from Beilstein-Institut.]

The loss of ECSA can happen even without observable changes in structure or dispersion. Some molecules existing in reaction environments as impurities or byproducts can adsorb strongly onto catalyst surfaces, and block the active sites for further reactions. CO is one of the most commonly discussed poisons, especially for PGMs. It is a strongly adsorbed intermediate in electro-oxidation of some small organic molecules like methanol, ethanol or formic acid. It is also a byproduct in hydrogen production through the steam reforming from hydrocarbons. CO is preferentially adsorbed onto metal surfaces through the carbon atom. It adopts a range of bonding geometries, such as on-top (with one metal atom), bridge (with two atoms) and hollow (with three atoms). Once an adsorbed CO layer forms on the Pt or Pd electrode surfaces, a potential at least higher than 0.7 V vs. RHE is necessary to electrochemically remove the adsorbed CO [147, 148]. Small NPs, which have a high ratio of low-coordinated atoms, tend to have a stronger bond with CO than their bulk material [149]. Therefore, CO poisoning of NPs is one of the most intensively studied topics, and the fundamental understanding is continuously promoting the development of the CO-tolerant materials.

2.4 Ionic liquids

ILs are molten salts whose melting point is below some arbitrary temperature such as 100 °C. Their properties are entirely different from ordinary molecular liquids such as water: they are composed only by ions, thus their ionic density and conductivity are very high; they are liquids at ambient temperature with a very wide available temperature window; they are nonvolatile, nonflammable and with a high thermal stability [150]. The hygroscopicity of ILs cannot be neglected. In most cases, ILs must be dried under vacuum at elevated temperatures and stored in a dry atmosphere. There are many different possible cations and anions thereof as building blocks for ILs so that the ILs are designable with unlimited combinations. Figure 2.10 shows the structures of some commonly used cations and anions. Quaternary ammonium cations, such as ammonium-based, imidazolium-based, piperidinium-based, pyridinium-based, pyrrolidinium-based ions, are usually employed. Additionally, phosphonium-based and sulfonium-based cations are two major categories. The anions contain halides, bis(trifluoromethylsulfonyl)imide, tetrafluoroborate, hexafluorophosphate, cyanide-based ions and so on.

In electrochemical applications, ILs are used as electrolytes. Any electroactive species in the ILs can influence the apparent potential window. Therefore, the purity of ILs is important. Even for a highly purified IL, the solubility of O_2 should be considered as well. The dissolved O_2 can be reduced to superoxide in the absence of protic species, which is unfavorable for the electrodeposition of active metals [151, 152]. Pt, W and carbon materials are often used as working electrodes for electrochemical measurements in ILs. The working electrode is preferred to have a small active area in order to minimize the ohmic potential drop, since most of the ILs have a relatively lower conductivity in comparison to aqueous solutions [150]. Reference electrodes,

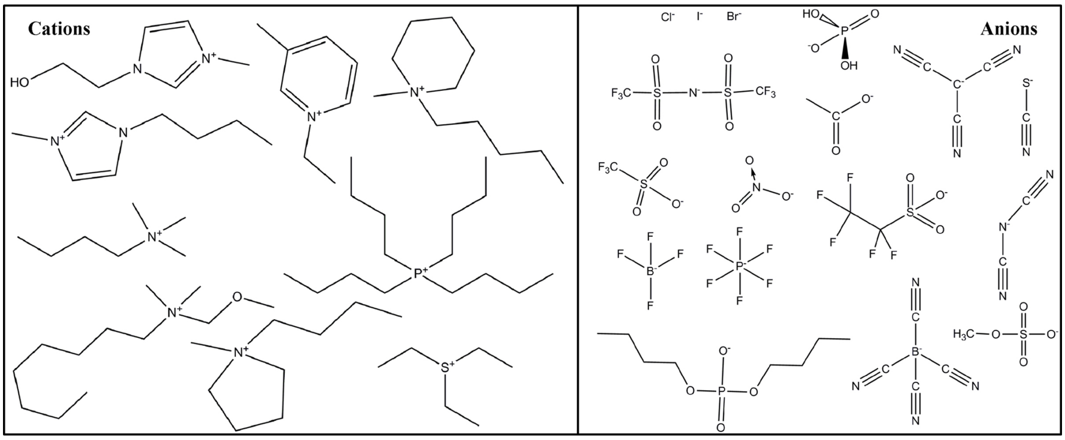

Figure 2.10: Structures of cations and anions of commonly used ILs. There are many possibilities by combinations of the cations and anions.

such as Ag / AgCl consisting of a Ag / Ag^+ redox couple, based on the ILs are recommended to use with a liquid-liquid junction connecting into the electrolyte. A metal piece, such as Pt, Li or Ag, immersed in ILs without redox couple can be used as a quasi-reference electrode when the potential is proved to be stable. The potential of the reference electrode depends on the composition in the electrolyte. Therefore, the comparison of potentials measured in different ILs is difficult, even though the recorded values are referring to the same reference electrode. The redox potential of Fc / Fc^+ can be used as a standard potential due to its independence of applied electrolytes.

The electrochemical potential window of an IL can be estimated by running cyclic voltammetry or linear sweep voltammetry up to the oxidation and reduction potentials of the electrolyte. However, the selection of the potential limits to identify the onset of the oxidation or reduction of the IL ions is difficult, since the oxidation and reduction of the IL ions, which are normally irreversible, do not show specific potentials [153, 154]. Therefore, a certain current density, at which the reaction is considered to begin, is always selected to evaluate the upper and lower potential limits. The specified current density is called cut-off current density. The measured current density with a potential sweep method is proportional to the square root of the scan rate ($j \sim \sqrt{\nu}$). In the comparison of potential windows, the scan rate should be specified in addition to the cut-off current density.

The electrodeposition of metals in ILs has been intensively investigated. The background for the application of ILs in electrodeposition is to deposit active metals which have much lower standard electrode potentials than hydrogen. In alkali metals, lithium (Li) and sodium (Na) have been successfully deposited from tetrachloroaluminate-based ILs [155, 156]. In alkali earth metals, the electrodeposition of magnesium (Mg) metal has been reported in pyrrolidinium-based and tetra-alkylammonium-based ILs [157, 158]. Some other main group metals, such as aluminum (Al), Gallium (Ga), Bismuth (Bi) and so on, can be electrodeposited from ILs as well [150]. The challenge of metal deposition in ILs is electrodepositing early transition metals and REMs. Tantalum (Ta) can be electrodeposited from a TaF_5

precursor in pyrrolidinium-based ILs [159]. However, the contamination of fluoride in deposits cannot be avoided, although the atomic ratio of F / Ta can be reduced as low as to 1 / 4. In REMs, La has been reported to be successfully deposited from pyrrolidinium-based ILs [160], but no further investigation can support the result. Hussey's group [161–163] studied the reduction behavior of several lanthanide trivalent ions (Ce^{3+}, Pr^{3+}, Nd^{3+}, Sm^{3+}, Eu^{3+}, Yb^{3+}) in ILs, and suggested that the trivalent ions can be partially reduced to the bivalent states. The redox process of the trivalent and bivalent species is quasi-reversible. All species are readily accessible in the ILs to form complexes. Until now, no solid evidence has proved that REMs can be electrodeposited from ILs.

Chapter 3

Materials and methods

This chapter introduces the used chemicals, materials, experimental techniques and setups. The chemicals contain metal precursors, solvents and gases. The electrode materials, especially HOPG, N-HOPG and Au thin-layer electrodes, are introduced in detail. Some experimental techniques and setups for electrochemical, microscopic and spectroscopic measurements are summarized.

3.1 Chemicals and materials

The chemicals used in this thesis are listed in Table 3.1.

All solutions were prepared with deionized water (Milli-Q water). Peroxymonosulfuric acid (Caro's acid) was prepared with H_2SO_4 (95 - 97 %, p.a.) and H_2O_2 (30 %) at a volume ratio of 1:1.

Platinum (99.99 %) and gold (99.995%) wires with diameters of 0.25 mm and 0.5 mm were purchased from MaTecK GmbH. Palladium (99.95 %) wire with a diameter of 0.5 mm was purchased from MaTecK GmbH. Palladium (99.95 %) wire with a diameter of 0.25 mm was purchased from Ögussa. All metal wires were flame annealed with a Bunsen burner and cleaned in Caro's acid and Milli-Q water before introducing into electrochemical cells. Platinum / iridium (Pt / Ir) wire, as the tip material for scanning tunneling microscopy (STM), with an atomic ratio of Pt : Ir = 80 : 20 was purchased from MaTecK GmbH. The diameter of the Pt / Ir wire is 0.25 mm. An Apiezon wax (Plano) was used to cover Pt / Ir tips when the tips were applied in electrochemical STM (EC-STM). A Teflon® tape (No. 75100) was bought from CMC Klebetechnik GmbH. All glass- and Teflon-ware was cleaned in Caro's acid and rinsed with deionized water.

The purchased ILs were pretreated to remove the oxygen and water contents before transfer into the Ar-filled glovebox. Each IL was stored in a Schlenk flask with the side arm connecting to a diaphragm pump (055Z, Ilmvac). The bottom of the flask was embedded into a heating block (Drysyn) which was supported on top of a ceramic heating plate (IKA, C-MAG-H57). When the diaphragm pump started to work, the high vacuum stopcock at the side arm of the flask was opened. The temperature at the heating plate was set to 140 °C, and the temperature measured

Table 3.1: All chemicals containing metal precursors, solvents and gases.

Chemical	**Formula**	**Quality**	**Provider**
Sulfuric acid	H_2SO_4	96 %, Suprapur	Merck
Sulfuric acid	H_2SO_4	95 - 97 %, p.a.	Merck
Chloric acid	HCl	32 %, extra pure	Merck
Formic acid	$HCOOH$	94.50 %	Amresco
Bis(trifluoromethyl sulfonyl)imide acid	$HN(SO_2CF_3)_2$	$\geqslant$ 95 % (F-NMR)	Fluka
Palladium(II) nitrate solution	$Pd(NO_3)_2$	16.27 %	MaTecK
Palladium(II) nitrate hydrate	$Pd(NO_3)_2 \cdot xH_2O$	p.a.	Sigma-Aldrich
Chloroplatinic acid hexahydrate	$H_2PtCl_6 \cdot 6H_2O$	99.995 %	Sigma-Aldrich
Yttrium(III) nitrate hexahydrate	$Y(NO_3)_3 \cdot 6H_2O$	99.80 %	Sigma-Aldrich
Sodium sulfate	Na_2SO_4	99.50 %	Merck
Milli-Q water	H_2O	18.2 MΩ cm, 3ppm TOC	Merck Millipore
Hydrogen peroxide	H_2O_2	30 %	Merck
1-Octyl-1-methyl pyrrolidinium bis(trifluoromethyl sulfonyl)imide	$C_{15}H_{28}F_6N_2O_4S_2$	99 %	iolitec
N,N-diethyl-N-methyl -N-(2-methoxyethyl) ammonium tetrafluoroborate	$C_8H_{20}BF_4NO$	$>$ 98 %	iolitec
Isopropanol	C_3H_8OH	p.a.	Sigma-Aldrich
Aceton	C_3H_6O	p.a.	Sigma-Aldrich
Argon	Ar	5.0	Westfalen
Hydrogen	H_2	5.0	Linde
Oxygen	O_2	5.0	Linde
Carbon monoxide	CO	3.7	Linde

at the heating block was 110 °C. Each IL was pretreated at 110 °C in vacuum for 24 hours. After pretreatment, both ILs were transferred into a glovebox ($O_2 \leqslant 0.6$ ppm, $H_2O \leqslant 0.6$ ppm, MBraun). When the ILs were filled into glass bottles, they were heated up to 110 °C again for 24 hours in Ar atmosphere for further drying.

3.2 Electrode materials

In this thesis, three electrode materials were used apart from the noble metal wires in reference measurements. They are HOPG, N-HOPG and thin gold layers on quartz and glass. Pure HOPG and thin gold layers on quartz and glass were commercially available. N-HOPG samples were prepared in Prof. Gaetanno Granozzi's group at the University of Padova.

3.2.1 Highly oriented pyrolytic graphite

HOPG (grade ZYB ($0.8° \pm 0.2°$, mosaic spread)) was purchased from Mikromasch. HOPG, which has large grains and atomic-level flatness, is suitable to be used as a substrate in scanning probe microscopy (SPM). Its chemical inertia and weak binding to supported materials are advantages for use as a model electrode in electrochemical analysis. Its parallel-stacked graphene layers allow the facile cleaving of very thin layers such that the surface of the sample can be refreshed easily. Once a fresh HOPG surface was required in the experiment, the HOPG sample was prepared by cleaving the graphite surface with an adhesive tape for several times until a smooth surface without visible defects was obtained. The HOPG surface was partially covered with a Teflon® tape in order to expose a well-defined surface area in contact with the electrolyte. Before the deposition of metal NPs on HOPG, more defects on the HOPG surface were intentionally produced by applying a short and high oxidation potential. The oxidation potential applied in this work was 5.73 V vs. RHE for 100 μs in O_2 saturated electrolytes [42]. The intentionally produced defects and original edges and defects were nucleation sites for metal deposition.

3.2.2 Nitrogen doped HOPG

The crystalline structure of HOPG is parallel-stacked graphene. Graphene is highly inert due to its tightly packed carbon atoms and sp^2 hybridization. Supported metal NPs interact with the HOPG surface nearly exclusively by van-der-Waals forces. When nitrogen functional groups are introduced by ion implantation into the top layers of a HOPG sample, the electronic states of the substrate as well as the morphology are modified. Several chemical defects, i.e. C-sp^2-N defects (pyridinic, pyrrolic and N substitutional), -C≡N terminal groups and trapped N^+ and N^{2+} ions in carbon vacancies, are expected to be generated. Geometrical defects, which can be considered as carbon vacancies, are also produced during ion implantation [164–166]. In this work, N-HOPG was prepared from pure HOPG by ion implantation. Before the ion implantation, clean HOPG samples were annealed cyclically from 500 °C to

800 °C in the UHV chamber. The base pressure of the UHV environment is lower than 5×10^{-9} mbar. During the ion implantation, a cold plasma was produced in a 2.2×10^{-6} mbar background of N_2. The annealed HOPG samples were exposed to the plasma with a beam energy of 100 eV for 45 min. The incidence angle of the ion beam equaled to 45 °C with respect to the sample surface. The ionic current measured during the ion implantation was 1.5 μA, and the total dose of implanted nitrogen was around 1×10^{16} ion cm^{-2}. The nitrogen amount was determined by normalizing the intensity of the N 1s XPS peak to the integrated area of the C 1s photoemission line, obtaining a nitrogen dose of 7.5 at%. Monto Carlo simulations of the nitrogen implantation process have been carried out in order to quantitatively estimate the distribution of the chemical and geometrical defects (shown in Figure 3.1). The N^+ distribution is centered at 9 Å depth from the surface with a full width at half maximum (FWHM) of 6 Å, while the N_2^+ distribution is closer to the surface with a centered depth of 6.7 Å and a straggling of 8 Å. The sum of the two distributions is characterized as a centered depth of 7.9 Å with a FWHM of 10.3 Å. The graphite lattice constant perpendicular to the surface is equal to 3.35 Å. Therefore, the functional groups and defects are distributed primarily at the topmost, i.e. from one to three, graphene layers.

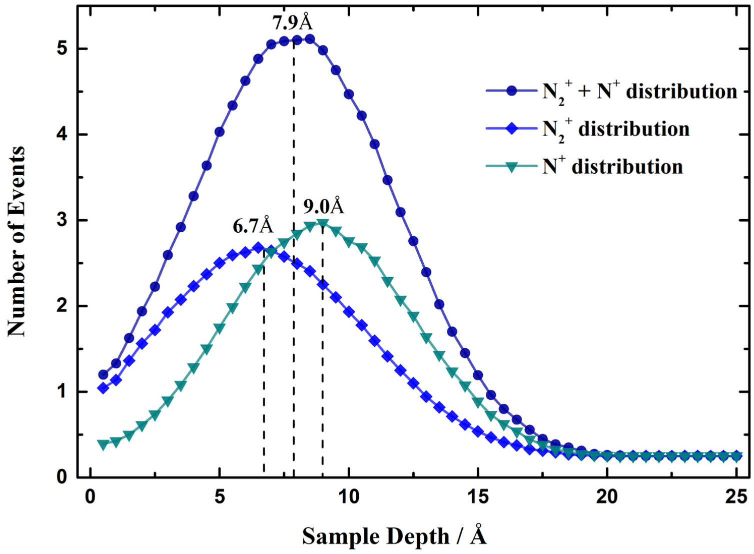

Figure 3.1: Profiles of implanted nitrogen ions in a HOPG obtained from Monte Carlo simulations of the implantation process.

3.2.3 Thin gold layers on glass and quartz

The samples of thin gold layers on glass (11 mm × 11 mm) were purchased from Arrandee metal GmbH. The sample consisted of a borosilicate glass support, a 2.5 ± 1.5 nm chromium interlayer and a 250 ± 50 nm gold overlayer. The gold layer was initially polycrystalline. A flame annealing process is necessary to reform the surface in order to obtain well-defined Au(111) terraces with sizes of several hundred

nanometers. Each sample was heated by a Bunsen burner to dark red glowing, and then removed from flame for a 30-second cooling. The procedure was repeated two to three times leading to the formation of well-defined Au(111) terraces.
The thin-gold-layer electrodes on 10 MHz quartz resonators were purchased from KVG Quartz Crystal Technology. The quartz resonator (d = 12 mm) was obtained by slicing the quartz rod with an angle of 35°25' to the crystallographic $z-$axis (AT cut). The keyhole shaped Au layers (with a chromium adhesion layer underneath) were deposited on both sides of the quartz as electrodes to establish an alternating electrical field.

3.3 Instrumentation and techniques

3.3.1 Electrochemical setups

Electrochemical setups were used in metal deposition, electrochemical characterization and reactivity measurements. An electrochemical workstation, which combines potentiostat and galvanostat functions, was connected to a standard three-electrode cell, and acquired potential or current signals at the time scale. Many methods, such as potential step, potential sweep, cyclic voltammetry, impedance spectroscopy and so on, were applied for different purposes.

Potentiostat

A potentiostat is an electronic device which enforces a controlled potential at a working electrode. A function generator produces the desired potential perturbation at the working electrode, which is related to the potential of a reference electrode. The corresponding current goes through a closed circuit, which consists of a working electrode, electrolyte, a counter electrode and electron conductors. A recording system measures the potential and current at the time scale. The relations of potential, current and time can be displayed in voltammetric, chronopotentiometric and chronoamperometric curves. A galvanostat, in contrast, applies a controlled current through the working and counter electrodes, meanwhile, records the corresponding potential difference between working and reference electrodes. In this thesis, an Autolab PGSTAT 30 (Metrohm Autolab B.V.) and an Ivium CompactPlus potentiostat (Ivium Technologies B.V.) were used. The data were acquired by GPES, Nova (1.7 to 1.9) and Iviumsoft.

Electrochemical glass cell

In electrochemical measurements, the reactions at the interface between the working electrode and electrolyte are of interest. In order to study the behavior of the working electrode, a polarization, either cathodic or anodic, is imposed through potential or current. The potential of the working electrode is measured with respect to the reference electrode. Only when the potential of the reference electrode is fixed, the recorded potential difference can be reliable, and any changes at the working electrode can be correlated to the potential change. Therefore, a large current passing through the reference electrode, which may cause a potential change, should be avoided. In a three-electrode arrangement shown in Figure 3.2, the reference electrode connects to the potentiostat with a high input impedance, so that the current through it is negligible. In this work, mercury/mercury sulfate (Hg / Hg_2SO_4) electrodes in 0.1 M H_2SO_4 (B3610, Schott) and saturated calomel (Hg / Hg_2Cl_2) electrodes (B3410, Schott) in saturated potassium chloride solution were used as reference electrodes in aqueous solutions. The compartment for the reference electrode was connected to the main part of the cell via a Luggin capillary, of which the end approached the surface of the working electrode within a few millimeters in order to minimize the ohmic potential drop in the electrolyte. The current flows between the working and counter electrodes. The electrochemical properties of the counter electrode do not influence the behavior of the working electrode. The material of the counter electrode should be highly conductive and inert in the used electrolyte. Additionally, any contamination through the counter reaction should be avoided. When Pd ions in electrolytes or Pd NPs on supports were involved in the measurements, Pd wires with a diameter of 0.5 mm were used as counter electrodes. Pt wires with a diameter of 0.5 mm were employed as counter electrodes in the cases of Pt ions or Pt NPs in investigations.

The atmosphere in the electrochemical cell can be adjusted by gas purging. Two gas inlets were plugged into the cell for two operating modes: a long one was dipped into the electrolyte for liquid-phase deaeration; a short one was kept above the electrolyte for purging the gas phase. A gas outlet, which was filled with water, allowed the gas flowing outwards, and prevented the air diffusion into the cell.

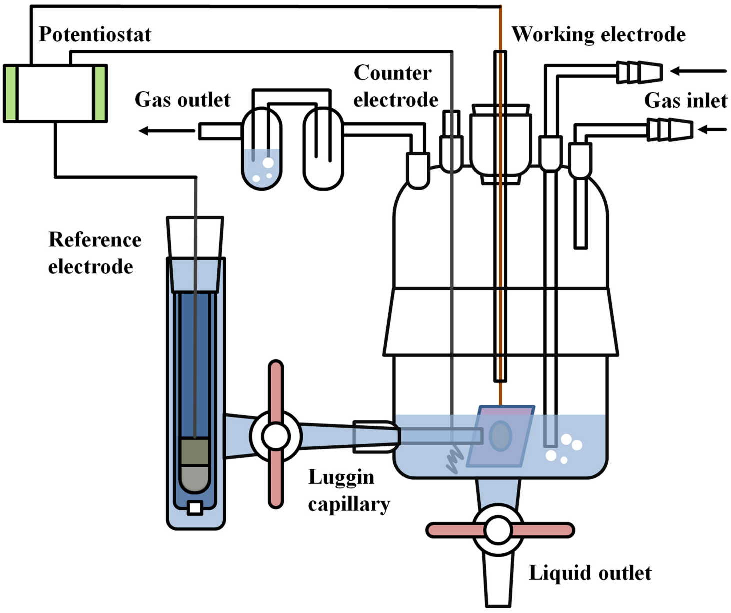

Figure 3.2: Scheme of the three-electrode glass cell for electrochemical measurements with aqueous solutions.

Electrochemical mini-cell

The electrochemical mini-cell, which is shown in Figure 3.3, was used specifically for the measurements with ILs as electrolytes. The mini-cell consists of a Teflon® ring with a volume of about 80 μL. The Teflon® ring is pressed on top of the working electrode surface by a piece of binder plate which is fixed with two clips at two spring pillars. The exposed surface area of the working electrode is about 0.13 cm^2. A Pt wire was used as a quasi-reference electrode. The counter electrode was a circular-shape Pt wire when the substrate was HOPG, or a gold wire when the substrate was a thin gold layer. All Pt and Au wires were annealed in flame and cleaned by Caro's acid and deionized water extensively. All measurements with ILs as electrolytes were carried out in an Ar-filled glovebox ($O_2 \leqslant 0.6$ ppm, $H_2O \leqslant 0.6$ ppm).

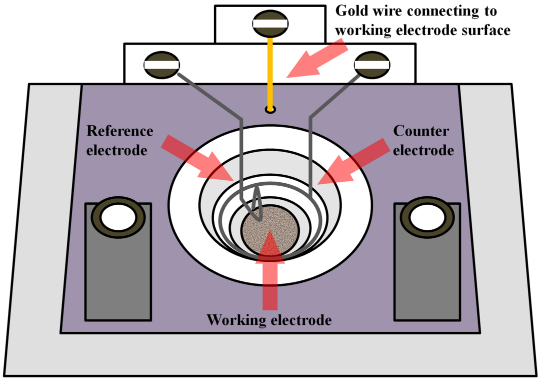

Figure 3.3: Scheme of the mini-cell for electrochemical measurements with ILs.

Electrochemical quartz crystal microbalance

An electrochemical quartz crystal microbalance (EQCM) works as a thickness monitor in electrochemical processes. The technique is based on the piezoelectric properties of a thin quartz crystal sandwiched between two electrodes. Piezoelectricity is the effect that a mechanical stress to a crystal which is lacking of centrosymmetry creates an electric field. EQCM is based on the converse piezoelectric effect that an applied alternating electrical field causes an oscillation of the quartz, which produces a transverse acoustic wave reflecting at the crystal surfaces. For a quartz crystal with a given thickness, the quartz oscillates at its resonance frequency with formation of a standing wave by interference of the original and the reflected waves. Once a deposited layer forms on top of one electrode surface, the resonance frequency of the quartz changes due to the mechanical interaction between quartz and deposited layer. Normally, the resonance frequency decreases with the accumulation of deposits. There is a linear relationship between the mass change (Δm) per cm^2 on the working electrode and the frequency change (Δf), which is described by the Sauerbrey equation [167]:

$$\Delta f = -\frac{2{f_0}^2}{\sqrt{\rho_q \mu_q}} \Delta m \tag{3.1}$$

where f_0 is the resonance frequency of the quartz at the initial state, ρ_q is the density of quartz (2.648 g cm^{-2}), and μ_q is its shear modulus (2.947×10^{11} g cm^{-1} s^{-2}). According to the simultaneously recorded charge transfer during electrochemical processes, the mass accumulation per mole of electron transfer can be evaluated. However, the actually measured Δf does not depend only on Δm, but contains contributions from the electrolyte, the temperature and pressure as well as the roughness and slippage of deposited layers. The Sauerbrey equation is valid for acoustically thin, rigid films, and assumes no slip conditions [168].

The mechanical properties of the quartz resonator can be characterized by a network analyzer through the equivalent electrical signal which is the electrical admittance (or impedance) between the two gold electrodes. The real part of the admittance is a function of the frequency f with a Lorentz shape. The frequency at the peak of the real-part admittance is characterized as the resonance frequency, and the FWHM, which is a measure for the energy losses of the quartz crystal due to the viscoelastic behavior or roughness, is called damping w [168–170]. One important constraint for the applicability of the Sauerbrey equation is that the change of the damping (Δw) is equal or less than 10 % of the change of the frequency (Δf) in the same process [171].

In this thesis, 10 MHz quartz resonators with two gold-layer electrodes were employed, and one of the gold electrodes was used as the working electrode in electrochemical processes. The quartz was placed at the bottom of a Teflon® electrochemical cell (shown in Figure 3.4) with one Au electrode exposed to the electrolyte. Fluoropolymer (Simriz^{TM}) O-rings with a diameter of 10 mm and a thickness of 2 mm were used to seal the electrochemical cell. The reference and counter electrodes were both Pt wires with a diameter of 0.25 mm. The electrical admittance between the two Au electrodes was measured in a frequency range around the resonance frequency with an Agilent E5100A network analyzer. The electrochemical data were acquired by an Ivium CompactPlus potentiostat.

3.3.2 Microscopic and spectroscopic techniques

SPM and XPS were used to characterize the morphology, composition and oxidation states of samples. The frequently used SPM techniques in this thesis including STM, EC-STM, and TM-AFM.

Scanning probe microscopy

Two different SPM setups were used to characterize the morphology of electrode surfaces. A Veeco Multimode Electrochemical Scanning Tunneling Microscope / Atomic Force Microscope (EC-STM/AFM) system (Mode No. 920-006-101) was applied for the measurement in air. The system was controlled by Nanoscope 5.31r1

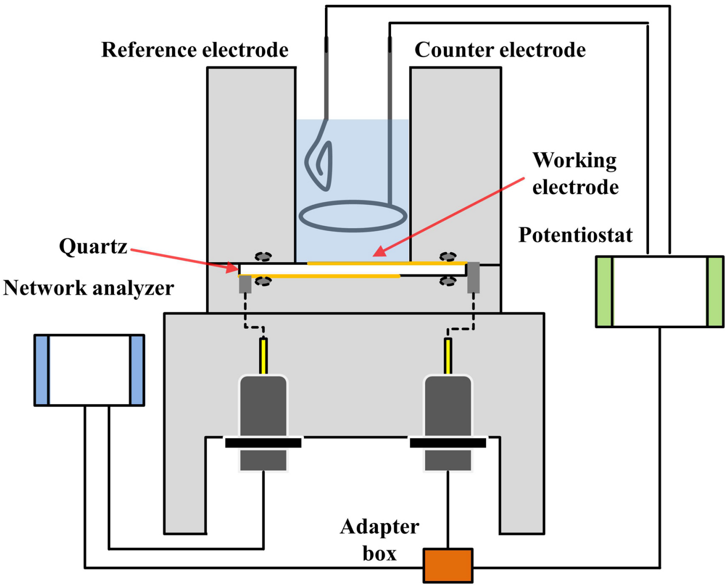

Figure 3.4: Scheme of the electrochemical cell for EQCM measurements with ILs.

software, which provided SPM and EC data acquisition. In this setup, the sample was placed on top of the piezoelectric scanner, which was able to move in $xyz-$direction with a range of 10 μm × 10 μm × 2.5 μm. The position of the tip was fixed.

The other SPM setup was homebuilt consisting of a Nanoscope IIIA controller (Veeco Instruments Inc.), a PicoSPM STM base (Molecular Imaging) and an EC-Tec bipotentiaostat / galvanostat BP600 with a bi-scangenerator SG600. The system was controlled by Nanoscope v 4.43r6 software which provided SPM date acquisition, whereas the electrochemical data were recorded with a LabVIEW program BP600. In this system, the tip was held by the piezoelectric scanner, which was able to scan on the fixed sample in $xyz-$direction. The sample was mounted on a ferromagnetic sample holder, which was magnetically hung under the scanner via three micrometer screws. Two screws served for a manual approach of the tip to the sample surface. The third screw was electronically controlled for a fine approach. The scanner was able to scan in a range of 5 μm × 5 μm × 2 μm in $xyz-$direction.

STM tips were prepared from Pt / Ir wire by small-angle clipping. For EC-STM measurements, the Pt / Ir tips were insulated with Apiezon® wax in order to reduce the exposed tip surface, furthermore, to minimize the faradaic current through the tip. Tapping mode AFM (TM-AFM) tips were commercial phosphorus (n) doped Si cantilevers with a nominal tip radius of 8 nm (RTESPA, Bruker). The SPM images were evaluated with WSxM 4.0 image analysis software (Nanotec Electronica S.L.) [172].

X-ray photoemission spectroscopy

The XPS technique, which is based on the photoelectric effect, has an extensive application in surface science to measure the binding energies of electrons in matter. The X-ray photon with a certain frequency ionizes an atom and emits a photoelectron which possesses a kinetic energy. The maximum kinetic energy of an emitted photoelectron, which is equal to the difference of the photon energy and the electron binding energy, can be considered as the finger print of an element. The spectrum of the kinetic energy provides information of the composition in matter and the oxidation states of elements. In this thesis, the XPS system, belonging to the Surfaces and Catalysts Group in Padova, was used. A double anode (Mg / Al) X-ray source (Omicron DAR 400, maximum power 300 W) was installed in a Multi-Technique UHV chamber (base pressure $< 5 \times 10^{-9}$ mbar). The energies of the X-ray commonly used in measurements were 1253.6 eV (Mg $K\alpha$) and 1486.7 eV (Al $K\alpha$). The X-ray source was operated at a potential of 15 kV with an emission current of 20 mA. A 5-channeltron electron hemispherical analyzer (Omicron EA 125 Energy Analyzer) interfaced with the X-ray source. The sample was held by a XPS / STM bi-functional sample holder, which was controlled by a 5-degree-freedom (x, y, z, polar angle θ and azimuthal angle φ) manipulator (VG Scienta). The sample was able to be heated up to 1000 K by an electron-beam bombardment at the contact area of the sample holder. The data acquisition was carried out by MATRIX software (Omicron). The data were fitted and analyzed by XPSPEAK 4.1 software [173].

Chapter 4

Electrochemical deposition of Pd nanoparticles

Pd NPs were electrochemically deposited on HOPG and N-HOPG. Section 1 introduces the properties of substrates, which were characterized by electrochemical, morphological and spectroscopic methods. Section 2 describes the double-pulse electrochemical deposition method in detail. The characterizations of supported Pd NPs, including active surface area, size distribution, particle dispersion, chemical state and stability, is the 3^{rd} section.

4.1 Characterization of substrates

4.1.1 Highly oriented pyrolytic graphite

HOPG was used as a support material due to its chemical inertia and weak binding to supported materials. The electrochemical properties of freshly prepared HOPG surfaces were investigated in Ar saturated 0.1 M H_2SO_4 solution. A cyclic voltammogram is shown in Figure 4.1. The potential was scanned in a range of -0.35 to 2.0 V at a scan rate of 100 mV s^{-1}. When the applied potential was in the thermodynamic potential window of water (0 to 1.23 V), the current density, which was contributed only by the double-layer charging, was in the range of ± 0.5 μA cm^{-2}. The electrolysis of water at the HOPG electrode occurred at strong polarizations so that the HER initiated at around -0.2 V and the oxygen evolution reaction (OER) happened at around 1.7 V. This result indicates a weak adsorption of water molecules on the HOPG surface, and HOPG is inactive for both HER and OER. In the investigations of HER / HOR and OER / ORR, the contribution of the HOPG substrate to the current density can be neglected.

The morphology of the pure HOPG surface was characterized with SPM techniques. Figure 4.2 a shows the microscopic image of a HOPG surface acquired by TM-AFM within an actual area of 2 μm × 2 μm. Figure 4.2 b shows the image of a HOPG surface acquired by STM within an actual area of 500 nm × 500 nm. It can be observed in both images that the HOPG surface has a large area of atomic-level-

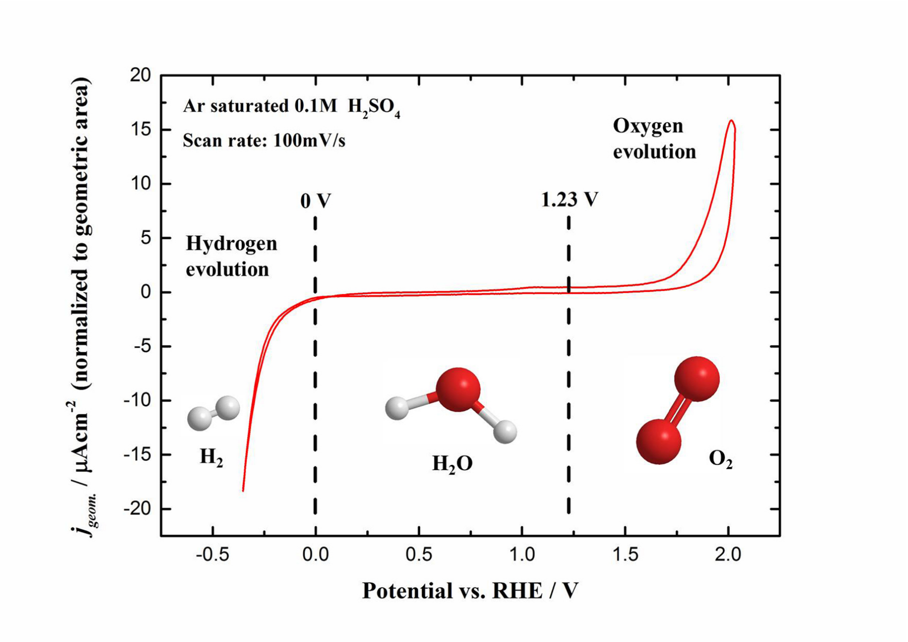

Figure 4.1: Cyclic voltammogram of HOPG in Ar saturated 0.1 M H_2SO_4 at a scan rate of 100 mV s^{-1}. The electrolysis of water happens at strong polarizations shown as the sharply increased current densities.

smooth terraces with few randomly placed steps. The diameters of individual crystals in HOPG are typically in the range of 1 to 10 μm [174]. The height of steps equals to the height of a single or several graphene layers. Figure 4.2 d depicts the height of the surface along the track marked in Figure 4.2 b. The track passes through two steps, of which the height differences between two sides are both around 0.34 nm. The thickness of a graphene monolayer is 0.335 nm. Therefore, each of the two steps is the edge of a single graphene layer. An image of a HOPG terrace in atomic resolution is shown in Figure 4.2 c. Due to the drift of the tip in $y-$direction, the orthohexagonal arrangement of carbon atoms was imaged with a compression in y-direction. The lattice of graphene consists of two equivalent triangular sub-lattices, which interpenetrate each other as a hexagram. The carbons in a hexagon are labeled in different colors (red and blue) in Figure 4.2 c in order to separate them into two sub-lattices. The atomic distance between the closest carbons in different sub-lattices is around 1.42 Å, while the distance in the same sub-lattice is around 2.46 Å [175]. Usually, the atomic pattern of graphene observed in the SPM image shows bright spots originating from three carbon atoms out of six in a graphene hexagon. Each apparent carbon atom is obviously surrounded by six neighbors, which are all in the same sub-lattice. The distance between any two of them is around 2.46 Å.

4.1.2 Nitrogen doped HOPG

N-HOPG samples were prepared from HOPG by ion implantation. In order to characterize the chemical state of the N-HOPG samples, XPS was carried out in the UHV chamber with a base pressure of 5×10^{-10} mbar. The survey spectrum was acquired in an energy range from 0 to 600 eV shown in Figure 4.3. The

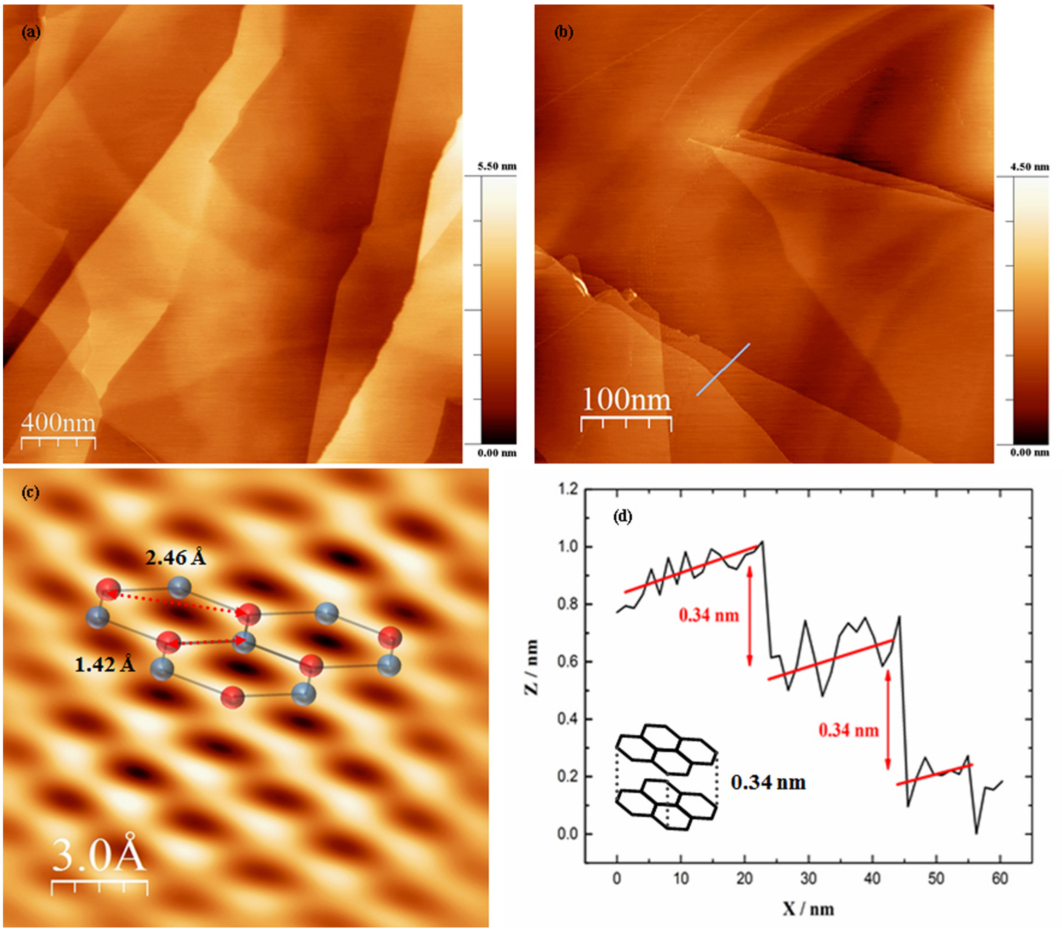

Figure 4.2: Morphological characterization of HOPG surface. (a) AFM image of a HOPG within an area of 2 μm × 2 μm; (b) STM image of a HOPG within an area of 500 nm × 500 nm; (c) STM image of a HOPG within an area of 15 Å × 15 Å with an atomic resolution; (d) The height profile of HOPG steps along the track marked in (b).

survey spectrum of HOPG was acquired in the same range as a reference. The photoionization peak of the C 1s in an energy range from 270 to 300 eV can be observed as main feature for both materials. The N-HOPG sample shows an N 1s peak which is centered at 400 eV. In the survey scan of the HOPG surface, a small peak of the O 1s appears which can be attributed to C-O groups existing at the step edges or defects. The fact that the O 1s peak disappears at the N-HOPG sample can be attributed to the thermal annealing under the UHV such that adsorbed oxygen has been removed.

More precise information about the chemical properties of the defects induced by the ion implantation was investigated by recording the C 1s and N 1s energy regions with a high resolution. The corresponding peaks were fitted with Voigt functions imposing a FWHM in the energy range from 1.0 to 1.4 eV [176]. Figure 4.4 shows the multi-peak analysis of the C 1s signals acquired from pure HOPG (4.4 a) and N-HOPG (4.4 b). For pure HOPG, carbon atoms are sp^2 hybridized to form the graphitic lattice. Therefore, its C 1s peak is centered at 284.4 eV. For N-HOPG, the sp^2 hybridized carbon (sp^2-C) dominates the surface. Three additional peaks, which are centered at 285.5 eV, 286.5 eV and 287.8 eV, respectively, can be observed. The

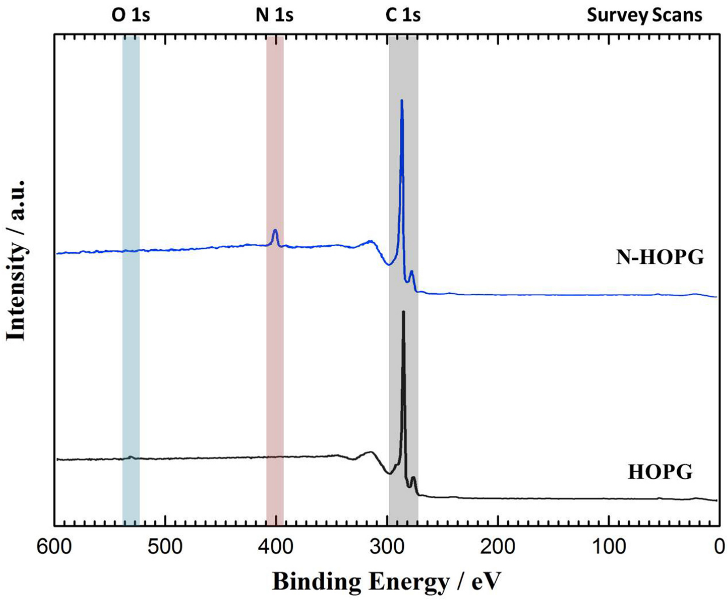

Figure 4.3: XPS survey spectra of HOPG (black) and N-HOPG (blue) in an energy range from 0 to 600 eV.

one at 285.5 eV connects to sp^3 hybridized carbon (sp^3-C) suggesting the formation of tetragonaly coordinated carbon clusters [177, 178]. The peak at 286.5 eV can be assigned to C-N bonds [179]. The small peak at 287.8 e V is related to C=O bonds, which are from the oxygen contamination [180]. From the analysis of the C 1s data, the nitrogen doping has introduced chemical defects which are nitrogen-containing. The C-N signal accounts for about 12 % of the total C 1s photoemission events. Further information about the C-N bonds was obtained from the multi-peak analysis of the N 1s signals shown in Figure 4.5 a. Five different components have been identified: peaks centered at 398.1 eV, 400.2 eV and 401.2 eV correspond to sp^2 C-N bonds, which can be described as pyridinic (N1), pyrrolic (N3) and substantial (N4) nitrogen defects, respectively [164–166]. The peak at 398.9 eV connects to the -C≡N terminal groups (N2). The component centered at 402.7 eV can be attributed to trapped nitrogen ions in graphite vacancies (N5)[165]. All the nitrogen defects are pictorially depicted in Figure 4.5 b, in which carbon, nitrogen and oxygen atoms are colored as gray, blue and red, respectively. Due to the existence of oxygen contaminate, the formation of N-O bonds is expected.

The morphology of N-HOPG was characterized by TM-AFM shown in Figure 4.6. As compared with the surface of pure HOPG, the 2D graphene structure was destroyed after the nitrogen implantation. Figure 4.6 a shows the morphology in an area of 5 μm × 5 μm. Although the steps of graphene layers are still observable, the roughness of the terrace region has increased, which indicates that the topmost layer underwent an amorphization to form 3D structures. Figure 4.6 b shows a 2D image acquired in an area of 2 μm × 2 μm, and an insert for a 3D projection of the surface within an area of 1 μm × 1 μm. The amorphous structure distributes on the surface homogeneously with an average height of around 0.5 nm, which agrees with the

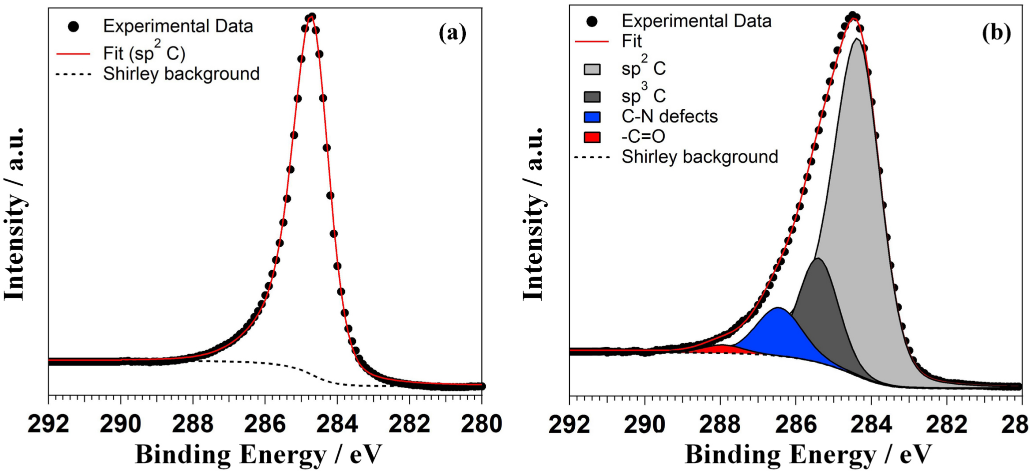

Figure 4.4: Core level photoemission spectra of C 1s and relative deconvolution into single chemical components for pure HOPG (a) and N-HOPG (b).

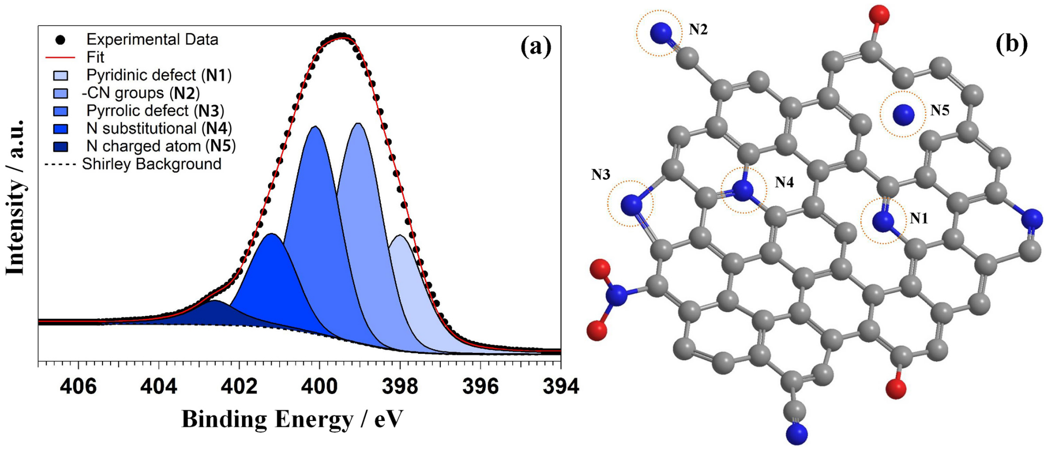

Figure 4.5: (a) Core level photoemission spectrum of N 1s and relative deconvolution into single chemical components for N-HOPG. (b) The pictorial model of the N-HOPG surface consisting of the mentioned nitrogen-based defects in (a). Carbon, nitrogen and oxygen atoms are colored as gray, blue and red, respectively.

implantation of nitrogen atoms in the top first and second layers.

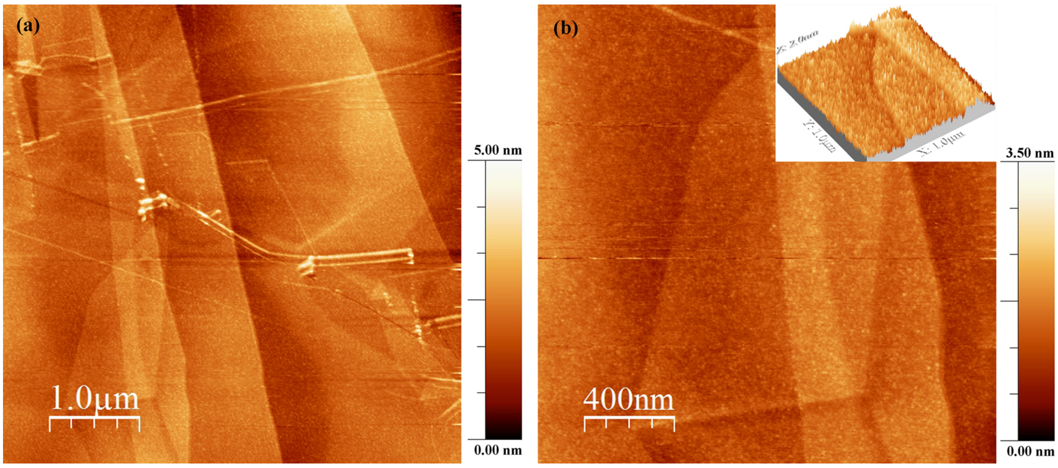

Figure 4.6: AFM images obtained on N-HOPG within an area of 5 $\mu m \times 5$ μm (a) and an area of 2 $\mu m \times 2$ μm (b). The inset in (b) shows a 3D magnification of the surface after the ion implantation in an area of 1 $\mu m \times 1$ μm.

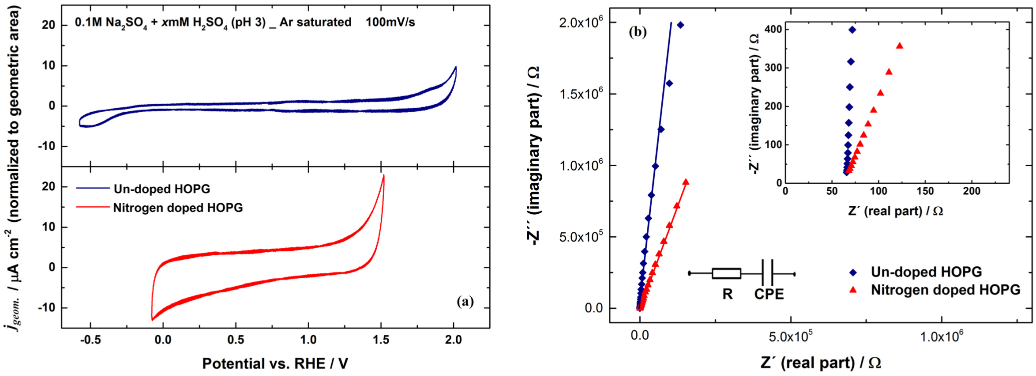

Figure 4.7: (a) CVs of HOPG and N-HOPG in Ar saturated 0.1 M Na_2SO_4 + x mM H_2SO_4 (pH=3) solution at a scan rate of 100 mV s^{-1}. Both currents are normalized to the geometric area of the electrode of 0.126 cm^2; (b) Nyquist plots of HOPG and N-HOPG impedance spectra measured at OCP. The x- and y-axis are plotted in linear scale. The inset corresponds to a zoom for the same plot to the high frequency region from 10k to 500 Hz. The inserted circuit diagram simulates the electrode / electrolyte interface.

The electrochemical properties of N-HOPG were investigated by cyclic voltammetry and electrochemical impedance spectroscopy in Ar saturated 0.1 M Na_2SO_4 + x mM H_2SO_4 solution (pH = 3). The pH 3 solution was used in this measurement in order to obtain the electrochemical data which are comparable with the data acquired from the Pd / N-HOPG samples in the same solution. In the pH 3 solution, Pd NPs supported on N-HOPG showed a higher stability in potential cycles. The electrochemical properties of pure HOPG were studied in the same conditions for a comparison with N-HOPG. Figure 4.7 a shows the CVs of pure HOPG and N-HOPG. Both measured currents were normalized to the geometric area of 0.126 cm^2. In contrast to the chemical inertia of pure HOPG for HER and OER, the N-HOPG electrode behaves more active for those reactions such that the onset potentials for HER and OER are more closer to their corresponding thermodynamic equilibrium potentials. Therefore, it has been already expected that N-HOPG has an increased activity for ORR. The current density during double-layer charging at the HOPG / electrolyte interface is only $\frac{1}{4}$ of the current density measured at the N-HOPG / electrolyte interface. From the currents in the double layer region, capacitances for HOPG and N-HOPG can be derived as 8.5 ± 0.2 μF cm^{-2} and 38.9 ± 1.4 μF cm^{-2}, respectively. Figure 4.7 b shows the impedance behavior of HOPG and N-HOPG at OCP in pH 3 solution. The inset corresponds to a zoom for the same plot in the high frequency region from 10k to 500 Hz. The Nyquist plots of both electrodes show linear relations between the real part of the impedance and the imaginary part, which indicates that the interface can be equivalent to a series circuit of a resistor (R) and a constant phase element (CPE). The resistor represents the electrolyte resistance, and the CPE is related to the double layer capacitance. The impedance expressed in terms of a CPE is

$$Z(\omega)_{CPE} = R_{\varepsilon} + \frac{1}{(j\omega)^{\alpha}Q} \tag{4.1}$$

where R_{ε} is a resistance, ω is the angular frequency, α and Q are the CPE parameters which do not depend on the frequency [181]. According to the relationship for a blocking electrode between the effective interfacial capacitance C_{eff} and the CPE parameters Q [182], the C_{eff} can be expressed as

$$C_{eff} = (QR_{\varepsilon}{}^{1-\alpha})^{\frac{1}{\alpha}} \tag{4.2}$$

when the value of α is closer to unity, the surface is more approaching the ideal 2D surface. The logarithm of the absolute imaginary part of the impedance is linearly fitted as a function of $ln(\omega)$. The value of α and Q for HOPG and N-HOPG are obtained as $\alpha_{HOPG} = 0.977$, $\alpha_{N-HOPG} = 0.896$, $Q_{HOPG} = 0.79 \times 10^{-6}$ s$^{\alpha}$ Ω^{-1} cm^{-2} and $Q_{N-HOPG} = 1.71 \times 10^{-6}$ s$^{\alpha}$ Ω^{-1} cm^{-2}, respectively. The results of full impedance spectra were calculated from equation 4.1, and were included in Figure 4.7 as solid lines. The results for the CPE parameters indicate that the HOPG surface is very flat and close to the ideal 2D capacitance behavior, while the N-HOPG has a rough surface which is indicated by the α_{N-HOPG} with a lower value. These properties are highly consistent with the AFM images. The capacitance values, which were calculated based on equation 4.2, are 5.01 μF cm^{-2} for HOPG and 4.75 μF cm^{-2} for N-HOPG. The similar C_{eff} values for both materials indicates that the impedance is to a lesser extent influenced by the contribution of introduced chemical defects. The higher interfacial capacitance of N-HOPG obtained by cyclic voltammetry is, therefore, mainly attributed to the higher roughness compared to the pure HOPG.

In summary, the surface modification from the nitrogen doping process enhanced the activities for OER and HER, and increased the double layer capacitance as compared with pure HOPG. A pure HOPG surface performs more like a semi-metal on the terrace region due to the low electronic density of states (EDOS) near the Fermi level [183]. The physical and chemical defects introduced by the doping process have a higher EDOS such that the electrons with suitable energy transfer to a redox system with a higher probability [165]. Furthermore, nitrogen functional groups are hydrophilic so that the binding with water molecules become stronger than on pure HOPG terraces [184]. Both modifications can enhance the activities of N-HOPG for HER and OER.

4.2 Deposition method

Pd NPs were electrochemically deposited on HOPG and N-HOPG. In order to obtain Pd NPs with narrow size- and density-distribution, the potentiostatic double-pulse deposition technique was applied. The double-pulse process consists of one short-time high-overpotential nucleation pulse followed by a long-time low-overpotential growth pulse. There are many advantages for the double-pulse deposition as compared with the single-pulse technique. In single-pulse deposition, the applied potential is suitable for both particle nucleation and growth. Therefore, new particles nucleate progressively during growth, and the growth durations of individual particles are distributed over time. As a result, the size distribution will be broadened, and the particle number density depends on the growth duration. In contrast to the single-pulse deposition, the applied potentials for the double-pulse deposition are different for nucleation and growth. Normally, the double-pulse deposition is able to be applied when the formation of nuclei occurs at a potential much lower than the growth potential. Figure 4.8 shows the sequential CVs of a bare HOPG electrode in Ar saturated 0.5 mM $Pd(NO_3)_2$ + 0.5 M H_2SO_4 solution. The onset potential, which has been defined at which the deposition current started to exponentially increase, of Pd deposition on a bare HOPG surface can be observed at around 0.275 V in the 1^{st} CV, while it shifts to a more positive value of around 0.665 V in the 2^{nd} and 3^{rd} scans correlating to the Pd deposition on previously formed Pd nuclei. The potential difference is attributed to the different thermodynamics of Pd deposition on bare HOPG and Pd metal. In double-pulse deposition, the separation of nucleation and growth makes it possible to control the particle density only by the nucleation pulse and the particle size by the growth pulse.

In the experiments described in this thesis, a high-overpotential nucleation pulse was applied in order to deplete the Pd^{2+} ions at the electrode surface rapidly. The pulse duration was limited to a small interval of 10 ms such that very few ions can be supplied from the bulk solution into the interfacial region. The density of NPs on the substrate, hence, remains similar for different samples when the nucleation was carried out under the same conditions. The parameters for the nucleation pulse are listed in Table 4.1.

The growth mechanism of a spherical particle has been widely discussed (shown in Figure 4.9) [44, 45]. If the consumption of metal ions in growth is much slower than the ion transfer in the electrolyte, the concentration gradient of metal ions is restricted to a small distance near the particles, which is even smaller than the radius

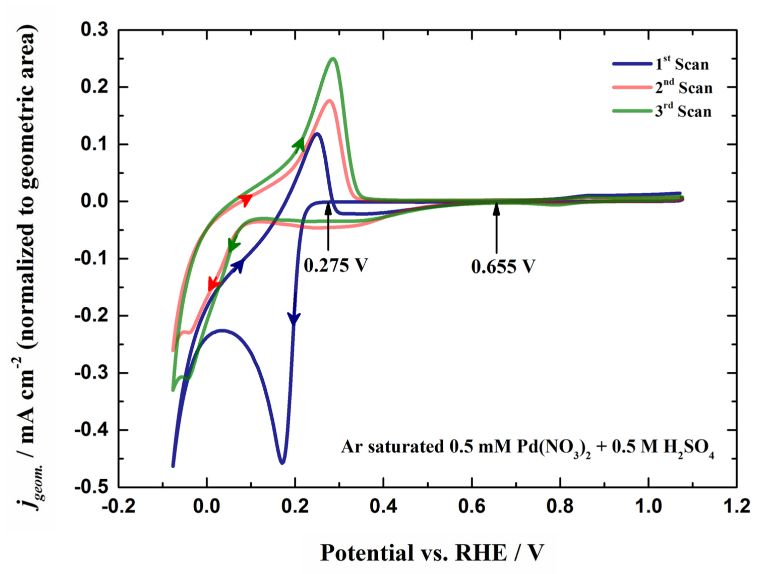

Figure 4.8: Sequential CVs of HOPG in Ar saturated 0.5 mM $Pd(NO_3)_2$ + 0.5 M H_2SO_4 solution at a scan rate of 50 mV s^{-1} The current is normalized to the geometric area of HOPG.

Table 4.1: Parameters for nucleation and growth pulses applied with two Pd precursors.

Precursor	**Nucleation potential / V vs. RHE**	**Nucleation duration / s**	**Growth potential / V vs. RHE**	**Growth duration / s**
0.5 mM $Pd(NO_3)_2$ + 0.1 M H_2SO_4, ($Pd(NO_3)_2$ solution, 16.27 %, MaTecK)	-0.07	0.01	0.22	0.01 ~ 200
0.5 mM $Pd(NO_3)_2$ + 0.5 M H_2SO_4, ($Pd(NO_3)_2$ $\cdot\, x$ H_2O, p.a., Sigma-Aldrich)	0.024	0.01	0.424	1 ~ 300

of the particle. The particles grow only under kinetic control. In such a case, the radius of a single particle increases in direct proportion to the deposition time:

$$r_k(t) = \frac{Mj_k}{zF\rho}t \tag{4.3}$$

where j_k is the kinetically controlled current density, z, F, M and ρ are the number of charge transferred per metal ion, Faraday constant, molar weight and density, respectively. If the consumption of metal ions in growth is much faster than the ion

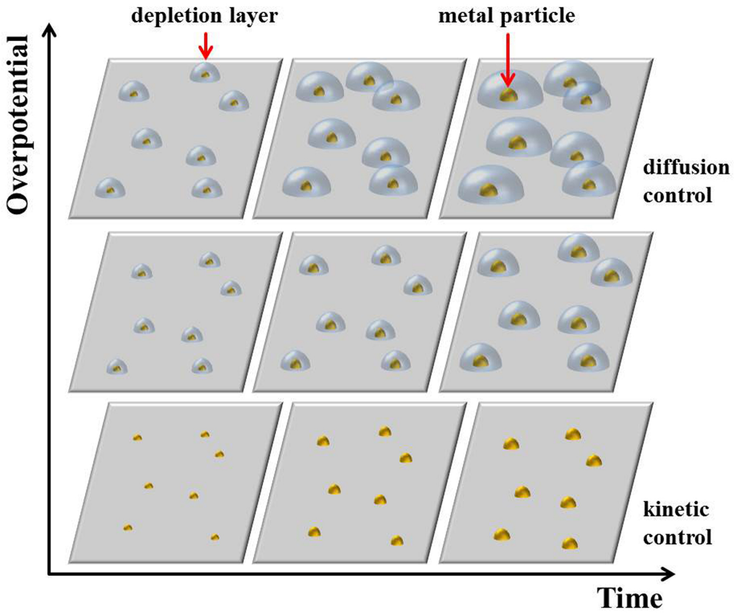

Figure 4.9: Schematic description of the effect of deposition overpotential on the extension of the depletion layer from the metal surface, and the influence on the particle size distribution.

transfer in electrolyte, a concentration gradient of metal ions forms at the electrode surface and extends into the bulk solution. Under spherical diffusion control, the radius of a single particle increases proportionally with the square root of time:

$$r_d(t) = \frac{2D_M{}^{\frac{1}{2}} C_M^* M}{\pi^{\frac{1}{2}} \rho} t^{\frac{1}{2}} \tag{4.4}$$

where D_M and C_M^* are the diffusion coefficient and bulk concentration of metal ions, respectively. The uniform growth of particles under diffusion control can be achieved when the neighboring particles do not have an overlap of the depletion layers. Otherwise, the particles will be widely dispersed in size due to the effect of interparticle diffusional coupling.

In this thesis, the overpotential for the growth pulse was carefully selected so that the growth of particles occurred under diffusion control, but the depletion layers surrounding the particles were confined to a small scale in order to avoid the diffusional coupling. The deposition current, in such a case, was nearly invariant in time, which can be identified as constant current growth. The radius of a hemispheric particle increases in the constant-current-growth mode with the cube root of time:

$$r_c(t) = (\frac{3i_{dep}M}{2\pi zF\rho N})^{\frac{1}{3}}\, t^{\frac{1}{3}} \tag{4.5}$$

where i_{dep} is the deposition current, and N is the number of nuclei. The used parameters for the growth pulse are listed in Table 4.1. In reality, the influence of the diffusional coupling among neighboring particles can be significantly weakened, but cannot be eliminated completely.

Three selected deposition pulses and their corresponding chronoamperometric data are shown in Figure 4.10. The measurements were carried out in 0.5 mM $Pd(NO_3)_2$ + 0.1 M H_2SO_4 solution with listed parameters. The measured current density in the nucleation pulse, which is due to the double-layer charging and charge transfer correlated to Pd deposition (nucleation and initial growth), reaches in the transient as high as -135 mA cm^{-2} as shown in Figure 4.10 c. The three chronoamperograms during the nucleation pulse are highly overlapping, which indicates the nucleation processes for them are very similar. After the nucleation pulse, Pd^{2+} ions were depleted near the electrode surface. The current density in the growth pulse increased in 20 s to a constant value of around -15 μA cm^{-2}. Then the particle growth followed the constant current mode.

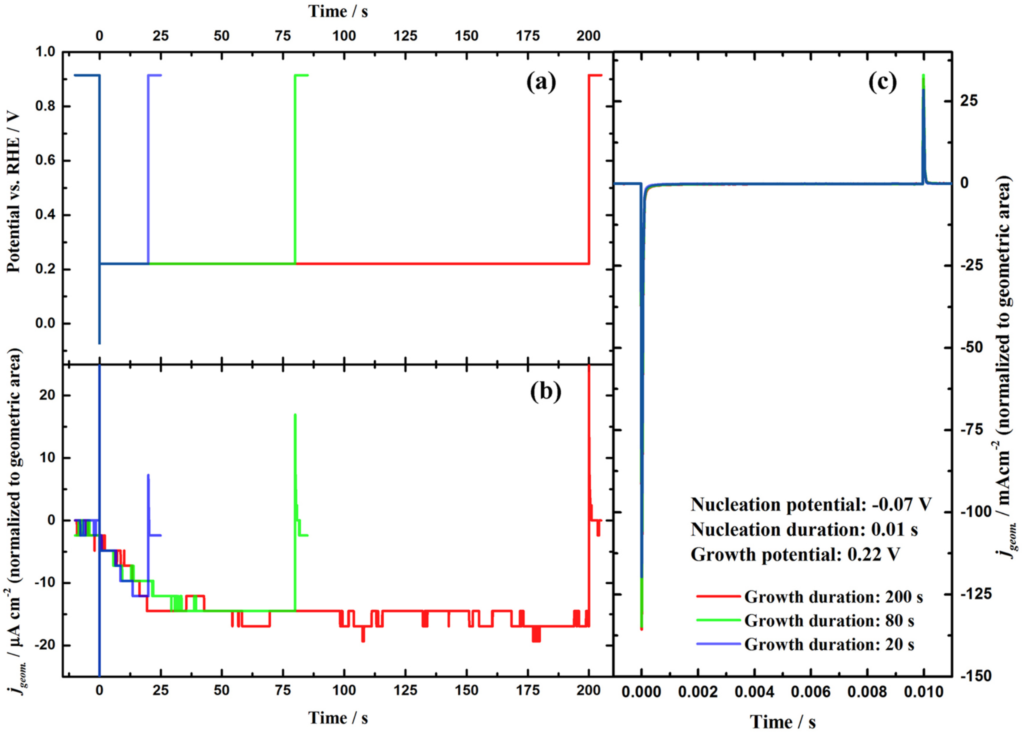

Figure 4.10: Double-pulse method for Pd deposition on HOPG: (a) three applied potentials versus time, the durations of the growth pulse are 20 s, 80 s and 200 s, respectively; (b) the corresponding current densities; (c) the current densities measured during the nucleation pulse with a high temporal resolution.

4.3 Characterizations of Pd nanoparticles

Pd NPs were electrochemically deposited on HOPG and N-HOPG samples. The active surface area, particle size and density distribution, chemical states and stability of Pd NPs were characterized with electrochemical, microscopic and spectroscopic methods.

4.3.1 Electrochemical characterization

Pd / HOPG samples

Pd has an outstanding catalytic activity for many electrochemical reactions and a high resistance to chemical attack. In the cyclic voltammetry scanned in a potential range apart from the HER and OER, there are four major reactions on a polycrystalline Pd electrode, i.e. hydrogen desorption and Pd oxidation in the anodic scan, as well as Pd oxide reduction and hydrogen ad-/absorption in the cathodic scan (shown in Figure 4.11). The electrochemical hydrogen absorption occurs on an electrode in a potential range where the hydrogen under-potential deposition (0 V to 0.3 V) is taking place as well as in the hydrogen evolution range [185, 186]. The onset potential of the Pd electro-oxidation is in the range of 0.6 to 0.75 V, where the bare metal atoms interact with O-containing species in the electrolyte (H_2O in acid and OH^- in alkaline) [91]. The potentials for oxide formation on different Pd facets show significant difference, e.g., the oxidation of Pd(111) happens at a potential around 0.2 V more positive than for other low-index facets (Pd(100) and Pd(110)) and steps [148]. Therefore, three oxidation peaks can be observed at the oxidation potentials of polycrystalline Pd: two peaks appear at potentials lower than 0.8 V and one peak is centered at around 1.0 V. Once the potential scans up to 1.45 V, a complete Pd monoxide (PdO) layer forms on the electrode surface [187]. The PdO reduction, which begins at ca. 0.8 V, shows a unique cathodic peak. The surface area of a Pd electrode can be characterized by the charge transferred in the reduction peak. When the upper potential of the CV is above 1.45 V, a reduction peak can be observed in the cathodic scan in the potential range of 1.3 to 1.1 V, which is attributed to the reduction of Pd dioxide (PdO_2) [188–190].

The electrochemically active surface area of supported Pd NPs was determined both from the charge transferred in PdO reduction and CO monolayer stripping. Figure 4.12 a shows the CV of Pd NPs supported on HOPG (Pd/HOPG) in Ar saturated 0.1 M H_2SO_4 with upper and lower potentials of 1.45 V and 0.3 V, respectively. The active area of Pd is proportional to the charge transferred during the PdO reduction, which can be obtained by the integration of the shaded region, with a parameter of 424 μC cm^{-2} [91]. For CO stripping measurements, an adsorbed CO monolayer was formed at a held potential of 0.52 V in 0.1 M H_2SO_4 with CO gas purging for 10 min. Thereafter, the solution was purged with Ar gas for 40 min to expel the dissolved CO. The cyclic voltammetry scanned over the same potential range as above. The transferred charge in CO stripping was integrated over the shaded region labeled in Figure 4.12 b. The parameter of 330 μC cm^{-2} was used for the calculation of Pd active area from the CO stripping charge [191]. The error was given by the difference of the two methods.

The interfacial energy between the supported metal NPs and the graphite plane surface is very low, which is mainly due to the interaction via van der Waals force. Therefore, the growth of metal NPs on HOPG follows the Volmer-Weber mode, in which metal NPs grow uniformly in all directions in three dimensions. For 3D NPs,

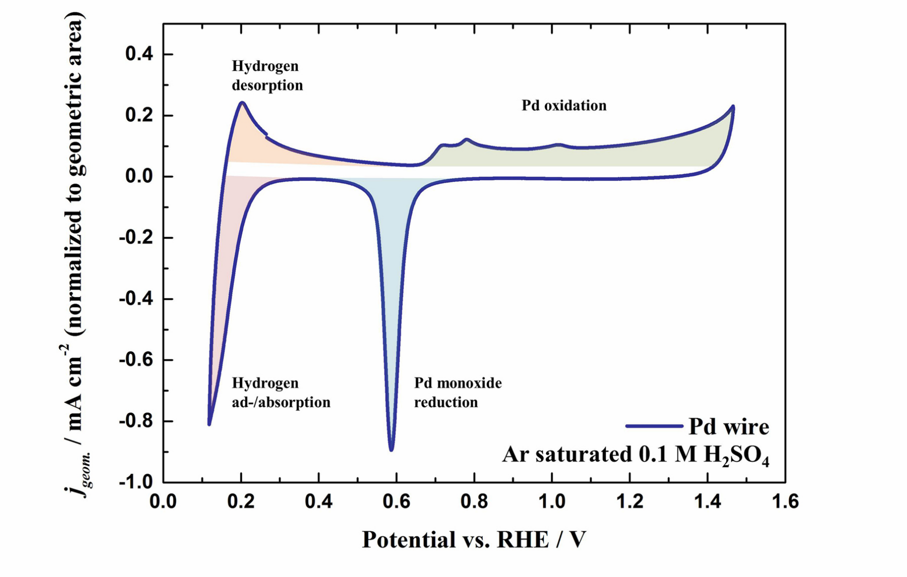

Figure 4.11: Cyclic voltammogram of a polycrystalline Pd electrode in Ar saturated 0.1 M H_2SO_4 at a scan rate of 50 mV s^{-1}. The currents correlated to the four major reactions, hydrogen ad-/absorption, hydrogen desorption, Pd oxidation and PdO reduction, are highlighted with colors.

the surface area (S) has a relation with their volume (V) as $S \sim V^{\frac{2}{3}}$. The total volume of deposited Pd NPs is proportional to the charge transferred in deposition (Q). Therefore, the 3D growth of Pd NPs on HOPG can be confirmed by the relation between the active surface area of Pd and the charge transferred during the deposition as $S \sim Q^{\frac{2}{3}}$. The surface area of Pd is plotted versus the charge transferred during deposition shown in Figure 4.12 c. All points were fitted with a power function shown as the red dashed line, which is identical to the relation of $S \sim Q^{\frac{2}{3}}$.

Pd / N-HOPG samples

Pd / N-HOPG exhibits a different CV in the potential range from 0.38 to 1.45 V as compared with that of Pd / HOPG (shown in Figure 4.13). The currents of substrates in the same potential range are plotted as dashed lines. The contribution of the Pd NPs to the total capacitance of the specimens is negligible, whereas the contribution of the substrates to the Faradaic processes is minor. It can be observed that the onset potentials of Pd oxidation and PdO reduction for both samples are located at equal values. However, the currents measured in the cathodic scan in the potential range of 0.38 to 0.52 V are not in agreement. The reduction peak of PdO on the Pd / HOPG sample is a typical Gaussian curve with a peak potential centered at 0.54 V. The reduction peak of PdO on Pd / N-HOPG sample is asymmetric with an excess charge transfer compared to that during the PdO reduction. The evaluation of the active surface area of Pd NPs on N-HOPG should exclude the excess charge transfer. In analysis, the active area was approximately determined by the charge integrated over a Gaussian curve shown in Figure 4.13 b as the shaded region. The

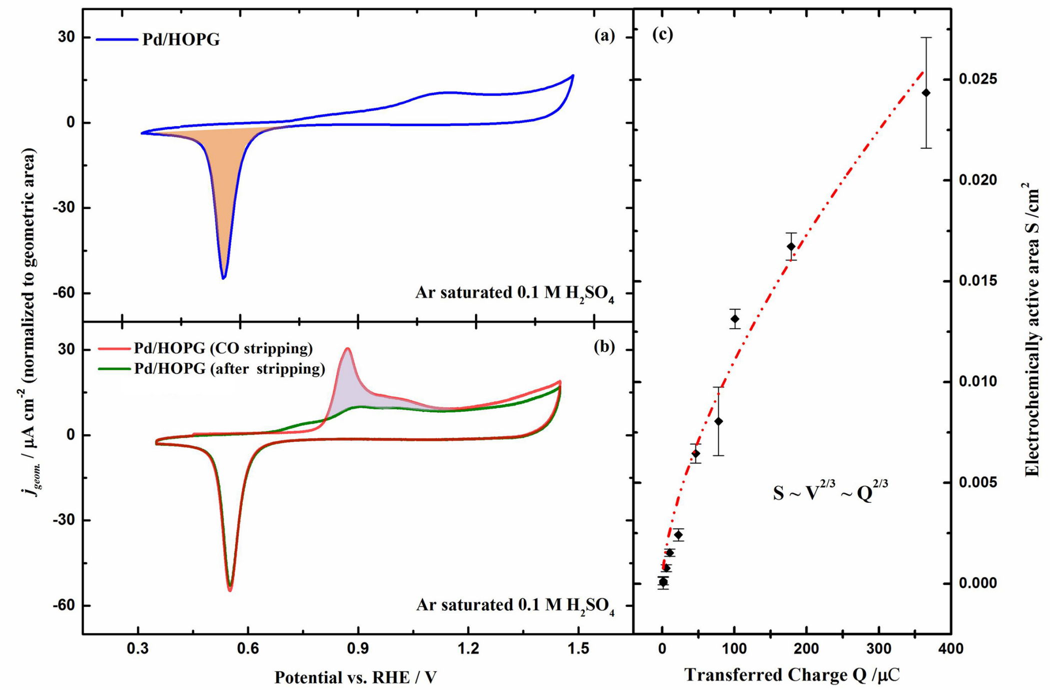

Figure 4.12: The active surface area of deposited Pd NPs was determined by the charge transferred in PdO reduction (a) and in CO stripping (b). The active area is plotted against the charge transferred during deposition (c), and the area is proportional to the $\frac{2}{3}$ power of the charge (S $\sim$ Q$^{\frac{2}{3}}$).

curve was fitted based on the right half peak in the cathodic scan. The excess charge transfer can be attributed to the ORR on N-HOPG surface. Many authors have reported that nitrogen-doped graphene performs as a metal-free catalyst for ORR showing enhanced catalytic activity in both alkaline and acidic solutions [192–197]. Liu et al. [192] observed that the ORR catalyzed by nitrogen-doped graphene foam occurred at 0.83 V vs. RHE in the O_2 saturated 0.1 M $HClO_4$ solution. In our work, the ORR catalyzed by N-HOPG has been observed when the potential is lower than 0.6 V. Therefore, the current contributed by the ORR catalyzed by N-HOPG in the potential range of 0.38 to 0.52 V cannot be neglected. The reactive O_2 originated from the OER at the Pd NPs during the anodic scan above 1.23 V, and transferred to the nitrogen functional groups.

The transferred charge integrated from 0.9 to 1.45 V in the anodic scan (oxidation charge) is larger than that evaluated from the PdO reduction peak (reduction charge) in the cathodic scan. For the Pd / HOPG sample, the oxidation charge is almost 1.5 times the one of the reduction charge. The excess charge is contributed by the OER and evaluation errors caused by the decreasing of Pd active area due to dissolution and agglomeration. For Pd / N-HOPG, the oxidation charge is nearly 3 times the one of the reduction charge. Besides the contribution from OER, the higher excess charge suggests a higher loss of Pd active area on N-HOPG as compared with that on pure HOPG substrate. This issue is discussed in the stability measurement.

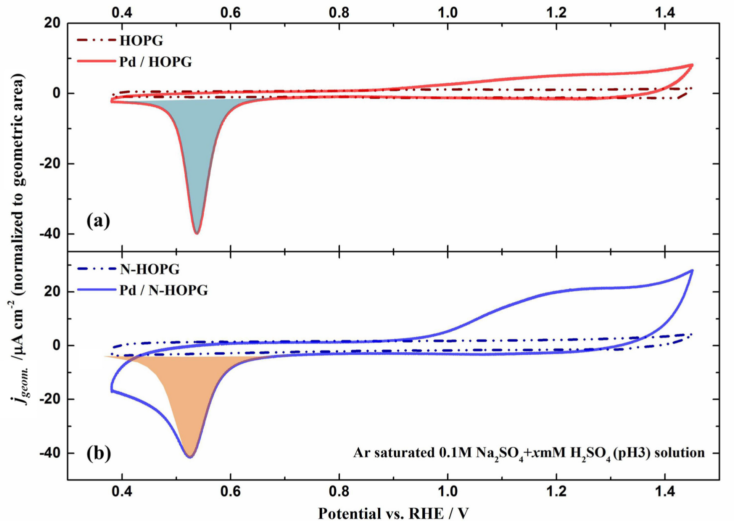

Figure 4.13: Cyclic voltammograms of Pd / HOPG and Pd / N-HOPG in Ar saturated 0.1 M Na_2SO_4 + x mM H_2SO_4 (pH=3) solution at a scan rate of 50 mV s^{-1}. The CVs of HOPG and N-HOPG are plotted as the baselines. The charge transferred in the reduction peak is shown as the integration over the shadow region.

4.3.2 AFM characterization

Pd / HOPG samples

The morphology of Pd NPs on HOPG was characterized by ex-situ TM-AFM. Figure 4.14 shows selected AFM images of deposited Pd NPs on HOPG. NPs were deposited in Ar saturated 0.5 mM $Pd(NO_3)_2$ + 0.1 M H_2SO_4 solution with varied growth durations from 0.01 to 200 s. In these images, it can be observed that NPs are located at the steps and defects due to the stronger binding of Pd atoms at low-coordinated carbons than at saturated terrace carbons. The particle size was evaluated by the height instead of the measured width because of the overestimation in width caused by the convolution with the tip size [198]. The particle-height distributions of 6 samples are shown in Figure 4.15. For each sample, three frames within an actual area of 2 μm × 2 μm were used for analysis. The percentage of NPs in each height interval is plotted as the y axis. For the sample prepared with a 0.01 s growth pulse, the NPs with a height in the range of 1 ± 0.25 nm show the highest percentage of 41.6 %. All the NPs are distributed from 0 to 3.25 nm. When the growth pulse is extended up to 5 s, the highest percentage of the NPs is located in the height interval of 6 ± 0.25 nm. The distribution of the height of NPs becomes broader than that of the former one. It is obvious that the average particle height becomes larger with the increase of growth duration. Meanwhile, the distribution of NPs in height becomes broader. The average height is plotted versus the growth duration in Figure 4.16 a. The error bars are given by the root-mean-square (RMS) deviations. All points were fitted with a power function shown as the red line. The average height, which is equivalent to the radius of the hemispherical particle, is proportional to the $\frac{1}{3}$ power of the growth duration, which is in agreement with the constant-current-growth mode.

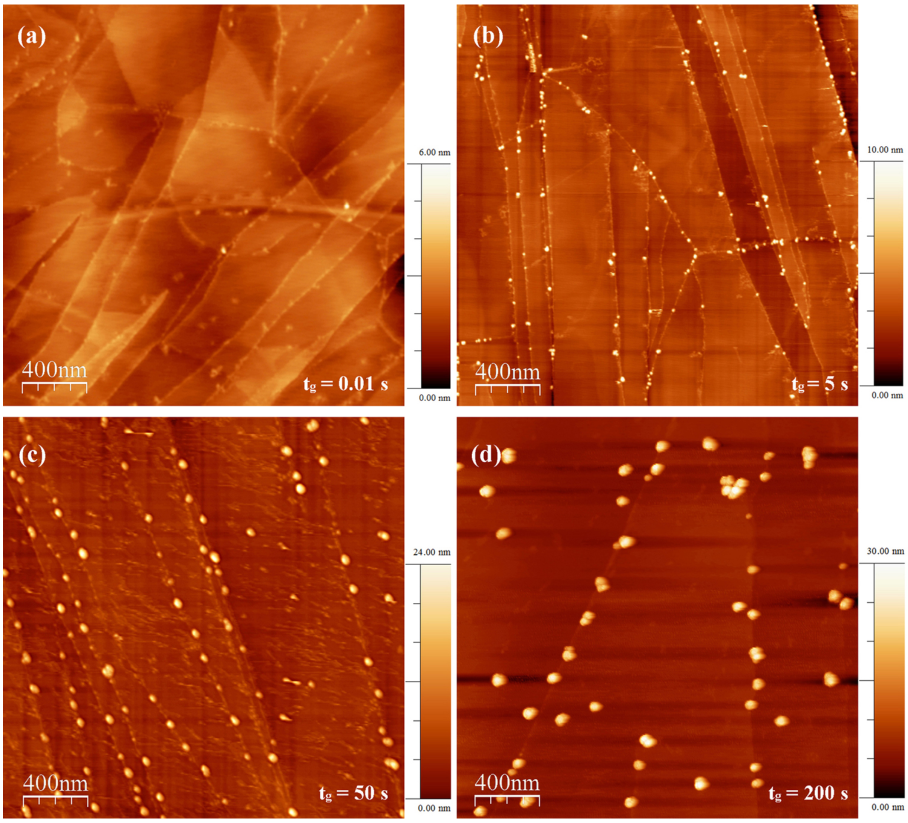

Figure 4.14: TM-AFM images of Pd / HOPG surfaces. Pd NPs were prepared with growth pulses of 0.01 s (a), 5 s (b), 50 s (c) and 200 s (d).

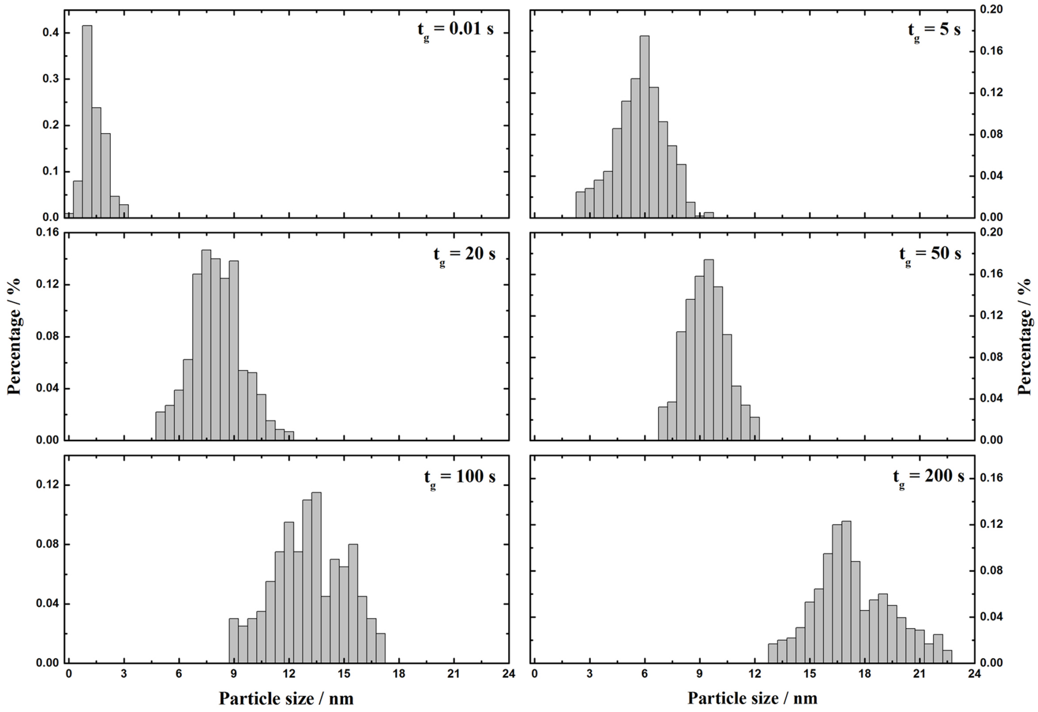

Figure 4.15: Histograms of the particle height distribution for Pd / HOPG samples prepared with growth pulses of 0.01 s, 5 s, 20 s, 50 s, 100 s and 200 s.

The particle density was evaluated according to the AFM images as well. It is plotted versus the growth duration in Figure 4.16 b. The error bars are given by the RMS deviations. For all samples, the particle densities are in the same order of magnitude of ca. 10^9 cm^{-2}. The samples with a growth duration shorter than 20 s have higher particle densities as compared with those growing longer (50 to 200 s), which can be attributed to the gradual agglomeration of neighboring NPs during a long-time growth.

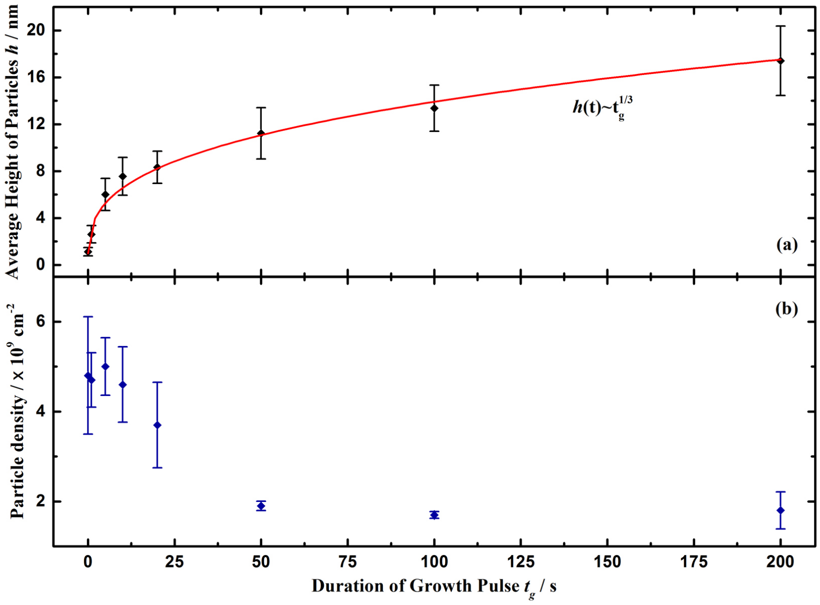

Figure 4.16: (a) Average height of NPs versus the duration of growth pulse; the average height is proportional to the $\frac{1}{3}$ power of the growth time. (b) Particle density versus the duration of growth pulse.

Table 4.2: Average particle size, particle density and their root-mean-square deviations of electrodeposited Pd NPs as evaluated from TM-AFM images. Three frames for each sample with an actual area of 2 μm × 2 μm were used for analysis.

Growth duration / s	**Average particle size / nm**	**RMS deviation of particle size / %**	**Particle density / 10^9 cm^{-2}**	**RMS deviation of particle density / %**
0.01	1.1	31.3	4.8	27.2
1	2.6	28.0	4.7	12.9
5	6.0	22.0	5.0	12.8
10	7.6	21.4	4.6	18.2
20	8.3	16.5	3.7	25.7
50	11.2	19.5	1.9	5.4
100	13.4	14.7	1.7	5.4
200	17.4	17.0	1.8	23

Pd / N-HOPG samples

Pd NPs on HOPG and N-HOPG were both electrochemically deposited with a growth duration of 100 s. The morphology of Pd / N-HOPG shows significant differences to that of Pd / HOPG, which can be observed in the AFM images shown in Figure 4.17. Pd NPs on HOPG are located mainly at steps with an inhomogeneous dispersion. However, Pd NPs on N-HOPG disperse widely without preference to steps. The nucleation of Pd is facilitated on the N-HOPG surface. Consequently, under the same deposition conditions, a higher particle density can be observed with respect to corresponding NPs grown on pure HOPG.

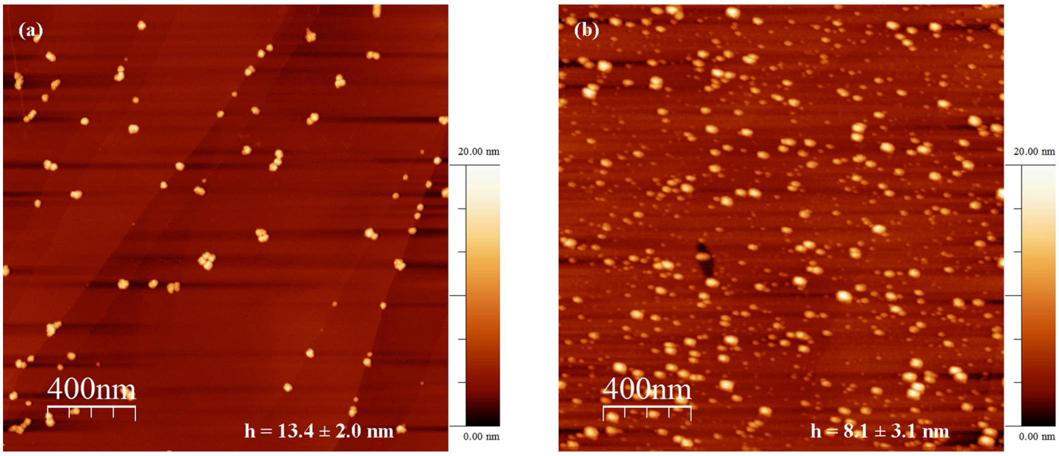

Figure 4.17: AFM images of Pd / HOPG (a) and Pd / N-HOPG (b) deposited with a growth duration of 100 s. The nucleation and growth potentials are -0.07 V and 0.22 V, respectively. The duration of the nucleation pulse is 0.01 s.

The charge transferred for Pd NPs deposition on N-HOPG was less than that on HOPG, which means less amount of Pd loading at the Pd / N-HOPG sample. However, the active area of Pd NPs on N-HOPG is similar to that on pure HOPG. Therefore, Pd NPs on N-HOPG have a higher surface-to-volume ratio than on HOPG, which can be explained by the morphology of Pd NPs on N-HOPG: smaller in size and more in number. As expected, the average height of Pd NPs on N-HOPG is 8.1 ± 3.1 nm, which is smaller than that on HOPG (13.4 ± 2.0 nm). The physical and chemical defects on N-HOPG, which were introduced by the ion-implantation process, are active sites for Pd nucleation. The presence of these defects also reduces the mobility of NPs. Therefore, even after a long time growth, the NPs are still widely dispersed with a much higher particle density as compared with that on HOPG. The drawback of the high particle density on N-HOPG is that the interparticle diffusion coupling influences strongly the particle growth. As a result, the NPs show a wide size distribution.

4.3.3 XPS characterization

XPS measurements were carried out to characterize the chemical states of Pd / HOPG and Pd / N-HOPG samples. No further electrochemical measurements aside from Pd deposition were carried out on these samples before XPS. In the survey

Table 4.3: Charge transferred in deposition, active surface area and average height of Pd NPs deposited on HOPG and N-HOPG in a growth duration of 100 s. The nucleation and growth potentials are -0.07 V and 0.22 V, respectively. The duration of the nucleation pulse is 0.01 s.

Sample	**Growth duration / s**	**Charge transferred in deposition / μC**	**Active area of Pd / cm^2**	**Average height / nm**
Pd / HOPG	100	-164	0.0130	13.4 ± 2.0
Pd / N-HOPG	100	-61	0.0139	8.1 ± 3.1

scans taken in the energy interval from 0 to 600 eV (Figure 4.18), the photoionization peaks of Pd 3d and O 1s can be observed in addition to the peaks originating from the substrates (C 1s and N 1s peaks). The Pd 3d peak is present in the energy interval from 333 to 345 eV shown as a double-peak structure. The peaks centered at 335 eV and 341 eV correlate to Pd $3d_{5/2}$ and Pd $3d_{3/2}$, respectively. The O 1s peak is centered at 531 eV, which originates from the oxygen groups at the steps and defects of the substrates formed during the metal deposition or adsorbed when exposing to atmosphere. The adsorbed oxygen atoms on the surface of Pd NPs can be an additional source. Due to the high sensitivity of Pd NPs to temperature, the thermal treatment, which is often used before XPS measurements for removing the adsorbed oxygen species, was avoided in this work in order to keep the original dispersion and chemical states of the NPs.

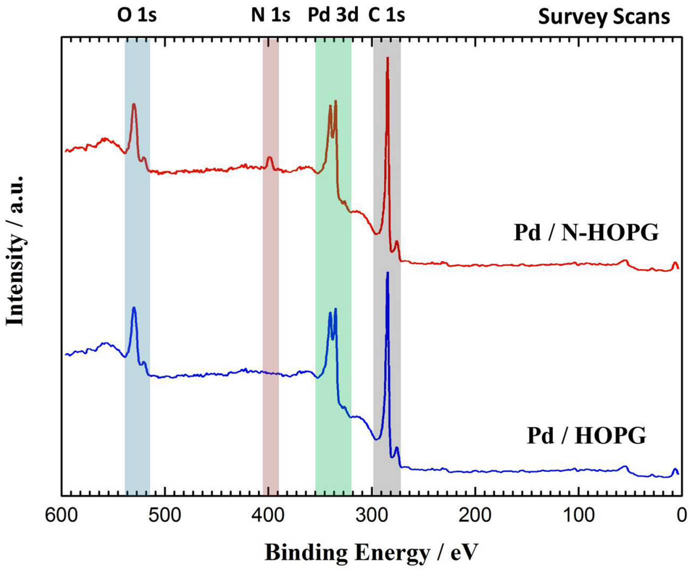

Figure 4.18: XPS survey spectra of Pd / HOPG and Pd / N-HOPG taken in the energy range of 0 to 600 eV. The spectra regions for the core level photoionization of C 1s, Pd 3d, N 1s and O 1s are highlighted.

The high-resolution spectra of Pd 3d were recorded in the energy interval from 330 to 350 eV under normal emission (0° with respect to the normal direction of the sample surface) and grazing emission (60° included angle with the normal direction of the sample surface) shown in Figure 4.19. The peaks of the metal Pd and Pd^{2+} are centered at 335.1 eV and 336.2 eV, respectively [199]. The Pd $3d_{5/2}$ peak covers the binding energy from 333.5 to 337.1 eV with a FWHM of 1.8 eV, which is compatible with the presence of both metal Pd and Pd^{2+} species. The presence of Pd^{2+}, which can be characterized at Pd / HOPG and Pd / N-HOPG samples, is attributed to the surface oxide of Pd formed during the exposure in air after the deposition. Moreover, the nitrogen functional groups on the N-HOPG can withdraw the electrons from Pd atoms due to the high difference of the electronegativity of C (2.50), N(3.05) and Pd(2.25) [200]. Therefore, the oxidation of Pd atoms to Pd^{2+} at the interface between Pd NPs and the nitrogen-rich surface is a reasonable reaction.

The Pd 3d peak for the Pd / N-HOPG sample measured under the normal emission conditions shows an additional component centered at 338.1 eV (shown in Figure 4.19 b) as compared with that for the Pd / HOPG. This peak is partially attenuated when the take-off angle at the grazing emission, which indicates that the component cannot exist at the surface of Pd NPs, but rather be located in the nanometric pits induced by the ion implantation. The lateral size of these small Pd clusters is smaller than 2 or 3 nm, since the mean free path for the photoelectrons coming from the Pd 3d level is equal to 1.2 nm. The interaction between Pd atoms and the nitrogen functional groups leads to the formation of Pd^{x+} species with $x = 2$ to 4 at the interface. Additionally, the formation of highly oxidized Pd^{x+} ions requires a large number of electron withdrawing groups surrounding the Pd atoms. The pits at the topmost layers, in which the nitrogen functional groups are enriched, satisfy the conditions that Pd clusters can be oxidized to high oxidation states. As a proof, Pd NPs supported on HOPG with deeply implanted nitrogen groups did not contain the Pd^{x+} species due to the low concentration of nitrogen groups at the topmost layers [201]. The pictorial model is shown in Figure 4.19 c.

4.3.4 Stability measurement

pH-dependent degradation

The stability of supported Pd NPs was studied with potential cycles in acidic solutions. A sample of Pd NPs on HOPG was prepared with a nucleation pulse of 0.01 s followed by a growth pulse of 20 s. Five sets of cyclic voltammetric scans were alternately applied to this sample in three Ar purged electrolytes. The applied potential ranges for the cyclic voltammetric scans in 0.1 H_2SO_4 (pH=1), 0.1 M Na_2SO_4 + x mM H_2SO_4 (pH=3) and 0.1 M Na_2SO_4 (pH=4.35) are 0.3 to 1.45 V (vs. SHE), 0.182 to 1.332 V (vs. SHE) and 0.102 to 1.252 V (vs. SHE), respectively. The lower and upper potentials used in different solutions were shifted according to the pH value of the electrolyte to compensate for the pH dependence of the PdO formation:

$$Pd + H_2O \rightleftharpoons PdO + 2H^+ + 2e^- \tag{4.6}$$

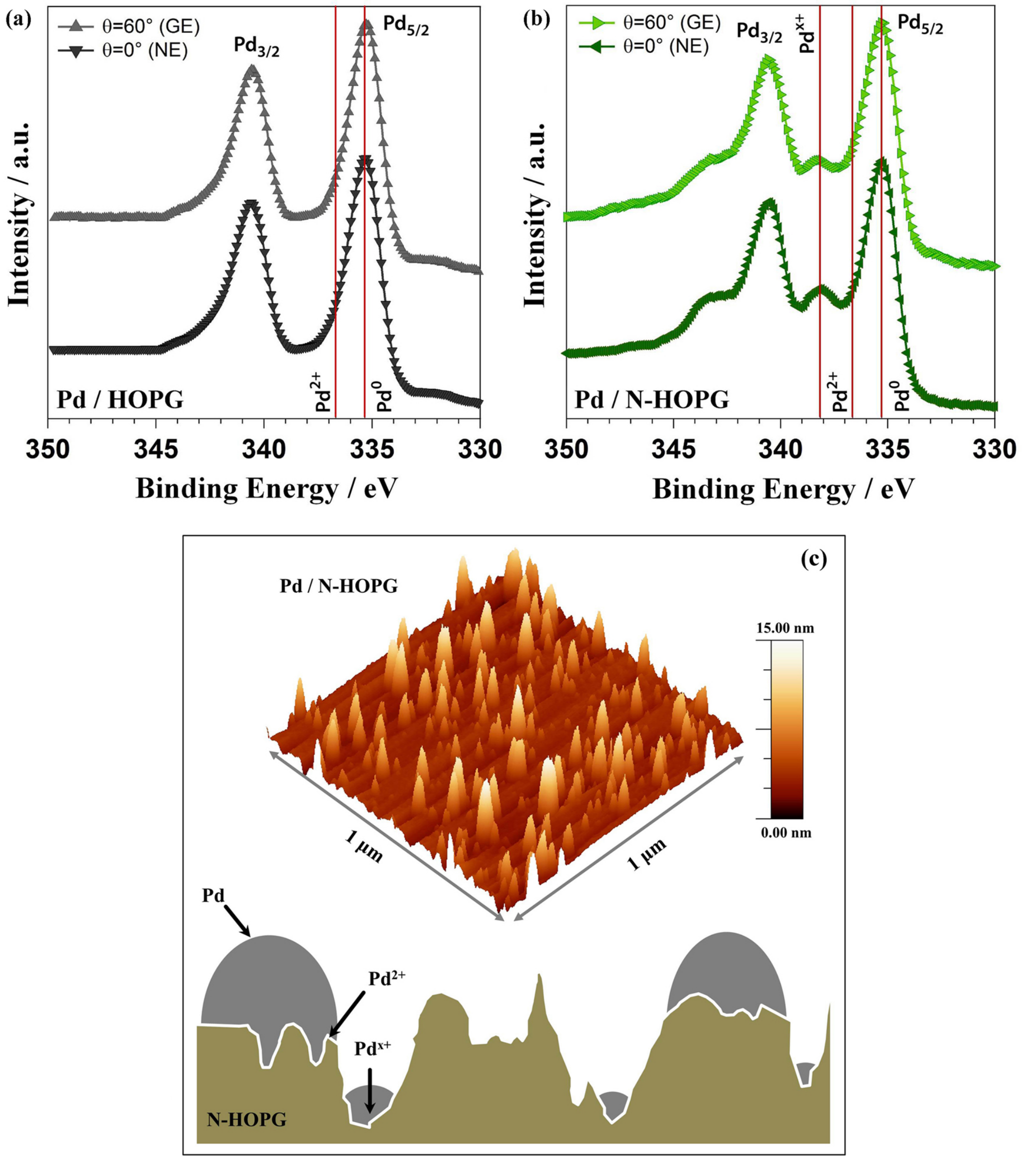

Figure 4.19: Pd 3d peaks for the Pd / HOPG (a) and Pd / N-HOPG (b) samples measured at the normal (0°) and grazing (60°) acquisition angles. (c) The 3D morphology of the Pd / N-HOPG obtained by AFM and the pictorial model of the surface. Pd^{2+} and Pd^{x+} are richly existing at the interface between the Pd NPs and the substrate, which is well supported by the angle-resolved core level spectroscopy of the Pd 3d peaks [180].

The active area of Pd NPs, which was evaluated from the charge transferred during PdO reduction, decreased continuously in the potential cycles shown in Figure 4.20. It can be observed that the Pd surface area decreases much faster in 0.1 M H_2SO_4 than in other solutions with higher pH values. In 0.1 M Na_2SO_4, the active area of Pd keeps almost the same. In the pH 3 solution, the Pd surface area decreases with a very low reduction rate. In summary, the dissolution of Pd NPs shows a pH-dependence so that a higher dissolution rate can be observed in the solution with a lower pH value.

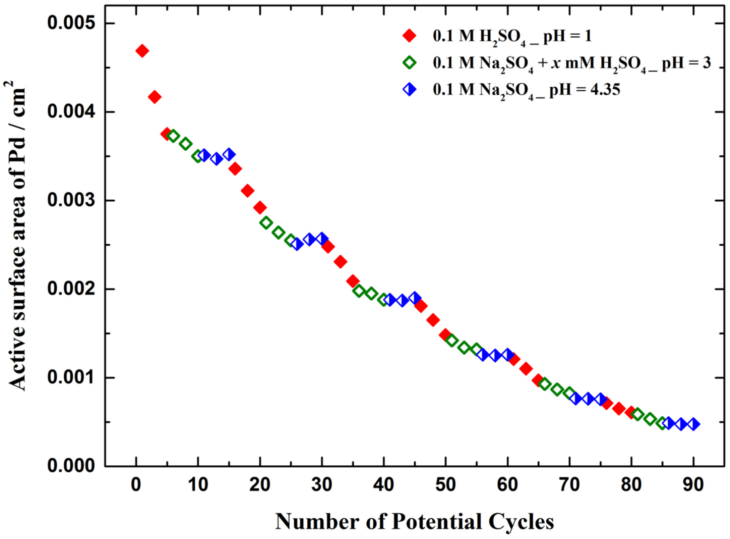

Figure 4.20: Stability measurement of a Pd / HOPG sample (prepared with a 20 s growth pulse) in three Ar saturated electrolytes with different pH values. Five potential cycles were applied to the sample each time in one electrolyte. The surface area is evaluated from the charge transferred in PdO reduction.

Size-dependent degradation

The size-dependent dissolution rate of Pd NPs on HOPG was investigated in pH 3 solution. Two Pd / HOPG samples were prepared with growth duration of 5 s and 100 s, respectively. The average particle height was estimated according to the power function reported in Figure 4.16 a, so that the sample with 5 s growth pulse was approximate to 6 nm, and with 100 s was almost 13 nm. To both samples, 20 potential cycles in the potential range of 0.25 to 1.45 V (vs. SHE) were applied. The amplitude of the PdO reduction peak decreased with potential cycles (shown in Figure 4.21 a and b). The active area of Pd NPs was evaluated from the charge transferred during the PdO reduction. The initial areas of the Pd / HOPG samples were 0.0056 cm^{-2} (for t_g = 100 s) and 0.00048 cm^{-2} (for t_g = 5 s) shown as 100% in Figure 4.21 c. The active area of both samples decreased exponentially. After 20 cycles, the sample of 13 nm Pd / HOPG remained 61 % of the initial Pd active area, but of 6 nm Pd / HOPG remained only 9 % of its initial active Pd area. This indicates that the smaller Pd NPs have a lower stability as compared with the bigger ones.

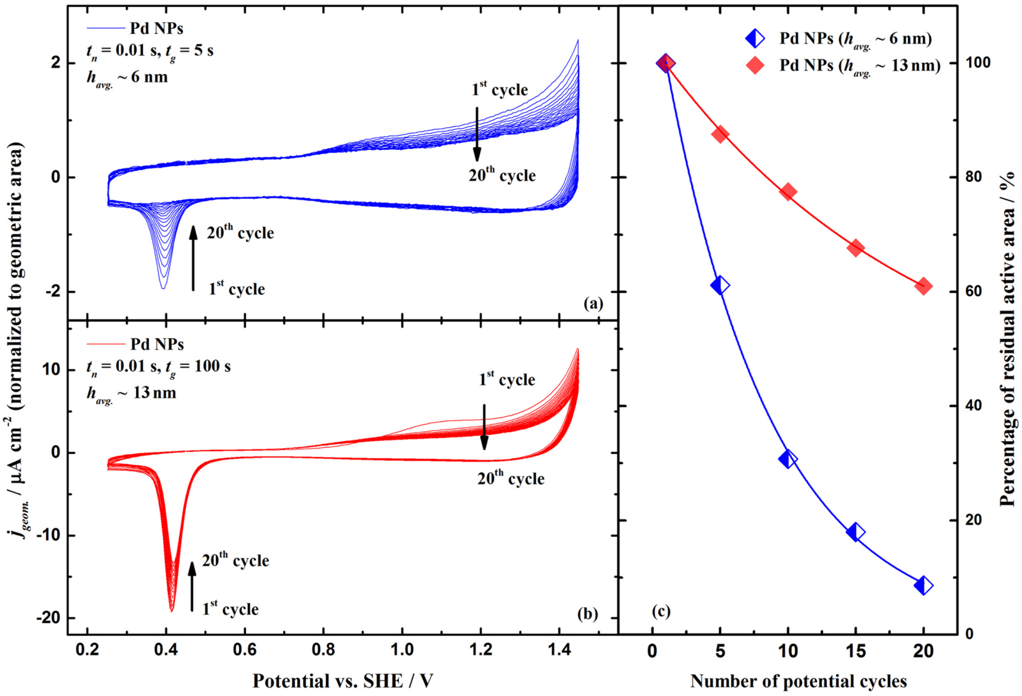

Figure 4.21: CVs of Pd (6 nm) / HOPG (a) and Pd (13 nm) / HOPG (b) in the stability measurements in Ar saturated pH 3 solution. (c) The active surface area of each sample was evaluated from the 1^{st}, 5^{th}, 10^{th}, 15^{th} and 20^{th} cycles and plotted as the percentage of residual active area corresponding to the initial area.

Morphological investigation

The morphological investigation of a Pd / HOPG sample in a stability measurement was performed with ex-situ TM-AFM after a certain number of potential cycles. The Pd / HOPG sample, which was prepared with a growth duration of 100 s, had an initial active area of 0.0089 cm^2. Potential cycles were applied in the potential range of 0.25 to 1.45 V (vs. SHE) in an Ar purged 0.1 M Na_2SO_4 + x mM H_2SO_4 (pH=3) solution. The electrochemically determined active area of Pd decreased exponentially with the number of potential cycles (shown in Figure 4.22 a), in agreement with the discussion of Figure 4.21. The active area remained at 12.3 % of the initial value after 100 potential cycles, and at only 0.28 % after 250 cycles. The morphologies of the Pd / HOPG surface before potential cycles and after 50, 150 and 250 cycles are showed in Figure 4.22 b, c, d and e, respectively. Before the potential cycles, the average height of the NPs was (13.3 ± 2.0) nm; and the HOPG surface was smooth with few steps and irregular structures. After 50 potential cycles, agglomerated NPs can be observed. Some irregular structures, which are much smaller than the Pd NPs, are present on the surface. With the increase of potential cycles, the average particle size decreased, and the particle size distribution became broader. In Figure 4.22 e, the irregular structures, which have heights of around 1 to 2 nm, can be observed clearly. They are suspected to be roughened graphite, which underwent carbon oxidation during the anodic potential scans, or redeposited Pd atoms from the dissolved Pd^{2+}.

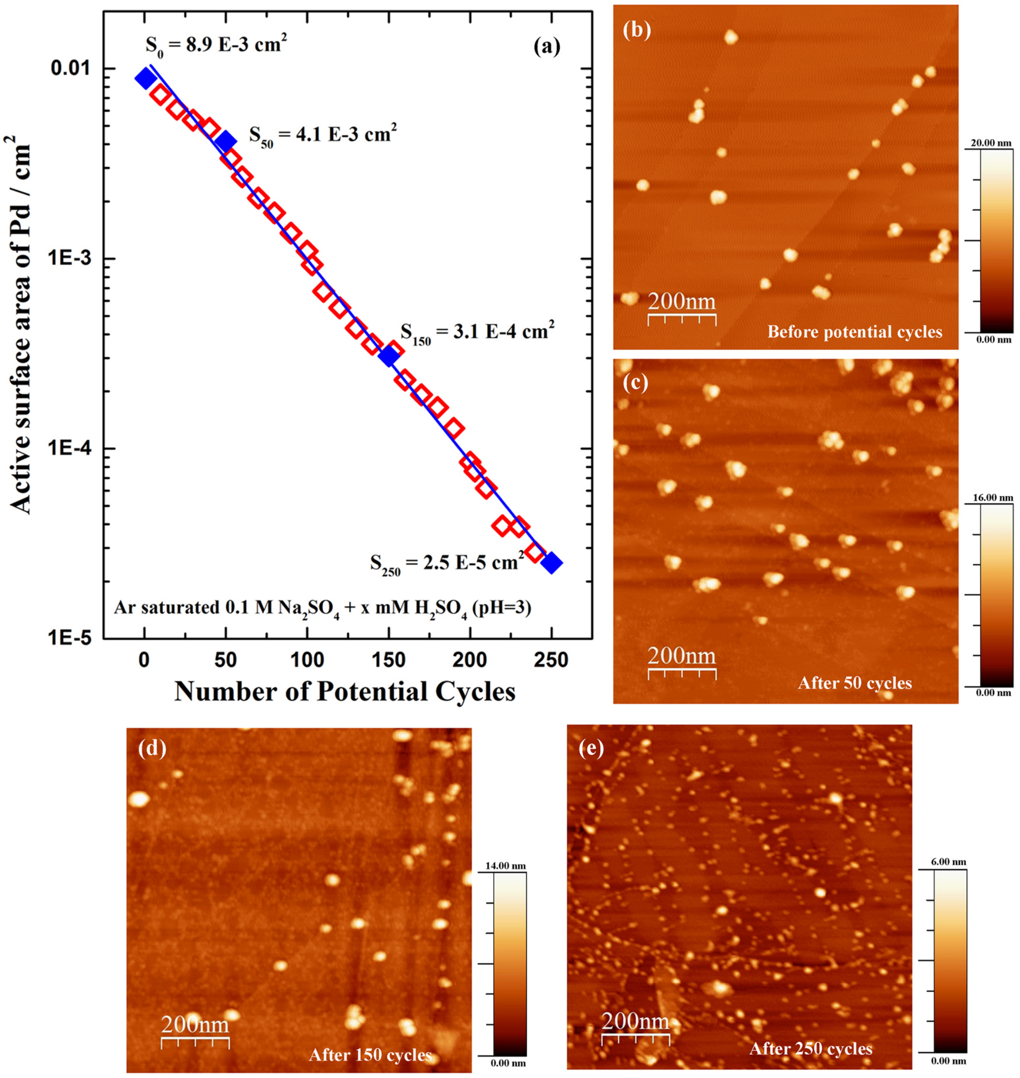

Figure 4.22: Stability measurement of a Pd / HOPG sample (prepared with a 100 s growth pulse) in a pH 3 solution. (a) The active surface area is plotted against the number of potential cycles. The Pd / HOPG sample was investigated with ex-situ AFM before potential cycles (b), after 50 cycles (c), after 150 cycles (d) and after 250 cycles (e).

Stability of Pd NPs on N-HOPG

Potential cycles were applied to Pd / HOPG and Pd / N-HOPG electrodes in order to test the stability of supported Pd NPs on the two substrates. Figure 4.23 a and b show the CVs of both samples in Ar saturated 0.1 M Na_2SO_4 + x mM H_2SO_4 (pH=3) solution. The applied potential is in the range of 0.25 to 1.45 V (vs. SHE). The loss of Pd active area during potential cycles can be observed directly from the change of the PdO reduction peak: the peak current density for Pd / HOPG decreased gradually from -29.2 μA cm^{-2} in the 1st scan down to -22.9 μA cm^{-2} in the 15th scan; while the value for the Pd / N-HOPG sample decreased from -22.2

μA cm^{-2} in the 1st scan down to -6.62 μA cm^{-2} in the 15th scan. It seems that the Pd active area of the Pd / N-HOPG sample decreases much faster than that of the Pd / HOPG sample. For a more accurate evaluation, the active area of Pd NPs, which was determined from the charge transferred during PdO reduction, was used to quantitatively compare the loss of Pd active area during the potential cycles. For Pd / HOPG and Pd / N-HOPG, the active areas of Pd (shown in Figure 4.23 c) were initially 0.0094 cm^{-2} and 0.0112 cm^{-2}, respectively. After 15 cycles, 69 % of Pd active area remained on the Pd / HOPG sample, but the Pd active area of the Pd / N-HOPG sample only remained at 31 %. The results confirmed that the Pd NPs on N-HOPG had a lower stability as compared with those on HOPG. From the CVs of Pd / N-HOPG, the reduction process at potentials lower than the PdO reduction in the cathodic scan is attributed, as aforementioned, to the ORR at nitrogen functional groups. This reduction current shows a clear decrease with the reducing of Pd coverage, which confirmed, from another aspect, that this process can happen depending on the Pd NPs: with the decrease of Pd coverage, less O_2 can be transferred to the adjacent nitrogen functional groups, as a result, the reduction current becomes smaller.

Based on the AFM images, the Pd NPs are dispersed more densely on N-HOPG with a short average distance. Therefore, the coalescence of Pd NPs on N-HOPG is a considerable reason of the active area loss. However, the chemical and geometric defects on N-HOPG seem to be effective obstacles against the migration of Pd NPs on the surface. Otherwise, the XPS results indicate that highly oxidized Pd^{x+} is present at the Pd and N-HOPG interface due to the strong electron withdrawing force of the nitrogen functional groups. The bottom of supported Pd NPs, at which the Pd^{x+} ions are enriched, can be considered as a vulnerable site to be attacked by the acidic solution. The nitrogen functional groups interact with the particles, accelerate the loss of Pd atoms and, further, the entire Pd NP. In conclusion, the introduction of nitrogen functional groups has strongly reduced the stability of supported Pd NPs in potential cycles.

4.4 Summary

Both HOPG and N-HOPG were used as substrates for the deposition of Pd NPs. HOPG, of which carbon atoms are sp^2 hybridized, was proven to be chemically inert and inactive for electrocatalyzed OER and HER. Its surface has large area of atomic-level-smooth terraces with randomly placed steps. The diameters of individual crystals are typically in the range of 1 to 10 μm. As compared with HOPG, N-HOPG underwent a surface modification by introducing nitrogen functional groups. Additional carbon states, which are sp^3 hybridized carbon and C-N, C=O bonds, were generated during the nitrogen-ion implantation. Five different nitrogen components have been identified which are sp^2 C-N bonds containing pyridinic, pyrrolic and substantial nitrogen defects, -C≡N terminal groups and trapped nitrogen ions in graphite vacancies. The nitrogen defects are primarily distributed in the topmost

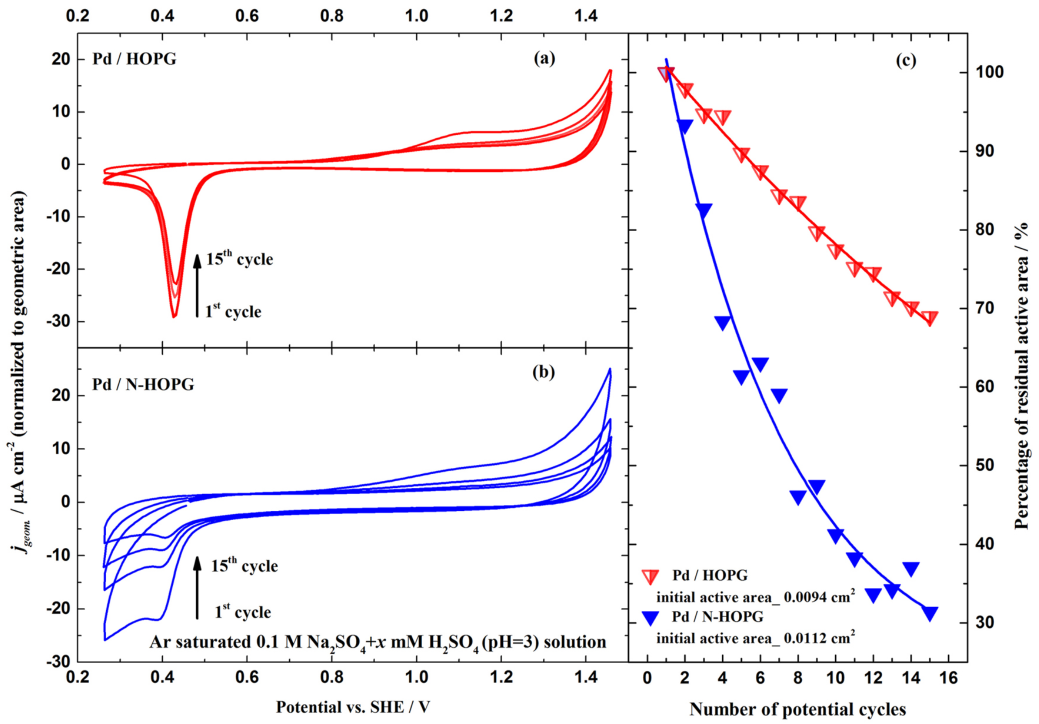

Figure 4.23: Cyclic voltammograms of Pd / HOPG (a) and Pd / HOPG (b) in the stability measurements in Ar saturated pH 3 solution. (c) The percentage of residual Pd active area is plotted against the number of potential cycles and fitted with an exponential curve.

three graphene layers. N-HOPG has a rough surface showing a high interfacial capacitance in the solution. Its activities for OER and HER were enhanced due to both physical (surface roughness) and chemical (nitrogen functional groups) defects. Pd NPs were electrochemically deposited on HOPG and N-HOPG with a double-pulse technique. During double-pulse deposition, a short-time high-overpotential nucleation pulse was applied before a long-time low-overpotential growth pulse. The applied overpotential during the growth pulse met the requirement of NPs growing in a constant-current-growth mode. The average particle size can be controlled by the duration of the growth pulse according to a relation of $r(t_g) \propto t_g^{\frac{1}{3}}$. The distribution of Pd NPs on HOPG depends strongly on the density of steps and defects, and shows an inhomogeneity. However, due to abundant defects on N-HOPG surface, the distribution of Pd NPs on N-HOPG is homogeneous.

The electrochemically active area of deposited Pd was determined both from the change transferred in PdO reduction and CO monolayer stripping. Due to the weak interfacial interaction between Pd NPs and HOPG, Pd NPs grew on HOPG following the Volmer-Weber mode. Therefore, the active area of deposited Pd is proportional to the $\frac{2}{3}$ power of their volume. The average particle size of Pd NPs has been confirmed to be proportional to the $\frac{1}{3}$ power of the growth duration by analyzing AFM images. The particle densities of all Pd / HOPG samples prepared with the same parameters in the nucleation pulse are in the same order of 10^9 cm^{-2}.

The XPS characterization of Pd / HOPG and Pd / N-HOPG indicates that both metallic Pd and Pd^{2+} species are present at the Pd surface of both samples. The presence of Pd^{2+} can be attributed to the surface oxide formed during the exposure in air. Moreover, for Pd / N-HOPG samples, the oxidation of metal Pd to Pd^{2+} at the interface between Pd NPs and the nitrogen-rich surface should be considered as well. In addition to Pd^{2+}, even higher Pd oxidation states have been observed by XPS on the Pd / N-HOPG samples. The formation of highly oxidized Pd requires abundant nitrogen functional groups surrounding the Pd atoms. The pits at the topmost layers, in which nitrogen functional groups are enriched, are suspected to be the sites which satisfy the conditions.

The stability of supported Pd NPs was investigated under electrochemical conditions. The degradation rate of Pd NPs is strongly dependent on the pH value of electrolytes which is why a faster degradation has been observed in a lower-pH solution. The initial particle size also influences the degradation rate as Pd NPs with a smaller average size degrade faster than bigger ones. The degradation of Pd NPs follows the mechanisms of Pd atom dissolution, particle detachment and agglomeration, Pd ions redeposition and Ostwald ripening as well as substrate corrosion. Pd NPs on N-HOPG show a lower stability as compared with those on HOPG, which is attributed to the existence of Pd^{x+} ($x = 2$ to 4) at the interfacial part with N-HOPG.

Chapter 5

Electrocatalytic properties of Pd nanoparticles

Electrocatalytic properties of Pd NPs for HER, ORR, CO stripping and FAO were investigated in this work. The size-dependent hydrogen absorption behavior of Pd NPs is discussed in section 1. The hydrogen content in the Pd lattice makes a strong influence to the activity of Pd NPs for HER. Therefore, for HER, the activity of Pd NPs is discussed in section 2 with the consideration of a size-dependent hydrogen content. For ORR, both the size and support effects were studied: a sequence of Pd NPs with different sizes were deposited on HOPG to investigate the size effect; and the Pd / N-HOPG sample was used to study the support effect. These results are reported and discussed in section 3. The binding strength of a CO molecule on a catalyst surface can be used to evaluate the CO tolerance of this material. The binding strength of CO on Pd NPs shows a size-dependence as well. The structural and electronic effects are both considered in the discussions in section 4. The size-dependent activity of Pd NPs for FAO is reported and discussed in section 5. The poisoning mechanism of Pd NPs during the electrocatalyzed FAO is analyzed; and a possible explanation is given.

5.1 Size-dependent hydrogen absorption

Pd exhibits a complex picture in electrochemical studies because of its strong hydrogen absorption behavior [47, 202]. In the potential range for HER, the situation becomes even more complex as three hydrogen-related reactions, -adsorption, absorption and evolution-, take place at the same time. Hydrogen absorption occurs in the potential range from 70 to 300 mV in 0.1 M H_2SO_4 leading to the formation of palladium hydride (PdH_x) [185]. At potentials more negative, underpotential hydrogen adsorption and hydrogen evolution are present [203]. The existence of two phases of PdH_x, $\alpha-PdH_x$ and $\beta-PdH_x$, has been widely accepted [204–206]. The $\alpha-PdH_x$ phase has a hydrogen content in the Pd lattice with an atomic ratio of H / Pd from 0 up to 0.025 ± 0.005. When the hydrogen content reaches the saturation limit of 0.025 ± 0.005, additional hydrogen uptake in the Pd lattice leads to the formation of the $\beta-\text{PdH}_x$ phase. The two phases coexist in equilibrium up to a maximum H / Pd ratio of about 0.62 to 0.67 [185], then the PdH_x becomes the pure $\beta-\text{PdH}_x$ phase. The OCP of PdH_x, which is measured in the same electrolyte, has been reported to depend on the hydrogen content.

Schuldiner et al. [207] has investigated the OCP of PdH_x in acidic solutions: the $\alpha-\text{PdH}_x$ phase at the hydrogen saturation limit (H / Pd = 0.025 ± 0.005) shows an OCP of 49.5 ± 0.5 mV in the mixtures of hydrogen-saturated sulfuric acid and sodium sulfate solution with pH values from 0.84 to 1.8; the OCP of the $\alpha-\text{PdH}_x$ phase with a hydrogen content lower than the saturation limit is even higher than 49.5 ± 0.5 mV; the PdH_x with a H / Pd ratio in the range from 0.03 to 0.36 contains both the α and β phases, but the OCP is determined by the α domains to be 49.5 ± 0.5 mV; for the ratio of H / Pd between 0.36 and 0.67, the OCP is a function of the hydrogen content such that it shifts negatively with the raise of hydrogen content until 0 V, which is corresponding to the value for the pure $\beta-\text{PdH}_x$ phase; the relation between the OCP and the atomic ratio of H / Pd is shown in Figure 5.1. The potential-determining reaction on the PdH_x electrode is an equilibrium between hydrogen ions in the solution and hydrogen atoms dissolved in the metal [208]. The electrochemical reactions are labeled in Figure 5.1. When hydrogen atoms are saturated in PdH_x (pure $\beta-\text{PdH}_x$ phase), the OCP is determined by the equilibrium of HER / HOR, which has a value of 0 V [207].

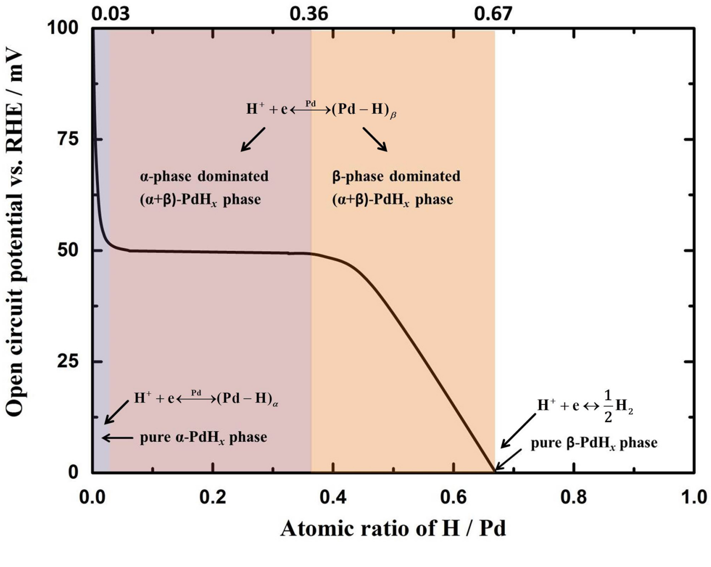

Figure 5.1: Variation of the OCP of PdH_x with the change of atomic ratio of H / Pd in H_2 saturated sulfuric acid − sodium sulfate mixture with pH values from 0.84 to 1.8. The OCPs of saturated $\alpha-$ PdH_x, $\alpha-$phase dominated $(\alpha+\beta)-\text{PdH}_x$ and $\beta-$phase dominated $(\alpha+\beta)-\text{PdH}_x$ are labeled with different colors.

The size-dependent hydrogen absorption on Pd NPs was investigated according to the relation between the atomic ratio of H / Pd and the OCP in hydrogen saturated 0.1 M H_2SO_4. The experiment was performed as a linear potential sweep in the cathodic direction from 80 to -220 mV at a scan rate of 10 mV s^{-1}. The electrochemically promoted hydrogen absorption proceeded at the Pd immediately, when the potential was applied. Hydrogen atoms were initially adsorbed onto the surface, and then diffused into the bulk. The absorption rate of hydrogen atoms into the bulk Pd is limited by the diffusion of hydrogen in the Pd lattice [209]. The diffusion coefficients are in the order of 10^{-7} cm^2 s^{-1} in the $\alpha-$PdH$_x$ phase and in the order of 10^{-6} cm^2 s^{-1} in the $\beta-$PdH$_x$ phase [205]. For the particles at the nanoscale, the diffusion limitation is ineffective so that the hydrogen atoms can permeate the Pd NPs immediately and quasi-freely [210]. The hydrogen content in such a case indicates the capability of Pd NPs for hydrogen absorption. The voltammograms of Pd NPs for HER / HOR are shown in Figure 5.2. The potential, at which the logarithm of the absolute current density is the minimum, is considered to be the OCP. The OCP measured at a Pd wire electrode, which was used as a reference, is around 48 mV (approaching the OCP of $\alpha-$PdH$_x$ dominated $(\alpha+\beta)-$PdH$_x$ phase). This value indicates that the PdH$_x$ at a bulk Pd surface is in the $(\alpha+\beta)-$phase with an atomic ratio of H / Pd lower than or approximate to 0.36. The OCP at Pd NPs with an average height larger than 8 nm is close to 0 V (approaching the OCP at the pure $\beta-$PdH$_x$ phase), which indicates that the Pd NPs have a very high hydrogen content approaching the saturated β-phase. When the average height of Pd NPs is smaller than 8 nm, the OCP at the Pd / HOPG sample shows a tendency to shift positively: the value shifts up to around 12 mV for the 5 to 6 nm NPs, and to around 23 mV for the 4 nm NPs. Even the OCP of Pd NPs with an average height of 2.4 nm is at 66 mV, which is more positive than that of bulk Pd. According to Figure 5.1, the positively shifted OCP can be explained by a lower hydrogen content in the small Pd NPs, as long as the OCP is determined by the hydrogen absorption equilibrium. Kolb and Baldauf [211] suggested that hydrogen absorption occurs at the Pd-overlayer / Au electrode only if the Pd overlayers are thicker than 2 ML; and the atomic ratio of H / Pd is less than 0.5, when the Pd overlayers are thinner than 10 ML; only once the thickness of Pd overlayers exceeds 20 ML, the atomic ratio of H / Pd can be higher than 0.6. The thickness of Pd overlayers can be analogous to the average height of Pd NPs as 10 ML approximates to 4 nm, and 20 ML corresponds to around 8 nm. The Pd NPs with average heights larger than 8 nm have the normal lattice structure so that the hydrogen content can reach the maximum ratio of around 0.67. When the Pd NPs are smaller than 8 nm, the change of lattice structure causes a reduced capability for hydrogen absorption. For Pd NPs with an average height of 2.4 nm, the ratio of H / Pd can be deemed lower than 0.03 according to the very positive OCP value. Therefore, the observed particle size-dependence of the OCP in Figure 5.2 can be fully understood by the size-dependence of the achievable hydrogen content in the NPs and the correlation shown in Figure 5.1.

5.2 Electrocatalytic activity for HER

The HER on Pd / HOPG samples was investigated by applying linear potential sweeps in H$_2$ saturated 0.1 M H$_2$SO$_4$. The specific current densities for the HER in the potential range of 0.08 to -0.22 V are shown in Figure 5.3 a. The corresponding

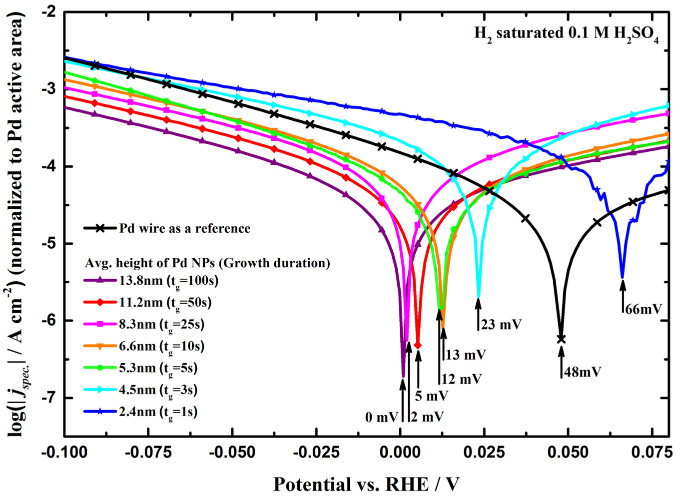

Figure 5.2: Tafel plots for HER of a Pd wire and Pd / HOPG samples with different average particle sizes. The OCPs are determined to be at the lowest current density.

Tafel plots are shown in Figure 5.3 b. The HER in acidic media follows the Volmer-Tafel mechanism when the coverage of adsorbed hydrogen atoms on Pd surface is low, and the Volmer-Heyrowsky mechanism when the coverage is high [49, 82]. When the Volmer step is the RDS, the Tafel slope will be -118 mV dec^{-1}. In this study, the Tafel slopes for the HER measured on all samples are in the range of -120 ± 15 mV dec^{-1}, which indicates that the reaction at the Pd surface is limited by the Volmer steps.

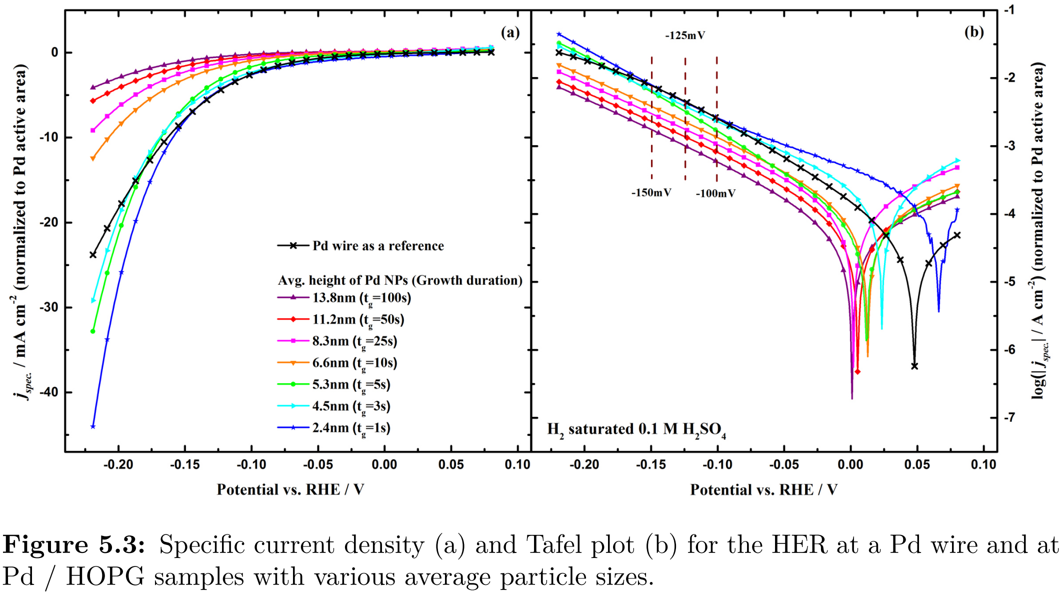

Figure 5.3: Specific current density (a) and Tafel plot (b) for the HER at a Pd wire and at Pd / HOPG samples with various average particle sizes.

In order to compare the size-dependent electrocatalytic activity of Pd NPs for HER, the current densities of Pd / HOPG samples at selected potentials (-100 mV, -125 mV and -150 mV) are plotted versus the average height shown in Figure 5.4. The current densities of bulk Pd are shown for comparison. It has been discussed above that the hydrogen absorption, which occurs on the Pd surface at potentials more positive than the equilibrium potential of HER / HOR, is size-dependent. The true composition of the Pd catalyst participating in the HER is therefore expected to be different for all samples. For bulk Pd, the surface composition corresponds to $\alpha-$phase dominated $(\alpha+\beta)-$PdH$_x$, while the surface composition of Pd NPs with an average height larger than 8 nm is almost pure $\beta-$phase PdH$_x$. For Pd NPs smaller than 8 nm, the surface composition changes from $\beta-$phase dominated $(\alpha+\beta)-$PdH$_x$ via $\alpha-$phase dominated $(\alpha+\beta)-$PdH$_x$ to pure $\alpha-$PdH$_x$ phase, with the decrease of particle size. The specific current density at bulk Pd is higher than that at Pd NPs with average height larger than 8 nm. This result indicates that $\alpha-$phase dominated $(\alpha+\beta)-$PdH$_x$ is more active for the HER than $\beta-$phase PdH$_x$; in other words, a Pd catalyst with a lower amount of absorbed hydrogen is more active for HER than that with a higher hydrogen content. This behavior can be explained by the activity change caused by the lattice strain. It has been reported that the lattice constant of Pd nanopowder changes from initially 3.898 Å to 3.972 Å after hydrogen absorption [212], and that the lattice expansion is positively correlated to the amount of absorbed hydrogen atoms [204]. The tensile strain caused by the hydrogen absorption leads to an upshift of the $d-$band center of Pd, so that the adsorbed hydrogen can bond to the Pd active sites strongly, even block further reactions. According to the considerations regarding the strain effect, a further increase in the hydrogen content can decrease the activity of Pd for the HER further, vice versa. Therefore, the tendency of a continuous increase of the specific current density of Pd NPs with an average height smaller than 8 nm with the decrease of particle size can be explained by the weakened tensile strain along with the reduced hydrogen content. The measured current density at the Pd NPs with the smallest average size (2.4 nm) is nearly the same as that at bulk Pd. Moreover, the observed OCPs at these two samples are rather approximate. Thus, the catalytic activity of Pd NPs for HER is predominantly determined by the content of absorbed hydrogen. The particle size itself, which is closely correlative to surface defects and exposed facets, instead, seems not to be an important factor.

5.3 Electrocatalytic activity for ORR

5.3.1 Size effect

The size-dependent electrocatalytic activity of Pd NPs was investigated by applying linear sweep voltammetry in O_2 saturated 0.1 M H_2SO_4 under stagnant conditions. The potential was swept cathodically from 0.9 to 0.32 V at a scan rate of 20 mV s^{-1}. Figure 5.5 a shows the voltammograms of Pd / HOPG samples and bulk Pd obtained in the ORR measurements. All current densities are normalized to the geometric area of electrodes. The unique geometric area of all the Pd / HOPG samples is 0.126 cm^2, and the geometric area of the bulk Pd electrode is 0.303 cm^2. The onset potential for the ORR on the bulk Pd electrode is at approximately 0.88 V, which is more positive than that on the Pd / HOPG samples. The current increases exponentially

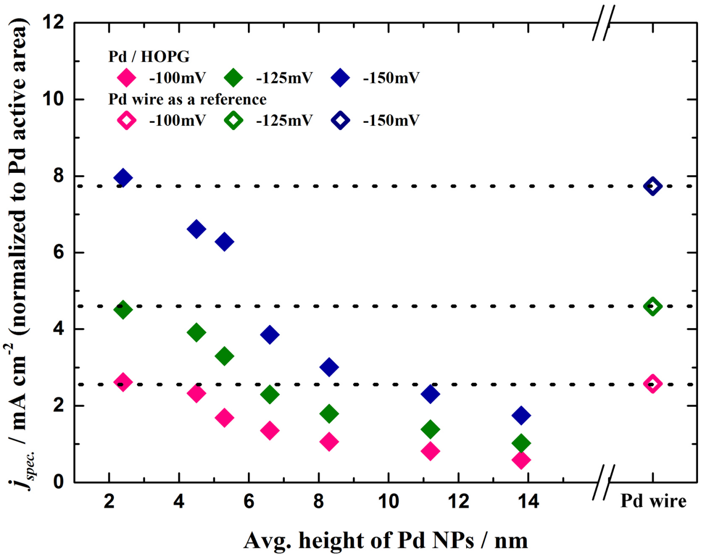

Figure 5.4: Specific current densities at selected potentials of -100, -125 and -150 mV for HER. The r_{avg} of Pd NPs was estimated from the duration of the growth pulse based on the curve shown in Figure 4.16.

at first, until the mass-transport control becomes more significant. The half-wave potential for bulk Pd is at 0.78 V, while the value shifts cathodically with particle size decrease down to 0.54 V for the Pd NPs with an average height of 6.6 nm. The peak potential, at which the maximum current density was measured due to coupling with mass transport, also shifts negatively with the decrease of Pd active area.

In order to compare the activity of Pd NPs for ORR, the current densities were normalized to the Pd active area. For rotating-disk electrode measurements, the Koutecký−Levich equation is frequently used to obtain the kinetic current density, which would be observed under kinetic control without any mass-transport effects. The Koutecký−Levich equation can be derived from equation 5.1 below, and the Levich equation relating the diffusion-limited current to the rotation rate of the electrode. In this work, the voltammetry was measured under stagnant conditions, and the concentration of reactants at the electrode surface is potential and time-dependent. Therefore, the Koutechý−Levich equation cannot be used in analysis. However, the contribution of mass transport can be neglected for potentials where the measured current density is less than 10% of the maximum value caused by the diffusion limitation [41]. For an extended potential range, the influence from mass transport can still be significantly reduced by using the equation:

$$\frac{1}{j} = \frac{1}{j_k} + \frac{1}{j_d} \tag{5.1}$$

where j is the measured current density, j_k and j_d are the kinetic and diffusion-limited current densities, respectively. In this work, the peak current densities of the respective curves in Figure 5.5 a were taken instead of j_d. The validity of this approach was carefully checked by analyzing the mathematical background using the simplified model for a totally irreversible one electron transfer reaction [60]. The

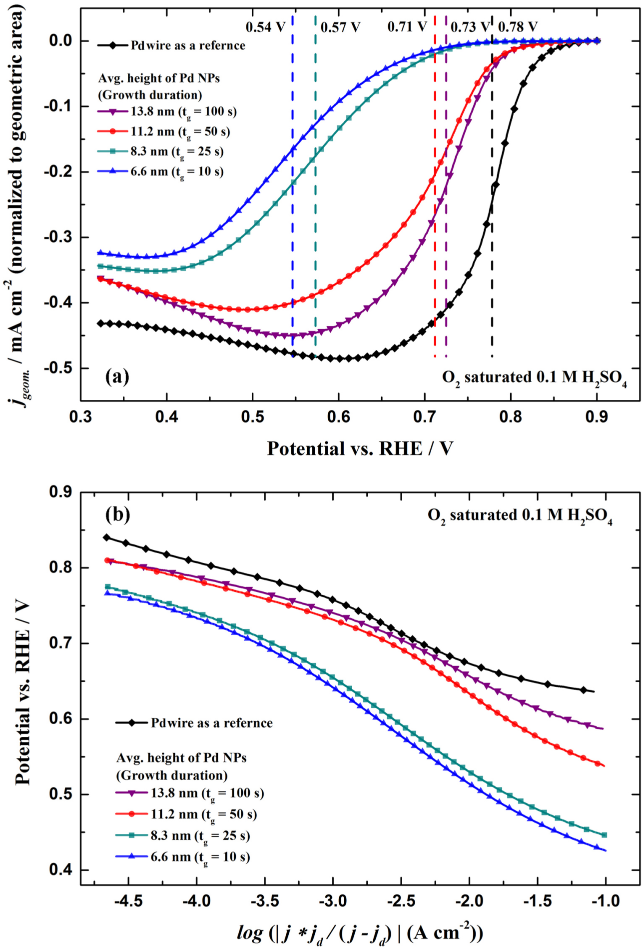

Figure 5.5: (a) Current-potential curves of bulk Pd and Pd / HOPG samples in the cathodic potential sweep for ORR. Scan rate is 20 mV s^{-1}. (b) Mass-transfer-corrected Tafel plot for ORR. The kinetic current density is obtained from equation 5.1.

resulting mass-transport-corrected Tafel plots of the ORR are shown in Figure 5.5 b. It can be observed that two regions with distinct Tafel slopes exist in the curve. The kinetic current densities at 0.75 V as well as the Tafel slopes are listed in Table 5.1.

Many authors [33, 34, 93] have reported that the Tafel slope at bulk and nanostructured Pd catalysts in sulfuric acid is -60 ± 10 mV dec^{-1} at a low current density and -120 ± 20 mV dec^{-1} at a high current density. The values are similar to the ORR on Pt electrodes at the low and high current densities, respectively. The change in the slope is attributed to the change of the Pd surface from highly oxidized at low current density (high potential) to a low coverage of Pd oxide, or even to a pure Pd surface, at high current density (low potential). The RDS at high potentials is a pseudo two-electron process, and at low potentials a one-electron transfer reaction for O_2 adsorption [94]. The potential range at which the Tafel slope changes from the high potential mode to the low potential mode indicates the change of the coverage of Pd oxide. For bulk Pd, the change happens at around 0.76 V. However, for Pd NPs, the change of Pd oxide coverage happens at potentials lower than 0.76 V, which means a stronger bond of oxygen atoms on the surface of Pd NPs. Additionally, the Tafel

Table 5.1: Tafel slopes for ORR at low and high current regions and specific current density at 0.75 V in mass-transfer corrected Tafel plot.

Sample	**Half-wave potential / V vs.RHE**	**Tafel slope / mV dec^{-1} (High-current region)**	**Tafel slope / mV dec^{-1} (Low-current region)**	**Kinetic current density at 0.75 V / mA cm^{-2}**
Pd wire	0.78	-47	-88	1.245
Pd / HOPG (13.8 nm)	0.73	-42	-97	0.666
Pd / HOPG (11.2 nm)	0.71	-49	-123	0.472
Pd / HOPG (8.3 nm)	0.57	-69	-122	0.072
Pd / HOPG (6.6 nm)	0.54	-72	-125	0.052

slopes for bulk Pd and Pd NPs larger than 10 nm are slightly less than -60 mV dec^{-1} in the low current range and less than -120 mV dec^{-1} in the high current range. The Tafel slopes for ORR measured at Pd NPs smaller than 10 nm are close to -60 and -120 mV dec^{-1} at low and high current densities, respectively. The results indicate that bulk Pd and large Pd NPs have higher activities for ORR than smaller NPs.

The size-dependent activity of Pd / HOPG for ORR has been evaluated in this work according to the kinetic current density of each sample. The bulk Pd has the largest kinetic current density at 0.75 V in all measured samples. The Pd / HOPG samples with the average height larger than 10 nm have a slightly smaller kinetic current density than that of bulk Pd. This result indicates that these large Pd NPs behave similar to the bulk material. However, the Pd / HOPG samples with an average height smaller than 10 nm have a kinetic current density much lower than that of bulk Pd (one order of magnitude lower). The sharply decreased catalytic activity of Pd NPs with size decrease can be attributed to the facet effect. Kondo et al. [97] reported that the Pd(100) is the most active facet for ORR in all of three low-index facets. This conclusion is supported by results on nano-sized catalysts as the catalytic activity of Pd cubes (mainly exposing (100) facets) for ORR is much higher than that of Pd octahedral (mainly exposing (111) facets) and Pd “spherical” (nonspecific orientation) NPs in acidic media [136]. Otherwise, Xiao et al. [213] reported that tailored Pd nanorods with Pd(110) as mainly exposed facets show a nearly tenfold higher activity than conventional Pd NPs due to the exceptionally weakened binding energy between oxygen ad-atoms and Pd(110) facets. Therefore, the role of different facets needs further clarification. Edge and corner atoms at Pd NPs are less active than terrace atoms due to their strong binding to oxygen atoms

[97]. It was confirmed by Cai et al. [214] that Pd NPs with smoother surface show a significantly enhanced activity for ORR. An electrodeposited NP can be analogous to a truncated octahedral shape. According to this model [140], the ratio of Pd(100) facets at the particle surface drops sharply from more than 20 % at 10 nm down to around 10 % at 5 nm. In contrast, the ratio of edge and corner atoms increases from around 20 % at 10 nm up to more than 40 % at 5 nm. With the decrease of particle size, the loss of Pd(100) facets and the increase of edge and corner atoms cause the decline of activity for ORR.

5.3.2 Support effect

The electrocatalytic activities of Pd / HOPG and Pd / N-HOPG for ORR were investigated in O_2 saturated 0.1 M Na_2SO_4 + x mM H_2SO_4 (pH=3) solution, where the low stability of Pd NPs on N-HOPG in pH 1 solution has been taken into consideration. The potential was swept cathodically from 0.765 to 0.275 V (vs. SHE) at a scan rate of 5 mV s^{-1}. The experiments were carried out under stagnant conditions, the concentration of O_2 at the electrode surface, hence, was time-dependent due to the sluggish mass transport of O_2 and lack of enough convection. The specific current densities for ORR are plotted versus the applied potential in Figure 5.6 a. The current density increases exponentially at first from the onset potential of ca. 0.7 V vs. SHE, until the mass transport becomes important. The kinetic current density was analyzed using equation 5.1. The peak current density of the respective curve was taken instead of the diffusion-limited current density, as the diffusion limited current density is not constant for stagnant conditions. The mass-transport corrected Tafel plots are shown in Figure 5.6 b. The Tafel slopes of both electrodes are around -64 ± 1 mV dec^{-1} at high potentials and -105 ± 3 mV dec^{-1} at low potentials. The ORR follows the same reaction mechanism on both samples; and the activities of both electrodes for ORR are nearly equal.

Basing on the specific current densities for both samples showing a high similarity, it is possible to conclude that the nitrogen functional groups do not affect the activity of supported Pd NPs for ORR. This conclusion is different to the reported results of Pt nanoclusters supported on nitrogen doped graphite. According to the volcano plot of ORR activity as a function of the oxygen binding energy [76], the Pt-O binding energy is a little stronger than the optimal value, and a slightly weakened Pt-O bond points to a higher activity for ORR. Pt nanoclusters supported on pyridinic and pyrrolic nitrogen defects at N-HOPG surface have a weaker binding to oxygen atoms due to the electron transfer from Pt to nitrogen defects [55]. Pd, as a member of PGMs, was expected to present the same behavior when it was supported on nitrogen defects. The XPS results of Pd / N-HOPG suggest that the oxidation states (+2 to +4) of Pd exist in addition to the Pd atoms. The increased oxidation states of Pd supported on nitrogen-functionalized carbon surface were reported by other authors [215–217] due to the formation of Pd-N and Pd-O bonds. In this work, the higher Pd oxidation states are mainly caused by the electron-withdrawing effect of the nitrogen functional groups. On Pd / N-HOPG, the particle-support interface was altered.

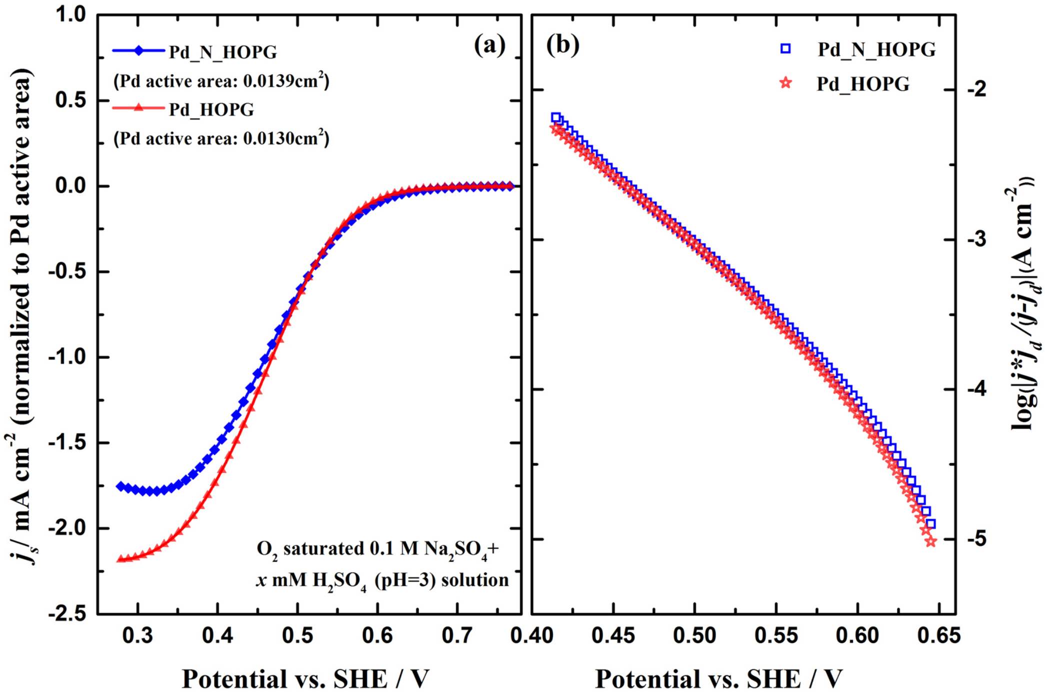

Figure 5.6: (a) Specific current density for ORR on Pd / HOPG and Pd / N-HOPG electrodes. (b) The mass-transfer corrected Tafel plot of ORR. The kinetic current density is obtained from equation 5.1.

However, the support effect is weakened gradually with the increase of the distance from the interface [218]. The estimated operation range of a support effect is within a few atomic layers [211, 219, 220]. For the electrochemically deposited Pd NPs with an average height of around 8 nm, the particle size has exceeded the operation range of the support effect. Therefore, the upper part of the NPs on N-HOPG possesses the same electrochemical properties as compared to that on HOPG. As a result, the observed intrinsic activities of both samples for ORR are similar.

Furthermore, particle size can significantly influence the activity of Pd NPs for ORR as discussed above. The electrocatalytic activity of Pd NPs for ORR decreases with the shrinking of particle size, and the onset potential of ORR becomes more negative in parallel. The critical particle size is considered to be 10 nm so that, when larger than this value, the Pd NPs behave similar as the bulk material. In this work, the average height of Pd NPs on N-HOPG is (8.1 ± 3.1) nm, and on HOPG is (13.4 ± 2.0) nm. A size-dependent activity was expected, but was not observed. This can be attributed to the broad distribution of particle size on the Pd / N-HOPG sample, which has been confirmed by the AFM images.

Overall, several effects, in such a case, should be considered to evaluate the activities of these samples: (a) the particle size effect, which has been known from the measurements on the Pd / HOPG samples; (b) the large size distribution of Pd NPs on N-HOPG, where the large NPs will have a higher share on the activity, but where also smaller NPs might contribute due to a support effect; (c) the relatively large average size, that might be too large for the support effect to act.

5.4 Carbon monoxide stripping

CO adsorbs on the Pd surface strongly so that the deactivation of Pd caused by CO poisoning should be taken into account. The binding strength of CO on a catalyst surface is a parameter to evaluate the CO tolerance of this material. In this work, the binding strength of CO molecules on Pd NPs with different size was studied by CO stripping measurements. The electro-oxidation of the CO monolayer on the Pd surface was investigated by applying cyclic voltammetry in 0.1 M H_2SO_4. The CO monolayer was formed on the Pd surface by holding the working electrode in 0.1 M H_2SO_4 at 0.46 V with CO gas purging for 10 min. Thereafter, Ar purging was carried out for 40 min in order to remove the remaining CO from the cell. The CVs were then measured in a potential range from 0.4 to 1.52 V at a scan rate of 50 mV s^{-1}.

Figure 5.7 shows selected CO stripping voltammograms recorded on polycrystalline bulk Pd and Pd / HOPG samples. In the first CV (solid line), a CO oxidation peak can be observed as compared to the second cycle (dashed line). The onset potential of CO oxidation on bulk Pd is above 0.8 V, and the maximum current density is at around 0.9 V (Peak I). The CO oxidation at 17.5 nm Pd NPs shows a similar profile such that the oxidation starts above 0.8 V with a peak potential at around 0.9 V. In addition to this dominant peak, a small shoulder peak can be observed above 1.0 V (Peak II). The voltammogram of CO oxidation at 14 nm Pd NPs shows a different profile as Peak I does not have an obvious dominance over Peak II, and two peaks are not very pronounced. Peak I and Peak II are centered at around 1.0 V and 1.12 V, respectively. For the Pd NPs with an average height smaller than 10 nm, Peak I cannot be observed in the CVs, only Peak II appears with a peak potential at around 1.12 V.

More data are presented in Figure 5.8 to trace the change of the CO oxidation peak with particle size. For each sample, the current density in the second voltammogram was considered to be the baseline, and subtracted from the current density measured during CO oxidation (the first voltammogram). The charge transferred during CO oxidation can be determined from the area between each curve and the corresponding $y = 0$ mA cm^{-2} axis. Obviously, Peak I dominates the CO oxidation at bulk Pd, 17.5 nm and 16 nm Pd NPs so that most of the adsorbed CO has been oxidized in the potential range below 1.0 V. At 14 nm Pd NPs, the peak current densities of Peak I and Peak II are almost the same. When Pd NPs are equal to or smaller than 13 nm, Peak II becomes more important in CO oxidation, while Peak I becomes a left shoulder peak until it disappears at Pd NPs equal to or smaller than 10 nm. For Pd NPs with average heights from 16 to 11.5 nm, Peak II is centered at the same value of around 1.12 V. However, the peak potential shifts positively with further decrease of particle size, e.g., the value shifts to 1.15 V at 10 nm Pd NPs, and to 1.17 V at 5 nm Pd NPs, and finally to 1.2 V at 3 nm Pd NPs. Two CO oxidation peaks, of which the peak potentials are separated by approximately 200 mV, indicate the existence of at least two different sites for CO adsorption. The binding energies

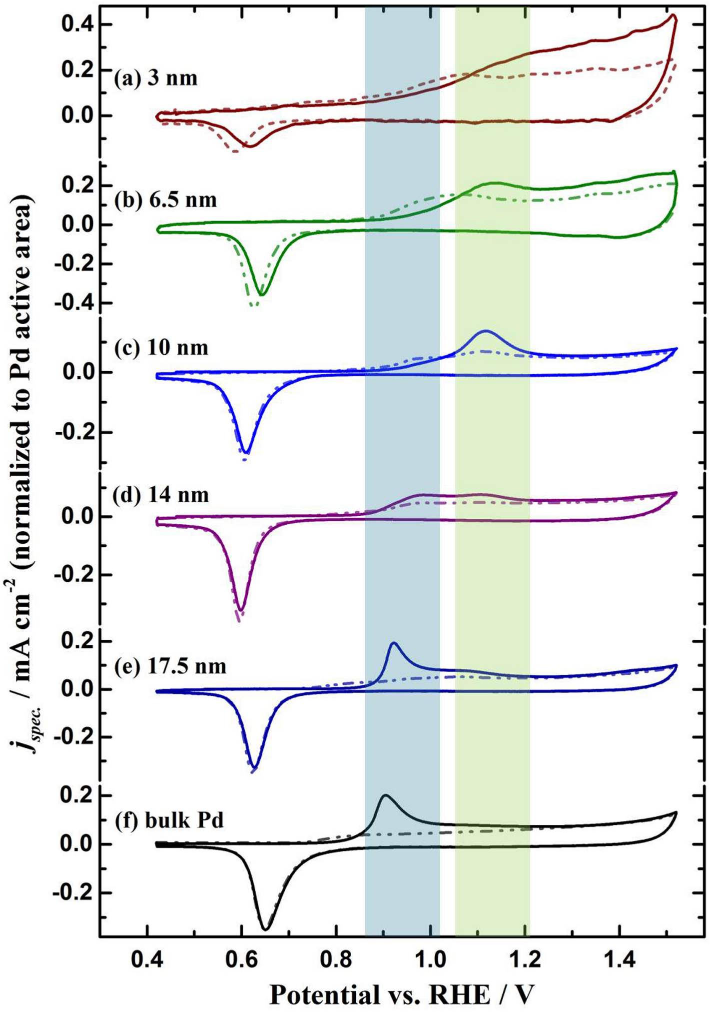

Figure 5.7: CO stripping voltammograms (solid lines) and the subsequent cyclic voltammograms (dashed lines) of Pd NPs in Ar-saturated 0.1 M H_2SO_4. The average particle sizes range from 3 to 17.5 nm (a-e). A bulk Pd sample was measured as a reference (f).

of CO on these sites are significantly different. The peak potential of Peak II shifts positively with the decrease of particle size suggesting an enhanced binding energy of CO on smaller Pd NPs.

It has been widely accepted that CO oxidation on Pd surface obeys the Langmuir-Hinshelwood (LH) mechanism [148]:

$$CO^* + OH^* \rightarrow CO_2 + H^+ + e^- + 2^* \qquad (5.2)$$

The formation of OH_{ads} is the first step to initiate the CO oxidation. An OH_{ads} is a reaction center so that a neighboring CO reacts with it to release two vacated Pd active sites for the OH_{ads} formation. The consumption of CO follows the mean-field (MF) model when the mobility of CO on the electrode surface is high; or the nucleation-growth (NG) model when the mobility is low [100, 149]. The density of OH_{ads} active sites and the onset potentials for OH_{ads} formation strongly influence the

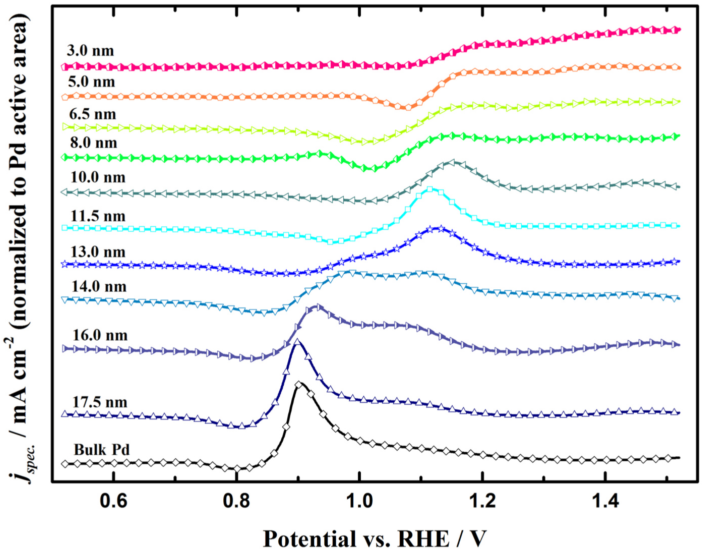

Figure 5.8: Current density of CO stripping measured on bulk Pd and Pd NPs. The current density of bare Pd in the same potential range (baseline, from the 2^{nd} cycle) was subtracted. A negative pit is visible at the left side of the oxidation peak, because there is in the 2^{nd} cycle a contribution from beginning Pd oxidation which is not present in the 1^{st} cycle due to site blocking by CO.

profile of CO oxidation, such as the peak width, peak potential as well as the number of oxidation peaks. It has been reported that the onset potential of OH$_{ads}$ formation on Pd (111) is approximately 200 mV higher than on two other Pd low-index facets (Pd(100) and Pd(110)) [148]. This behavior is highly consistent with the onset potential of CO oxidation on Pd low-index facets as the oxidation potential on the Pd(111) facet is nearly 200 mV higher than on the two other facets. Some authors [98, 100, 221] suggested that OH$_{ads}$ prefers to first form at the steps and, afterwards, on the terrace. El-Aziz et al. [222] reported that a perturbed Pd(111) surface, which contains a higher density of monoatomically high steps, showed a peak potential ca. 200 mV lower than well-ordered Pd(111). Therefore, the step sites as well as (100) and (110) facets are more active for CO oxidation; correspondingly, they show an oxidation peak at lower potential (centered at 0.9 V). The closely packed Pd(111) surface is rather inert to OH$_{ads}$ formation so that the CO oxidation peak can be observed at a higher potential (centered at 1.1 V).

The truncated-octahedral-shape particles, which are modeled as Wulff constructions of (100) and (111) facets with the minimized surface energy, can be considered as an approximate description for the shape of the electrochemically deposited Pd NPs [140]. According to this model, Pd(100) facets contribute more than 20 % to the particle surface when the particle size is equal to or larger than 15 nm. The ratio of (100) facets at a truncated-octahedral particle decreases significantly when the particle size is smaller than 13 nm. However, the ratio of (111) facets remains at ca. 60 % when the particle size is larger than 10 nm. The CO oxidation peaks in this work follow the trend of the diminishing of Peak I and the increasing of Peak II along with the change of particle size from 16 to 10 nm, which could indicate a change of surface structure towards more closely packed facets, i.e., well-ordered (111) facets. In the range of particle size from 16 to 10 nm, the ratio of edge and corner atoms increases with the size decrease. According to Nørskov's model [50], a stronger binding of CO to the edge and corner atoms is expected due to the upshift of the $d-$band center at the low-coordinated atoms. Yudanov et al. [223] also suggested that the strongest CO binding is at the bridge positions at cluster edges, and the adsorption energy on-top of low-coordinated Pd is larger than that for on-top sites of (111) and (100) facets. Therefore, the smaller Pd NPs, which have a higher ratio of edge and corner atoms, show a higher CO oxidation potential. On the other hand, the low-coordinated atoms are the active site for OH_{ads} formation. The competitive adsorption of CO and OH_{ads} at the low-coordinated atoms is a key issue to determine the reaction rate. The initially formed CO can block the subsequent OH_{ads} formation in a certain potential range. The blocking effect becomes stronger with the increase of CO coverage [224]. Friedrich et al. [225] observed that the coverage of CO on small Pt NPs is much higher than on a macroscopic surface, which is even above 1 for ca. 3 nm NPs; the CO overlayer thus can block the oxygen adsorption effectively. This enhanced blocking effect should be considered at small Pd NPs as well. Additionally, the CO molecules adsorbed at hollow, bridge and a-top sites, which should have a large difference in adsorption energy at low CO coverage, have, in contrast, the same binding strength to Pd atoms when the CO coverage nears saturation [101]. Although the average binding strength of CO with Pd becomes lower at a higher CO coverage, the vacating of a Pd atom for OH_{ads} formation is even more difficult in such a case due to the high ratio of CO to Pd surface atoms and the high mobility of CO, which is a result of the reduced binding strength, tending to occupy any free Pd site. In summary, the edge and corner atoms at a small Pd NP behave different to the steps and defects on bulk Pd in CO oxidation. The strong binding of CO at edge and corner atoms blocks OH_{ads} formation, and the high CO coverage at small Pd NPs increases the energy required for CO removal. Both effects can explain the positive shift of the CO oxidation peak at Pd NPs smaller than 10 nm.

5.5 Electrocatalytic activity for FAO

The electrocatalytic activity of Pd NPs for FAO was studied by cyclic voltammetry in Ar saturated 0.5 M HCOOH + 0.5 M H_2SO_4 solution. The potential was swept in a range of 0.1 to 0.95 V in order to cover the entire potential range for the FAO on the Pd surface. The applied scan rate is 20 mV s^{-1}. Figure 5.9 shows selected CVs recorded on polycrystalline bulk Pd and Pd / HOPG samples. The solid and dashed lines indicate the anodic and cathodic potential scans, respectively. For the bulk Pd electrode, the current density measured at 0.1 V is negative, which is due to the hydrogen ad- / absorption at this potential. When the potential is higher than 0.15 V, the FAO dominates the surface reaction, the current density, hence, becomes positive. Along with the anodic potential scan, the current density increases to the maximum value of 2.71 mA cm^{-2} at ca. 0.43 V, and then decreases. When the potential reaches 0.95 V, the Pd surface has been partially covered by Pd oxide. In the cathodic scan, the current density keeps almost constant from 0.95 to 0.85 V due to the inactivity of Pd oxide for FAO. When the potential is lower than 0.85 V, the reduction of Pd oxide occurs, and the current density for FAO increases again. A shoulder peak can be observed in the potential range of 0.85 to 0.65 V, and then a broad dominant peak appears in the lower potential range. For Pd NPs with an average height of 31.6 nm, the CV is similar to that of bulk Pd except the inconspicuous hydrogen ad- / absorption and two dominant FAO peaks in the cathodic scan. The maximum current density in the cathodic scan is lower than that in the anodic scan for the two samples, which can be explained by the lowering of the formic acid concentration at electrode surfaces or the loss of Pd active area during the measurement. For the other three samples, only one dominant peak can be observed, and the maximum current densities in the anodic and cathodic scans are similar. The current density of PdO reduction is one order of magnitude lower than the that of the FAO in the same potential range so that it can be neglected.

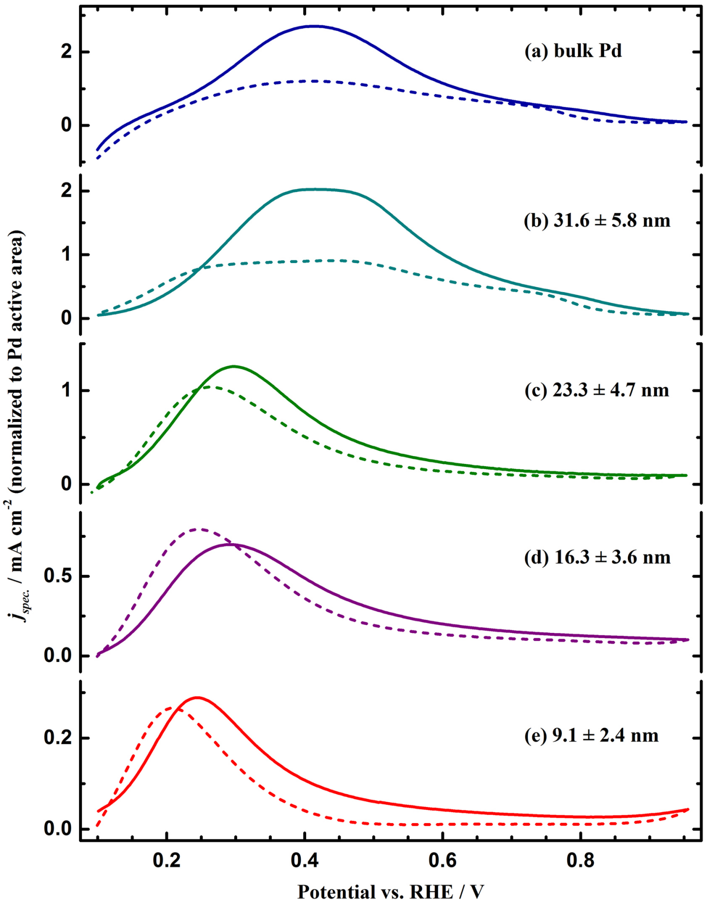

Figure 5.9: Cyclic voltammograms of FAO measured on bulk Pd and Pd NPs with average sizes from 9.1 to 31.6 nm. Solid lines indicate the anodic scan, and dashed lines show the cathodic scan.

More anodic voltammograms of bulk Pd and Pd / HOPG samples for FAO are shown in Figure 5.10. The average particle size changes from 43.2 ± 8.2 nm to 5.5 ± 2.3 nm. Obviously, the peak current density diminishes with the decrease of particle size, meanwhile, the peak potential shifts to a lower potential. In Figure 5.11, peak potentials (Figure 5.11 a), peak current densities (Figure 5.11 b) and current densities at 0.2 V (Figure 5.11 c) are plotted as a function of particle size. The corresponding values of bulk Pd are indicated as dashed lines. The peak current density of 43.2 nm Pd NPs for FAO is 2.68 mA cm^{-2}, which is almost the same as that of bulk Pd. With the decrease of average particle size, the peak current density diminishes from 2.68 mA cm^{-2} down to 0.22 mA cm^{-2} measured at the 5.5 nm Pd NPs. The peak potential, on the other hand, dose not shift monotonically with the particle size, but a trend of a negative shift is clear with the decrease of particle sizes, resulting in the potentials as low as 0.25 V.

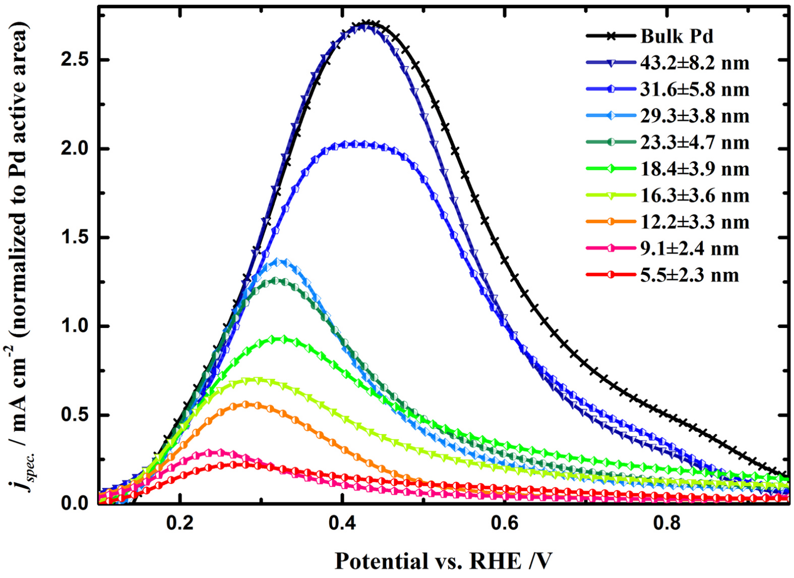

Figure 5.10: Anodic potential scans for FAO on bulk Pd and Pd NPs with average sizes from 5.5 to 43.2 nm. The average sizes were evaluated from the TM-AFM images.

It has been confirmed by many authors in Pd single crystal and nanocrystal studies that the peak potential and peak current density for FAO are structure sensitive [135, 226, 227]. Pd(100) in all the three Pd low-index facets shows the highest peak current density for FAO, which is more than two times higher than two other facets. On the stepped and kinked-stepped surfaces, the peak current density follows a trend of decrease with the increase of the step density, except for some special structures such as Pd(322) and Pd(911) [135, 228]. The onset and peak potentials measured at Pd(100) are more positive than those at the two other facets as well as at a defective surface [135]. For example, the peak potential was measured at Pd(100)-dominated nanocubes above 0.5 V, while the value at Pd(111)-dominated nano-tetrahedra is lower than 0.4 V [226, 227]. For a polycrystalline surface, the ratio of the (100) facet in the overall surface area can directly influence the peak potential and the correlating current density. The trend of the negative shift of the peak potential and

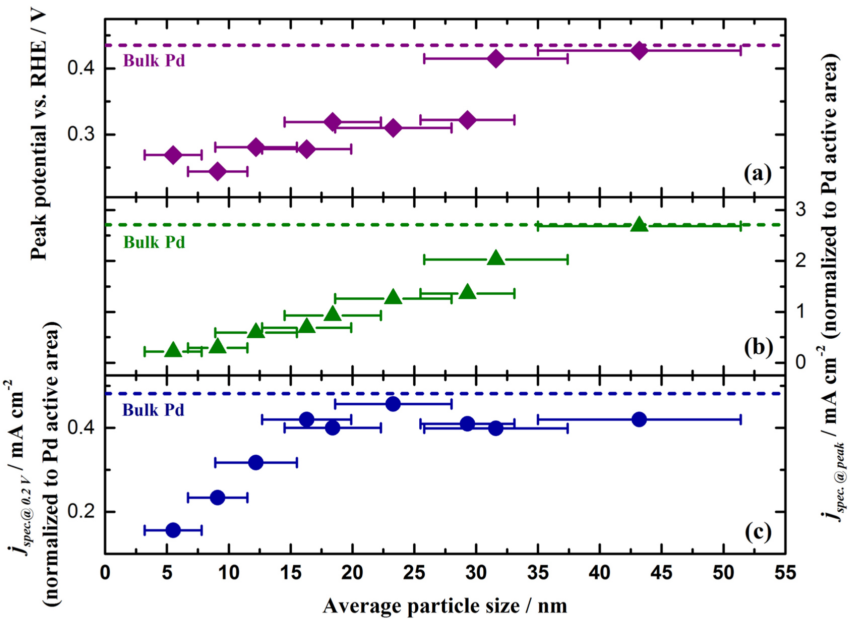

Figure 5.11: The peak potentials (a), peak current densities (b) and current densities at 0.2 V (c) for FAO. The correlated value of bulk Pd is indicated as dashed line.

the diminishing of the peak current density along with the decrease of the particle size points to the structure-related effect such that the ratio of the (100) facet becomes less for the smaller NPs, and the smaller Pd NPs tend to possess more closely packed (111) facets.

The current densities of all the samples at 0.2 V are shown in Figure 5.11 c. The onset potential for FAO at Pd(100) facet is at, or above, 0.2 V [220], so that the current density contributed from Pd(100) facets can be neglected at this potential. The current densities for all Pd / HOPG samples at 0.2 V show a different behavior as compared to the peak current density as the Pd NPs with average sizes larger than 15 nm show a nearly constant current density of 0.42 ± 0.03 mA cm^{-2} at 0.2 V. When the NPs are smaller than 15 nm, the current densities decrease almost linearly along with the change of particle size. If the current density at 0.2 V is contributed by the (111) facet and low-coordinated atoms (edge and corner atoms), then the linear decrease of the current density cannot be simply attributed to the structure effect, but some other effects should be considered.

The reaction mechanism of FAO is widely accepted to be a dual-pathway: a direct pathway in which formic acid dehydrogenates to form the final product CO_2, and an indirect pathway via dehydration to generate a poisoning intermediate (adsorbed CO) [105–107]. According to DFT calculations, initial formic acid adsorption on a Pt surface is energetically more favorable via its carbon atom so that the dehydration process is predominant. However, a formic acid molecule prefers to adsorb on a Pd surface via its oxygen atoms, the dehydrogenation, hence, occurs subsequently [229]. It has been confirmed experimentally that a Pt surface can be rapidly poisoned in FAO by CO intermediates; in contrast to Pt, Pd shows a very high activity for FAO [104, 230]. However, an activity loss of Pd over the period of FAO measurement was observed and attributed to the formation of adsorbed CO [38, 102, 129]. One possible explanation for the apparent contradiction is that the CO is electrochemically produced by reduction of the FAO product CO_2 at low potentials [130, 131, 231]. Wang et al. [130] studied the electrochemical CO_2 reduction in CO_2 saturated 0.1 M $HClO_4$ by ATR-SEIRA spectra, and observed the formation of CO at Pd electrodes at potentials from 0.4 to 0 V vs. RHE. The edge and corner atoms at Pd NPs are active sites for CO_2 reduction [231]. When Pd NPs are larger than 15 nm, the current density at 0.2 V is almost the same due to the low ratio and negligible influence of low-coordinated atoms. When Pd NPs are smaller than 15 nm, according to the model of truncated-octahedral-shaped particle [140], the fraction of edge and corner atoms increases rapidly, such that the influence of these low-coordinated sites becomes more significant. The edge and corner atoms are active sites for CO_2 reduction, and can be quickly poisoned. The loss of active Pd surface for FAO reduces the current density at 0.2 V. An increasing ratio of edge and corner atoms aggravates the poisoning effect. Additional effects, such as the adsorption of (bi)sulfate ($HSO_4{}^-$ / $SO_4{}^{2-}$), by which the Pd active sites can be blocked, cannot be ruled out in this work.

5.6 Summary

The OCP of a PdH_x electrode in an acidic solution can be used to estimate the hydrogen content in the Pd lattice. For Pd NPs with average size smaller than 8 nm, a size-dependent hydrogen content has been observed according to the change of the OCP with the particle size. Smaller Pd NPs tend to have a lower hydrogen content which can be attributed to the change of the lattice structure. The electrocatalytic activity of Pd for HER can be influenced by many factors such as composition (hydrogen content), lattice constant and the ratio of low-coordinated atoms. In this work, the hydrogen content is the most significant factor to influence the activity. The hydrogen absorption generates a tensile strain of the Pd lattice, leading to a shift of the electron energy bands, causing a change of the adsorption enthalpy of reactants or products on the Pd surface and changing the reaction kinetics. Normally, the binding strength of a hydrogen atom on an extended Pd surface is a little bit stronger than the optimum. The tensile strain effect enhances the binding strength, conversely, reduces the activity of Pd for HER. The smallest Pd NPs prepared in this work have the lowest hydrogen content, which means the smallest lattice tensile. Therefore, the highest activity for HER has been observed.

The activity of Pd NPs for ORR is size-dependent such that the smaller NPs show the lower activity. For both bulk Pd and Pd NPs, two Tafel slopes can be observed at high and low potentials, which correlate to a high coverage of surface oxide and a low one, respectively. The reduction of Pd oxide on Pd NPs happens at a lower potential than on bulk Pd, which indicates a stronger bond of oxygen atoms on Pd NPs. The binding strength becomes even higher with the decrease of particle size. The decrease of activity with particle size can be attributed to the increase of the ratio of low-coordinated atoms.

The binding strength of CO on a catalyst surface is a parameter for evaluation of the CO tolerance of this material. In this work, CO stripping measurements were carried out on Pd NPs with various sizes in order to investigate the size-dependent CO binding strength. It has been observed that the peak potential for CO stripping shifts from around 0.9 V positively to around 1.1 V with the decrease of particle size. The diminishing of the low potential peak and the increasing of the high potential peak happen when the particle size changes from 16 nm to 13 nm. The smaller Pd NPs tend to have a stronger binding with CO molecules, which can be explained by the more closely packed surface (high ratio of Pd(111) surface). According to the Wulff-structure particle, the ratio of edge and corner atoms increases dramatically when the particle becomes smaller than 10 nm. The edge and corner atoms can bond strongly with both OH_{ads} and CO so that a competitive adsorption of both species should be taken into account. For a Pd NP with highly saturated CO monolayer, the formation of OH_{ads} is blocked. Therefore, the energy required for CO removal becomes higher.

The electrocatalytic activity of Pd NPs for FAO was studied as well. The voltammograms of Pd NPs during FAO showed a trend of the negative shift of the peak potential and the reducing of the peak current density, which can be explained by the decrease of the active sites. The Pd(100) facet has been proven to be more active than other facets and low-coordinated atoms; and the onset and peak potentials measured on a Pd(100) surface are more positive than those on two other low-index facets and on a defective surface [135]. The decrease of the ratio of Pd(100) in all Pd surface structures causes the diminishing of the peak current density and the negative shifting of the peak potential observed in this work. Therefore, for smaller Pd NPs, the ratio of Pd(100) facets becomes less leading to the corresponding performance. The current densities of all the samples at 0.2 V were analyzed. When Pd NPs are larger than 15 nm, the current densities are nearly constant; while the current densities decrease with the average size of NPs when Pd NPs are smaller than 15 nm. The increase of the ratio of low-coordinated atoms causes the low activity for FAO. Furthermore, the CO poisoning, which initiates from the electro-reduction of CO_2 to CO at low potentials, can be a possible reason.

In general, smaller Pd NPs tend to have a high ratio of low-coordinated atoms, such as the edge and corner atoms. It has been widely accepted that, when the coordination number of an atom becomes lower, the $d-$band width of this atom will become narrower so that the $d-$band center will shift up in order to keep the constant filling of electrons at the Fermi level, which results in a stronger bonding [74]. The decrease of the coordination number of surface atoms with the particle size shrinking is an important factor in the analysis of the size-dependent activity. For the elements at the left arm of the volcano plot shown in Figure 2.6 which have a stronger binding energy with an oxygen atom than the optimum, it can be expected that the smaller NPs tend to have a lower specific activity for ORR. The method of getting a higher specific activity for ORR through the size shrinking seems to work for the elements at the right arm of the volcano. Actually, the enhanced activity of small Au NPs for ORR has been observed in a previous work [41]. If a stronger binding strength is unwanted in a specific reaction, such as the electro-oxidation of adsorbed CO molecules on Pd NPs, the decrease of particle size is not recommended. If the low-coordinated atoms play a harmful role in a reaction, e.g., the CO poisoning of the Pd surface in the FAO, the small NPs are not favorite as well.

Chapter 6

Metal deposition in ionic liquids

The state-of-the-art PEMFCs require relatively high loadings of Pt (0.45 mg_{Pt} cm^{-2}, namely, 0.05 / 0.40 mg_{Pt} cm^{-2} anode / cathode) [232], which drives up the cost, and limits the commercialization of this technique. One strategy of lowering the Pt loading without activity loss is to apply more active Pt-alloy catalysts for ORR. The promising candidates should have, at least, a two- to four-fold improvement in mass activity for ORR as compared with that of pure Pt NPs [233]. Some Pt-based rare earth metal (REM) alloys, such as Pt_3Y, Pt_5Gd, Pt_5La and Pt_5Ce, show high activities for the ORR and good stabilities in acidic media [21, 27–29]. The implementation of these Pt-REM alloys in nanoscale has a promising prospect.

However, the preparation of Pt-REM alloys is not reported hitherto with electrochemical methods. Due to the highly negative standard electrode potentials of these REMs (La^{3+} / La $\sim$ -2.379 V, Y^{3+} / Y $\sim$ -2.372 V, Gd^{3+} / Gd $\sim$ -2.279 V vs. SHE [60]), the electrochemical deposition in aqueous solution is prevented by the decomposition of water at a relatively more positive potential. The standard electrode potential of Pt^{2+} / Pt is 1.188 V vs. SHE, which is nearly 3.5 V more positive than that of these REMs. Therefore, a solvent, which has a high ionic conductivity, a broad potential window and inertia toward the deposited metals, is necessary for the synthesis of Pt-REM alloys. ILs, which are ionic materials remaining in liquid form below 100 °C [62], have a great potential to be used as a solvent for the electrochemical deposition of Pt-REM alloys.

In this chapter, some early-stage investigations of metal deposition in ILs are discussed. Section 6.1 introduces the properties of the used ILs. Pt metal deposition is discussed in section 6.2. The electrochemical behavior of Y^{3+} ion in ILs and Y deposition are discussed in section 6.3. Some initial results of Pt and Y co-deposition are presented in section 6.4.

6.1 Characteristics of the ionic liquids

In this work, two ILs, 1-octyl-1-methyl-pyrrolidinium bis(trifluoromethylsulfonyl)imide ([OcMePy][TFSI]) and N,N-diethyl-N-methyl-N-(2-methoxyethyl)ammonium tetrafluoroborate ($[N_{122,2O1}][BF_4]$), were used as solvent. The molecular diagrams and formulas of the anion and cation of [OcMePy][TFSI] are shown in Figure 6.1 a. The pyrrolidinium cation possesses a unit positive charge located at the quaternary ammonium nitrogen atom. Two alkyl chains, one containing eight carbon atoms and the other containing one carbon atom, are bound to the nitrogen atom besides two carbons in the heterocycle. The [TFSI]$^-$ anion possesses a unit negative charge centered at the nitrogen atom bonding with two trifluoromethylsulfonyl functional groups. Figure 6.1 c shows the [OcMePy][TFSI] contained in a Schlenk flask. [OcMePy][TFSI] has a light yellow color. The molecular diagrams and formulas of the anion and cation in [N$_{122,2O1}$][BF$_4$] are shown in Figure 6.1 b. The quaternary ammonium nitrogen atom connects to three alkyl chains and one methoxyethyl chain. The unit positive charge is centered at the nitrogen atom. The [BF$_4$]$^-$ anion possesses a unit negative charge located at the boron atom. It can be observed from Figure 6.1 d that [N$_{122,2O1}$][BF$_4$] is transparent. Both ILs were stored in a glove box filled with dry Ar gas (H_2O and O_2 contents lower than 0.6 ppm).

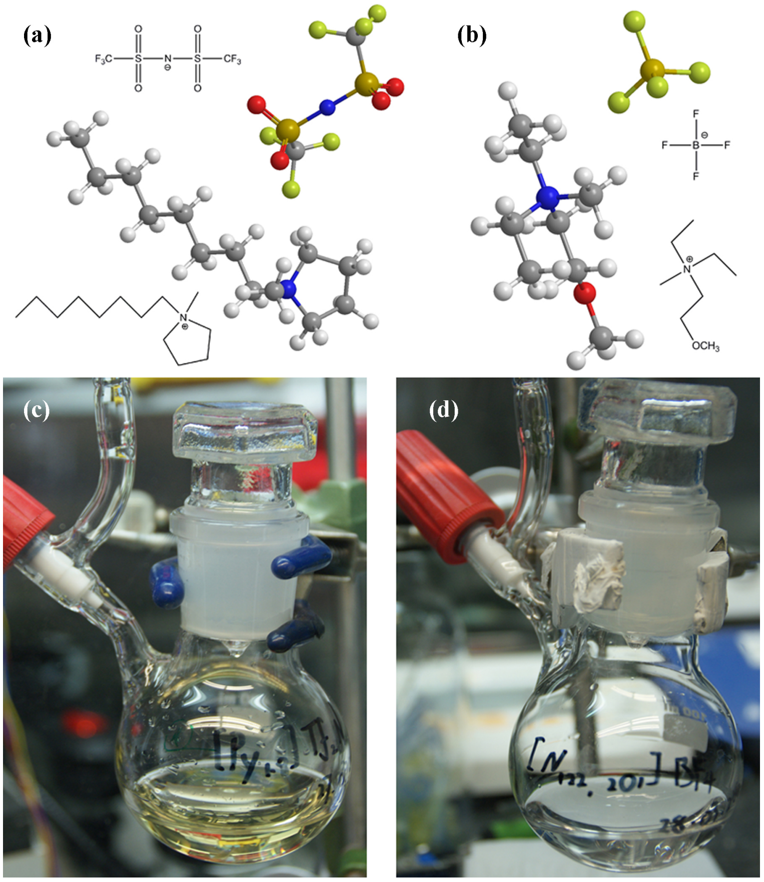

Figure 6.1: Molecular diagrams and formulas of [OcMePy][TFSI] (a) and [N$_{122,2O1}$][BF$_4$] (b). Both ILs ([OcMePy][TFSI] (c) and [N$_{122,2O1}$][BF$_4$] (d)) were kept in Schlenk flasks in an Ar-filled glovebox.

Cyclic voltammetry was used to estimate the electrochemical potential windows of both ILs. The measurements were carried out in a mini three-electrode cell. A HOPG substrate with 0.126 cm^2 exposed surface area was used as working electrode. Pt wires were used as counter and reference electrodes. In order to make a comparison, the CV of HOPG in Ar saturated 0.1 M H_2SO_4 solution at a scan rate of 50 mV s^{-1} is plotted in Figure 6.2 a. The potential was swept in the range of -0.57 to 2.03 V vs. RHE. The potential window of the H_2SO_4 solution is limited by the HER and ORR, which occur theoretically at 0 V and 1.23 V, respectively. At a HOPG electrode, the measured potential window is about 1.63 V according to the cut-off current density of ± 2 μA cm^{-2}.

The current densities in the double-layer region, which are measured at the HOPG electrode in both ILs, are one order of magnitude higher than that measured in the aqueous solution. Figure 6.2 b shows the CV of HOPG in [OcMePy][TFSI] at a scan rate of 50 mV s^{-1}. The potential was swept in the range of -2.85 to 1.75 V vs. Pt (If not explicitly denoted, all potentials in this chapter are referred to a Pt wire quasi-reference electrode). One oxidation peak centered at 0.8 V and one reduction peak centered at -2.6 V can be observed in the CV with three more small peaks. There is no obvious correlation among the oxidation and reduction peaks. When the potential is higher than 1.6 V, or lower than -2.8 V, the current density monotonically increases with the potential, which is attributed to the irreversible decomposition of ions in [OcMePy][TFSI]. The cut-off current density is selected at ± 100 μA cm^{-2}. Therefore, the potential window of [OcMePy][TFSI] is about 3.45 V. The CV of HOPG in [$N_{122,2O1}$][BF_4] at a scan rate of 50 mV s^{-1} is shown in Figure 6.2 c. The potential was swept in the range of -2.5 to 1.7 V. Four pairs of redox peaks can be observed in the CV, which are supposed to correlate to the specific adsorption and desorption of ions. When the potential is above 1.7 V or below -2.3 V, the decomposition of anions or cations occurs, respectively. If the cut-off current density is selected at ± 20 μA cm^{-2}, the potential window of [$N_{122,2O1}$][BF_4] is about 3.66 V. It is obvious that the potential windows of both ILs are much broader than that of an aqueous solution.

6.2 Pt deposition in ionic liquids

6.2.1 Pt deposition in [OcMePy][TFSI]

The Pt precursor solution was prepared by dissolving $H_2PtCl_6 \cdot 6H_2O$ into [OcMePy][TFSI]. Water molecules were introduced from the hydrates into the solution. A heating treatment up to 100 °C in the Ar filled glovebox was tried to evaporate the water. However, the Pt precursor decomposed to Pt black, and precipitated at the bottom of the glass bottle, which is due to the low stability of ${PtCl_6}^{2-}$ ions at high temperature. Therefore, the heating treatment is unavailable. The water traces in the solution cannot be avoided.

The CV of HOPG was measured in 13.2 mM H_2PtCl_6 + [OcMePy][TFSI] (designated Pt-[OcMePy][TFSI]) solution shown in Figure 6.3. A CV of HOPG in pure [OcMePy][TFSI] is given for comparison. In the Pt-[OcMePy][TFSI] solution, the current density in the double-layer region is much higher than that one measured in the pure [OcMePy][TFSI], which indicates a larger double-layer capacitance at the

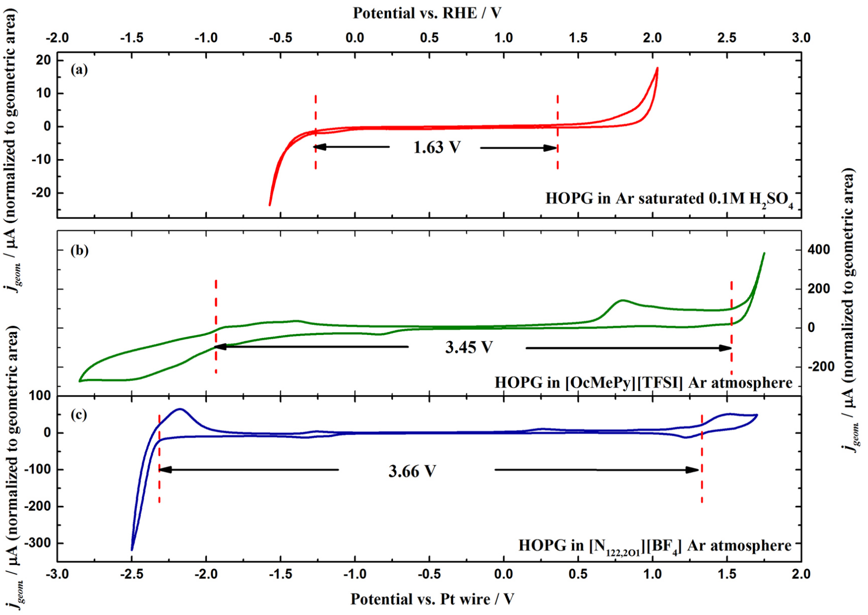

Figure 6.2: CVs of HOPG in 0.1 M H_2SO_4 (a), [OcMePy][TFSI] (b) and [$N_{122,2O1}$][BF_4] (c). The reference electrode in (a) is Hg / Hg_2SO_4 in 0.1 M H_2SO_4. Pt wire quasi-reference electrode is used in (b) and (c). The scan rates for all the three measurements are 50 mV s^{-1}.

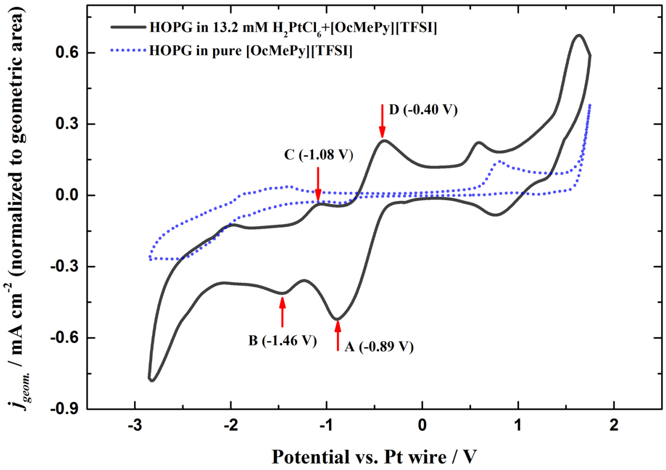

Figure 6.3: CVs of HOPG in Pt-[OcMePy][TFSI] (solid line) and in pure [OcMePy][TFSI] (dashed line). Scan rate: 50 mV s^{-1}.

HOPG and Pt-[OcMePy][TFSI] interface. In the potential range from 0 to -2.0 V, four peaks, two in the cathodic scan (peak A and B) and two in the anodic scan (peak C and D), are highlighted. Electrochemical reduction of Pt^{4+} to Pt^0 in ILs has been discussed by some authors [234, 235]. Not like the direct reduction of Pt^{4+} to Pt^0 in aqueous solutions, the reduction in ILs is a two-step process via an intermediate state of Pt^{2+} . The reduction potential of Pt^{2+} to Pt^0 is lower than that of Pt^{4+} to Pt^{2+}. In the cathodic scan, the reduction peak A (-0.89 V) and B (-1.46 V) are considered to correlate with the two reduction reactions [235]

$$Pt^{IV}Cl_6{}^{2-} + 2e^- \rightarrow Pt^{II}Cl_4{}^{2-} + 2Cl^- \tag{6.1}$$

and

$$Pt^{II}Cl_4{}^{2-} + 2e^- \rightarrow Pt^0 + 4Cl^- \tag{6.2}$$

respectively. Peak C (-1.08 V) and D (-0.40 V) are suspected to correlate to the oxidation of Pt^0 to Pt^{2+} and Pt^{2+} to Pt^{4+}.

The viscosity of ILs is normally higher than that of aqueous solutions at room temperature. Therefore, the diffusion coefficient of ions in ILs is rather low. When a single potential step, in which the working electrode was held at a potential lower than -1.46 V, was used for Pt deposition, the migration direction of $\mathrm{PtCl_6}^{2-}$ is opposite to the direction of diffusion which leads to a low yield. In this work, a repeated potential-step method was applied for Pt deposition. The potential was held at the OCP of -0.2 V for 5 s in order to complement $\mathrm{PtCl_6}^{2-}$ ions by diffusion. Then the potential was switched to -1.5 V for 5 s to reduce $\mathrm{PtCl_6}^{2-}$ to Pt metal at the electrode surface. This potential step was repeated for 100 times. Figure 6.4 a and b show the applied potentials and their corresponding current densities at a time scale. The double-layer charging causes a large current density when the potential switches from OCP to the deposition potential. The current density decreases nearly to a constant value in 5 s. The current density at the end of each deposition period, which is marked as a red cross in Figure 6.4 b, is extracted and plotted versus time in Figure 6.4 c. Only the period of deposition is accounted for in the time scale. The constant current density decreases from the initial value of -0.14 mA cm^{-2} down to around -0.04 mA cm^{-2}, which can be exactly fitted by a function shown in the figure. The $\mathrm{PtCl_6}^{2-}$ concentration at the electrode surface has decreased significantly with the deposition time .

The deposits were electrochemically and microscopically studied. Before characterizations, the sample was rinsed repeatedly in isopropanol, ethanol and deionized water in order to remove the residual IL. The electrochemical properties were investigated by cyclic voltammetry in Ar saturated 0.1 M H_2SO_4 and potential sweeps in O_2 saturated 0.1 M H_2SO_4. The CV of the deposit on HOPG is shown in Figure 6.5 a, which is a typical profile of Pt measured in sulfuric acid with peaks of Pt oxidation / reduction and hydrogen ad- / desorption. The active area of deposited Pt is determined by the charge transferred during the hydrogen adsorption. The current for Pt catalyzed ORR is normalized to the Pt active area. The current densities obtained at different scan rates are shown in Figure 6.5 b. The onset potential of ORR at Pt / HOPG is at around 0.95 V vs. RHE. The current density increases exponentially at first until mass-transport limitation of oxygen becomes relevant. After the peak, it becomes smaller due to the extension of the oxygen diffusion layer. The curve obtained at a scan rate of 5 mV s^{-1} is different as no cathodic peak is observed at all. The maximum current density is linearly related to the square root of the scan rate ($j_{geom.} \propto \sqrt{\nu}$). The electrochemical characterizations confirm that

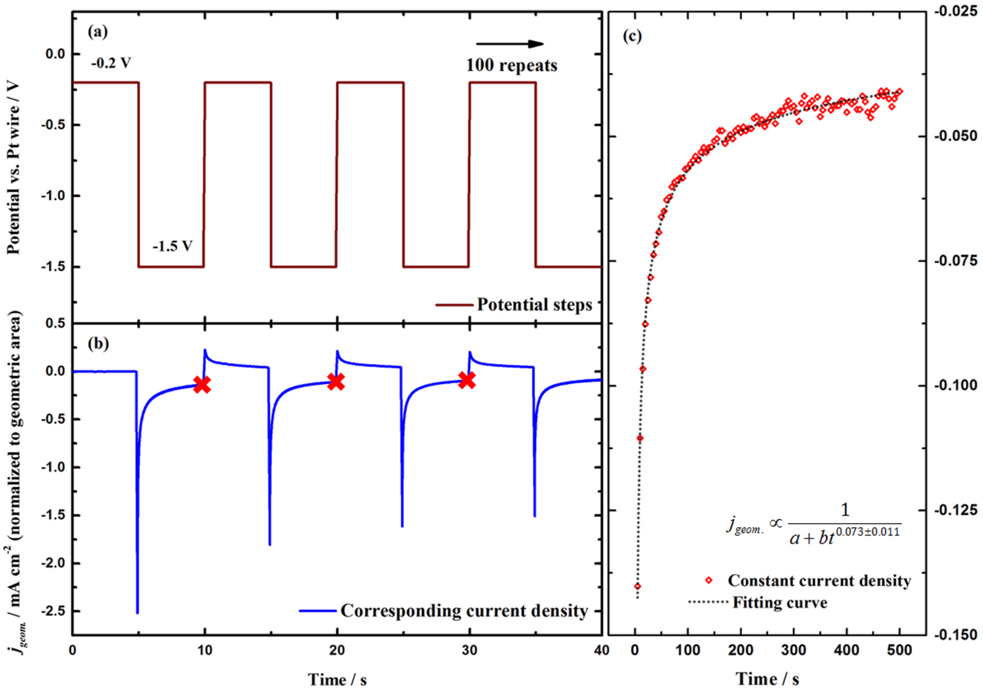

Figure 6.4: Repeated potential steps (a) and corresponding current density (b) for Pt deposition in Pt-[OcMePy][TFSI]. (c) The current density at the end of each deposition period is plotted against time and fitted by the inserted equation indicating a decrease of $PtCl_6{}^{2-}$ concentration with the deposition time.

Pt metal has been successfully deposited from Pt-[OcMePy][TFSI].

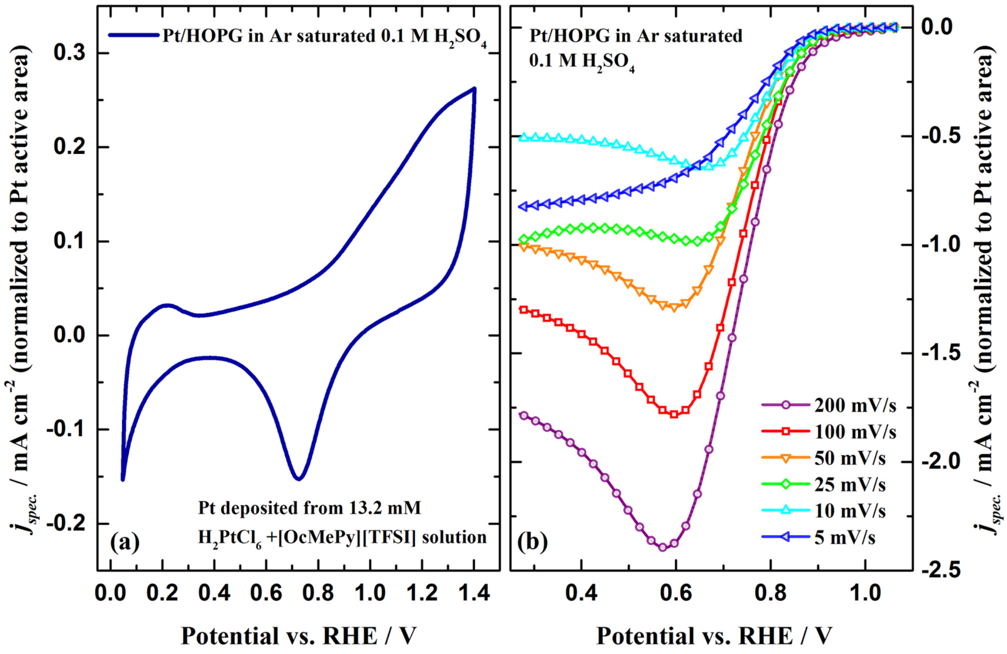

Figure 6.5: (a) CV of Pt / HOPG in Ar saturated 0.1 M H_2SO_4. (b) Voltammograms of Pt / HOPG for ORR in O_2 saturated 0.1 M H_2SO_4 at different scan rates.

The morphology of Pt deposited from Pt-[OcMePy][TFSI] was investigated by TM-AFM in atmosphere as shown in Figure 6.6. Four regions, which are marked in Figure 6.6 a, can be observed on the electrode surface. Region A is smooth without obvious structures, so it is the exposed HOPG surface. Region B is covered by nanoclusters with an average height of around 3 nm. The nanoclusters are considered to be agglomerated Pt clusters, which formed in each deposition period as small clusters, and then agglomerated. Region C is blurred. The substance does not show a distinct boundary so that it should be in liquid phase, which is highly possible to be a residual ionic-liquid drop. Some big particles, such as the one marked in region D, exist on the electrode surface with an average height larger than 10 nm. They are considered to be Pt NPs continuously growing during the deposition process. Therefore, the size is much larger than for other Pt clusters.

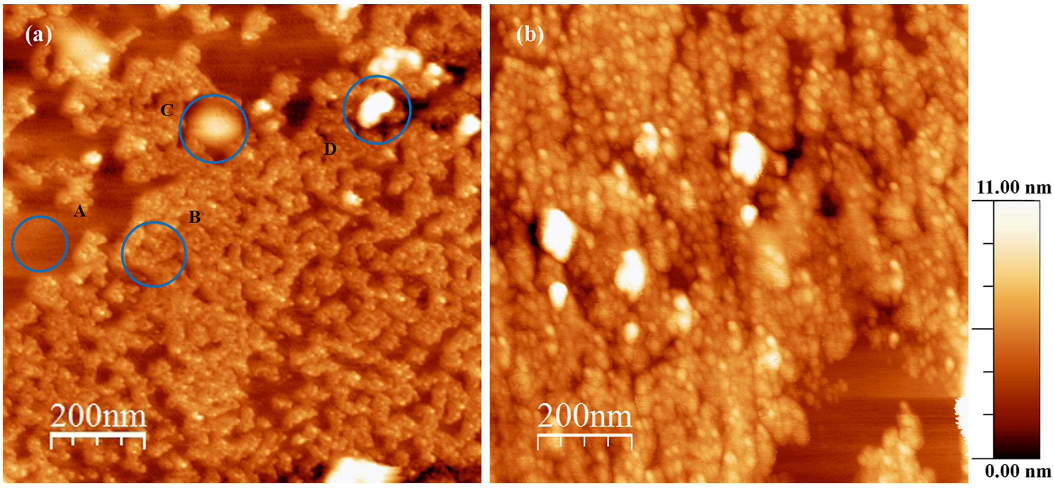

Figure 6.6: AFM images of Pt / HOPG samples prepared with the repeated potential steps in Pt-[OcMePy][TFSI].

6.2.2 Pt deposition in $[N_{122,2O1}][BF_4]$

The Pt precursor solution was prepared by dissolving $H_2PtCl_6 \cdot 6H_2O$ into $[N_{122,2O1}][BF_4]$. In order to prepare a 4.4 mM H_2PtCl_6 + $[N_{122,2O1}][BF_4]$ solution, 4.6 mg of $H_2PtCl_6 \cdot 6H_2O$ was added into 2 ml $[N_{122,2O1}][BF_4]$. However, the solubility of H_2PtCl_6 in $[N_{122,2O1}][BF_4]$ is so low that the solution reached saturation before all salt dissolved. The accurate mass of the undissolved salt cannot be measured. Therefore, the prepared solution is named as saturated H_2PtCl_6 + $[N_{122,2O1}][BF_4]$ solution (Pt-$[N_{122,2O1}][BF_4]$). The heating treatment is not suitable for this Pt precursor because of the poor stability of H_2PtCl_6 at high temperature. The water traces, hence, cannot be avoided in this precursor.

The CV of a HOPG electrode in Pt-$[N_{122,2O1}][BF_4]$ was measured in the potential range of -2.5 to 1.6 V at a scan rate of 50 mV s^{-1}. As compared with the CV of HOPG recorded in pure $[N_{122,2O1}][BF_4]$ (dotted line in Figure 6.7), four peaks were present newly of which two peaks are in the cathodic scan (peak A and B) and two in the anodic scan (peak C and D). As discussed above, the electrochemical reduction of Pt^{4+} to Pt^0 in ILs follows a two-step process. The potential of peak A (-1.0 V) here is close to the value of peak A (-0.89) in Figure 6.3, which indicates the same reaction occurs in this potential range. The potential of peak B (-2.0 V) in this measurement is much lower than the value of peak B (-1.46 V) in Figure 6.3 so that there seems to be no correlation between them. Further studies have been carried out to understand the peaks.

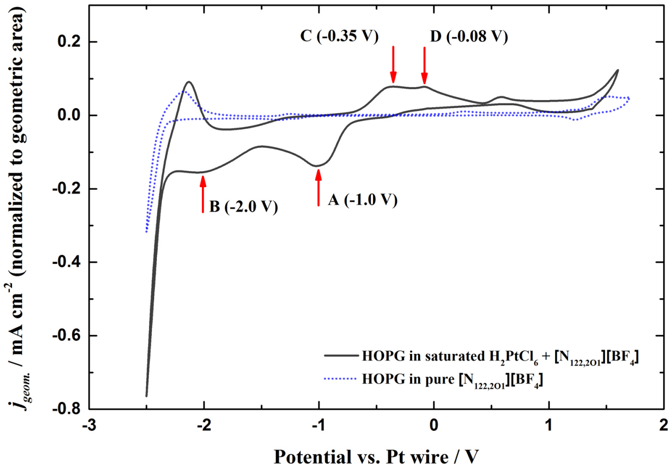

Figure 6.7: CVs of HOPG in Pt-[$N_{122,2O1}$][BF_4] (solid line) and in pure [$N_{122,2O1}$][BF_4] (dashed line). Scan rate: 50 mV s^{-1}.

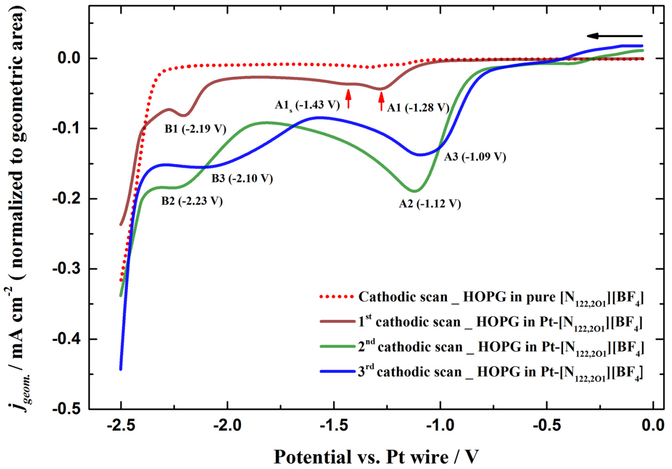

Figure 6.8: Cathodic potential sweeps of HOPG in Pt-[$N_{122,2O1}$][BF_4] (solid line) and in pure [$N_{122,2O1}$][BF_4] (dashed line) from 0 to -2.5 V. Scan rate: 50 mV s^{-1}.

Three sequent potential scans of HOPG in Pt-[$N_{122,2O1}$][BF_4] were measured from -0.05 to -2.5 V. The voltammograms are shown in Figure 6.8. For all the three scans, two dominant peaks can be observed. From the 1^{st} to the 3^{rd} scan, the peak potentials of A1 to A3 shift positively from -1.28 to -1.09 V. The positive shift of these potentials can be explained by the different thermodynamics of Pt deposition on bare HOPG and Pt metal. Normally, the deposition of Pt atoms on HOPG requires higher energy than on Pt metal. In the 1st scan, the initial nucleation of Pt on the HOPG surface occurs at a relatively low potential. After the 1st scan, some Pt nuclei have already formed on the HOPG surface. Therefore, the deposition of Pt atoms on Pt nuclei happened at a relatively low overpotential in the 2nd scan. A small shoulder peak of A1 (A1$_s$) can be observed with a peak potential centered at -1.43 V. This potential is very close to the potential of peak B in Figure 6.3, which correlates to the $PtCl_4{}^{2-}$ reduction. Therefore, peak A1 and A1$_s$ indicate the two-step reduction of $PtCl_6{}^{2-}$. Although the shoulder peak cannot be observed in Peak A2 and A3, it can be considered that the broad peaks consist of, at least, two sub-peaks which correlate to the two steps of $PtCl_6{}^{2-}$ reduction. The reduction potentials of the two steps have a very small difference. This behavior is different to the $PtCl_6{}^{2-}$ reduction in Pt-[OcMePy][TFSI], in which the reduction peaks of the two steps are distinctly separated. In Figure 6.7, the oxidation peaks of C and D in the anodic scan are close to each other, which indicates a small potential difference for the two-step Pt oxidation in the Pt-[$N_{122,2O1}$][BF_4]. From peak B1 to B3, the peak potentials do not have a clear trend of shift, but the peak becomes broader with scans. They are deemed to correlate to the adsorption of cations on the Pt surface.

Repeated potential steps of -0.27 V (5 s) → -2.2 V (5 s) → -1.5 V (3 s) → -0.27 V (5 s) for 100 repeats were applied on the HOPG electrode to deposit Pt from Pt-[$N_{122,2O1}$][BF_4]. The OCP of HOPG in Pt-[$N_{122,2O1}$][BF_4] is at -0.27 V. During the deposition, the working electrode was kept at OCP before and after each deposition period for 5 s in order to complement the $PtCl_6{}^{2-}$ ions.

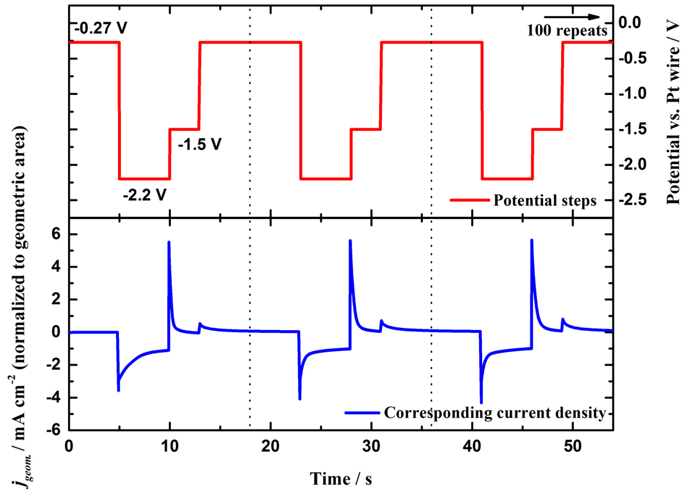

Figure 6.9: Repeated potential steps (upper) and corresponding current density (lower) for Pt deposition in Pt-[$N_{122,2O1}$][BF_4].

The electrochemical properties of deposited material on HOPG were investigated by cyclic voltammetry in Ar saturated 0.1 M H_2SO_4 and potential sweeps in O_2 saturated 0.1 M H_2SO_4. The CV is shown in Figure 6.10 a. The profile is a typical CV of Pt in sulfuric acid. The active area of deposited Pt is determined by the charge transferred in hydrogen adsorption. The voltammograms for Pt catalyzed ORR at various scan rates are shown in Figure 6.10 b. The current is normalized to the Pt active area. This profile is unusual for ORR in a stagnant measurement. The current density increases exponentially at first to the maximum, and then remains constant, which is different to that shown in Figure 6.5 b. The current density remaining constant indicates a sluggish reaction rate at the electrode surface, or small Pt clusters widely separated so that the oxygen diffusion to the electrode surface obtains a balance with the oxygen consumption. The maximum current density holds the linear relation with the square root of the scan rate. Another contributing factor could be residual ionic liquid on the sample. For some catalysts it has been observed in literature that impregnation with ionic liquid is beneficial for ORR due to a larger oxygen solubility in the IL [236–238].

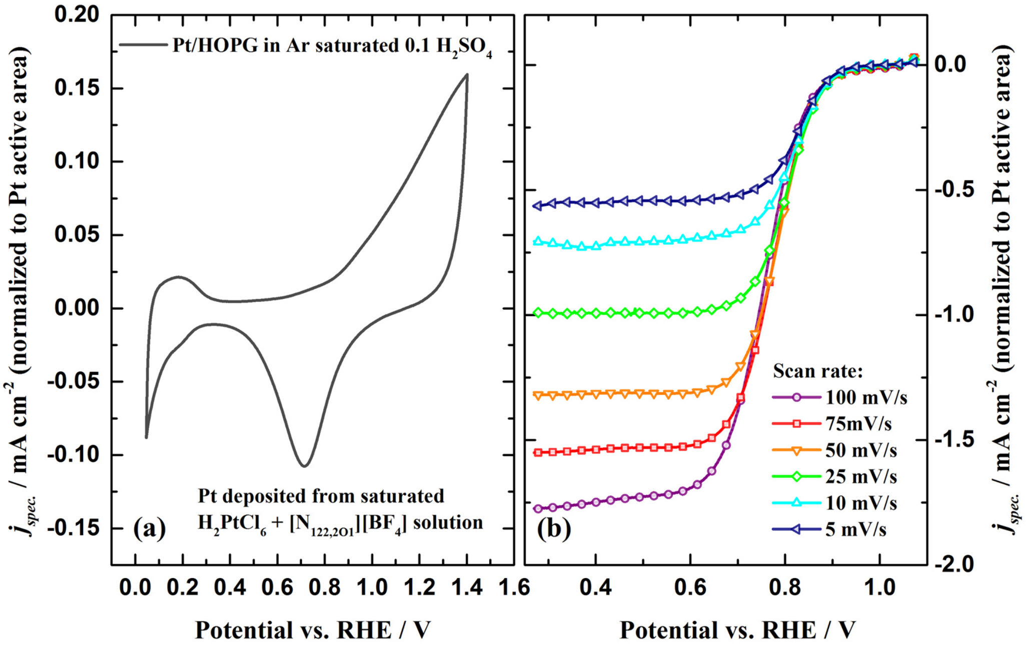

Figure 6.10: (a) CV of Pt / HOPG in Ar saturated 0.1 M H_2SO_4. (b) Voltammograms for Pt catalyzed ORR in O_2 saturated 0.1 M H_2SO_4 at different scan rates.

The Pt / HOPG sample, which was prepared in Pt-[$N_{122,2O1}$][BF_4], was imaged by TM-AFM shown in Figure 6.11. Before imaging, the electrode has been meticulously cleaned and checked with cyclic voltammetry in H_2SO_4 solution to confirm that only Pt was left on the electrode. Some big particles, like the one marked in region A, can be observed on the electrode with average heights larger than 20 nm. They are Pt NPs continuously growing during the whole deposition process. Besides the region A, some small structures, like the one marked in region B, are considered to be Pt clusters, which were formed by agglomeration of Pt clusters growing in a single or several deposition pulses. Figure 6.11 b shows such structures at a small scale. The clusters with an average height of around 3 nm agglomerated randomly to form nano-structures without a regular shape. Region C and D are the substrate. Region

C is smooth without observable structures, which is deemed to be the original HOPG surface. Some structures with average heights from 0.5 to 1 nm exist in region D. They are assumed to be roughened HOPG surface formed at a high electropolarization. The intercalation of IL cations into graphene layers, which can expand the interlayer distance, is another option to explain the roughened surface.

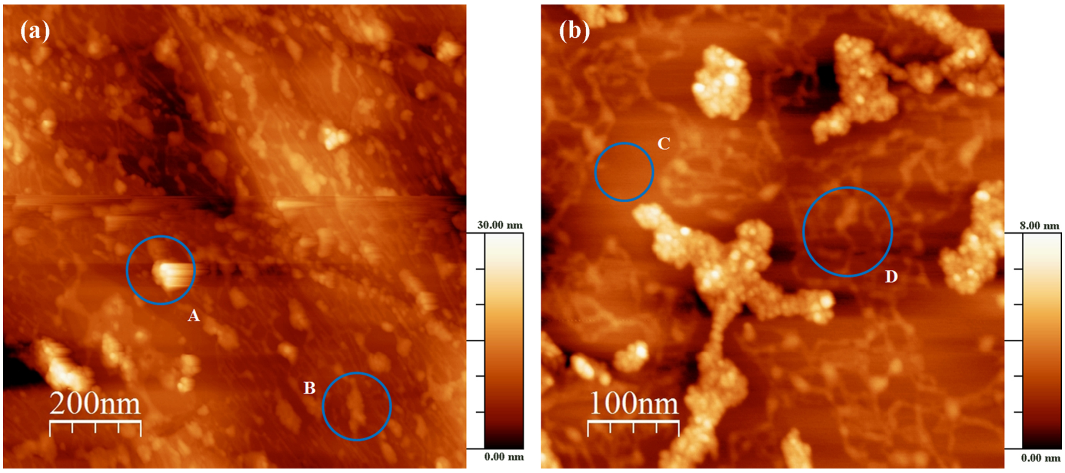

Figure 6.11: AFM images of Pt / HOPG samples prepared with the repeated potential steps in Pt-[$N_{122,2O1}$][BF_4].

6.3 Y deposition in ionic liquids

6.3.1 Y deposition in [OcMePy][TFSI]

Yttrium (Y) is the first d-block element in the 5^{th} period, has an electronegativity of 1.22, which is comparable to some lanthanide elements. The standard electrode potential of Y^{3+} / Y is -2.372 V vs. SHE [60]. The pure bulk Y is relatively stable in air due to the passivation from the dense protective Y_2O_3 layer on the surface. However, finely divided Y is very active in air to react with O_2 and H_2O. Therefore, Y deposition must be carried out in Ar atmosphere. The O_2 and H_2O content should be controlled to an extremely low level. [OcMePy][TFSI] was used for an initial attempt of the electrochemical Y deposition. The Y precursor electrolyte was prepared by dissolving $Y(NO_3)_3 \cdot 6H_2O$ into [OcMePy][TFSI]. In this work, a 40 mM $Y(NO_3)_3$ + [OcMePy][TFSI] (Y-[OcMePy][TFSI]) solution was prepared. The initially prepared solution was heated up to 110 °C for 24 h in Ar-filled glovebox in order to remove the water introduced by the hydrate. After the heating treatment, the color of Y-[OcMePy][TFSI] changed from light yellow to brown.

The sequent CVs of HOPG in Y-[OcMePy][TFSI] are shown in Figure 6.12. The CVs were measured in a potential range of 0.4 to -2.5 V at a scan rate of 50 mV s^{-1}. In the 1^{st} scan, a cathodic peak, of which the peak potential is centered at -2.06 V, can be observed. As compared with the CV of HOPG in pure [OcMePy][TFSI], this cathodic peak is distinct in Y-[OcMePy][TFSI]. The charge transferred in the cathodic peak, which is obtained by integrating the current on the time scale, is

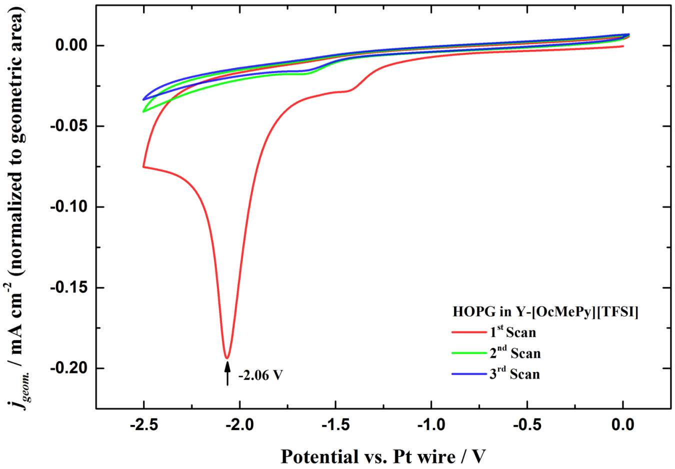

Figure 6.12: CVs of freshly prepared HOPG in Y-[OcMePy][TFSI] solution at a scan rate of 50 mV s^{-1}. A reduction peak with a peak potential of -2.06 V can be observed in the 1st scan.

1.15 mC cm^{-2}. From the 2nd scan, only the double-layer current can be observed in this potential range instead of the cathodic peak. In order to understand the disappearance of the cathodic peak, a series of experiments were carried out on a HOPG electrode. If the depletion of reactants at the electrode surface after the 1st scan is a reason of the disappearance of the cathodic peak, a strong stirring in the electrolyte, or replacing with fresh Y-[OcMePy][TFSI], can recover the cathodic peak. However, the recovery was not observed, which means the depletion of reactants is not true. The disappearance of the cathodic peak indicates that some substance, which was produced in the 1st cathodic peak, can block the further faradaic process. The passivation layer prohibits the further faradaic reactions in Y-[OcMePy][TFSI]. However, it cannot block the electrochemical process when the electrolyte was replaced to Pt-[OcMePy][TFSI]. In an experiment, the passivation layer has been formed on a HOPG surface by running cyclic voltammetry in Y-[OcMePy][TFSI]. Afterwards, Y-[OcMePy][TFSI] was replaced by Pt-[OcMePy][TFSI]. Sequent CVs of the same electrode in Pt-[OcMePy][TFSI] were measured and shown in Figure 6.13. In the 1st scan, the cathodic current density becomes higher as compared with that measured at the passivated HOPG electrode in Y-[OcMePy][TFSI]. A reduction peak can be observed, which means the passivation layer does not prevent the reduction of Pt. In the 5th scan, two typical reduction peaks, which are correlated to the reduction of Pt^{4+} to Pt^{2+} and Pt^{2+} to Pt^{0}, respectively, can be observed in the cathodic scan. Two corresponding oxidation peaks are in the anodic scan. The peak potentials of these four peaks are similar to the values labeled in Figure 6.3, which confirms that Pt deposition on HOPG occurs. This work indicates that the passivation layer cannot block Pt deposition, even cannot influence the deposition potential of Pt on HOPG (except in the very beginning).

After cyclic voltammetry in Pt-[OcMePy][TFSI], Pt metal was present on the electrode. The non-passivated Pt surface was exposed to the electrolyte so that it

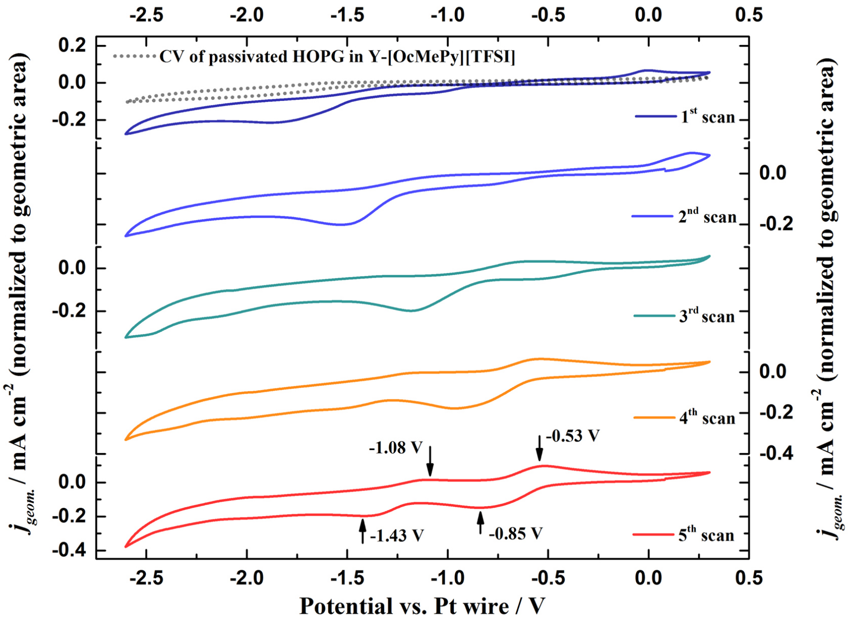

Figure 6.13: Sequent CVs of passivated HOPG electrode in Pt-[OcMePy][TFSI] (solid lines) and in Y-[OcMePy][TFSI] (dashed line).

can be considered to the new working electrode surface. A following experiment was carried out to investigate the passivation effect of Pt in Y-[OcMePy][TFSI]. Pt-[OcMePy][TFSI] was replaced by Y-[OcMePy][TFSI] in the same cell. Sequent CVs were measured in the same potential range and shown in Figure 6.14. A cathodic peak, which is similar to the one in the 1^{st} CV of HOPG in Y-[OcMePy][TFSI], can be observed in the 1^{st} CV with a peak potential of -2.3 V. The negatively shifted peak potential indicates a change of the interface, which can be the composition of the electrode (Pt on HOPG surface) or the concentration and the purity of Y-[OcMePy][TFSI] (low Y^{3+} concentration and $PtCl_6{}^{2-}$ ions existing near the electrode surface). From the 2^{nd} scan, the cathodic peak disappeared again showing that the passivation layer formed after the 1^{st} CV.

The change of the electrode surface in the aforementioned series of experiments has been summarized in Figure 6.15. The passivation layer can form on both HOPG and Pt metal surface and block the further reactions in Y-[OcMePy][TFSI]. According to the results, the electrode materials, here HOPG and Pt metal, are chemically inert in the electrochemical processes. The electrochemical reaction of Y-[OcMePy][TFSI] at a potential lower than -2.0 V produces some kind of material, which covers the electrode surface. This material has a poor electronic or ionic conductivity that the further reactions in Y-[OcMePy][TFSI] are prohibited. However, the passivation layer is not strongly and compactly adhering on the electrode surface. When the passivated HOPG surface is exposed to Pt-[OcMePy][TFSI], Pt metal can be deposited on the electrode surface. This indicates that $PtCl_6{}^{2-}$ ions are able to penetrate the passivation layer. The composition and structure of this passivation layer is still unknown. Further investigations with other techniques are necessary.

In situ electrochemical STM (EC-STM) was used to study the morphology of the

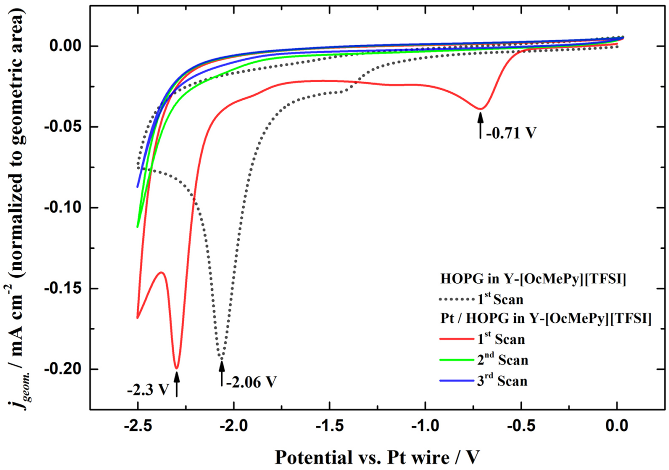

Figure 6.14: CVs of Pt / HOPG electrode in Y-[OcMePy][TFSI] solution at a scan rate of 50 mV s^{-1}. A reduction peak with a peak potential of -2.3 V can be observed in the 1st scan.

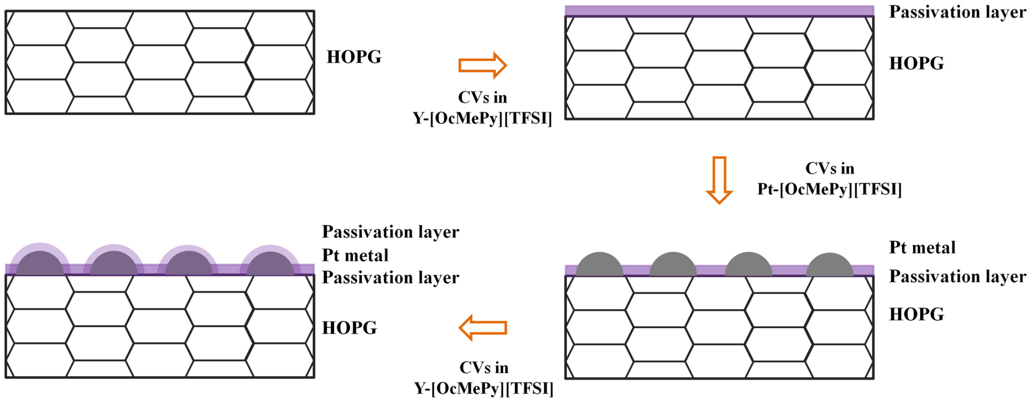

Figure 6.15: Schematic representation of the passivation effect in the experiments discussed above. The passivation layer can form on both HOPG and Pt surfaces and block the further reactions in Y-[OcMePy][TFSI].

passivation layer on HOPG. Figure 6.16 a shows the STM image of HOPG in dry Ar atmosphere. The typical HOPG surface structure, which consists of large terraces and several steps, can be observed in the image. Figure 6.16 b shows the STM image of HOPG in Y-[OcMePy][TFSI] at 0 V (OCP). The electrolyte does not influence the imaging quality at 0 V so that the HOPG structure can be clearly observed. During the imaging of Figure 6.16 c, the potential was initially held at 0 V for 52 s, and then cyclically swept down to -2.3 V and back to 0 V at a scan rate of 10 mV s^{-1}, which is shown as the blue line. The corresponding current density is shown as the red line. A cathodic peak with a peak potential at around -2.0 V is present in the chronoamperogram. When the applied potential was above -1 V, there was no faradaic process at the electrode surface and the HOPG surface could be imaged in a high quality. When the potential was swept in the range from -1.0 to -1.5 V, the cathodic current started to increase to a peak centered at around -1.5 V. The quality of the image became lower: some noise, especially at steps, occurred. In the STM imaging with a constant current mode, the noise indicates a large current change at the tip, which can result in tip withdrawal. At the positions shown as high-current noise (bright pixels), the tip is more approaching the surface. The adsorption of cations at the electrode surface can decrease the distance between tip and substrate. Another possible explanation is that an electron screening layer forms on the electrode surface, which causes the decrease of the tunneling current at the tip. In order to compensate, the tip approaches to the substrate, which increases the risk of a crash. The high-current noise at the steps can be attributed to a slight crash of the tip to the edges of graphene layers. When the potential was lower than -1.5 V, a reaction occurred so strongly that the morphological information of the substrate was covered by the noise. Although the potential difference between the tip and substrates was kept at a constant value of +100 mV, the strong reaction at the electrode surface, which was associated with an intensive charge transfer, perturbed the acquisition of efficient tunneling data so that the image quality became worse. When the potential was lower than -1.75 V, the tip could not image the HOPG surface. When the potential swept anodically above -1.5 V, the image of the HOPG substrate reemerged with some noise. When the potential was higher than -1.0 V, the quality of the image recovered to that before the cyclic voltammetry. Some cracked graphene layers overlap on the surface, which can be caused by the scratch of tip on the substrate or the violent reaction on the surface. Figure 6.16 d shows the morphology of the HOPG at 0 V, which was recorded after the cyclic voltammetry. The terraces and steps of graphene layers are clearly shown in the image. However, no specific structures correlating to a passivation layer can be observed. Figure 6.16 e shows a 3D image in an area of 150 nm × 150 nm. As compared with the freshly prepared HOPG surface, the steps of a graphene layer, shown in this image, are much higher, of which the height is almost two times of the initial value. The tilting at the steps can be attributed to the ion intercalation into HOPG interlayers at the cathodic potential. In the EC-STM study, the passivation layer was not observed, which, from another perspective, confirms that the passivation layer covers the electrode surface with a very weak adhesive force. It is suspected to be a molecular layer, which can be produced in the reduction process and cannot be imaged with STM.

6.3.2 Y deposition in $[\mathrm{N}_{122,2O1}][\mathrm{BF}_4]$

The electrochemical deposition of Y in $[\mathrm{N}_{122,2O1}][\mathrm{BF}_4]$ was investigated in this work. 38.2 mg $\mathrm{Y(NO_3)_3 \cdot 6H_2O}$ was added into 5 ml $[\mathrm{N}_{122,2O1}][\mathrm{BF}_4]$ in order to prepare a 10 mM $\mathrm{Y(NO_3)_3}$ + $[\mathrm{N}_{122,2O1}][\mathrm{BF}_4]$ (Y-$[\mathrm{N}_{122,2O1}][\mathrm{BF}_4]$) solution. The solution was heated up to 110 °C in Ar-filled glovebox for 24 h to remove the water which was introduced by the hydrate. When the solution was cooled down to room temperature, some salt still existed in the glass bottle, which indicates that the solution is saturated, or that dissolution is extremely sluggish.

Sequent CVs of HOPG in Y-$[\mathrm{N}_{122,2O1}][\mathrm{BF}_4]$, which are shown in Figure 6.17, were measured in the potential range of 1.6 to -2.5 V at a scan rate of 50 mV s^{-1}. As compared with the CV of HOPG in pure $[\mathrm{N}_{122,2O1}][\mathrm{BF}_4]$ in Figure 6.17 a, the CV

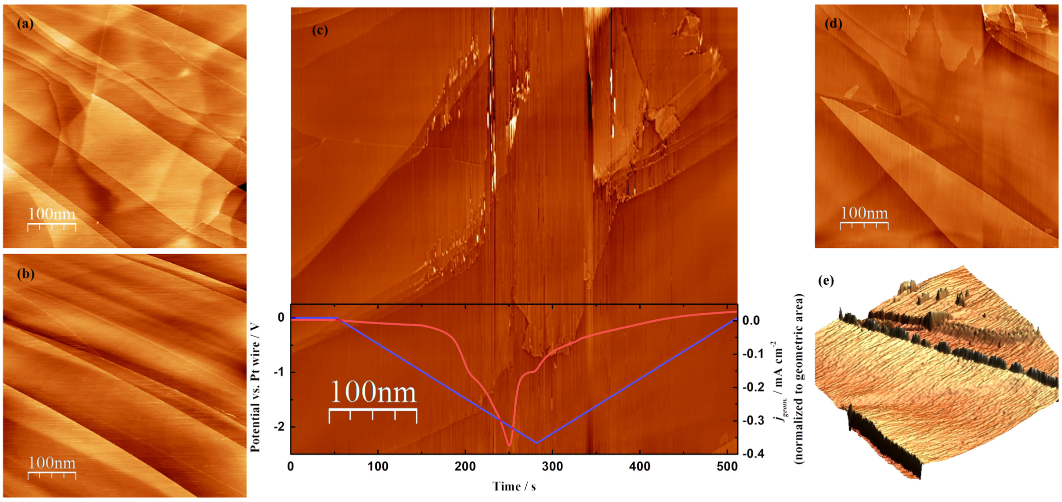

Figure 6.16: EC-STM invesigation of a HOPG electrode in Y-[OcMePy][TFSI]. (a) The morphology of HOPG in Ar atmosphere. (b) The morphology of HOPG in Y-[OcMePy][TFSI] at OCP. (c) HOPG surface was imaged along with the cyclic voltammetric measurement. The applied potential (blue line) and corresponding current density (red line) are plotted along with the imaging process. (d) The morphology of HOPG in Y-[OcMePy][TFSI] after the cyclic voltammetry. The image was recorded at the same location with (c). (e) 3D image recorded at the step edge of HOPG after the cyclic voltammetry.

profile in Y-[$N_{122,2O1}$][BF_4] shows significant differences at potentials below -1.0 V. The current density increases gradually with the lowering of the potential. Three cathodic peaks, which are centered at -1.43 V, -1.66 V and -1.93 V, respectively, can be observed. If the three peaks are correlated to the three steps of Y^{3+} reducing to Y^0 via Y^{2+} and Y^+, the result will be plausible to meet the requirement. But the assumption should be confirmed by other techniques. Figure 6.17 b shows the consecutive CVs of HOPG in Y-[$N_{122,2O1}$][BF_4]. The inset (6.17 c) shows some details of peak C. In the first 3 scans, there are two peaks (C1 and C2) in this potential range. The peak current density of C1 increases with the number of cycles, while the peak C2, which is dominant in the first 2 scans, becomes a shoulder peak in the 3^{rd} scan, and disappears from the 4^{th} scan. The change of cathodic peaks along with the potential cycles indicates that the interfacial condition between electrode and electrolyte has changed. However, the cathodic peaks are so small that the numerical analysis concerning these peaks is inaccurate. The concentration of the Y precursor should be increased in order to achieve a conspicuous cathodic peak.

For the purpose of increasing the Y^{3+} concentration in [$N_{122,2O1}$][BF_4], high purity anhydrous acetone was used to assist the $Y(NO_3)_3$ dissolution. 5 ml acetone was mixed with 5 ml [$N_{122,2O1}$][BF_4]. 383 mg $Y(NO_3)_3 \cdot 6H_2O$ was added into the mixture and kept at 60 °C for 2 h until all solids dissolved completely. The solution was heated up to 110 °C in Ar atmosphere for 72 h to evaporate the acetone and water. After the heating treatment, the solution separated into two phases: a precipitate at the bottom and an orange solution above. The solution was used for Y deposition.

EQCM was used to study the mass change at the electrode connected to the reduction process. A quartz single crystal resonator coated with keyhole-shape Au electrodes on both sides was used, one of these electrodes served as working electrode.

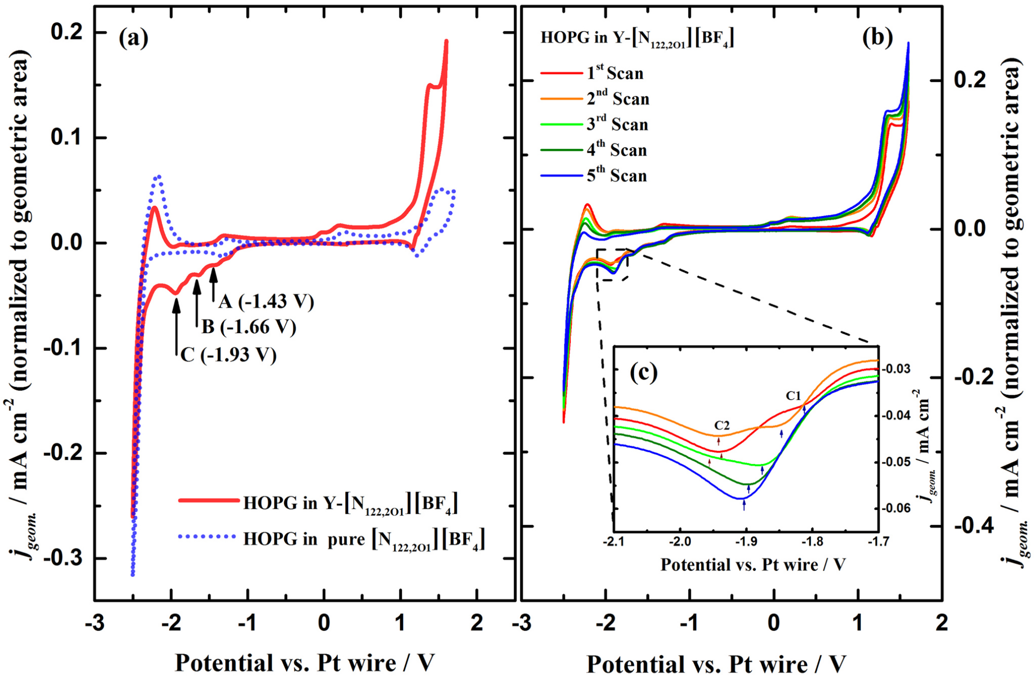

Figure 6.17: (a) CVs of HOPG in Y-$[N_{122,2O1}][BF_4]$ (solid line) and in pure $[N_{122,2O1}][BF_4]$ (dashed line). (b) Sequent CVs of HOPG in Y-$[N_{122,2O1}][BF_4]$. (c) Detailed profiles of the sequent CVs in the potential range of -2.1 to -1.7 V.

The electrochemically active geometric area of the Au electrode is 0.29 cm^2. The piezoelectric active area of the quartz is 0.19 cm^2. In the experiment, a network analyzer was online measuring the electrical admittance of the resonator between the two Au electrodes in the vicinity of its resonance frequency ($\sim$ 10 MHz). From the fit of the real part of the admittance with a Lorentzian function, both the resonance frequency and the damping were determined. The damping indicates the energy loss related to the surface roughness or solution viscosity. The resonance frequency before deposition was measured as a reference point. From the change of frequency during the electrochemical measurement, the mass change at the electrode surface can be calculated from the Sauerbrey equation, as long as the changes in the resonance frequency significantly exceed the changes in the damping. Figure 6.18 a shows the EQCM results during the cyclic voltammetric measurement in the potential range of 0 to -2.6 V at a scan rate of 5 mV s^{-1}. One obvious cathodic peak centered at ca. -2.25 V and its correlated anodic peak centered at ca. -2.14 V are present in the CV (black line). Besides the two dominant peaks, two small cathodic peaks can be observed as well. In the cathodic scan, the resonance frequency of the quartz single crystal starts to decrease at the 1st cathodic peak at ca. -1.5 V. The change of the frequency shows a high simultaneity with the current change in the CV. When the potential is lower than -2.1 V, the cathodic current density increases sharply to the maximum of around -0.11 mA cm^{-2}, and the resonance frequency reduces nearly by 1.75 kHz. Meantime, the damping increases by about 5 kHz, which indicates a rougher surface or a higher viscosity of the electrolyte close to the electrode surface.

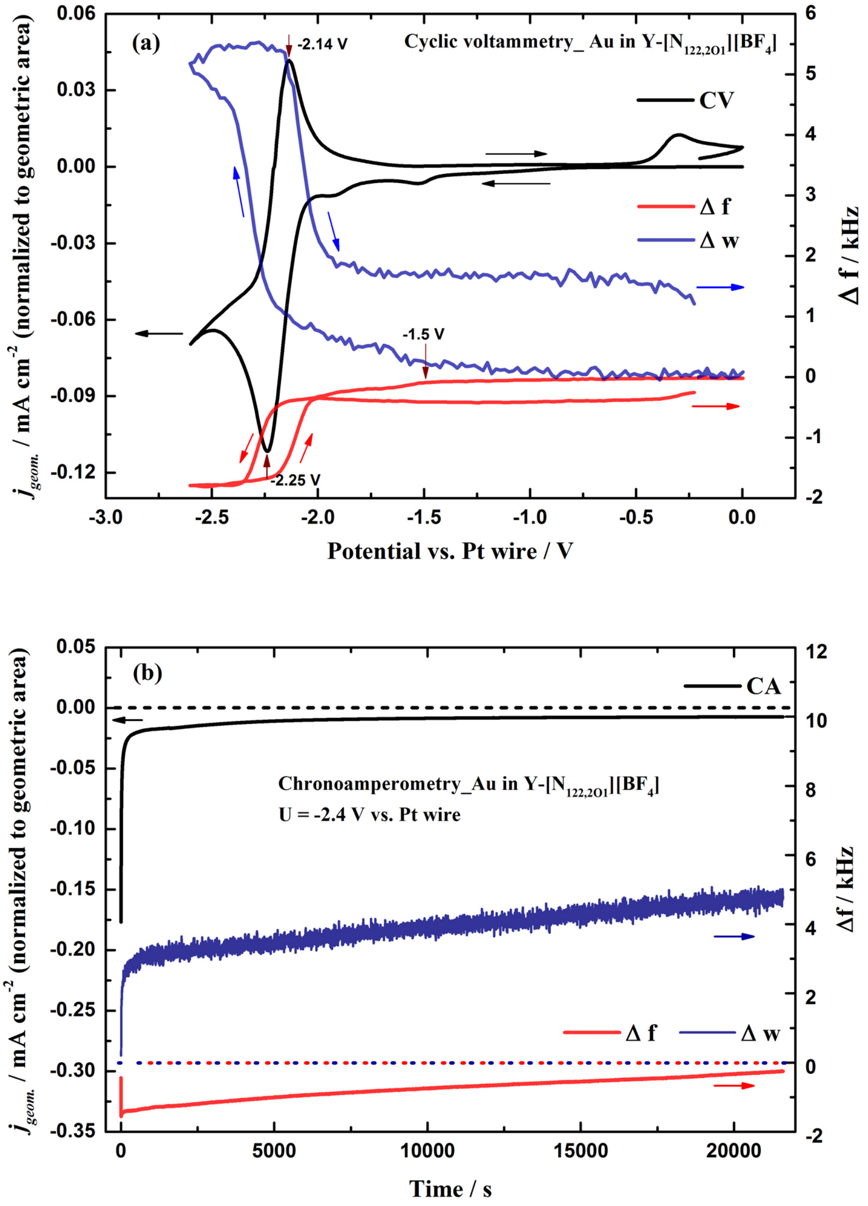

Figure 6.18: EQCM measurement at a gold-coated quartz crystal resonator as working electrode in concentrated Y-[$N_{122,2O1}$][BF_4]. (a) The CV in a potential range of 0 to -2.6 V. (b) The chronoamperogram recorded at -2.4 V for 21600 s. Red and blue lines represent the resonance frequency change and the damping frequency change, respectively.

In the anodic scan, the resonance frequency started to increase at ca. -2.25 V to a frequency which is equal to the value at -2.0 V in the cathodic scan, and then keeps constant. The damping reduces in parallel to a constant value as well. In the EQCM results, two small peaks in the cathodic scan are supposed relating to the adsorption of solvent or precursor ions. The change in the resonance frequency during the redox process does not exceed the change in damping. Therefore, it is inaccurate to state that the mass change at the electrode surface causes the change in frequency. The coupled dominant peaks can be the redox pair correlated to the Y^{3+} and partially reduced Y ions (Y^{n+}, $0 < n < 3$). The partially reduced Y^{n+} can only exist at a potential lower than -2.0 V. The change in oxidation state of the cation might induce a change in the viscosity, explaining the EQCM response.

Chronoamperometry was measured on the Au electrode at -2.4 V for 21600 s shown in Figure 6.18 b. The black curve shows that the current density initiates from ca. -0.175 mA cm^{-2}, and quickly decreases to -0.02 mA cm^{-2} after 1000 s. Then the current density decreases slowly to a constant value of ca. -0.01 mA cm^{-2}. The oscillation frequency decreases by 1.75 kHz at beginning, but, thereafter, the value increases slowly with time. The damping increases quickly in the initial 1000 s and then slowly in the remaining time. The initial decrease of oscillation frequency accompanying with the increase of damping frequency indicates that some materials adsorbs at the electrode surface leading to an increase of both mass and roughness. However, the change of the oscillation frequency cannot be used to estimate the mass change at the electrode surface due to the great change of the damping. After the initial stage, the oscillation frequency does not decrease continuously, but increases with time. The reason of the behavior is still not clear. The increase of oscillation frequency points out that the adsorbed materials bind weakly with the electrode surface, and their amount does not increase in the following reaction. It is supposed that some material at the electrode surface dissolved or mechanically detached during the longtime measurement. The EQCM measurements cannot prove that Y has been deposited on the Au electrode at a potential lower than -2.0 V. This behavior is more like partially reduced Y^{n+} ions adsorbing at the electrode surface in this potential range.

The repeated potential-step method was used for Y deposition on HOPG from Y-$[N_{122,2O1}][BF_4]$. The applied potential on the working electrode was firstly held at the OCP of -0.76 V for 5 s, and then switched to the deposition potential of -2.2 V for 5 s. This 10 s process is a complete cycle for Y deposition, and this cycle was repeated for 200 times. After the deposition, the sample was investigated by ex situ AFM imaging in atmosphere. Y is very sensitive to oxygen and water, especially, when Y is in nanoscale. Even if Y metal was obtained in the deposition process, it could not stay metallically in atmosphere. Therefore, the observed deposits in AFM images should not be the Y metal, but may be yttrium oxide. Figure 6.19 shows the deposits on the HOPG surface. The clusters are higher than 20 nm. As compared with the HOPG substrate, the surface of the deposit is much rougher, as the agglomeration of many small clusters.

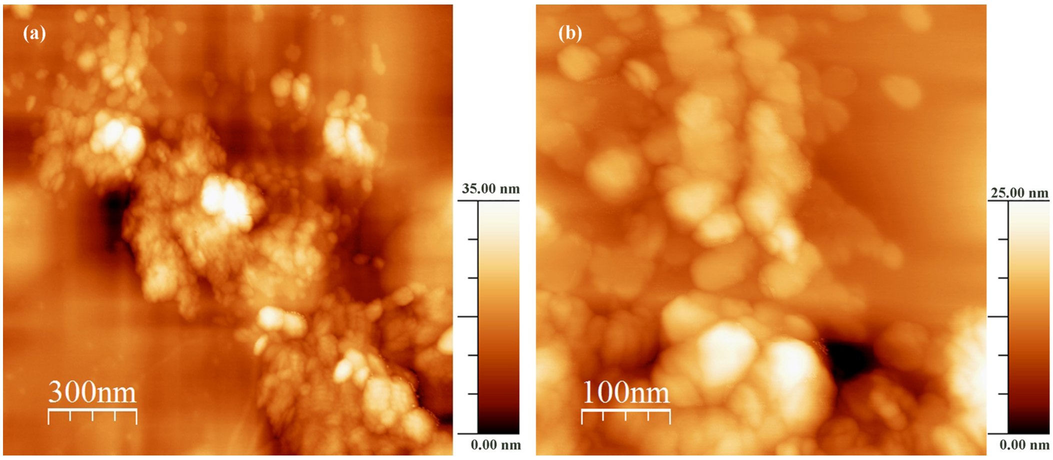

Figure 6.19: AFM images of deposits prepared with the repeated potential steps in Y-$[N_{122,2O1}][BF_4]$.

6.4 Pt-Y codeposition in $[N_{122,2O1}][BF_4]$

The first attempt for Pt-Y codeposition was carried out in $[N_{122,2O1}][BF_4]$ in order to obtain the Pt_xY alloy. Although no evidence can confirm that pure Y metal has been successfully deposited from $[N_{122,2O1}][BF_4]$, the codeposition was worth to try. Because the Pt_xY has a high alloying energy [21], Pt ions in the solution are probably to react with Y ions at a low overpotential to form a Pt_xY alloy. The precursor was prepared by mixing the saturated Pt-$[N_{122,2O1}][BF_4]$ and saturated Y-$[N_{122,2O1}][BF_4]$ at a volume ratio of 1:1. A repeated potential-step method of -0.26 V (5 s) → -1.25 V (5 s) → -2.2 V (5 s) for 200 repeats was applied on the HOPG electrode. The OCP of HOPG in Pt-Y-$[N_{122,2O1}][BF_4]$ is -0.26 V. A negative potential of -1.25 V was applied for the production of Pt^{2+}, which was needed for the further reduction. The deposition potential was selected at -2.2 V, because this potential should be negative enough for both Y and Pt reduction, and the cation decomposition can be avoided. After the codeposition, the sample was characterized with Energy-dispersive X-ray spectroscopy (EDS) in order to determine the elements of the deposit. The result is shown in Figure 6.20. A strong signal of C can be attributed to the HOPG substrate. Y, F and O are observed in the EDS, but the Pt signal is not detected. The disappearance of the Pt signal is difficult to understand. The applied potential is negative enough for the reduction of $PtCl_6{}^{2-}$ to Pt metal, but there is no Pt deposit observed. The existence of $Y(NO_3)_3$ in $[N_{122,2O1}][BF_4]$ may influence the adhesion of Pt metal on HOPG, or even block the Pt deposition. It can also be attributed to the low sensitivity of EDS to extremely small particles. Strong Y signal are detected, which indicates that the deposit contains Y. However, the strong signals of F was unexpected. The O element comes from air when transferring the sample from the glovebox to the vacuum chamber of EDS. The F element indicates that Y^{3+} may react with the F containing in $[N_{122,2O1}][BF_4]$ to form YF_3. The Pt-Y codeposition in $[N_{122,2O1}][BF_4]$ was unsuccessful.

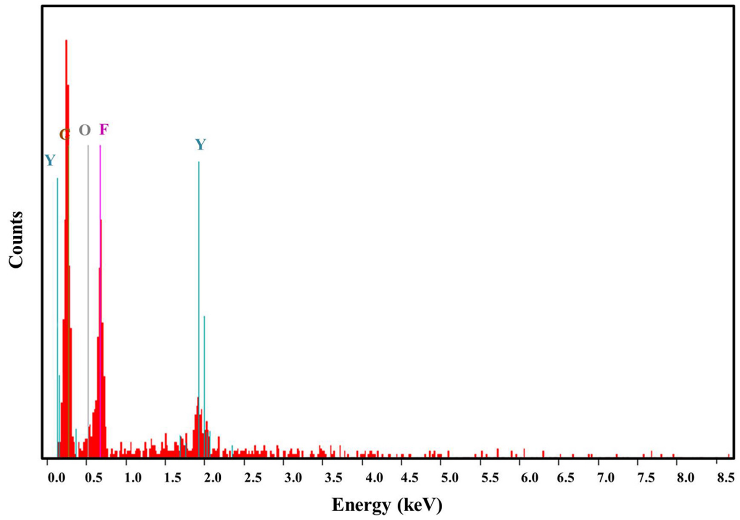

Figure 6.20: EDS spectrum of deposits prepared with the Pt-Y codeposition method. The peaks of Y, C, O and F elements are labeled.

6.5 Summary

Two ILs, [OcMePy][TFSI] and $[N_{122,2O1}][BF_4]$, have been studied for electrochemical deposition of Pt, Y and Pt_xY alloy. The potential windows of [OcMePy][TFSI] and $[N_{122,2O1}][BF_4]$ are 3.45 V and 3.66 V, respectively, which are much broader than the potential window of aqueous solutions.

Until now, significant experience about Pt and Y deposition in both [OcMePy][TFSI] and $[N_{122,2O1}][BF_4]$ has been collected. The deposition of Pt in both ILs can be implemented very well as Pt^{4+} undergoes a two-step process to be reduced to Pt^0. However, the Y deposition in [OcMePy][TFSI] is blocked by the formation a passivation layer. The passivation layer, which forms at a potential lower than -2.0 V in Y-[OcMePy][TFSI], can prevent the further deposition in Y-[OcMePy][TFSI], but, when the passivated electrode is exposed to Pt-[OcMePy][TFSI], the further electrochemical process can happen as normal, which means the passivation layer is not strongly and compactly adhering on the electrode surface. EC-STM cannot image the passivation layer, which from another perspective confirms that the passivation layer covers the electrode surface with a very weak adhesive force. Y deposition in $[N_{122,2O1}][BF_4]$ has resulted in some products, which can be observed in AFM images. However, the EQCM results cannot prove that Y has been deposited on the electrode in the metallic state. The CV profile indicates that Y^{3+} is more like partially reduced to Y^{n+} $(0 < n < 3)$ when the applied potential is lower than -2.0 V.

The first attempt for Pt-Y codeposition has been carried out with a repeated potential-step method in Pt-Y- $[N_{122,2O1}][BF_4]$. After the codeposition, the sample was characterized with EDS to determine the elements of the deposit. In the EDS result, no Pt signal can be detected. Y element can be observed, while the strong signals of O and F cannot be neglected, which means that the deposited Y is not in the metallic state but in the form of YF_3 or Y_2O_3. The attempt for Pt-Y codeposition in $[N_{122,2O1}][BF_4]$ was unsuccessful.

Chapter 7

Conclusions

This thesis focuses on the preparation and characterization of supported NPs in order to obtain model structures and understand the influence of some factors to the electrocatalytic activities for specific reactions. The intrinsic factors (electronic and structural factors) as well as the factors frequently discussed in applications (size and support factors) were considered and discussed in order to achieve a fundamental understanding and to guide the design of active catalysts for applications.

Pd, as a member of PGMs, has a potential to replace Pt as catalysts for electrocatalyzed HER and ORR. In this work, Pd NPs were electrochemically deposited on HOPG by the potentiostatic double-pulse technique in order to obtain model structures. The particle shape on HOPG is approximately hemispherical; the particle size distribution is confined to a relatively narrow range; the particle density for all the samples is in the same order of magnitude. With an approximately constant current during the growth pulse, the particle growth is under hemispherical diffusion control so that the average particle size is proportional to the $\frac{1}{3}$ power of growth time. The particle size can be controlled by the adjustment of growth time. Therefore, the size-dependent activities and properties can be investigated with these samples.

A size-dependent hydrogen content of Pd NPs has been observed when the average size of NPs is smaller than 8 nm. The smaller Pd NPs tend to have a low hydrogen content which can be attributed to the change of lattice structure. The electrocatalytic activity of Pd NPs for HER shows a size-dependence which can be attributed to many factors such as surface structures, lattice constant and composition. In this work, the hydrogen content has been concluded as the most significant factor as a lower hydrogen content in the Pd lattice leads to a smaller lattice extension, as a result, the activity for HER is relatively higher. The size-dependent activity of Pd NPs for ORR has been observed such that the activity becomes lower with the decrease of particle size. According to the Wulff-structure particle, smaller Pd NPs tend to have a higher ratio of edge and corner atoms, which can bond strongly with oxygen atoms leading to a slow reaction rate. The binding strength of CO on Pd NPs increases with the decrease of average particle size, which has been explained by the more closely packed surface and a higher ratio of low-coordinated atoms of the smaller NPs. The analysis of both reactions above suggests that the surface structure of electrochemically deposited Pd NPs can be described with the Wulff-structure particle. The electrochemical properties of the NPs, which are influenced by the structural factors, can be analyzed with this model. In the investigation of activity for FAO, the structural effects are considered as the primary factors so that the decrease of active sites (Pd(100) facet here) leads to the diminishing of current density during the reaction, meanwhile, the increased number of edge and corner atoms causes a more serious CO poisoning. If only considering the performance in activity measurements, the extremely small Pd NPs (at least smaller than 3 nm) are suitable for the application as anodic catalyst in the PEMFC for HER due to their high activity and low ability for hydrogen absorption, but small Pd NPs are not suggested to be cathode catalyst because of the poor activity for ORR. If the CO poisoning should be considered in the reactions, small Pd NPs seems not recommended due to their strong binding with CO molecules. In FAO, the poor activity of small Pd NPs should be paid attention to as well.

The stability tests on Pd NPs at different pH values and at different average size revealed some other issues, which should be considered in addition to the performance in activity. Pd NPs undergo a serious dissolution in a low-pH ($pH < 2$) solution. Small Pd NPs degrade much faster than large ones. The degradation of Pd NPs follows the mechanisms of dissolution, particle detachment and agglomeration as well as Ostwald ripening. In order to obtain a stable Pd NPs decorated electrode, the average Pd NPs size should be large enough (at least larger than 10 nm); and the particle size distribution should be very narrow in order to efficiently reduce the Ostwald ripening. The corrosion of substrate should be taken into account, because it can accelerate the detachment of entire NPs. An effort to enhance the stability of an entire electrode should be made to enhance the stability of both NPs and support.

N-HOPG was used as substrate to investigate the influence of nitrogen functional groups to the activity and stability of supported Pd NPs. Five different nitrogen components have been identified which are sp^2 C-N bonds containing pyridinic, pyrrolic and substantial nitrogen defects, -C≡N terminal groups and trapped nitrogen ions in graphite vacancies. The defects improve the distribution of Pd NPs to be more homogeneous; and more particles can be observed per unit area. The oxidation of metal Pd to Pd^{2+} and even higher oxidation states has been detected by XPS at the interface between Pd NPs and nitrogen-rich surface due to the strong electron withdrawing force of the nitrogen functional group. The existence of oxidized Pd states at the interface lowers the stability of Pd NPs, because the oxidized Pd is vulnerable so that it can be attacked by the acidic solution. Pd NPs on N-HOPG did not show enhanced activity for ORR, which is unlike to Pt NPs. This is explained by the limited operation range of a support effect as the Pd NPs investigated in this work have an average size of around 8 nm, which has exceeded the operation range. Even when the Pd NPs are small enough so that the support effect is able to modify the electronic structures of Pd surface atoms, so that a weaker bond to oxygen atoms can be expected, then the stability issue still limits the application of N-HOPG supported Pd NPs.

Some Pt-REM alloys, such as Pt_3Y, Pt_5Gd, Pt_5La and Pt_5Ce, show high activities for ORR and enhanced stabilities in acidic solutions. Therefore, the synthesis of these Pt-REM alloys with a cheap and scalable method has a promising prospect. In this work, some early-stage investigations of Pt, Y and Pt_xY deposition in ILs were carried out. The electrochemical deposition of Pt can be implemented in both [OcMePy][TFSI] and [$N_{122,2O1}$][BF_4]. Y deposition in [OcMePy][TFSI] is blocked by the formation a passivation layer; and in [$N_{122,2O1}$][BF_4] has resulted in some products, which can be observed in AFM images, but no further evidence can confirm that they are metallic Y. Additional techniques should be involved to understand the reduction process of Y^{3+} in ILs. The potential windows of the used ILs seem not to be wide enough for REMs deposition. Therefore, the development of new ILs with even broader potential windows is necessary. F atoms have been detected in the products from Pt-Y codeposition, which indicates the formation of YF_3. Therefore, other ILs, which do not contain halide atoms, may be better suited solvent for REMs deposition.

a

Appendix A

Symbols and Abbreviations

α_a	Apparent transfer coefficient of an anodic reaction
α_c	Apparent transfer coefficient of a cathodic reaction
a	Activity
A	Frequency factor
β_a	Anodic transfer coefficient
β_c	Cathodic transfer coefficient
C	Concentration
C_{eff}	Effective interfacial capacitance
D	Diffusion coefficient
E	Potential difference at external circuit
E_{00}	Standard potential
E_A	Activation energy
$\Delta E^{\ddagger}$	Standard internal energy of activation
F	Faraday constant
f	Frequency
G_{00}	Standard Gibbs free energy
$\bar{G}$	Gibbs free energy at an equilibrium state
$\Delta G^{\ddagger}$	Standard free energy of activation
η	Overpotential
h	Planck constant
h	Height
$\Delta H^{\ddagger}$	Standard enthalpy of activation
θ	Coverage
i	Current
j	Current density
$\vec{J}$	Mass flux
κ	Transmission coefficient
k	Rate coefficient
k_0	Standard rate coefficient
k_a	Rate coefficient of an anodic reaction
k_c	Rate coefficient of a cathodic reaction

k_B	Boltzmann constant
μ	Chemical potential
$\bar{\mu}$	Electrochemical potential
m	Mass
M	Molar weight
ν	Stoichiometric number
N	Number of moles
ω	Angular frequency
p	Pressure
ρ	Density
Q	Charge
R	Universal gas constant
r	Radius
S	Entropy
$\Delta S^{\ddagger}$	Standard entropy of activation
S	Surface area
T	Temperature
t	Time
υ	Reaction rate
V	Volume
φ	Electrical potential
$\Delta\varphi^{ref}$	Potential drop at a reference electrode
$\Delta\varphi^{m/s}$	Potential drop at a metal-solution interface
$\varphi_{GC}(\sigma, c)$	Potential at the Gouy-Chapman layer
$\varphi_H(\sigma)$	Potential at the Helmholtz layer
z	Number of transferred electrons
Z	Impedance
Au	Gold
Ce	Cerium
CO	Carbon monoxide
CO_2	Carbon dioxide
CO_{ads}	Adsorbed carbon monoxide
$^*COOH$	Carboxylic acid species
Fc	Ferrocene
Gd	Gadolinium
H	Hydrogen atom
H_2	Hydrogen molecule
H_2O	Water
H_2O_2	Hydrogen peroxide
H_{opd}	Overpotential adsorbed hydrogen atom
H_{upd}	Underpotential adsorbed hydrogen atom
$HCOO^*$	Adsorbed formate
$HCOO^-$	Formate ion

HCOOH	Formic acid
La	Lanthanum
O	Oxygen atom
O_2	Oxygen molecule
O_{ads}	Adsorbed oxygen atom
OH_{ads}	Adsorbed hydroxyl
OOH_{ads}	Adsorbed superhydroxyl
Pd	Palladium
Pt	Platinum
Y	Yttrium
2D	Two-dimensional
3D	Three-dimensional
BEP	Brønsted-Evans-Polanyi
CPE	Constant phase element
CV	Cyclic voltammogram
DAFC	Direct alcohol fuel cell
DFAFC	Direct formic acid fuel cell
DFT	Density functional theory
DOE	Department of energy
ECSA	Electrochemically active surface area
EC-STM	Electrochemical scanning tunneling microscopy
EDOS	Electronic density of states
EDS	Energy-dispersive X-ray spectroscopy
emf	Electromotive force
EQCM	Electrochemical quartz crystal microbalance
FAO	Formic acid oxidation
fcc	Face-center-cubic
FWHM	Full width at half maximum
hcp	Hexagonal-close-packing
HER	Hydrogen evolution reaction
HOPG	Highly oriented pyrolytic graphite
HOR	Hydrogen oxidation reaction
IHP	Inner Helmholtz plane
IL	Ionic liquid
MEA	Membrane electrode assembly
NHE	Normal hydrogen electrode
N-HOPG	Nitrogen doped highly oriented pyrolytic graphite
NP	Nanoparticle
OCP	Open circuit potential
OER	Oxygen evolution reaction
OHP	Outer Helmholtz plane
ORR	Oxygen reduction reaction
PEMFC	Proton exchange membrane fuel cell

PES	Potential energy surface
PGM	Platinum-group metals
QRE	Quasi-reference electrode
RDS	Rate-determining step
REM	Rare earth metal
RHE	Reversible hydrogen electrode
RMS	Root-mean-square
SCE	Saturated calomel electrode
SHE	Standard hydrogen electrode
SPM	Scanning probe microscopy
STM	Scanning tunneling microscopy
TM-AFM	Taping-mode atomic force microscopy
UHV	Ultrahigh vacuum
XPS	X-ray photoemission spectroscopy

Appendix B

Publications

Parts of this thesis have been published in the following articles:

[**1**] W. Ju, M. Favaro, C. Durante, L. Perini, S. Agnoli, O. Schneider, U. Stimming, G. Granozzi, Pd Nanoparticles deposited on nitrogen-doped HOPG: New insights into the Pd-catalyzed oxygen reduction reaction, *Electrochimica Acta*, **141**, 89-101, 2014.

[**2**] J. Ma, L. Seidl, W. Ju, E. Mostafa, L. Asen, S. Martens, U. Stimming, O. Schneider, Applications of ionic liquids in electrochemical energy conversion and storage, *ECS Transactions*, **64(4)**, 407-423, 2014.

[**3**] W. Ju, T. Brülle, M. Favaro, L. Perini, C. Durante, O. Schneider, U. Stimming, Palladium nanoparticles supported on highly oriented pyrolytic graphite: Preparation, reactivity and stability, *ChemElectroChem*, **2**, 547-558, 2015.

[**4**] W. Ju, R. Valiollahi, R. Ojani, O. Schneider, U. Stimming, The electrooxidation of formic acid on Pd nanoparticles: an Investigation of size-dependent performance, *Electrocatalysis*, **7**, 149-158, 2016.

Bibliography

[1] J. Tollefson and R. Monastersky. More than ever, nations are powering themselves from abundant supplies of fossil fuels. *Nature*, 491:654–655, 2012.

[2] BPstats. BP statistical review of world energy, 64th edition. Technical report, Economics Team of BP, 2015.

[3] J.G. Olivier, G. Janssens-Maenhout, M. Muntean, and J.A.H.W. Peters. *Trends in global CO2 emissions: 2014 report.* The Hague, 2014.

[4] D. Sperling and D. Gordon. Two billion cars transforming a culture. *TR News*, (259):1–7, 2008.

[5] L.D. Burns. A vision of our transport future. *Nature*, 497:181–182, 2013.

[6] W. Vielstich. *Handbook of Fuel Cells*, volume 1, chapter Ideal and effective efficiencies of cell reactions and comparison to carnot cycles. John Wiley & Sons, Ltd., 2010.

[7] F. Barbir and T. Gómez. Efficiency and economics of proton exchange membrane (PEM) fuel cells. *Int. J. Hydrogen Energy*, 22(10):1027–1037, 1997.

[8] Y. Wang, K. S. Chen, J. Mishler, S. C. Cho, and X. C. Adroher. A review of polymer electrolyte membrane fuel cells: Technology, applications, and needs on fundamental research. *Appl. Energy*, 88(4):981–1007, 2011.

[9] DOE. Fuel cell technologies office multi-year research, development, and demonstration plan. Technical report, Fuel Cell Technologies Office, U.S. Department of Energy, Washington, DC, 2012.

[10] M. K. Debe. Advanced cathode catalysts and supports for PEM fuel cells. Technical report, 3M Company, 2011.

[11] D. Strmcnik, K. Kodama, D. van der Vliet, J. Greeley, V.R. Stamenkovic, and N.M. Marković. The role of non-covalent interactions in electrocatalytic fuel-cell reactions on platinum. *Nat. Chem.*, 1(6):466–472, 2009.

[12] M. T. Koper. Structure sensitivity and nanoscale effects in electrocatalysis. *Nanoscale*, 3:2054–2073, 2011.

[13] A. S. Bandarenka and M.T.M. Koper. Structural and electronic effects in heterogeneous electrocatalysis: Toward a rational design of electrocatalysts. *J. Catal.*, 308:11–24, 2013.

[14] Z. Quan, Y. Wang, and J. Fang. High-index faceted noble metal nanocrystals. *Acc. Chem. Res.*, 46:191–202, 2011.

[15] D.L. Feldheim. The new face of catalysis. *Science*, 316:699–700, 2007.

[16] Z. Y. Zhou, N. Tian, J. T. Li, I. Broadwell, and S. G. Sun. Nanomaterials of high surface energy with exceptional properties in catalysis and energy storage. *Chem. Soc. Rev.*, 40:4167–4185, 2011.

[17] H. Li, F. Calle-Vallejo, M. J. Kolb, Y. Kwon, Y. Li, and M.T.M. Koper. Why (1 0 0) terraces break and make bonds: Oxidation of dimethyl ether on platinum single-crystal electrodes. *J. Am. Chem. Soc.*, 135(38):14329–14338, 2013.

[18] H. Li, Y. Li, M.T.M. Koper, and F. Calle-Vallejo. Bond-making and breaking between carbon, nitrogen, and oxygen in electrocatalysis. *J. Am. Chem. Soc.*, 136(44):15694–15701, 2014.

[19] F. Calle-Vallejo, D. Loffreda, M.T.M. Koper, and P. Sautet. Introducing structural sensitivity into adsorption–energy scaling relations by means of coordination numbers. *Nat. Chem.*, 7(5):403–410, 2015.

[20] P. Sabatier. Hydrogénations et deshydrogénations par catalyse. *Ber Dtsch. Chem. Ges.*, 44(3):1984–2001, 1911.

[21] J. Greeley, I.E.L. Stephens, A.S. Bondarenko, T.P. Johansson, H.A. Hansen, T.F. Jaramillo, J. Rossmeisl, I. Chorkendorff, and J.K. Nørskov. Alloys of platinum and early transition metals as oxygen reduction electrocatalysts. *Nat. Chem.*, 1(7):552–556, 2009.

[22] M. Valden, X. Lai, and D.W. Goodman. Onset of catalytic activity of gold clusters on titania with the appearance of nonmetallic properties. *Science*, 281 (5383):1647–1650, 1998.

[23] B. Yoon, H. Häkkinen, U. Landman, A.S. Wörz, J. Antonietti, S. Abbet, K. Judai, and U. Heiz. Charging effects on bonding and catalyzed oxidation of CO on Au8 clusters on MgO. *Science*, 307(5708):403–407, 2005.

[24] V.R. Stamenkovic, B. Fowler, B.S. Mun, G. Wang, P.N. Ross, C.A. Lucas, and N.M Marković. Improved oxygen reduction activity on Pt3Ni (111) via increased surface site availability. *Science*, 315(5811):493–497, 2007.

[25] J. Greeley, T.F. Jaramillo, J. Bonde, I. Chorkendorff, and J.K. Nørskov. Computational high-throughput screening of electrocatalytic materials for hydrogen evolution. *Nat. Mater.*, 5(11):909–913, 2006.

[26] I.E.L. Stephens, A.S. Bondarenko, F.J. Perez-Alonso, F. Calle-Vallejo, L. Bech, T.P. Johansson, A.K. Jepsen, R. Frydendal, B.P. Knudsen, J. Rossmeisl, and I. Chorkendorff. Tuning the activity of Pt (111) for oxygen electroreduction by subsurface alloying. *J. Am. Chem. Soc.*, 133(14):5485–5491, 2011.

[27] M. Escudero-Escribano, A. Verdaguer-Casadevall, P. Malacrida, U. Grønbjerg, B.P. Knudsen, A.K. Jepsen, J. Rossmeisl, I.E.L. Stephens, and I. Chorkendorff. Pt5Gd as a highly active and stable catalyst for oxygen electroreduction. *J. Am. Chem. Soc.*, 134(40):16476–16479, 2012.

[28] I.E.L. Stephens, A.S. Bondarenko, U. Grønbjerg, J. Rossmeisl, and I. Chorkendorff. Understanding the electrocatalysis of oxygen reduction on platinum and its alloys. *Energy & Environmental Science*, 5(5):6744–6762, 2012.

[29] P. Malacrida, M. Escudero-Escribano, A. Verdaguer-Casadevall, I.E.L. Stephens, and I. Chorkendorff. Enhanced activity and stability of Pt–La and Pt–Ce alloys for oxygen electroreduction: the elucidation of the active surface phase. *J. Mater. Chem.A*, 2(12):4234–4243, 2014.

[30] B.E. Hayden. Particle size and support effects in electrocatalysis. *Acc. Chem. Res.*, 46(8):1858–1866, 2013.

[31] H.A. Gasteiger, J.E. Panels, and S.G. Yan. Dependence of PEM fuel cell performance on catalyst loading. *J. Power Sources*, 127(1):162–171, 2004.

[32] M. Shao. Palladium-based electrocatalysts for hydrogen oxidation and oxygen reduction reactions. *J. Power Sources*, 196(5):2433–2444, 2011.

[33] A. Sarapuu, A. Kasikov, N. Wong, C.A. Lucas, G. Sedghi, R.J. Nichols, and K. Tammeveski. Electroreduction of oxygen on gold-supported nanostructured palladium films in acid solutions. *Electrochim. Acta*, 55(22):6768–6774, 2010.

[34] H. Erikson, A. Kasikov, C. Johans, K. Kontturi, K. Tammeveski, and A. Sarapuu. Oxygen reduction on nafion-coated thin-film palladium electrodes. *J. Electroanal. Chem.*, 652(1):1–7, 2011.

[35] A. Anastasopoulos, J.C. Davies, L. Hannah, B.E. Hayden, C.E. Lee, C. Milhano, C. Mormiche, and L. Offin. The particle size dependence of the oxygen reduction reaction for carbon-supported platinum and palladium. *ChemSusChem*, 6(10): 1973–1982, 2013.

[36] W. Zhou, M. Li, O.L. Ding, S.H. Chan, L. Zhang, and Y. Xue. Pd particle size effects on oxygen electrochemical reduction. *Int. J. Hydrogen Energy*, 39 (12):6433–6442, 2014.

[37] W.P. Zhou, A. Lewera, R. Larsen, R.I. Masel, P.S. Bagus, and A. Wieckowski. Size effects in electronic and catalytic properties of unsupported palladium nanoparticles in electrooxidation of formic acid. *J. Phys. Chem. B*, 110(27): 13393–13398, 2006.

[38] W. Zhou and J.Y. Lee. Particle size effects in pd-catalyzed electrooxidation of formic acid. *J. Phys. Chem. C*, 112(10):3789–3793, 2008.

[39] Y. Suo and I.M. Hsing. Size-controlled synthesis and impedance-based mechanistic understanding of Pd/C nanoparticles for formic acid oxidation. *Electrochim. Acta*, 55(1):210–217, 2009.

[40] T. Brülle and U. Stimming. Platinum nanostructured HOPG–preparation, characterization and reactivity. *J. Electroanal. Chem.*, 636(1):10–17, 2009.

[41] T. Brülle, W. Ju, P. Niedermayr, A. Denisenko, O. Paschos, O. Schneider, and U. Stimming. Size-dependent electrocatalytic activity of gold nanoparticles on HOPG and highly boron-doped diamond surfaces. *Molecules*, 16(12):10059–10077, 2011.

[42] W. Ju, T. Brülle, M. Favaro, L. Perini, C. Durante, O. Schneider, and U. Stimming. Palladium nanoparticles supported on highly oriented pyrolytic graphite: Preparation, reactivity and stability. *ChemElectroChem*, 2(4):547–558, 2015.

[43] J.V. Zoval, J. Lee, S. Gorer, and R.M. Penner. Electrochemical preparation of platinum nanocrystallites with size selectivity on basal plane oriented graphite surfaces. *J. Phys. Chem. B*, 102(7):1166–1175, 1998.

[44] H. Liu, F. Favier, K. Ng, M.P. Zach, and R.M. Penner. Size-selective electrodeposition of meso-scale metal particles: a general method. *Electrochim. Acta*, 47 (5):671–677, 2001.

[45] R.M. Penner. Mesoscopic metal particles and wires by electrodeposition. *J. Phys. Chem. B*, 106(13):3339–3353, 2002.

[46] M. Ueda, H. Dietz, A. Anders, H. Kneppe, A. Meixner, and W. Plieth. Double-pulse technique as an electrochemical tool for controlling the preparation of metallic nanoparticles. *Electrochim. Acta*, 48(4):377–386, 2002.

[47] T. Maoka and M. Enyo. Hydrogen absorption by palladium electrode polarized in sulfuric acid solution containing surface active substances-I. the cathodic region. *Electrochim. Acta*, 26(5):607–614, 1981.

[48] B.R. Cuenya. Synthesis and catalytic properties of metal nanoparticles: Size, shape, support, composition, and oxidation state effects. *Thin Solid Films*, 518 (12):3127–3150, 2010.

[49] N.M. Marković and P.N. Ross. Surface science studies of model fuel cell electrocatalysts. *Surf. Sci. Rep.*, 45(4):117–229, 2002.

[50] B. Hammer and J.K. Nørskov. Theoretical surface science and catalysis-calculations and concepts. *Adv. Catal.*, 45:71–129, 2000.

[51] L.A. Kibler, A.M. El-Aziz, and D.M. Kolb. Electrochemical behaviour of pseudomorphic overlayers: Pd on Au (1 1 1). *J. Mol. Catal. A: Chem.*, 199(1): 57–63, 2003.

[52] S. Pandelov and U. Stimming. Reactivity of monolayers and nano-islands of palladium on Au (111) with respect to proton reduction. *Electrochim. Acta*, 52 (18):5548–5555, 2007.

[53] P. Quaino, E. Santos, H. Wolfschmidt, M.A. Montero, and U. Stimming. Theory meets experiment: electrocatalysis of hydrogen oxidation/evolution at Pd–Au nanostructures. *Catal. Today*, 177(1):55–63, 2011.

[54] Y. Zhou, R. Pasquarelli, T. Holme, J. Berry, D. Ginley, and R. O'Hayre. Improving pem fuel cell catalyst activity and durability using nitrogen-doped carbon supports: observations from model Pt/HOPG systems. *J. Mater. Chem.*, 19(42):7830–7838, 2009.

[55] T. Holme, Y. Zhou, R. Pasquarelli, and R. O'Hayre. First principles study of doped carbon supports for enhanced platinum catalysts. *Phys. Chem. Chem. Phys.*, 12(32):9461–9468, 2010.

[56] Y. Zhou, T. Holme, J. Berry, T.R. Ohno, D. Ginley, and R. O'Hayre. Dopant-induced electronic structure modification of HOPG surfaces: implications for high activity fuel cell catalysts. *J. Phys. Chem. C*, 114(1):506–515, 2009.

[57] M. Shao, P. Liu, J. Zhang, and R. Adzic. Origin of enhanced activity in palladium alloy electrocatalysts for oxygen reduction reaction. *J. Phys. Chem. B*, 111(24):6772–6775, 2007.

[58] P. Hernandez-Fernandez, F. Masini, D.N. McCarthy, C.E. Strebell, D. Friebel, D. Deiana, P. Malacrida, et al. Mass-selected nanoparticles of PtxY as model catalysts for oxygen electroreduction. *Nat. Chem.*, 6:732–738, 2014.

[59] A. Velázquez-Palenzuela, F. Masini, A.F. Pedersen, M. Escudero-Escribano, D. Deiana, P. Malacrida, T.W. Hansen, D. Friebel, A. Nilsson, I.E.L. Stephens, and I. Chorkendorff. The enhanced activity of mass-selected PtxGd nanoparticles for oxygen electroreduction. *J. Catal.*, 328:297–307, 2015.

[60] A.J. Bard and L.R. Faulkner. *Electrochemical methods: fundamentals and applications (2nd Ed.)*. Wiley New York, 2000.

[61] F. Endres. Ionic liquids: solvents for the electrodeposition of metals and semiconductors. *ChemPhysChem*, 3(2):144–154, 2002.

[62] F. Endres, D. MacFarlane, and A. Abbott. *Electrodeposition from ionic liquids*. John Wiley & Sons, 2008.

[63] B. Dilasari, K. Kwon, C.K. Lee, and H. Kim. Electrodeposition of some selective metals belonging to light, refractory and noble metals from ionic liquid electrolytes. *J. Korean Electrochem. Soc.*, 15(3):135–148, 2012.

[64] A. Ispas and A. Bund. Electrodeposition in ionic liquids. *Electrochem. Soc. Interface*, Spring:47–51, 2014.

[65] H. von Helmholtz. Ueber einige Gesetze der Vertheilung elektrischer Ströme in körperlichen Leitern, mit Anwendung auf die thierisch-elektrischen Versuche (Schluss.). *Ann. Phys.*, 165(7):353–377, 1853.

[66] M. Gouy. Sur la constitution de la charge electrique a la surface d'un electrolyte. *J. Phys. Theor. Appl.*, 9(1):457–468, 1910.

[67] D.L. Chapman. Li. a contribution to the theory of electrocapillarity. *The London, Edinburgh, and Dublin Philosophical Magazine and Journal of Science*, 25(148):475–481, 1913.

[68] O. Stern. Zur Theorie der elektrolytischen Doppelschicht. *Z. Elektrochem. Angew. P.*, 30(21-22):508–516, 1924.

[69] D.C. Grahame. The electrical double layer and the theory of electrocapillarity. *Chem. Rev.*, 41(3):441–501, 1947.

[70] O.A. Petrii and G.A. Tsirlina. *Electrode Potentials*, volume 1, chapter 1, pages 3–23. Wiley-VCH, 2002.

[71] L. Meites. *Handbook of Analytical Chemistry.* McGraw-Hill Inc., 1st edition, 1963.

[72] R.R. Gagne, C.A. Koval, and G.C. Lisensky. Ferrocene as an internal standard for electrochemical measurements. *Inorg. Chem.*, 19(9):2854–2855, 1980.

[73] G. Inzelt. *Handbook of Reference Electrodes*, chapter Pseudo-reference electrodes, pages 331–332. Springer, 2013.

[74] J.K. Nørskov, F. Studt, F. Abild-Pedersen, and T. Bligaard. *Fundamental concepts in heterogeneous catalysis.* John Wiley & Sons, 2014.

[75] H. Eyring. The activated complex in chemical reactions. *J. Chem. Phys.*, 3(2): 107–115, 1935.

[76] J.K. Nørskov, J. Rossmeisl, A. Logadottir, L. Lindqvist, J.R. Kitchin, T. Bligaard, and H. Jonsson. Origin of the overpotential for oxygen reduction at a fuel-cell cathode. *J. Phys. Chem. B*, 108(46):17886–17892, 2004.

[77] J.O'M. Bockris and Z. Nagy. Symmetry factor and transfer coefficient. a source of confusion in electrode kinetics. *J. Chem. Educ.*, 50(12):839, 1973.

[78] I. Streeter and R.G. Compton. Diffusion-limited currents to nanoparticles of various shapes supported on an electrode; spheres, hemispheres, and distorted spheres and hemispheres. *J. Phys. Chem. C*, 111(49):18049–18054, 2007.

[79] T.J. Davies, C.E. Banks, and R.G. Compton. Voltammetry at spatially heterogeneous electrodes. *J. Solid. State. Electrochem.*, 9(12):797–808, 2005.

[80] I. Streeter, R. Baron, and R. G. Compton. Voltammetry at nanoparticle and microparticle modified electrodes: theory and experiment. *J. Phys. Chem. C*, 111(45):17008–17014, 2007.

[81] C.H. Hamann, A. Hamnett, and W. Vielstich. *Electrochemistry.* Wiley-VCH, 2nd edition, 2007.

[82] B.E. Conway and B.V. Tilak. Interfacial processes involving electrocatalytic evolution and oxidation of H2, and the role of chemisorbed H. *Electrochim. Acta*, 47(22):3571–3594, 2002.

[83] R. Parsons. The rate of electrolytic hydrogen evolution and the heat of adsorption of hydrogen. *Trans. Faraday Soc.*, 54:1053–1063, 1958.

[84] P. Dabo, L. Brossard, H. Me, P. Tremblay, et al. Hydrogen activation of spectroscopic graphite surface by argon plasma etching. *J. Appl. Electrochem.*, 28(6):601–606, 1998.

[85] N.M. Marković, B.N. Grgur, and P.N. Ross. Temperature-dependent hydrogen electrochemistry on platinum low-index single-crystal surfaces in acid solutions. *J. Phys. Chem. B*, 101(27):5405–5413, 1997.

[86] S. Trasatti. Work function, electronegativity, and electrochemical behaviour of metals: III. electrolytic hydrogen evolution in acid solutions. *J. Electroanal. Chem. Interfacial Electrochem.*, 39(1):163–184, 1972.

[87] N.M. Marković, C.A. Lucas, V. Climent, V. Stamenkovic, and P.N. Ross. Surface electrochemistry on an epitaxial palladium film on Pt (111): surface microstructure and hydrogen electrode kinetics. *Surf. Sci.*, 465(1-2):103–114, 2000.

[88] H.S. Wroblowa, Y.C. Pan, and G. Razumney. Electroreduction of oxygen: a new mechanistic criterion. *J. Electroanal. Chem. Interfacial Electrochem.*, 69 (2):195–201, 1976.

[89] A. Frumkin. Hydrogen overvoltage and the structure of the double layer. *Z. Physik. Chem. A*, 164:121–133, 1933.

[90] P.N. Ross. Oxygen reduction reaction on smooth single crystal electrodes. *Handbook of Fuel Cells*, 2010.

[91] M. Grdeń, M. Łukaszewski, G. Jerkiewicz, and A. Czerwiński. Electrochemical behaviour of palladium electrode: oxidation, electrodissolution and ionic adsorption. *Electrochim. Acta*, 53(26):7583–7598, 2008.

[92] N. Wakabayashi, M. Takeichi, M. Itagaki, H. Uchida, and M. Watanabe. Temperature-dependence of oxygen reduction activity at a platinum electrode in an acidic electrolyte solution investigated with a channel flow double electrode. *J. Electroanal. Chem.*, 574(2):339–346, 2005.

[93] H. Erikson, M. Liik, A. Sarapuu, J. Kozlova, V. Sammelselg, and K. Tammeveski. Oxygen reduction on electrodeposited pd coatings on glassy carbon. *Electrochim. Acta*, 88:513–518, 2013.

[94] C. Song and J. Zhang. *PEM fuel cell electrocatalysts and catalyst layers*, chapter Electrocatalytic oxygen reduction reaction, pages 89–134. Springer, 2008.

[95] C. Song, Y. Tang, J. Zhang, J. Zhang, H. Wang, J. Shen, S. McDermid, J. Li, and P. Kozak. PEM fuel cell reaction kinetics in the temperature range of 23–120 °c. *Electrochim. Acta*, 52(7):2552–2561, 2007.

[96] A. Damjanovic and V. Brusić. Oxygen reduction at Pt-Au and Pd-Au alloy electrodes in acid solution. *Electrochim. Acta*, 12(9):1171–1184, 1967.

[97] S. Kondo, M. Nakamura, N. Maki, and N. Hoshi. Active sites for the oxygen reduction reaction on the low and high index planes of palladium. *J. Phys. Chem. C*, 113(29):12625–12628, 2009.

[98] A. Hitotsuyanagi, S. Kondo, M. Nakamura, and N. Hoshi. Structural effects on the oxygen reduction reaction on n (111)–(100) series of Pd. *J. Electroanal. Chem.*, 657(1):123–127, 2011.

[99] A.K. Santra and D.W. Goodman. Catalytic oxidation of CO by platinum group metals: From ultrahigh vacuum to elevated pressures. *Electrochim. Acta*, 47(22):3595–3609, 2002.

[100] T.H.M. Housmans, C.G.M. Hermse, and M.T.M. Koper. CO oxidation on stepped single crystal electrodes: A dynamic monte carlo study. *J. Electroanal. Chem.*, 607(1):69–82, 2007.

[101] C.D. Zeinalipour-Yazdi, D.J. Willock, L. Thomas, K. Wilson, and A.F. Lee. CO adsorption over Pd nanoparticles: A general framework for IR simulations on nanoparticles. *Surf. Sci.*, 646:210–220, 2016.

[102] X. Yu and P.G. Pickup. Recent advances in direct formic acid fuel cells (DFAFC). *J. Power Sources*, 182(1):124–132, 2008.

[103] C. Rice, S. Ha, R.I. Masel, P. Waszczuk, A. Wieckowski, and T. Barnard. Direct formic acid fuel cells. *J. Power Sources*, 111(1):83–89, 2002.

[104] C. Rice, S. Ha, R.I. Masel, and A. Wieckowski. Catalysts for direct formic acid fuel cells. *J. Power Sources*, 115(2):229–235, 2003.

[105] A. Capon and R. Parson. The oxidation of formic acid at noble metal electrodes: I. review of previous work. *J. Electroanal. Chem. Interfacial Electrochem.*, 44 (1):1–7, 1973.

[106] A. Capon and R. Parsons. The oxidation of formic acid on noble metal electrodes: II. a comparison of the behaviour of pure electrodes. *J. Electroanal. Chem. Interfacial Electrochem.*, 44(2):239–254, 1973.

[107] A. Capon and R. Parsons. The oxidation of formic acid at noble metal electrodes part III. intermediates and mechanism on platinum electrodes. *J. Electroanal. Chem. Interfacial Electrochem.*, 45(2):205–231, 1973.

[108] S.G. Sun, J. Clavilier, and A. Bewick. The mechanism of electrocatalytic oxidation of formic acid on Pt (100) and Pt (111) in sulphuric acid solution: an emirs study. *J. Electroanal. Chem. Interfacial Electrochem.*, 240(1-2):147–159, 1988.

[109] J. Lipkowski and P.N. Ross. *Electrocatalysis.* Wiley-VCH, 1998.

[110] A. Miki, S. Ye, and M. Osawa. Surface-enhanced IR absorption on platinum nanoparticles: an application to real-time monitoring of electrocatalytic reactions. *Chem. Commun.*, (14):1500–1501, 2002.

[111] H. Miyake, T. Okada, G. Samjeské, and M. Osawa. Formic acid electrooxidation on Pd in acidic solutions studied by surface-enhanced infrared absorption spectroscopy. *Phys. Chem. Chem. Phys.*, 10(25):3662–3669, 2008.

[112] G. Samjeské and M. Osawa. Current oscillations during formic acid oxidation on a Pt electrode: Insight into the mechanism by time-resolved IR spectroscopy. *Angew. Chem. Int. Ed.*, 117(35):5840–5844, 2005.

[113] G. Samjeské, A. Miki, S. Ye, and M. Osawa. Mechanistic study of electrocatalytic oxidation of formic acid at platinum in acidic solution by time-resolved surface-enhanced infrared absorption spectroscopy. *J. Phys. Chem. B*, 110(33): 16559–16566, 2006.

[114] M. Osawa, K. Komatsu, G. Samjeské, T. Uchida, T. Ikeshoji, A. Cuesta, and C. Gutiérrez. The role of bridge-bonded adsorbed formate in the electrocatalytic oxidation of formic acid on platinum. *Angew. Chem. Int. Ed.*, 50(5):1159–1163, 2011.

[115] A. Cuesta, G. Cabello, C. Gutiérrez, and M. Osawa. Adsorbed formate: the key intermediate in the oxidation of formic acid on platinum electrodes. *Phys. Chem. Chem. Phys.*, 13(45):20091–20095, 2011.

[116] A. Cuesta, G. Cabello, M. Osawa, and C. Gutieérrez. Mechanism of the electrocatalytic oxidation of formic acid on metals. *ACS Catal.*, 2(5):728–738, 2012.

[117] Y. Chen, S. Ye, M. Heinen, Z. Jusys, M. Osawa, and R.J. Behm. Application of in-situ attenuated total reflection-fourier transform infrared spectroscopy for the understanding of complex reaction mechanism and kinetics: formic acid oxidation on a Pt film electrode at elevated temperatures. *J. Phys. Chem. B*, 110(19):9534–9544, 2006.

[118] Y.X. Chen, M. Heinen, Z. Jusys, and R.J. Behm. Bridge-bonded formate: active intermediate or spectator species in formic acid oxidation on a Pt film electrode? *Langmuir*, 22(25):10399–10408, 2006.

[119] Y.X. Chen, M. Heinen, Z. Jusys, and R. J. Behm. Kinetics and mechanism of the electrooxidation of formic acid - spectroelectrochemical studies in a flow cell. *Angew. Chem. Int. Ed.*, 45(6):981–985, 2006.

[120] Y. Chen, M. Heinen, Z. Jusys, and R.J. Behm. Kinetic isotope effects in complex reaction networks: Formic acid electro-oxidation. *ChemPhysChem*, 8 (3):380–385, 2007.

[121] M. Neurock, M. Janik, and A. Wieckowski. A first principles comparison of the mechanism and site requirements for the electrocatalytic oxidation of methanol and formic acid over Pt. *Faraday Discuss.*, 140:363–378, 2009.

[122] J. Joo, T. Uchida, A. Cuesta, M.T.M. Koper, and M. Osawa. Importance of acid–base equilibrium in electrocatalytic oxidation of formic acid on platinum. *J. Am. Chem. Soc.*, 135(27):9991–9994, 2013.

[123] J. Joo, T. Uchida, A. Cuesta, M.T.M. Koper, and M. Osawa. The effect of pH on the electrocatalytic oxidation of formic acid/formate on platinum: A mechanistic study by surface-enhanced infrared spectroscopy coupled with cyclic voltammetry. *Electrochim. Acta*, 129:127–136, 2014.

[124] K. Jiang, H. Zhang, S. Zou, and W. Cai. Electrocatalysis of formic acid on palladium and platinum surfaces: from fundamental mechanisms to fuel cell applications. *Phys. Chem. Chem. Phys.*, 16(38):20360–20376, 2014.

[125] A. Cuesta, M. Escudero, B. Lanova, and H. Baltruschat. Cyclic voltammetry, ftirs, and dems study of the electrooxidation of carbon monoxide, formic acid, and methanol on cyanide-modified Pt (111) electrodes. *Langmuir*, 25(11): 6500–6507, 2009.

[126] Y. Yang, Z. Zhou, and S. Sun. In situ FTIRS studies of kinetics of HCOOH oxidation on Pt (110) electrode modified with antimony adatoms. *J. Electroanal. Chem.*, 500(1):233–240, 2001.

[127] S. Chang, Y. Ho, and M.J. Weaver. Applications of real-time infrared spectroscopy to electrocatalysis at bimetallic surfaces: I. electrooxidation of formic acid and methanol on bismuth-modified Pt (111) and Pt (100). *Surf. Sci.*, 265 (1):81–94, 1992.

[128] R. Zhang, H. Liu, B. Wang, and L. Ling. Insights into the preference of CO2 formation from HCOOH decomposition on Pd surface: a theoretical study. *J. Phys. Chem. C*, 116(42):22266–22280, 2012.

[129] X. Yu and P.G. Pickup. Mechanistic study of the deactivation of carbon supported Pd during formic acid oxidation. *Electrochem. Commun.*, 11(10): 2012–2014, 2009.

[130] J. Wang, H. Zhang, K. Jiang, and W. Cai. From HCOOH to CO at Pd electrodes: a surface-enhanced infrared spectroscopy study. *J. Am. Chem. Soc.*, 133(38):14876–14879, 2011.

[131] M.D. Obradović and S.L. Gojković. HCOOH oxidation on thin Pd layers on Au: Self-poisoning by the subsequent reaction of the reaction product. *Electrochim. Acta*, 88:384–389, 2013.

[132] C. Buzea, I.I. Pacheco, and K. Robbie. Nanomaterials and nanoparticles: sources and toxicity. *Biointerphases*, 2(4):MR17–MR71, 2007.

[133] S. Eustis and M.A. El-Sayed. Why gold nanoparticles are more precious than pretty gold: noble metal surface plasmon resonance and its enhancement of the radiative and nonradiative properties of nanocrystals of different shapes. *Chem. Soc. Rev.*, 35(3):209–217, 2006.

[134] P. Buffat and J.P. Borel. Size effect on the melting temperature of gold particles. *Phys. Rev. A*, 13(6):2287, 1976.

[135] N. Hoshi, K. Kida, M. Nakamura, M. Nakada, and K. Osada. Structural effects of electrochemical oxidation of formic acid on single crystal electrodes of palladium. *J. Phys. Chem. B*, 110(25):12480–12484, 2006.

[136] M. Shao, J. Odell, M. Humbert, T. Yu, and Y. Xia. Electrocatalysis on shape-controlled palladium nanocrystals: Oxygen reduction reaction and formic acid oxidation. *J. Phys. Chem. C*, 117(8):4172–4180, 2013.

[137] H. Erikson, A. Sarapuu, N. Alexeyeva, K. Tammeveski, J. Solla-Gullón, and J.M. Feliu. Electrochemical reduction of oxygen on palladium nanocubes in acid and alkaline solutions. *Electrochim. Acta*, 59:329–335, 2012.

[138] R. A. Van Santen. Complementary structure sensitive and insensitive catalytic relationships. *Acc. Chem. Res.*, 42(1):57–66, 2008.

[139] O. Kitakami, H. Sato, Y. Shimada, F. Sato, and M. Tanaka. Size effect on the crystal phase of cobalt fine particles. *Phys. Rev. B*, 56(21):13849, 1997.

[140] G.A. Tritsaris, J. Greeley, J. Rossmeisl, and J.K. Nørskov. Atomic-scale modeling of particle size effects for the oxygen reduction reaction on Pt. *Catal. Lett.*, 141(7):909–913, 2011.

[141] L.A. Kibler, A.M. El-Aziz, R. Hoyer, and D.M. Kolb. Tuning reaction rates by lateral strain in a palladium monolayer. *Angew. Chem. Int. Ed.*, 44(14): 2080–2084, 2005.

[142] M.H. Shao, T. Huang, P. Liu, J. Zhang, K. Sasaki, M.B. Vukmirovic, and R.R. Adzic. Palladium monolayer and palladium alloy electrocatalysts for oxygen reduction. *Langmuir*, 22(25):10409–10415, 2006.

[143] V.R. Stamenkovic, B.S. Mun, K.J.J. Mayrhofer, P.N. Ross, and N.M. Marković. Effect of surface composition on electronic structure, stability, and electrocatalytic properties of Pt-transition metal alloys: Pt-skin versus Pt-skeleton surfaces. *J. Am. Chem. Soc.*, 128(27):8813–8819, 2006.

[144] H. Hoster, B. Richter, and R.J. Behm. Catalytic influence of Pt monolayer islands on the hydrogen electrochemistry of Ru (0001) studied by ultrahigh vacuum scanning tunneling microscopy and cyclic voltammetry. *J. Phys. Chem. B*, 108(38):14780–14788, 2004.

[145] L.K. Ono and B. Roldan Cuenya. Formation and thermal stability of Au2O3 on gold nanoparticles: size and support effects. *J. Phys. Chem. C.*, 112(12): 4676–4686, 2008.

[146] J.C. Meier, C. Galeano, I. Katsounaros, J. Witte, H.J. Bongard, A.A. Topalov, C. Baldizzone, S. Mezzavilla, F. Schüth, and K.J.J. Mayrhofer. Design criteria for stable Pt/C fuel cell catalysts. *Beilstein J. Nanotechnol.*, 5(1):44–67, 2014.

[147] G. García and M. Koper. Carbon monoxide oxidation on pt single crystal electrodes: understanding the catalysis for low temperature fuel cells. *ChemPhysChem*, 12(11):2064–2072, 2011.

[148] M. Hara, U. Linke, and Th. Wandlowski. Preparation and electrochemical characterization of palladium single crystal electrodes in 0.1 M H2SO4 and HClO4: Part I. low-index phases. *Electrochim. Acta*, 52(18):5733–5748, 2007.

[149] F. Maillard, M. Eikerling, O.V. Cherstiouk, S. Schreier, E. Savinova, and U. Stimming. Size effects on reactivity of Pt nanoparticles in CO monolayer oxidation: The role of surface mobility. *Faraday Discuss.*, 125:357–377, 2004.

[150] H. Ohno, editor. *Electrochemical aspects of ionic liquids.* John Wiley & Sons, 2011.

[151] M.T. Carter, C.L. Hussey, S.K.D. Strubinger, and R.A. Osteryoung. Electrochemical reduction of dioxygen in room-temperature imidazolium chloride-aluminum chloride molten salts. *Inorg. Chem.*, 30(5):1149–1151, 1991.

[152] Y. Katayama, H. Onodera, M. Yamagata, and T. Miura. Electrochemical reduction of oxygen in some hydrophobic room-temperature molten salt systems. *J. Electrochem. Soc.*, 151(1):A59–A63, 2004.

[153] M. Lipsztajn and R.A. Osteryoung. Electrochemical reduction of N-(1-butyl) pyridinium cation in 1-methyl-3-ethylimidazolium chloride-aluminium chloride ambient temperature ionic liquids. *Electrochim. Acta*, 29(10):1349–1352, 1984.

[154] L. Xiao and K.E. Johnson. Electrochemistry of 1-butyl-3-methyl-1H-imidazolium tetrafluoroborate ionic liquid. *J. Electrochem. Soc.*, 150(6):E307–E311, 2003.

[155] B.J. Piersma, D.M. Ryan, E.R. Schumacher, and T.L. Riechel. Electrodeposition and stripping of lithium and sodium on inert electrodes in room temperature chloroaluminate molten salts. *J. Electrochem. Soc.*, 143(3):908–913, 1996.

[156] K. Kim, C. Lang, R. Moulton, and P.A. Kohl. Electrochemical investigation of quaternary ammonium/aluminum chloride ionic liquids. *J. Electrochem. Soc.*, 151(8):A1168–A1172, 2004.

[157] D. Aurbach, R. Turgeman, O. Chusid, and Y. Gofer. Spectroelectrochemical studies of magnesium deposition by in situ FTIR spectroscopy. *Electrochem. Commun.*, 3(5):252–261, 2001.

[158] C. Liebenow, Z. Yang, and P. Lobitz. The electrodeposition of magnesium using solutions of organomagnesium halides, amidomagnesium halides and magnesium organoborates. *Electrochem. Commun.*, 2(9):641–645, 2000.

[159] S.Z. El Abedin, H.K. Farag, E.M. Moustafa, U. Welz-Biermann, and F. Endres. Electroreduction of tantalum fluoride in a room temperature ionic liquid at variable temperatures. *Phys. Chem. Chem. Phys.*, 7(11):2333–2339, 2005.

[160] S. Legeai, S. Diliberto, N. Stein, C. Boulanger, J. Estager, N. Papaiconomou, and M. Draye. Room-temperature ionic liquid for lanthanum electrodeposition. *Electrochem. Commun.*, 10(11):1661–1664, 2008.

[161] Y. Pan and C.L. Hussey. Electrochemical and spectroscopic investigation of Ln^{3+} (Ln= Sm, Eu, and Yb) solvation in bis(trifluoromethylsulfonyl) imide-based ionic liquids and coordination by N, N, N', N'-tetraoctyl-3-oxa-pentane diamide (TODGA) and chloride. *Inorg. Chem.*, 52(6):3241–3252, 2013.

[162] L.H. Chou, W.E. Cleland Jr, and C.L. Hussey. Electrochemical and spectroscopic study of Ce (III) coordination in the 1-butyl-3-methylpyrrolidinium bis (trifluoromethylsulfonyl) imide ionic liquid containing chloride ion. *Inorg. Chem.*, 51(21):11450–11457, 2012.

[163] L.H. Chou and C.L. Hussey. An electrochemical and spectroscopic study of Nd (III) and Pr (III) coordination in the 1-butyl-1-methylpyrrolidinium bis (trifluoromethylsulfonyl) imide ionic liquid containing chloride ion. *Inorg. Chem.*, 53(11):5750–5758, 2014.

[164] D. Usachov, O. Vilkov, A. Gruneis, D. Haberer, A. Fedorov, V.K. Adamchuk, A.B. Preobrajenski, P. Dudin, A. Barinov, M. Oehzelt, et al. Nitrogen-doped graphene: efficient growth, structure, and electronic properties. *Nano Lett.*, 11 (12):5401–5407, 2011.

[165] M. Favaro, L. Perini, S. Agnoli, C. Durante, G. Granozzi, and A. Gennaro. Electrochemical behavior of N and Ar implanted highly oriented pyrolytic graphite substrates and activity toward oxygen reduction reaction. *Electrochim. Acta*, 88:477–487, 2013.

[166] N. Hellgren, J. Guo, Y. Luo, C. Såthe, A. Agui, S. Kashtanov, J. Nordgren, H. Ågren, and J.E. Sundgren. Electronic structure of carbon nitride thin films studied by X-ray spectroscopy techniques. *Thin Solid Films*, 471(1):19–34, 2005.

[167] G. Sauerbrey. Verwendung von Schwingquarzen zur Wägung dünner Schichten und zur Mikrowägung. *Z. Physik*, 155(2):206–222, 1959.

[168] S. Martens. *Ultrasound supported electrodeposition of metals and preparation of metal/ceramic composites, colloidal nanoparticles and oxide materials.* PhD thesis, Clausthal University of Technology, 2011.

[169] A. Bund and G. Schwitzgebel. Investigations on metal depositions and dissolutions with an improved eqcmb based on quartz crystal impedance measurements. *Electrochim. Acta*, 45(22):3703–3710, 2000.

[170] L. Daikhin, E. Gileadi, G. Katz, V. Tsionsky, M. Urbakh, and D. Zagidulin. Influence of roughness on the admittance of the quartz crystal microbalance immersed in liquids. *Anal. Chem.*, 74(3):554–561, 2002.

[171] R. Lucklum, C. Behling, and P. Hauptmann. Gravimetric and non-gravimetric chemical quartz crystal resonators. *Sens. Actuators, B*, 65(1):277–283, 2000.

[172] I. Horcas, R. Fernández, J.M. Gomez-Rodriguez, J. Colchero, J.W.S.X.M. Gómez-Herrero, and A.M. Baro. WSXM: a software for scanning probe microscopy and a tool for nanotechnology. *Rev. Sci. Instrum.*, 78(1):013705, 2007.

[173] R.W.M. Kwok. XPS peak fitting program for WIN95/98 XPSPEAK version 4.1. Technical report, Department of Chemistry, The Chinese University of Hong Kong, 2000.

[174] A.W. Moore. Highly oriented pyrolytic graphite. *Chem. Phys. Carbon*, 11 (69-187), 1973.

[175] R.C. Tatar and S. Rabii. Electronic properties of graphite: A unified theoretical study. *Phys. Rev. B*, 25(6):4126, 1982.

[176] J.J. Olivero and R.L. Longbothum. Empirical fits to the voigt line width: A brief review. *J. Quant. Spectrosc. Radiat. Transfer*, 17(2):233–236, 1977.

[177] D.g Wei, Y. Liu, Y. Wang, H. Zhang, L. Huang, and G. Yu. Synthesis of N-doped graphene by chemical vapor deposition and its electrical properties. *Nano Lett.*, 9(5):1752–1758, 2009.

[178] T.S. Wang, J.J. Ding, R. Cheng, H.B. Peng, X. Lu, and Y.T. Zhao. Diamond-like carbon produced by highly charged ions impact on highly oriented pyrolytic graphite. *Nucl. Instrum. Methods Phys. Res., Sect. B*, 272:15–17, 2012.

[179] C. Zhang, L. Fu, N. Liu, M. Liu, Y. Wang, and Z. Liu. Synthesis of nitrogen-doped graphene using embedded carbon and nitrogen sources. *Adv. Mater.*, 23 (8):1020–1024, 2011.

[180] W. Ju, M. Favaro, C. Durante, L. Perini, S. Agnoli, O. Schneider, U. Stimming, and G. Granozzi. Pd nanoparticles deposited on nitrogen-doped HOPG: New insights into the pd-catalyzed oxygen reduction reaction. *Electrochim. Acta*, 141:89–101, 2014.

[181] M.E. Orazem and B. Tribollet. *Electrochemical impedance spectroscopy*, volume 48. John Wiley & Sons, 2011.

[182] G.J. Brug, A.L.G. Van Den Eeden, M. Sluyters-Rehbach, and J.H. Sluyters. The analysis of electrode impedances complicated by the presence of a constant phase element. *J. Electroanal. Chem. Interfacial Electrochem.*, 176(1):275–295, 1984.

[183] K.K. Cline, M.T. McDermott, and R.L. McCreery. Anomalously slow electron transfer at ordered graphite electrodes: Influence of electronic factors and reactive sites. *J. Phys. Chem.*, 98(20):5314–5319, 1994.

[184] M.F. Juarez, L. Mohammadzadeh, and W. Schmickler. The double-layer capacity of nitrogen-doped graphite. *Electrochem. Commun.*, 36:50–52, 2013.

[185] H. Duncan and A. Lasia. Separation of hydrogen adsorption and absorption on Pd thin films. *Electrochim. Acta*, 53(23):6845–6850, 2008.

[186] G. Jerkiewicz. Hydrogen sorption AT / IN electrodes. *Prog. Surf. Sci.*, 57(2): 137–186, 1998.

[187] A. Czerwiński. The adsorption of carbon oxides on a palladium electrode from acidic solution. *J. Electroanal. Chem.*, 379(1):487–493, 1994.

[188] A.E. Bolzán. An interpretation of the different processes involved in the electroreduction of thick palladium oxide films. *J. Electroanal. Chem.*, 437(1): 199–208, 1997.

[189] L.H. Dall'Antonia, G. Tremiliosi-Filho, and G. Jerkiewicz. Influence of temperature on the growth of surface oxides on palladium electrodes. *J. Electroanal. Chem.*, 502(1):72–81, 2001.

[190] A.J. Zhang, M. Gaur, and V.I. Birss. Growth of thin, hydrous oxide films at Pd electrodes. *J. Electroanal. Chem.*, 389(1):149–159, 1995.

[191] L. Fang, Q. Tao, M. Li, L. Liao, D. Chen, and Y. Chen. Determination of the real surface area of palladium electrode. *Chin. J. Chem. Phys.*, 23(5):543–548, 2010.

[192] J. Liu, K. Sasaki, and S.M. Lyth. Electrochemical oxygen reduction on metal-free nitrogen-doped graphene foam in acidic media. *ECS Trans.*, 58(1):1529–1540, 2013.

[193] K.R. Lee, K.U. Lee, J.W. Lee, B.T. Ahn, and S.I. Woo. Electrochemical oxygen reduction on nitrogen doped graphene sheets in acid media. *Electrochem. Commun.*, 12(8):1052–1055, 2010.

[194] L. Feng, L. Yang, Z. Huang, J. Luo, M. Li, D. Wang, and Y. Chen. Enhancing electrocatalytic oxygen reduction on nitrogen-doped graphene by active sites implantation. *Sci. Rep.*, 3, 2013.

[195] L. Lai, J.R. Potts, D. Zhan, L. Wang, C.K. Poh, C. Tang, H. Gong, Z. Shen, J. Lin, and R.S. Ruoff. Exploration of the active center structure of nitrogen-doped graphene-based catalysts for oxygen reduction reaction. *Energy & Environmental Science*, 5(7):7936–7942, 2012.

[196] Y. Shao, S. Zhang, M.H. Engelhard, G. Li, G. Shao, Y. Wang, J. Liu, I. A Aksay, and Y. Lin. Nitrogen-doped graphene and its electrochemical applications. *J. Mater. Chem.*, 20(35):7491–7496, 2010.

[197] L. Qu, Y. Liu, J.B. Baek, and L. Dai. Nitrogen-doped graphene as efficient metal-free electrocatalyst for oxygen reduction in fuel cells. *ACS Nano*, 4(3): 1321–1326, 2010.

[198] M. Raşa, B.W.M. Kuipers, and A.P. Philipse. Atomic force microscopy and magnetic force microscopy study of model colloids. *J. Colloid Interface Sci.*, 250(2):303–315, 2002.

[199] M.H. Seo, S.M. Choi, J.K. Seo, S.H. Noh, W.B. Kim, and B. Han. The graphene-supported palladium and palladium–yttrium nanoparticles for the oxygen reduction and ethanol oxidation reactions: Experimental measurement and computational validation. *Appl. Catal., B*, 129:163–171, 2013.

[200] L.C. Pauling. *The chemical bond.* Cornell Univ., 1967.

[201] M. Favaro, S. Agnoli, L. Perini, C. Durante, A. Gennaro, and G. Granozzi. Palladium nanoparticles supported on nitrogen-doped HOPG: a surface science and electrochemical study. *Phys. Chem. Chem. Phys.*, 15(8):2923–2931, 2013.

[202] T. Maoka and M. Enyo. Hydrogen absorption by palladium electrode polarized in sulfuric acid solution containing surface active substances- II. the anodic region. *Electrochim. Acta*, 26(5):615–619, 1981.

[203] A. Lasia. On the mechanism of the hydrogen absorption reaction. *J. Electroanal. Chem.*, 593(1):159–166, 2006.

[204] E.A. Owen and J.I. Jones. The effect of pressure and temperature on the occlusion of hydrogen by palladium. *Proc. Phys. Soc.*, 49(5):587, 1937.

[205] F.A. Lewis. The palladium–hydrogen system. III. - alloy systems and hydrogen permeation. *Platinum. Met. Rev.*, 26(3):121–128, 1982.

[206] R.C. Salvarezza, M.C. Montemayor, E. Fatas, and A.J. Arvia. Electrochemical study of hydrogen absorption in polycrystalline palladium. *J. Electroanal. Chem. Interfacial Electrochem.*, 313(1):291–301, 1991.

[207] S. Schuldiner, G.W. Castellan, and J.P. Hoare. Electrochemical behavior of the palladium-hydrogen system. I. potential-determining mechanisms. *J. Chem. Phys.*, 28(1):16–19, 1958.

[208] H.P. Stout. The electrodeposition of hydrogen on palladium. *Discuss. Faraday Soc.*, 1:107–114, 1947.

[209] W. Zhang, Z. Zhang, X. Zhang, and F. Wu. Numerical simulation of hydrogen (deuterium) absorption into β-phase hydride (deuteride) palladium electrodes under galvanostatic conditions. *J. Electroanal. Chem.*, 474(2):123–129, 1999.

[210] V.A. Vons, H. Leegwater, W.J. Legerstee, S.W.H. Eijt, and A. Schmidt-Ott. Hydrogen storage properties of spark generated palladium nanoparticles. *Int. J. Hydrogen Energy*, 35(11):5479–5489, 2010.

[211] M. Baldauf and D.M. Kolb. A hydrogen adsorption and absorption study with ultrathin Pd overlayers on Au (111) and Au (100). *Electrochim. Acta*, 38(15): 2145–2153, 1993.

[212] D. Jose and B.R. Jagirdar. Nature of hydrogen atom trapped inside palladium lattice. *Int. J. Hydrogen Energy*, 35(13):6804–6811, 2010.

[213] L. Xiao, L. Zhuang, Y. Liu, and J. Lu. Activating Pd by morphology tailoring for oxygen reduction. *J. Am. Chem. Soc.*, 131(2):602–608, 2008.

[214] Y. Cai, C. Ma, Y. Zhu, J.X. Wang, and R.R. Adzic. Low-coordination sites in oxygen-reduction electrocatalysis: their roles and methods for removal. *Langmuir*, 27(13):8540–8547, 2011.

[215] M. Hasik, A. Bernasik, A. Drelinkiewicz, K. Kowalski, E. Wenda, and J. Camra. XPS studies of nitrogen-containing conjugated polymers–palladium systems. *Surf. Sci.*, 507:916–921, 2002.

[216] V.B. Parambhath, R. Nagar, and S. Ramaprabhu. Effect of nitrogen doping on hydrogen storage capacity of palladium decorated graphene. *Langmuir*, 28 (20):7826–7833, 2012.

[217] X. Xu, Y. Li, Y. Gong, P. Zhang, H. Li, and Y. Wang. Synthesis of palladium nanoparticles supported on mesoporous N-doped carbon and their catalytic ability for biofuel upgrade. *J. Am. Chem. Soc.*, 134(41):16987–16990, 2012.

[218] L.A. Kibler. Hydrogen electrocatalysis. *ChemPhysChem*, 7(5):985–991, 2006.

[219] A. Roudgar and A. Groß. Local reactivity of thin Pd overlayers on Au single crystals. *J. Electroanal. Chem.*, 548:121–130, 2003.

[220] M. Baldauf and D.M. Kolb. Formic acid oxidation on ultrathin Pd films on Au (hkl) and Pt (hkl) electrodes. *J. Phys. Chem.*, 100(27):11375–11381, 1996.

[221] T.H.M. Housmans and M.T.M. Koper. CO oxidation on stepped Rh [n (111)×(111)] single crystal electrodes: a chronoamperometric study. *J. Electroanal. Chem.*, 575(1):39–51, 2005.

[222] A.M. El-Aziz and L.A. Kibler. Influence of steps on the electrochemical oxidation of CO adlayers on Pd (111) and on Pd films electrodeposited onto Au (111). *J. Electroanal. Chem.*, 534(2):107–114, 2002.

[223] I.V. Yudanov, R. Sahnoun, K.M. Neyman, N. Rösch, J. Hoffmann, S. Schauermann, V. Johanek, H. Unterhalt, G. Rupprechter, J. Libuda, et al. CO adsorption on Pd nanoparticles: Density functional and vibrational spectroscopy studies. *J. Phys. Chem. B*, 107(1):255–264, 2003.

[224] H. Conrad, G.l. Ertl, and J. Küppers. Interactions between oxygen and carbon monoxide on a Pd (111) surface. *Surf. Sci.*, 76(2):323–342, 1978.

[225] K.A. Friedrich, F. Henglein, U. Stimming, and W. Unkauf. Size dependence of the CO monolayer oxidation on nanosized Pt particles supported on gold. *Electrochim. Acta*, 45(20):3283–3293, 2000.

[226] F.J. Vidal-Iglesias, R.M. Aran-Ais, J. Solla-Gullon, E. Garnier, E. Herrero, A. Aldaz, and J.M. Feliu. Shape-dependent electrocatalysis: formic acid electrooxidation on cubic Pd nanoparticles. *Phys. Chem. Chem. Phys.*, 14(29): 10258–10265, 2012.

[227] S. Choi, J.A. Herron, J. Scaranto, H. Huang, Y. Wang, X. Xia, T. Lv, J. Park, H. Peng, M. Mavrikakis, et al. A comprehensive study of formic acid oxidation on palladium nanocrystals with different types of facets and twin defects. *ChemCatChem*, 7(14):2077–2084, 2015.

[228] N. Hoshi, M. Nakamura, and K. Kida. Structural effects on the oxidation of formic acid on the high index planes of palladium. *Electrochem. Commun.*, 9 (2):279–282, 2007.

[229] C.M.Y. Yue and K.H. Lim. Adsorption of formic acid and its decomposed intermediates on (100) surfaces of pt and pd: a density functional study. *Catal. Lett.*, 128(1-2):221–226, 2009.

[230] M. Arenz, V. Stamenkovic, T.J. Schmidt, K. Wandelt, P.N. Ross, and N.M. Marković. The electro-oxidation of formic acid on Pt-Pd single crystal bimetallic surfaces. *Phys. Chem. Chem. Phys.*, 5(19):4242–4251, 2003.

[231] D. Gao, H. Zhou, J. Wang, S. Miao, F. Yang, G. Wang, J. Wang, and X. Bao. Size-dependent electrocatalytic reduction of CO2 over Pd nanoparticles. *J. Am. Chem. Soc.*, 137(13):4288–4291, 2015.

[232] H.A. Gasteiger, W. Gu, R. Makharia, M.F. Mathias, and B. Sompalli. *Beginning-of-life MEA performance - efficiency loss contributions.* Wiley Online Library, 2003.

[233] H.A. Gasteiger, S.S. Kocha, B. Sompalli, and F.T. Wagner. Activity benchmarks and requirements for Pt, Pt-alloy, and non-Pt oxygen reduction catalysts for PEMFCs. *Appl. Catal. B*, 56(1):9–35, 2005.

[234] P. He, H. Liu, Z. Li, and J. Li. Electrodeposition of platinum in room-temperature ionic liquids and electrocatalytic effect on electro-oxidation of methanol. *J. Electrochem. Soc.*, 152(4):E146–E153, 2005.

[235] D. Zhang, W.C. Chang, T. Okajima, and T. Ohsaka. Electrodeposition of platinum nanoparticles in a room-temperature ionic liquid. *Langmuir*, 27(23): 14662–14668, 2011.

[236] J. Snyder, K. Livi, and J. Erlebacher. Oxygen reduction reaction performance of [MTBD][beti]-encapsulated nanoporous NiPt alloy nanoparticles. *Adv. Funct. Mater.*, 23(44):5494–5501, 2013.

[237] J. Snyder, T. Fujita, M.W. Chen, and J. Erlebacher. Oxygen reduction in nanoporous metal–ionic liquid composite electrocatalysts. *Nat. Mater.*, 9(11): 904–907, 2010.

[238] C. Chen, Y. Kang, Z. Huo, Z. Zhu, W. Huang, H. L Xin, J.D. Snyder, D. Li, J.A. Herron, M. Mavrikakis, et al. Highly crystalline multimetallic nanoframes with three-dimensional electrocatalytic surfaces. *Science*, 343(6177):1339–1343, 2014.

List of Figures

List of Tables